

**Common Metabolites, Distinct Pathways:
The Use of High-field NMR Spectroscopy
Metabolomics in
Neurology and Immunology**

Dissertation

der Mathematisch-Naturwissenschaftlichen Fakultät
der Eberhard Karls Universität Tübingen
zur Erlangung des Grades eines
Doktors der Naturwissenschaften
(Dr. rer. nat.)

vorgelegt von
MSc, BEng Laimdota Zizmare
aus Alūksne, Lettland

Tübingen
2023

Gedruckt mit Genehmigung der Mathematisch-Naturwissenschaftlichen Fakultät der
Eberhard Karls Universität Tübingen.

Tag der mündlichen Qualifikation:

21.11.2023

Dekan:

Prof. Dr. Thilo Stehle

1. Berichterstatter/-in:

Prof. Dr. Bernd Pichler

2. Berichterstatter/-in:

Prof. Dr. Stefan Laufer

TABLE OF CONTENTS

I. SUMMARY	5
II. ZUSAMMENFASSUNG	7
III. LIST OF PUBLICATIONS	10
A. ACCEPTED PUBLICATIONS	10
i. First-author publications	10
ii. Shared first-author publication	10
iii. Collaborative co-authorships	10
B. SUBMITTED MANUSCRIPTS	12
i. Shared first-author publication	12
ii. Collaborative co-authorships	12
IV. AUTHOR CONTRIBUTIONS	13
A. PUBLICATION I	13
B. PUBLICATION II	14
V. LIST OF ABBREVIATIONS	16
VI. LIST OF FIGURES AND TABLES	18
1. INTRODUCTION	19
1.1. METABOLOMICS AS A TOOL FOR METABOLISM AND PHENOTYPE STUDIES	19
1.2. METABOLOMICS AND METABOLIC PATHWAYS	23
1.4. PRINCIPLES OF NMR SPECTROSCOPY	27
1.5. SAMPLES AND PREPARATION WORKFLOW	31
1.6. INFLAMMATION, IMMUNOLOGY AND IMMUNOMETABOLISM IN METABOLOMICS	36
1.7. GUT MICROBIOTA AND METABOLOMICS	36
1.8. KEY TOPICS OF THIS THESIS	39
2. OBJECTIVES AND EXPECTED OUTCOME	40
3. RESULTS	42
3.1. PUBLICATION I	42
3.2. PUBLICATION II	64
4. DISCUSSION	106

4.1.	REDOX METABOLISM	107
4.2.	ENERGY METABOLISM	108
4.3.	MEMBRANE LIPID SYNTHESIS AND BREAKDOWN PATHWAYS.....	110
4.4.	IDENTICAL METABOLITES BUT DIFFERENT CONDITIONS	111
4.5.	KETONE BODIES AND METABOLOMICS	111
4.6.	ONE-CARBON METABOLISM: FOLATE AND METHIONINE CYCLE	112
4.7.	GUT MICROBIOTA, DYSBIOSIS AND METABOLOMICS	113
4.8.	CONCLUSIONS AND OUTLOOK	114
5.	REFERENCES	116
6.	ACKNOWLEDGEMENTS.....	136
7.	APPENDIX	137
7.1.	CURRICULUM VITAE	139
7.2.	CO-AUTHORED PUBLICATIONS	141
7.3.	POSTER PRESENTATIONS.....	151

Practical work and supervision of this thesis was carried out between July 2019 and December 2022 in the Metabolomics and Systems Medicine research group at the Werner Siemens Imaging Center, Department of Preclinical Imaging and Radiopharmacy, University Hospital Tübingen, led by Dr. Christoph Trautwein.

I. Summary

While current metabolic imaging approaches, such as positron emission tomography, hyperpolarized magnetic resonance (MR) imaging and localized MR spectroscopy, provide information on localization and visualization of metabolically-active tissues and metabolites *in vivo*, additional *ex vivo* validation and investigations are used for a deeper molecular elucidation of biological events. Metabolomics provides an insight into ongoing cellular processes in a living organism by analyzing and investigating alterations of small molecule polar compounds and lipids. Many of these alterations are directly affected by environmental and genetic factors, such as RNA expression.

In recent years, besides mass spectrometry-based approaches, nuclear magnetic resonance (NMR) spectroscopy has been successfully established as an important analytical technique in metabolomics due to its non-destructive nature, high reproducibility and generation of absolute concentration values. NMR, furthermore, is one of the closest approaches to established *in vivo* MR technologies allowing a direct link from *in vivo* MR spectra to *ex vivo* NMR. NMR spectroscopy is, therefore, a perfect tool to quantitatively analyze small polar molecules, such as amino acids, short-chain fatty acids, energy, growth and redox metabolism-related compounds as well as metabolites of gut microbiota and lipids.

The broad variety of NMR applications has led to the development of increased sensitivity probes and fully-automated commercial assays. Inventions, such as the ultrasensitive 1.7 mm microprobe, have made it possible to analyze smaller tissue or biofluid amounts of precious samples, including small preclinical organs and tissues or patient tumor biopsies, with appropriate precision and minimal tissue metabolite dilution.

In this thesis project, we aimed to investigate and characterize specific metabolic alterations to clinically-relevant immunological and neurological conditions by employing NMR spectroscopy-based metabolomics. In line with the previous preclinical imaging work, two preclinical models – i) acute and chronic inflammation progression and ii) neurological gut-brain axis – were selected as core examples for a comprehensive *ex vivo* metabolome characterization.

In the first project i), the delayed-type hypersensitivity reaction (DTHR) mouse model was subjected to a dynamic immunometabolism and inflammation characterization

with the hypothesizing that the inflammation progression is related to dynamic systemic alterations for which metabolomics readout can elucidate the ongoing biomolecular events. The inflammation was induced by repeated contact tissue challenges on mouse ear tissue. Different metabolic patterns were identified arising from either acute or chronic DTHR that correlated with the resident immune cell response and further active cell infiltration to the inflamed location. Distinct metabolic events, including switches between the scavenging of reactive oxygen and nitrogen species, facilitated the detailed characterization of the detrimental effect of prolonged inflammation and the emergency state of the system. Continuous inflammation led to limited access to substrates for energy metabolism. Chronic DTHR further required alternative anabolic pathways to sustain the cellular growth and repair process.

In the second project ii), a gastric bypass surgery rat model was used for the metabolomic characterization of gut microbiota metabolites and potential gut-brain axis communication. We hypothesized that gut-brain axis communication could be responsible for the beneficial lasting effects after surgical intervention. Rats were fed a liquid sucrose diet to induce obesity since high-sugar beverages and liquid caloric consumption have become a pandemic in the adolescent population hindered by the general concept of the Western diet. Plasma and feces were studied as gut metabolism readout and further analyzed in the context of fecal microbiome, hepatic lipid profiles, and brain activity imaging to obtain a holistic overview of the systemic effects of the Roux-En-Y gastric bypass (RYGB) surgery. The gut metabolite γ -aminobutyrate (GABA) was increased in surgery animal feces together with GABA-producing microbiota species abundance compared to sham controls. RYGB surgery animals showed greater neuronal activation in midbrain regions that are known to be rich in GABAergic cells, pointing towards an activated gut-brain communication resulting from the surgery.

Two main projects demonstrate how the usage of optimized preanalytical procedures, together with harmonized analytical NMR workflows provide reproducible data with comprehensive insight into the metabolism of an organism *ex vivo*. Further outlook includes metabolomics result integration in the context of *in vivo* imaging data, as the combined result evaluation can facilitate the understanding of health and disease progression, and help to streamline diagnostic, such as novel radiotracer development, and therapeutic approaches.

II. Zusammenfassung

Derzeitige präklinische bildgebenden Verfahren ermöglichen die Lokalisierung und Visualisierung von stoffwechselaktivem Gewebe in vivo, jedoch mit begrenzter Auflösung und geringem molekularbiologischen Informationsgehalt. Deshalb werden zunehmend zusätzliche ex vivo Untersuchungen zur detaillierten Aufklärung molekularer und biologischer Ereignisse eingesetzt. Die Metabolomik bietet dabei einen Einblick in laufende zelluläre Prozesse in einem lebenden Organismus durch die Messung von Konzentrationsänderungen polarer und unpolarer Metaboliten. Diese Metaboliten sind das direkte Resultat von Gen- und RNA-Expression und werden außerdem durch Umwelt- und genetischen Faktoren stetig beeinflusst.

Als wichtige Analysetechnik in der Metabolomik hat sich in den letzten Jahren aufgrund ihrer zerstörungsfreien Natur, ihrer hohen Reproduzierbarkeit und der Erzeugung absoluter Konzentrationswerte die Kernspinresonanz- (NMR) Spektroskopie neben der Massenspektrometrie etabliert. Die NMR-Spektroskopie ist das perfekte Instrument zur quantitativen Analyse kleiner polarer Moleküle wie z.B. Aminosäuren, kurzkettige Fettsäuren, Energie-, Wachstums- und Redoxstoffwechselbezogene Verbindungen sowie Metaboliten der Darmflora und Lipide. Der breite Anwendungsbereich der NMR-Spektroskopie hat hierbei zur Entwicklung von Messsonden (= Probenköpfe) höherer Empfindlichkeit und sogar vollautomatischen kommerziellen Assays geführt. Weiterentwicklungen wie der ultrasensitive 1,7-mm-Mikroprobenkopf haben es möglich gemacht, geringste Gewebe- oder Bioflüssigkeitsmengen wertvoller Proben, einschließlich kleiner präklinischer Organe und Gewebe oder Tumorbiopsien von Patienten, mit angemessener Präzision und minimaler Verdünnung zu analysieren.

Dieses Dissertationsprojekt hatte zum Ziel, spezifische metabolische Veränderungen bei klinisch relevanten immunologischen und neurologischen Erkrankungen mit Hilfe von NMR-basierter Metabolomik zu untersuchen und zu charakterisieren. In Übereinstimmung mit vorangegangenen präklinischen Bildgebungsarbeiten wurden zwei präklinische Modelle als Kernbeispiele für eine umfassende ex vivo Metabolom-Charakterisierung ausgewählt: i) die akute und chronische Entzündungsprogression im Mausmodell und ii) die neurologische Darm-Hirn-Achse in der Ratte.

In i) wurde das Mausmodell der verzögerten Überempfindlichkeitsreaktion (DTHR) einer dynamischen Charakterisierung des Immunstoffwechsels und von

Entzündungsprozessen unterzogen. Hier wurde die Hypothese aufgestellt, dass das Fortschreiten einer Entzündung mit dynamischen systemischen Veränderungen des Gewebe-Metaboloms zusammenhängt. Im Modell wurde die Entzündung durch wiederholten Allergen-Gewebekontakt an Mäuseohren ausgelöst. In den Gewebeproben wurden anschließend verschiedene Stoffwechsellmuster identifiziert, die entweder durch akute oder chronische DTHR entstehen und mit der Aktivierung ansässiger Immunzellen und der weiteren aktiven Zellinfiltration an den Entzündungsherd korrelieren. Unterschiedliche dynamische Stoffwechselereignisse, einschließlich des Wechsels zwischen dem Abfangen reaktiver Sauerstoff- und Stickstoffspezies, ermöglichen eine detaillierte Charakterisierung schädlicher Auswirkungen einer anhaltenden Entzündung und systemischen Notfallzustands. Wir identifizierten außerdem, dass anhaltende Entzündungen zu einer eingeschränkten Zufuhr von Substraten des Energiestoffwechsels führt. Chronische DTHR hingegen resultiert in der Nutzung alternativer anabole Wege, um den zellulären Wachstums- und Reparaturprozess aufrechtzuerhalten.

In ii) kam ein Rattenmodell für Magenbypass-Operationen zum Einsatz. Hier untersuchten wir u.a. Metaboliten der Darmflora und deren potenzielle Kommunikation zwischen Darm und Gehirn. Wir stellten die Hypothese auf, dass die Darm-Hirn-Achse für gewichtsreduzierende vorteilhafte dauerhafte Effekte nach dem chirurgischen Eingriff verantwortlich sein könnte. Dies wurde durch Metabolom-Messungen und die Bildgebung der Gehirnaktivität bestätigt. Im Versuch wurden Ratten mit einer flüssigen Saccharose-Diät gefüttert, um die allgemeinen Konzepte der Adipositas zu untersuchen. Dies orientiert sich eng an der Realität, denn der Verzehr von zuckerhaltigen Getränken und flüssigen Kalorien hat sich zu einer Pandemie entwickelt, insbesondere in der jugendlichen Bevölkerung. Plasma und Fäkalien wurden als Indikatoren für den Darmstoffwechsel untersucht und im Zusammenhang mit dem fäkalen Mikrobiom, hepatischen Lipidprofilen und der Bildgebung des Gehirns analysiert, um einen ganzheitlichen und umfassenden Überblick über die systemischen Auswirkungen der Roux-En-Y-Magenbypass-Operation (RYGB) zu erhalten. Die Veränderungen der fäkalen Metaboliten nach der RYGB-Operation korrelierten mit den Veränderungen der mikrobiellen Artenvielfalt. So war beispielsweise der Darmmetabolit γ -Aminobutyrat (GABA) in den Fäkalien der operierten Tiere zusammen mit der Häufigkeit GABA-produzierender Mikrobiota im Vergleich zu Scheinkontrollen deutlich erhöht. Zudem deutete eine erhöhte 3-

Hydroxybutyrat-Konzentration in der RYGB-Gruppe auf eine hochregulierte Lipolyse hin. Dies wurde durch ein erhöhtes Verhältnis geradkettiger und ungeradkettiger Fettsäuren in der Leber sowie einen verringerten Leptinspiegel bestätigt. Die Tiere der RYGB-Gruppe wiesen außerdem eine erhöhte neuronale Aktivierung in Mittelhirnregionen auf, die bekanntermaßen reich an GABA-ergen Zellen sind, was auf eine veränderte Darm-Hirn-Kommunikation infolge des operativen Bypass-Eingriffs hindeutet.

Diese zwei Projektbeispiele zeigen, wie die Verwendung standardisierter und optimierter präanalytischer Verfahren zusammen mit harmonisierten analytischen Arbeitsabläufen in der NMR-Spektroskopie und der statistische Analyse die Gewinnung reproduzierbarer und zuverlässiger Informationen ermöglicht, welche einen umfassenden Einblick in den Stoffwechsel eines Organismus ex vivo erlauben. Weitere Anwendungsbeispiele über i) und ii) hinaus umfassen die Integration von Metabolomics-Daten im Kontext der in vivo Bildgebung. Hier kann eine kombinierte Ergebnisauswertung aus ex vivo und in vivo Daten das Verständnis von Gesundheit und Krankheitsverlauf verbessern und dazu beitragen, künftige diagnostische Ansätze, wie z.B. die Entwicklung neuer Radiotracer und therapeutische Ansätze zu vereinfachen und beschleunigen.

III. List of publications

a. Accepted publications

i. First-author publications

Zizmare, L.; Mehling, R.; Gonzalez-Menendez, I.; Lonati, C.; Quintanilla-Martinez, L.; Pichler, B.J.; Kneilling, M.; Trautwein, C. Acute and chronic inflammation alter immunometabolism in a cutaneous delayed-type hypersensitivity reaction (DTHR) mouse model. *Nature Communications Biology* 5, 1250 (2022). <https://doi.org/10.1038/s42003-022-04179-x>

Zizmare, L.; Boyle, C. N.; Buss, S.; Louis, S.; Kuebler, L.; Mulay, K.; Krüger, R.; Steinhauer, L.; Mack, I.; Rodriguez Gomez, M.; Herfert, K.; Ritze, Y.; Trautwein, C. Roux-en-Y gastric bypass (RYGB) surgery during high liquid sucrose diet leads to gut microbiota-related systematic alterations. *International Journal of Molecular Science*, 23, (3), 1126, (2022). <https://doi.org/10.3390/ijms23031126>

ii. Shared first-author publication

Bus, C.*, **Zizmare, L.***, Feldkaemper, M., Geisler, S., Zarani, M., Schaedler, A., Klose, F., Admard, J., Mageean, C., Arena, G., Fallier-Becker, P., Ugun-Klusek, A., Maruszczak, K. K., Kapolou, K., Schmid B., Rapaport, B., Ueffing, M., Casadei, N., Krüger, R., Gasser, T., Vogt-Weisenhorn, D., Kahle, P. J., Trautwein, C., Gloeckner, C. J., Fitzgerald, J. C. Human dopaminergic neurons lacking PINK1 exhibit disrupted dopamine metabolism related to vitamin B6 co-factors. *iScience*, 23, (12), 101797 (2020). (* equal contribution) <https://doi.org/10.1016/j.isci.2020.101797>

iii. Collaborative co-authorships

Trautwein, C.; **Zizmare, L.**; Mäurer, I.; Bender, B.; Bayer, B.; Ernemann, U.; Tatagiba, M.; Grau, S. J.; Pichler, B. J.; Skardelly, M.; Tabatabai, G. Tissue metabolites in diffuse glioma and their modulations by IDH1 mutation, histology and treatment. *JCI Insight*, 7, (3), e153526 (2022). <https://doi.org/10.1172/jci.insight.153526>

Laugwitz, L.; **Zizmare, L.**; Santhanakumaran, V.; Cannet, C.; Böhringer, J.; Okun, J.G.; Spraul, M.; Krägeloh-Mann, I.; Groeschel, S.; Trautwein, C. Identification of neurodegeneration indicators and disease progression in metachromatic leukodystrophy using quantitative NMR-based urinary metabolomics. *JIMD Reports*, 1-13, (2022). <https://doi.org/10.1002/jmd2.12273>

Lonati, C.; Dondossola, D.; **Zizmare, L.**; Battistin, M.; Wüst, L.; Vivona, L.; Carbonaro, M.; Zanella, A.; Gatti, S.; Schlegel, A.; Trautwein, C. Quantitative metabolomics of tissue,

perfusate, and bile from rat livers subjected to normothermic machine perfusion. *Biomedicines* 10, (3), 538, (2022). <https://doi.org/10.3390/biomedicines10030538>

Yang, Q.; Bae, G.; Nadiradze, G.; Castagna, A.; Berezhnoy, G.; **Zizmare, L.**; Kulkarni, A.; Singh, Y.; Weinreich, F. J.; Kommos, S.; Reymond, M. A.; Trautwein, C. Acidic ascites inhibits ovarian cancer cell proliferation and correlates with the metabolomic, lipidomic and inflammatory phenotype of human patients. *Journal of Translational Medicine* 20, 581 (2022). <https://doi.org/10.1186/s12967-022-03763-3>

Feldmann, J.; Martin, P.; Bender, B.; Laugwitz, L.; **Zizmare, L.**; Trautwein, C.; Krägeloh-Mann, I.; Klose, U.; Groeschel, S. MR-spectroscopy in metachromatic leukodystrophy: A model free approach and clinical correlation. *NeuroImage: Clinical*, 37, 103296 (2023). <https://doi.org/10.1016/j.nicl.2022.103296>

Schumacher, L.; Slimani, R.; **Zizmare, L.**; Ehlers, J.; Kleine Borgmann, F.; Fitzgerald, J.C.; Fallier-Becker, P.; Beckmann, A.; Grißmer, A.; Meier, C.; El-Ayoubi, A.; Devraj, K.; Mittelbronn, M.; Trautwein, C.; Naumann, U. TGF-Beta Modulates the Integrity of the Blood Brain Barrier In Vitro, and Is Associated with Metabolic Alterations in Pericytes. *Biomedicines*, 11, 214 (2023). <https://doi.org/10.3390/biomedicines11010214>

Christensen, G.; Chen, Y.; Urimi, D.; **Zizmare, L.**; Trautwein, C.; Schipper, N.; Paquet-Durand, F. Pyruvate-conjugation of PEGylated liposomes for targeted drug delivery to retinal photoreceptors. *Biomedicine & Pharmacotherapy*, 163, 114717 (2023). <https://doi.org/10.1016/j.biopha.2023.114717>

Mehling, R.; Schwenck, J.; Lemberg, C.; Trautwein, C.; **Zizmare, L.**; Kramer, D.; Müller, A.; Fehrenbacher, B.; Gonzalez-Menendez, I.; Quintanilla-Martinez, L.; Schröder, K.; Brandes, R. P.; Schaller, M.; Ruf, W.; Eichner, M.; Ghoreschi, K.; Röcken, M.; Pichler, B. J.; Kneilling, M. Immunomodulatory role of reactive oxygen species and nitrogen species during T cell-driven neutrophil-enriched acute and chronic cutaneous delayed-type hypersensitivity reactions. *Theranostics* 11, (2), 470 – 490 (2021). doi:10.7150/thno.51462. <http://www.thno.org/v11p0470.htm>

Singh, Y.; Trautwein, C.; Dhariwal, A.; Salker M. S.; Alauddin, M.; **Zizmare, L.**; Pelzl, L.; Feger, M.; Admard, J.; Casadei, N.; Föller, M.; Pachauri, V.; Park, D. S.; Mak, T. W.; Frick, J.; Wallwiener, D.; Brucker, S. Y.; Lang, F. & Riess, O. DJ-1 (Park7) affects the gut microbiome, metabolites and the development of innate lymphoid cells (ILCs). *Nature Scientific Reports* 10, 16131 (2020). <https://doi.org/10.1038/s41598-020-72903-w>

Kotsiliti, E.; Leone, V.; Schühle, S.; Govaere, O.; Li, H.; Wolf, M.; Horvatic, H.; Bierwirth, S.; Hundertmark, J.; Inverso, D.; **Zizmare, L.**; Sarusi-Portuguez, A.; Gupta, R.; O’Conor, T.; Giannou, A. D.; Shiri, A. M.; Beccaria, M. G.; Rennert, C.; Pfister, D.; Öllinger, R.; Gadjalova, I.; Ramadori, P.; Rahbari, M.; Rahbari, N.; Healy, M.; Fernandez, M.; Yahoo, N.; Janzen, J.; Singh, I.; Fan, C.; Liu, X.; Rau, M.; Feuchtenberger, M.; Schwaneck, E.; Wallace, S. J.; Cockell, S.; Wilson-Kanamori, J.; Ramachandran, P.; Kho, C.; Kendall, T. J.; Leblond, A-L.; Keppler, S. J.; Bielecki, P.; Steiger, K.; Hofmann, M.; Rippe, K.; Zitzlesberger, H.; Weber, A.; Malek, N.; Luedde, T.; Vucur, M.; Augustin, H. G.; Flavell, R.; Parnas, O.; Rad, R.; Pabst, O.; Henderson, N. C.; Huber, S.; Macpherson, A.; Knolle, P.; Claasen, M.; Geier, A.; Trautwein, C.; Unger, K.; Elinav, E.; Waisman, A.; Abdullah, Z.; Haller, D.; Tacke, F.; Anstee, Q. M.; Heikenwalder, M. Gastrointestinal B-cells license metabolic T-cell activation in NASH microbiota/antigen-independently and contribute to fibrosis by IgA-FcR signalling. *Journal of Hepatology*, 79, (2), 296-313 (2023). <https://doi.org/10.1016/j.jhep.2023.04.037>

b. Submitted manuscripts

i. Shared first-author publication

Chen, Y.*; **Zizmare, L.***; Calbiague, V.; Wang, L.; Yu, S.; Herberg, F. W.; Schmachtenberg, O.; Paquet-Durand, F.*; Trautwein, C.* The retina uncouples glycolysis and oxidative phosphorylation via Cori-, Cahill-, and mini-Krebs-cycle. <https://doi.org/10.7554/eLife.91141.1> (* equal contribution).

ii. Collaborative co-authorships

Gallage, S.; Ali, A.; Barragan Avila, J. E.; Seymen, N.; Ramadori, P.; Joerke, V.; **Zizmare, L.**, Kosla, J.; Li, X.; Focaccia, E.; Yousuf, S.; Sijmonsma, T.; Rahbari, M.; Kommoss, K. S.; Billeter, A.; Prokosch, S.; Rothermel, U.; Mueller, F.; Hetzer, J.; Heide, D.; Machauer, T.; Malek, N. P.; Longerich, T.; Rose, A. J.; Roth, S.; Schwenck, J.; Trautwein, C.; Karimi, M. M.; Heikenwalder, M. Beneficial effects of intermittent fasting in NASH and subsequent HCC development are executed by concerted PPAR α and PCK1 action in hepatocytes. Preprint: <https://doi.org/10.1101/2023.10.23.562885>

IV. Author contributions

a. Publication I

Zizmare, L.; Mehling, R.; Gonzalez-Menendez, I.; Lonati, C.; Quintanilla-Martinez, L.; Pichler, B.J.; Kneilling, M.; Trautwein, C. Acute and chronic inflammation alter immunometabolism in a cutaneous delayed-type hypersensitivity reaction (DTHR) mouse model. *Nature Communications Biology* 5, 1250 (2022). <https://doi.org/10.1038/s42003-022-04179-x>

Laimdota Zizmare

Sample preparation, NMR spectroscopy measurements, data processing, metabolite assignment, data analysis and interpretation, main writing of the manuscript, figure preparation.

Roman Mehling

Animal care and obtaining samples from animal model, discussion of results and interpretation, proofreading of the manuscript.

Dr. Irene Gonzalez-Menendez

Histology experiments and data interpretation, figure preparation, proofreading of the manuscript.

Dr. Caterina Lonati

Support on results interpretation, proofreading of the manuscript.

Prof. Dr. Leticia Quintanilla-Martinez

Histology data interpretation, proofreading of the manuscript.

Prof. Bernd J. Pichler

Generation, initiation, financing of the project, proofreading and final approval of the manuscript.

PD Dr. Manfred Kneilling

General idea generation, coordination, supervision, data interpretation, financing the project, proofreading and final approval of the manuscript, corresponding author.

Dr. Christoph Trautwein

General idea generation, coordination, data interpretation, supervision, proofreading and final approval of the manuscript, corresponding author.

b. Publication II

Zizmare, L.; Boyle, C. N.; Buss, S.; Louis, S.; Kuebler, L.; Mulay, K.; Krüger, R.; Steinhauer, L.; Mack, I.; Rodriguez Gomez, M.; Herfert, K.; Ritze, Y.; Trautwein, C. Roux-en-Y gastric bypass (RYGB) surgery during high liquid sucrose diet leads to gut microbiota-related systematic alterations. *International Journal of Molecular Science*, 23, (3), 1126, (2022). <https://doi.org/10.3390/ijms23031126>

Laimdota Zizmare

Plasma and feces sample preparation, NMR spectroscopy measurements, data processing, metabolite assignment, data analysis and interpretation, coordination, main writing of the manuscript, figure preparation.

Dr. Christina N. Boyle

Conceptualization, the gastric bypass surgery, discussion of results and interpretation, proofreading of the manuscript.

Sabrina Buss

Animal care, sample collection, functional [¹⁸F]FDG-PET data acquisition, analysis, discussion of results and interpretation, figure preparation, proofreading of the manuscript.

Dr. Sandrine Louis

Liver sample preparation and analysis, microbiota sequencing analysis, figure preparation, discussion of results and interpretation, writing and proofreading of the manuscript.

Laura Kuebler

Animal care, data interpretation, data visualization, proofreading the manuscript.

Ketki Mulay

Confocal microscopy, early gene (c-Fos) histochemical staining and data analysis, figure preparation, writing and proofreading of the manuscript.

Dr. Ralf Krüger

Liver sample analysis, discussion of results and interpretation, proofreading of the manuscript.

Lara Steinhauer

Immune and hormonal parameter profiling, data analysis, figure preparation, proofreading of the manuscript.

Dr. Isabelle Mack

Discussion of results and interpretation, proofreading of the manuscript.

Dr. Manuel Rodriguez Gomez

Methodology, immune and hormonal parameter profiling supervision, data interpretation, writing and proofreading of the manuscript.

Prof. Dr. Kristina Herfert

General idea generation, coordination, data interpretation, financing the project, supervision, proofreading of the manuscript.

Dr. Yvonne Ritze

General idea generation, initiation, coordination, supervision, data interpretation, financing the project, writing, proofreading and final approval of the manuscript, corresponding author.

Dr. Christoph Trautwein

Coordination, data interpretation, supervision, proofreading and final approval of the manuscript.

V. List of abbreviations

<u>Abbreviation</u>	<u>Full title</u>
1D	One dimensional
¹ H	Proton, hydrogen
2D	Two dimensional
3D	Three dimensional
3-HPPA	3-(3-hydroxyphenyl) propionate
¹³ C	Carbon-13 isotope
¹⁵ N	Nitrogen-15 isotope
¹⁹ F	Fluorine-19 isotope
³¹ P	Phosphorus-31
acetyl-CoA	Acetyl coenzyme A
ADP	Adenosine diphosphate
AI	Artificial intelligence
ANOVA	Analysis of variance
ATP	Adenosine triphosphate
B ₀	Magnetic field
BBO	Broadband observe
BCAA	Branched-chain amino acid
CNVs	Copy number variations
CoA	Coenzyme A
COSY	Correlation spectroscopy
CPMG	Carr-Purcell-Meiboom-Gill
DAD	Diode array detector
dd	Doublet of doublets
DJ-1	Parkinson's disease-related protein 7 (protein deglycase)
DNA	Deoxyribonucleic acid
DSS-d ₆	4,4-dimethyl-4-silapentane-1-sulfonate
dt	Doublet of triplets
DTHR	Delayed-type hypersensitivity reaction
ΔE	Difference in energy
ETC	Electron transport chain
FACS	Fluorescence-activated cell sorting
fid	Free induction decay
FT	Fourier transformation
GABA	γ-Aminobutyrate
GC	Gas chromatography
GHz	Gigahertz
GMP	Guanosine monophosphate
GPC	<i>sn</i> -Glycero-3-phosphocholine
GSSG	Glutathione disulfide
GWAS	Genome-wide association studies
HMBC	Heteronuclear multiple bond correlation

HMDB	Human metabolome database
HR-MAS	High-resolution magic angle spinning
HSQC	Heteronuclear single quantum coherence
IDH	Isocitrate dehydrogenase
JRES	J-resolved spectroscopy
KEGG	Kyoto encyclopaedia of genes and genomes
KO	Knockout
LC	Liquid chromatography
lncRNA	Long noncoding ribonucleic acid
M1	Pro-inflammatory macrophage
MHz	Megahertz
mRNA	Messenger ribonucleic acid
miRNA	Micro ribonucleic acid, single-stranded, non-coding RNA
MLD	Metachromatic leukodystrophy
MR	Magnetic resonance
MS	Mass spectrometry
MTBE	Methyl <i>tert</i> -butyl ether
MWAS	Metabolome-wide association studies
NAA	N-acetylaspartate
NAD ⁺	Nicotinamide adenine dinucleotide
NADP ⁺	Nicotinamide adenine dinucleotide phosphate
NMR	Nuclear magnetic resonance
NOESY	Nuclear Overhauser effect spectroscopy
OXPHOS	Oxidative phosphorylation
PCA	Principal component analysis
PET	Positron emission tomography
pH	Potential of hydrogen
PLS-DA	Partial least-squares discriminant analysis
ppm	Parts per million
Ptd	Phosphatidyl-
RNA	Ribonucleic acid
RONS	Reactive oxygen and nitrogen species
RYGB	Roux-En-Y gastric bypass
SCFA	Short-chain fatty acid
SNPs	Single nucleotide polymorphisms
SOPs	Standard operation protocols
STOCSY	Statistical total correlation spectroscopy
T	Tesla
TCA	Tricarboxylic acid
TMA	Trimethylamine
TMAO	Trimethylamine N-oxide
TNCB	Trinitrochlorobenzene
TOCSY	Total correlation spectroscopy
tRNA	Transfer ribonucleic acid
TSP-d ₄	3-(Trimethylsilyl) propionate-2,2,3,3-d ₄

TXI	Triple resonance inverse
UV	Ultraviolet

VI. List of Figures and Tables

Figure 1: Main biological omics layers connecting environmental factors to phenotype..	20
Figure 2: The complexity of metabolomics pathways illustrated in a metabolite network map.....	24
Figure 3: Common metabolites and their interconnection within redox, energy, membrane growth and repair metabolic pathway network..	26
Figure 4: Physical principles of nuclear magnetic resonance.....	28
Figure 5: An example of a 1D NMR spectra of glioma tumor biopsy patient tissue, with assigned glucose, <i>myo</i> -inositol and <i>scyllo</i> -inositol.....	30
Figure 6: Harmonized workflow from sample preparation to data analysis for metabolomics.....	33
Figure 7: Common substrates and bacterial-origin metabolites..	38
Table 1: Metabolomics overview of significant metabolite concentration changes and pathway alterations. .	106
Supplementary Table 1: Common metabolites and pathways in different metabolomics studies.....	137

1. Introduction

1.1. Metabolomics as a tool for metabolism and phenotype studies

Metabolic imaging in vivo is of great clinical and practical importance as it provides real-time and dynamic information on the ongoing metabolic processes in a patient or an animal model ¹⁻³. However, current magnetic resonance imaging (MRI) and positron emission tomography (PET)-based approaches are restrained in their spatial resolution to truly elucidate ongoing processes on a molecular level. Novel approaches, such as hyperpolarized magnetic resonance (MR) imaging, overcome some of these limitations but are suited to detect only a limited number of metabolites and pathways. When an imaging approach indicates a metabolically active area of interest in the form of perfusion, oxygenation map or radiotracer uptake, further multimodal approaches can be used for the validation ex vivo. Such approaches, including autoradiography, immunohistochemistry, immunofluorescence, fluorescence-activated cell sorting (FACS) or different omics techniques, aim to provide a deeper understanding and detailed view of either cellular species or ongoing bio-molecular events.

Metabolomics, also referred to as metabonomics, is one of the youngest omics fields and lies at the very end of the omics cascade being the closest readout to the phenotype of an organism (Figure 1) ⁴⁻⁵. Thus, ex vivo metabolomics is well-suited to complement in vivo metabolic imaging obtained information on a deeper molecular level.

Metabolomics focuses on small molecule compounds with a molecular weight usually below 1,000 Dalton. These molecules include typical eukaryotic organism compounds, such as lipids, carbohydrates, amino acids and vitamins. The investigation of metabolite interactions, interconversions and their overall role in metabolism is the subject of the research field of metabolomics. Metabolomics, therefore, provides an inter-matrix, inter-species and inter-health/disease-comparable functional readout. Metabolites are directly or indirectly affected by the activity of proteins and peptides and can provide feedback for gene expression at the same time. Both metabolome and proteome are a readout of upstream genetic and transcriptomic preconditions and alterations ⁶ and are further regulated by the epigenome.

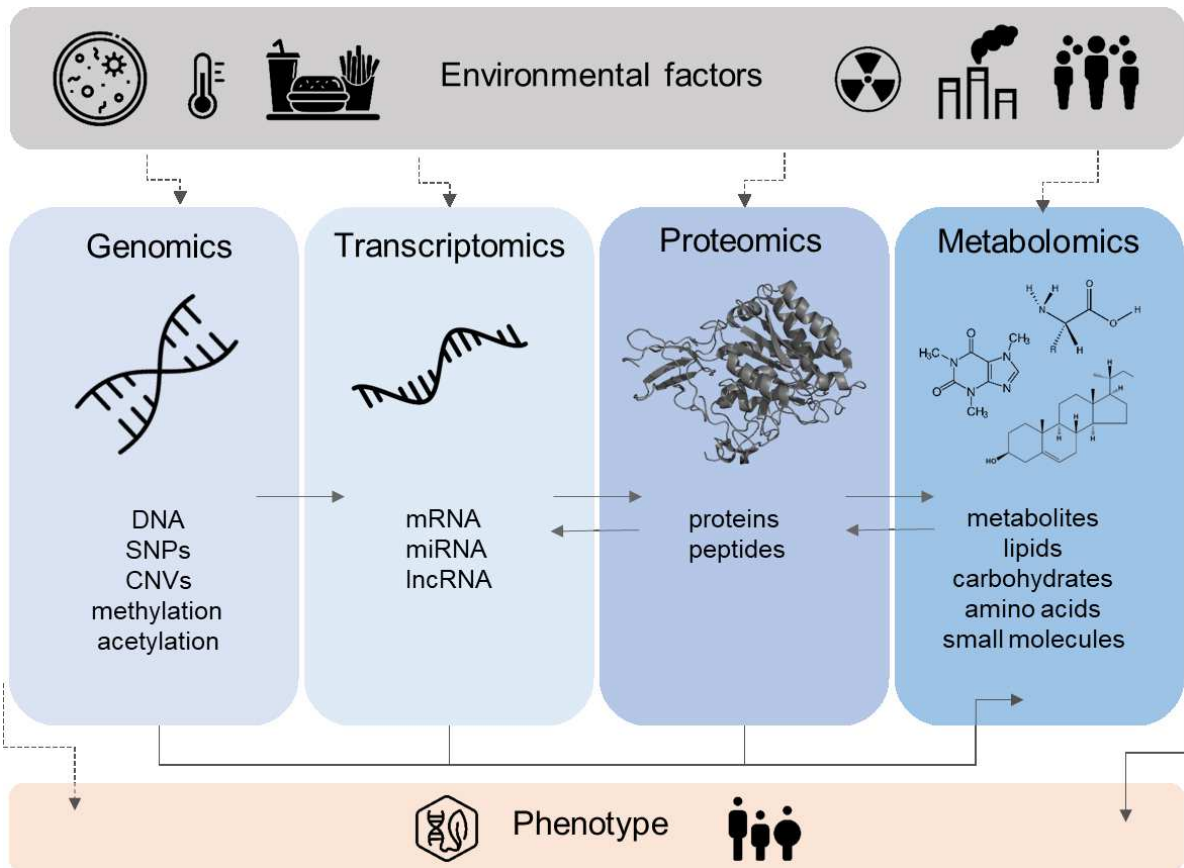


Figure 1: Main biological omics layers connecting environmental factors to phenotype. Metabolomics is the final layer of the cellular omics cascade and the closest small molecule readout point to the phenotype. External environmental alterations arising from population, pollution, radiation, microbes, temperature or diet, are directly or indirectly affecting the genome, and therefore downstream transcriptome, proteome and metabolome of living systems. Adapted from Krumsiek, J., et al. 2016 ⁶.

The complexity of the cascade is reduced from level to level. Many genes are involved in the production of a specific enzyme. Several enzymes, however, use the same metabolite as a substrate or product during specific enzymatic reactions. For example, glutamate is a small molecule metabolite, crucial for nucleic acid and protein biosynthesis. Glutamate can be used in the alanine-aspartate-glutamate metabolic pathway by glutamine synthetase and 1-pyrroline-5-carboxylate dehydrogenase; in arginine and proline metabolic pathway by glutamate 5-kinase; in histidine metabolism by glutamate formiminotransferase / 5-formyltetrahydrofolate cyclo-ligase; in taurine and hypotaurine metabolism by glutamate dehydrogenase; in butanoate metabolic pathway by glutamate decarboxylase; in glyoxylate and dicarboxylate metabolism by

methylaspartate mutase; in neomycin, kanamycin and gentamicin biosynthesis pathway by (butirosin acyl-carrier protein)--L-glutamate ligase; and in porphyrin metabolism via glutamyl-tRNA synthetase. This shows how at least 9 different enzymes can use the same metabolite as substrate. On top of that, the complexity increases in a similar manner as similarly to degradation, glutamate can be yielded via several different enzymatic reactions ⁷.

Hence, one of the biggest advantages of metabolomics – as a reduced complexity system and its closeness to the phenotype – is also its biggest challenge, often limited to the static readout of the metabolome at a specific point in time without detailed information about surrounding fluxes. Further knowledge of specific metabolite involvement in systemic events and surrounding metabolite concentration alterations within specific pathway networks can aid approximation and conclusions about the metabolic pathway in action. Isotope-labelled standards and substrates can be further employed for detailed flux analysis.

Metabolite concentrations are also matrix specific – demand for a certain metabolite and metabolic pathway activity varies from organ to organ. For example, in the case of glutamate, it is known that from the total glutamate load in an organism, only a small percentage is used for neurotransmitter (such as γ -aminobutyrate, GABA) synthesis, while the rest is used between protein production, energy and redox metabolism, transamination and translation processes, divided between liver, pancreatic β -cells and brain ⁸.

Additionally, the metabolome is the final readout of several environmental factors' impact, such as diet, economic and social background-related aspects, social environment, exposure to toxins, exhaust fumes and pollution, radiation, the temperature of the environment and bacteria (Figure 1) ⁵⁻⁶. Of note, the vast majority of metabolites within an organism are not produced by the organism itself but result from nutrition, external exposure and bacterial activity.

In the last two decades, metabolomics has gained popularity due to its versatile applications in life sciences. In the medical field, metabolomics aids the identification of biological targets for drug discovery ⁵ by elucidating pathways, identifying biomolecular processes affected by target engagement, determining a mode of action and quantifying unusual metabolite species in a context of a specific disease or

condition ⁹. Even though novel drug types based on peptides, proteins or gene transcripts are gaining importance, to date the vast majority of pharmaceuticals is based on small molecules. Thereof, especially pharmaco-metabolomics ¹⁰, plays a crucial role in different stages of drug development ¹¹. Here, drug response studies adopt cell culture or preclinical models ¹² to elucidate potential differences in individual response to treatment and set margins for expected success rate ^{9, 13}.

Despite the fast growth and economic investment in the world's pharmaceutical industry, the latest Biotechnology Innovation Organization report stated that only about 8% of drugs that enter phase I clinical trials reach approval ¹⁴. Moreover, an overview opinion article from 2001 claimed that 50 – 75% of patients appropriately respond to the majority of pharmaceutical treatments, with the lowest efficacy of around 25 – 30% estimated for oncological radiotherapy, and the highest of 80% response rate for cox-2 inhibitor-based treatments ¹⁵⁻¹⁷. As for now, the current estimation is that 1 in 10 compounds that enter clinical trials will succeed to reach patient bedside ¹⁸⁻¹⁹, despite the technological advancements and new approaches of target discovery and drug development over this time.

Isolated cell and preclinical models, poor translation and incomplete correlation with human functions, long clinical trials, patient diversity and cohort variations, and accumulating costs are just a few of the commonly speculated reasons for many unsuccessful drugs. Artificial intelligence (AI)-supported modelling of potential complex interactions, alterations and other information, otherwise hard to comprehend, could be a potential solution ²⁰. Here, we once again and more than ever depend on basic life science, a fundamental understanding of biomolecular events, pathways, molecular interactions and possible products, all potentially aided to some extent by metabolomics, in order to feed the AI with the most complete knowledge for functional models.

Since then the field of individualized medicine approaches based on genetic traits has been widely discussed and explored, including genome-wide association studies (GWAS). Metabolomics together with other omics approaches is therefore particularly interesting for metabolome-wide association studies (MWAS) to determine specific risk factors and biomarker fingerprints for better patient stratification and individualized treatment ²¹. Furthermore, omics readouts and conclusions can be used to propose lifestyle and nutrition interventions and to consult public health policy ²²⁻²⁴. The

identification of novel robust metabolic biomarkers and their addition to the routine laboratory card is something expected to fundamentally change our health system from treatment towards prevention and personalized precision medicine.

1.2. Metabolomics and metabolic pathways

All biological samples, whether deriving from cell culture, or being a biofluid or tissue biopsy, consist of a complex mixture of metabolites. A metabolite can be an intermediate or an end product of one or, more commonly, several metabolic pathways interconnected in a convoluted pathway network. Each pathway has a significant function in the buildup or breakdown of a specific molecular target for necessary cellular processes that can be altered upon a pathology. According to the Kyoto encyclopedia of genes and genomes (KEGG), there are ten main super pathways: carbohydrate metabolism, energy metabolism, lipid metabolism, nucleotide metabolism, amino acid metabolism, glycan metabolism, metabolism of cofactors and vitamins, biosynthesis of terpenoids and polyketides, biosynthesis of other secondary metabolites, and xenobiotics biodegradation (Figure 2). All super pathways are interconnected in a complex and overlapping metabolism network with a total of more than 400 sub-pathways ²⁵.

(Figure 2 legend continued) Metabolic super-pathways illustrated as individual colors – carbohydrate metabolism dark blue, energy metabolism purple, lipid metabolism dark green, nucleotide metabolism light orange, amino acid metabolism yellow, glycan metabolism light blue, metabolism of cofactors and vitamins pink, biosynthesis of terpenoids and polyketides light green, biosynthesis of other secondary metabolites dark pink, xenobiotics biodegradation dark orange – with metabolites as dots and reactions as nodes connecting the dots. Obtained from Kyoto encyclopedia of genes and genomes (KEGG) ²⁵.

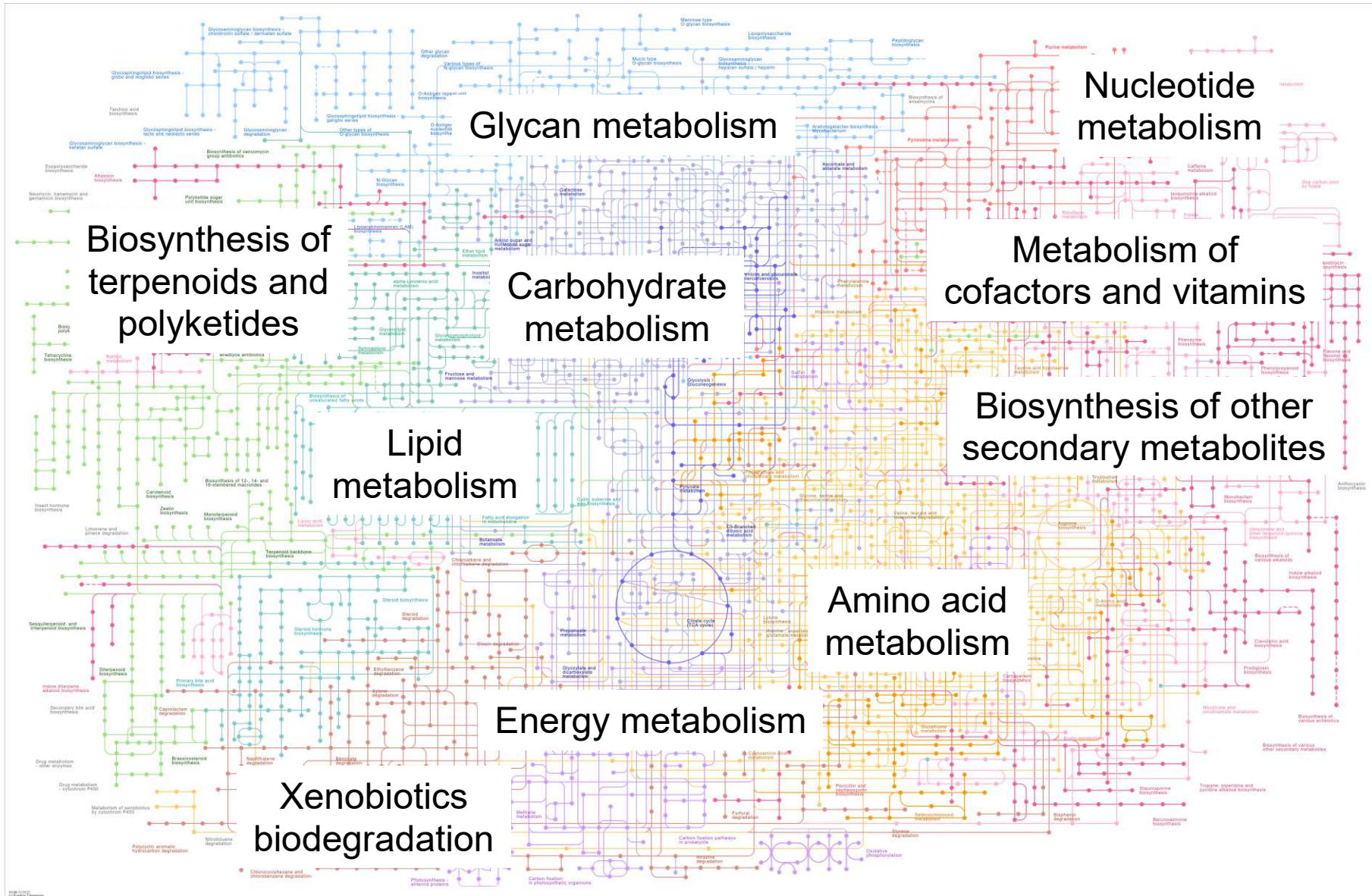


Figure 2: The complexity of metabolomics pathways illustrated in a metabolite network map.

As the youngest field in omics cascade, metabolomics still possesses a lot of unknowns. It is estimated that only around 2% of metabolome from a biological sample can be annotated to a known compound, which leaves the rest of 98% as the so-called 'dark matter' of metabolomics ²⁶.

Many metabolic pathways employ reactions of different amino acids, peptides, nucleotides, co-factors, vitamins, and lipids as substrates for cell growth, repair or energy demand (Figure 3).

Common energy-related metabolic pathways include glycolysis, oxidative phosphorylation (OXPHOS), and tricarboxylic acid (TCA) cycle, of which the main goal is ATP production ²⁷ and the regeneration of redox equivalents such as NAD⁺ or NADP⁺ (Figure 3, energy, yellow). Indeed, amino acids and their enzymatic conversions are not only important for protein synthesis but play also an important role in the maintenance of TCA cycle function serving as anaplerotic and cataplerotic substrates ²⁸.

One-carbon metabolism, including folate and methionine cycle, primarily aims to provide methyl components, one-carbon units, for the synthesis of purines, lipids, pyrimidines and translation factors but is also an important substrate provider for the trans-sulfuration pathway which produces glutathione – one of the most important scavengers of reactive oxygen species in cells ²⁹ (Figure 3, redox, green).

Phospholipid synthesis pathways are crucial for cellular maintenance, membrane buildup and degradation. Here, the Kennedy pathway fundamentally explains how intracellular ethanolamine and choline are used to synthesize phosphatidylethanolamine and phosphatidylcholine, which are two of the three major membrane lipids together with phosphatidylserine and phosphatidylinositol.

The Kennedy pathway is often altered in cancer and in genetic diseases ³¹⁻³² (Figure 3, growth and repair, blue).

Metabolites can be produced by enzymes and serve as substrates for several metabolic pathways. Therefore, the metabolic landscape is complex, interconnected and susceptible to deep perturbations in presence of a pathogen, mutation or other challenges.

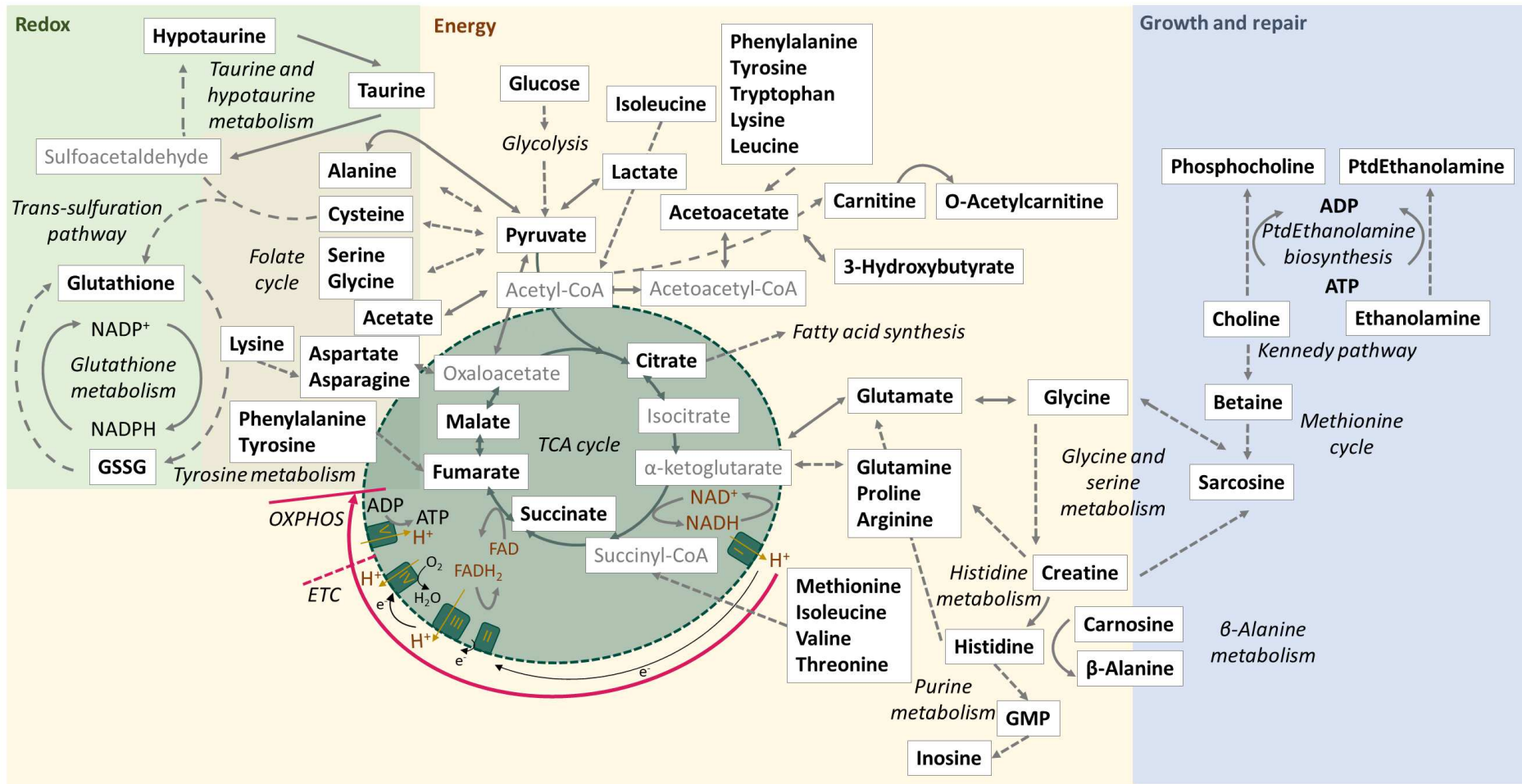


Figure 3: Common metabolites and their interconnection within redox, energy, membrane growth and repair metabolic pathway network. Metabolites in bold are quantified by NMR spectroscopy, while metabolites in grey are important metabolic points, yet were not quantified by NMR. Pink arrow illustrates electron transport chain (ETC) and oxidative phosphorylation (OXPHOS) at mitochondrial membrane and matrix (dark green). Numbers I – V represent mitochondrial complexes involved in ETC and OXPHOS. Figure created based on Martinez-Reyes, I. *et al.* 2020, and Inigo, M. *et al.* 2021^{27, 30}.
26

1.3. NMR spectroscopy as a tool for metabolomics research

The most common tools employed for metabolomics research are mass spectrometry (MS), commonly in hyphenation with gas or liquid chromatography (GC/LC), and NMR spectroscopy. LC/MS-based approaches largely dominate most omics fields due to the large variety of types of instruments, the possibility to couple them with chromatography and UV/DAD detectors, and potentially of most importance, the sensitivity of this method and, therefore, larger amounts of detected features ³³.

Meanwhile, the main advantages of NMR spectroscopy-based metabolomics include its non-destructive nature, robustness, fast measurement, inexpensive and straightforward sample preparation, and most importantly, intrinsic quantitative molecule identification. Moreover, the relatively simple sample preparation is also the reason why NMR spectroscopy-based metabolomics provides biologically relevant and almost unaltered insight into the metabolomic state of investigated system ³⁴.

1.4. Principles of NMR spectroscopy

The main principle behind NMR spectroscopy, as the name implies, is the detection of the intrinsic properties of the chemical element nuclear spin magnetic moment. The properties of an NMR and relaxation were first described by Felix Bloch in 1946 by mathematical analysis of a series of nuclear induction experiments ³⁵.

A proton (¹H), which is the most commonly investigated atom by NMR, has a 100% natural abundance, a nuclear spin of $\frac{1}{2}$, generating its own magnetic field, and is therefore widely used in NMR spectroscopy ³⁶.

Protons (and atoms in general) in their regular state have their individual magnetic field moments oriented in random directions (Figure 4a). Application of a strong external magnetic field (B_0) leads to the alignment of e.g. proton magnetic fields with or against the external magnetic field (Figure 4b) ³⁶.

This difference in energy (ΔE) between aligned spins with and against the magnetic field (Figure 4c) is what can be measured by NMR spectrometry in the range of radiofrequency of the electromagnetic spectrum. The strength of the external magnetic field directly influences how large the ΔE is. High-field NMR spectrometers are available in a wide range, up to 1.2 GHz (28.2 T), however, typically commercially available spectrometers are between 300 to 800 MHz (7.05 - 18.8 T) ³⁷. While

spectrometers > 800 MHz are typically used for the structure elucidation of large proteins, spectrometers between 500 and 700 MHz are used for metabolomics while instruments with lower frequency – are for food or chemistry applications.

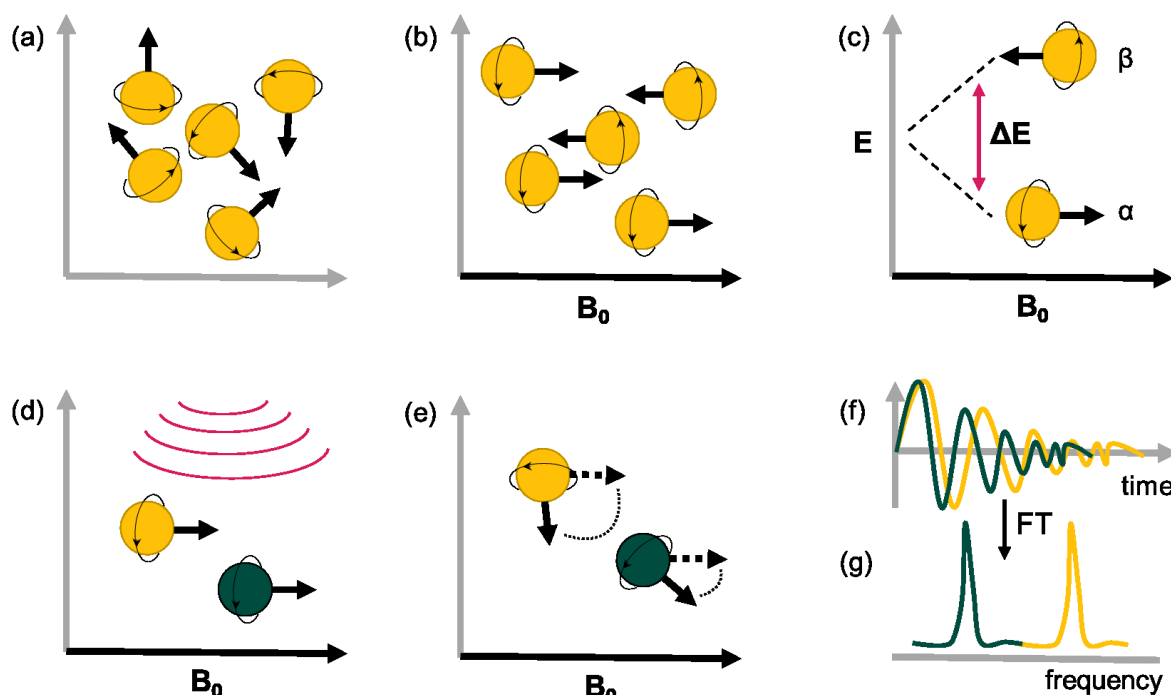


Figure 4: Physical principles of nuclear magnetic resonance. (a) Proton spin orientation in a regular environment is random; (b) when external magnetic field B_0 is applied (black x axis), protons align with or against it; (c) there is an energy difference (ΔE) between protons aligned with (α proton) and against (β proton) the magnetic field which is related to the B_0 strength; (d) radio wavelength pulsation is applied to disturb the proton alignment with the field (pink lines); (e) two protons with a chemically different environment are affected to a different capacity leading to different relaxation times back to the original direction of B_0 (dashed arrow); (f) the relaxation of protons is registered as free induction decay (fid) of different resonances (yellow and green); (g) individual proton peaks are resolved in the frequency domain after a mathematical Fourier transformation (FT) (yellow and green peak, colorblind-friendly color palette). Figure based on Holzgrabe, U. et al., 2008³⁸.

Protons, e.g. α and β (Figure 4c), then are excited with specific radiofrequency pulses (Figure 4d), aimed to match the change in energy, experience a spin flip, and a spectrometer can measure the absorbance of radio wave frequency during the relaxation (Figure 4e) (absorbance or emission of radio wave photons), also known as the resonance. This signal is detected, amplified and recorded as free induction decay

(fid) (Figure 4f), sinus waves with decreasing magnitude as the nucleus re-aligns itself with the B_0 (Figure 4e) ³⁶.

ΔE is not only dependent on the external magnetic field B_0 but also the structure of the molecule that these atoms are part of. As each proton is in a unique chemical environment and affected by the whole molecule's magnetic field, it leads to a slightly different fid in the time domain (Figure 4f) ³⁵. Further, the time domain is converted into a frequency domain via Fourier mathematical transformation (FT) ³⁹, which is more commonly known as the NMR spectrum with different protons visually represented as peaks (Figure 4g). Protons that have higher electron density around them due to specific molecular structure experiences a lower magnetic field and is, therefore, less shielded (de-shielded) by the external magnetic field, leading to their appearance more towards the left side of the spectrum downfield (Figure 4g, green peak). Meanwhile, protons in a less electron-rich environment will experience a stronger effect from the external magnetic field and will be, so-called, shielded resulting in their peak appearance being more up-field (on the right in frequency domain) ³⁶ (Figure 4g, yellow peak).

Not only that, protons attached to neighboring carbons have an additional influence from their neighbor protons. Magnetic spin state interactions lead to peak splitting into doublets, triplets and further multiples, depending of the number of non-identical neighboring proton interactions in the spin system and independent on the metabolite concentration. For instance, different metabolites with the same molecular formula, such as $C_6H_{12}O_6$, can have one (*scyllo*-inositol), few (*myo*-inositol) or many peaks (glucose) in the NMR spectrum (Figure 5). This is a key property for complex mixture elucidation, such as metabolome, allowing the identification of individual molecules based on their peak splitting patterns in the convoluted spectra.

As most metabolites do have several 1H -NMR resonances, this can result in a very busy spectrum and complicates the annotation. For example, a typical tissue or urine spectra may consist of between 50 to 90 metabolites ⁴⁰⁻⁴¹. To be able to elucidate such a metabolome, high-quality spectra are required, considering optimal shimming and solvent suppression. An optimal spectrometer configuration is therefore a prerequisite for performing NMR-based metabolomics successfully.

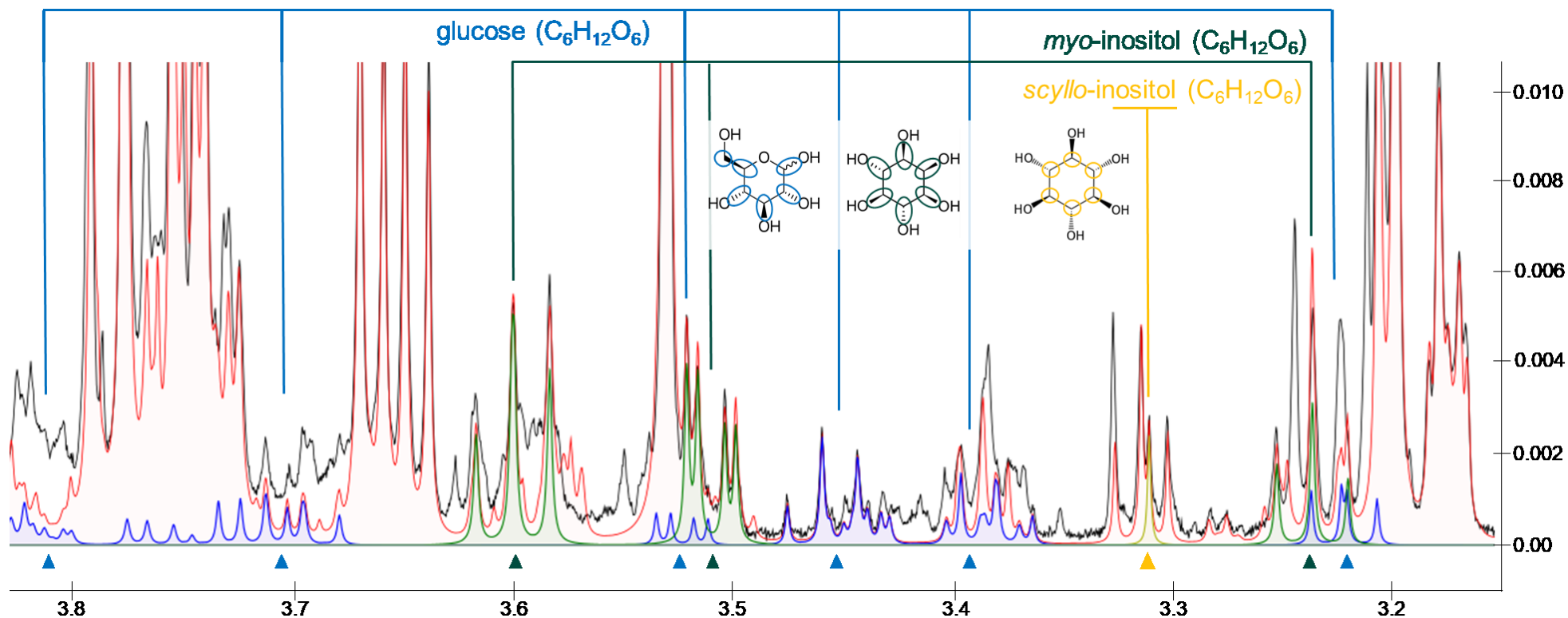


Figure 5: An example of a 1D NMR spectra of glioma tumor biopsy patient tissue, with assigned glucose, *myo*-inositol and *scyllo*-inositol. Partial NMR spectra between 3.2 and 3.8 ppm illustrating different metabolite peaks in relation to the ppm (x axis) and peak intensity (y axis) scale. All three illustrated metabolites have the same molecular formula of C₆H₁₂O₆, yet their molecular structure determines their unique peaks and separation in the NMR spectra. *scyllo*-Inositol (pink) is a singlet at 3.32 ppm. *myo*-Inositol (green) resonates as a triplet at 3.24 ppm, doublet of doublets (dd) at 3.51 ppm, triplet at 3.60 ppm and triplet at 4.0 ppm (not visible here). Glucose (blue) resonates as a dd with a shift of 3.22 ppm, dd at 3.39 ppm, doublet of triplets (dt) at 3.45 ppm, dd at 3.52 ppm, dd at 3.71 ppm, dd at 3.81 ppm and two doublets at 4.6 (β-glucose) and 5.22 (α-glucose) ppm (not visible here). The red outline shows the total assigned peak areas in the spectra and the black outline is the originally recorded spectra (representative NMR spectra of preclinical mouse ear tissue from own recorded dataset).

The most commonly applied nuclei for NMR spectroscopy are the already mentioned proton (^1H), but also carbon (^{13}C), nitrogen (^{15}N), fluorine (^{19}F), and phosphorous (^{31}P) as they have an odd number of protons and/or neutrons, which is the basis for nuclear magnetic resonance observation. For example, ^{31}P spectroscopy is especially interesting for phospholipid species investigations ⁴²⁻⁴³, as general cell membrane growth and repair-related species are often affected by disease state and progression, as it has been specifically reported in glioma IDH mutations-related brain tissues ⁴⁴⁻⁴⁵ and blood ⁴⁶. ^{13}C is often used as a complementary method to ^1H spectroscopy, as specific 2D experiments, such as heteronuclear multiple bond correlation (HMBC) experiment or heteronuclear single quantum coherence (HSQC), allow complex molecular structure elucidation and additional confirmations of individual molecules present in complex mixtures ⁴⁷⁻⁴⁸.

While there are specific applications for several nuclei in the metabolomics field, still the most commonly used nucleus remains ^1H due to its vast abundance, and therefore most standard operation protocols (SOPs) and studies are based on ^1H -NMR. Of note, there are different NMR probe diameters and nuclei configurations available, ranging from triple resonance inverse (TXI) to broadband observe (BBO) probes allowing for simple 1-2 dimensional homonuclear or sophisticated 2-4-dimensional heteronuclear experiments.

Furthermore, advanced pulse programs exist for further elucidation of molecules within mixtures. For example, a homonuclear 2D experiment of correlation spectroscopy (COSY) correlates between proton chemical shifts of protons in a near vicinity (geminal or vicinal) through their scalar couplings. Meanwhile, total correlation spectroscopy (TOCSY) provides information about all the protons within the same spin system ⁴⁹. Another 2D experiment can resolve J-couplings (JRES) to determine which protons are coupled within a spin system and reveal overlapping resonances of different spin systems by de-convoluting the spectrum ⁵⁰.

1.5. Samples and preparation workflow

^1H -NMR spectroscopy-based metabolomics analysis can be performed on a very wide range of samples – from individual cell cultures ⁵¹⁻⁵² or 3D cultures ⁵³, soil ⁵⁴, plants and their extracts, food ⁵⁵⁻⁵⁷, preclinical model organisms ⁵⁸, organs and biofluids ⁵⁹⁻⁶¹, to complex human biofluids ⁶²⁻⁶⁷, feces ⁶⁸, and tissue biopsies ⁶⁹⁻⁷⁰.

Crucial aspects of the metabolomics analysis in NMR are similar to MS-based metabolomics and other omics analysis. One of them is the requirement of sufficient experimental design ⁷¹. It is important to collect pre-analytical information about how large a cohort is investigated and if the size of the cohort is appropriate to answer the research question; how the samples are collected; possible time and temperature effects on sample collection; and the use of an optimized protocol for sample homogenization and metabolite extraction, appropriate for sample matrix ⁷².

Furthermore, to ensure the reproducibility and validity of the data, any analytical biases should be avoided during sample grouping in batches or possible sample degradation should be estimated. Here, several techniques such as randomization, blanks, quality control protocols, internal or reference standards, and dilution series can be applied to help avoid an analytical bias.

The final challenge is data interpretation. Appropriate statistical analysis needs to be employed for true biomarker and metabolic pattern discovery ⁷³. Depending on the sample type, different approaches can be used. Special attention should be paid to spectra assignment, appropriate choice of a statistical test related to cohort size and data distribution within the cohort, application of false discovery rate to correct for false positives, and estimation of confounding factors ⁷⁴. Additionally, the statistical total correlation spectroscopy (STOCSY) approach can be used to create pseudo-two-dimensional spectra where peak correlations can reveal biological covariance and metabolites involved in the same pathway ⁷⁵. For high-throughput data preprocessing, the spectral binning approach is used where spectral data is simplified by assigning a part of spectra to one categorical bin value, bins then are assigned to specific metabolites or their combinations, and analysis is performed on the bins rather than on individual metabolite annotations in spectra ⁷⁶.

A typical workflow for NMR spectroscopy-based metabolomics includes several consequent steps: sample preparation, spectra acquisition, spectra processing and metabolite annotation, statistical data analysis, interpretation and presentation (Figure 6). First, samples are obtained from a pre-clinical or clinical study with a specific research question and hypothesis, related to the chosen sample matrix (Figure 6a). Second, if samples are in a solid state (e.g. pre-clinical organs or clinical biopsies), a homogenization step, e.g. by means of cryogenic pulverization is necessary prior to metabolite extraction (Figure 6b).

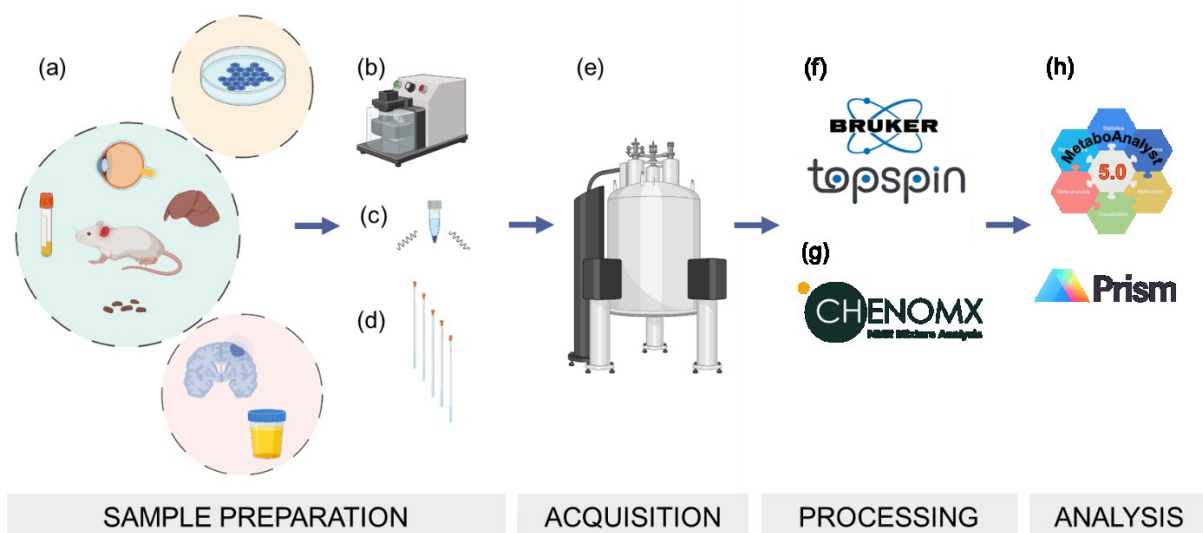


Figure 6: Harmonized workflow from sample preparation to data analysis for metabolomics. (a) For all sample matrices, e.g. cell culture, preclinical and clinical tissue samples, we use (b) standardized pulverization protocol using e.g. CP02 cryoPREP automated dry pulverizer, and (c) 1-phase or 2-phase ultra-sonicated extraction by e.g. optimized Covaris manufacturer's protocol. (d) Bruker Biospin 1.7 mm autosampler-compatible NMR tubes are filled with metabolite suspension in 1mM internal standard (TSP)-containing standardized phosphate buffer. (e) Measurements are acquired on a 600 MHz field strength NMR spectrometer for proton (^1H) measurements, and optimized pulse programs are used with water suppression (measurement time optimized for individual tissue/fluid amount/metabolite concentrations). (f) Bruker TopSpin software is used for spectral acquisition and for unified spectral processing. (g) Chenomx commercial software is used for metabolite assignment, employing internal standards for metabolite concentration calculations. (h) Statistical analysis is performed by MetaboAnalyst web server and Prism GraphPad software (parts of the figure created with Biorender.com).

Other samples, such as cell culture, preclinical blood or feces can be directly subjected to metabolite liquid extraction protocol by ultra-sonication ⁷⁷ (Figure 6c) or bead-beating ⁷⁸. Two solvent systems are commonly used for a simultaneous extraction of both polar and lipid metabolites. Cell culture metabolites are usually subjected to 1-phase methanol, chloroform and water mixture, as it is optimal for small molecular weight compounds ⁷⁹⁻⁸⁰. Metabolites from more complex matrices, such as tissue or feces, containing significant concentrations of lipid species are extracted by methanol, methyl *tert*-butyl ether (MTBE) and water mixture leading to 2 solvent phases ⁸¹. After

extraction, for the 2-phase protocol, polar and lipid phases are divided and analyzed separately.

As for $^1\text{H-NMR}$ spectroscopy, it is crucial to remove any excess proton signal that can shield lower concentrated metabolite protons in the spectra. Therefore, any extraction solvent containing protons has to be evaporated. For that, a vacuum concentration or lyophilization (freeze-drying) can be used. The dried metabolite pellet then is re-suspended in a deuterated water buffer solution containing potassium hydrogen phosphate, and sodium azide that is adjusted to neutral pH⁸² for polar phase analysis, or deuterated chloroform for lipid phase analysis. Moreover, an internal chemical standard is commonly used for later quantification. While there are limitations and extensive research on internal chemical standards and other quantification possibilities, commonly reported internal chemical standards include sodium 3-(trimethylsilyl) propionate-2,2,3,3- d_4 (TSP- d_4)⁸³, and sodium 4,4-dimethyl-4-silapentane-1-sulfonate (DSS- d_6)⁸⁴ for polar analysis, while tetramethylsilane (TMS) is commonly used in non-polar solutions⁵⁹. Moreover, some metabolites, such as fumarate and maleate are investigated as potential internal standards⁸⁵ yet mainly for protein spectroscopy, as these metabolites are intrinsic to several tissues and biofluids.

Once the metabolite mixture is prepared, NMR tubes can be filled (Figure 6d). Depending on the amount of sample, different sizes of tubes and filling volumes exist. For most pre-clinical applications and precious clinical tumor tissue biopsies, a 1.7 mm room temperature probe is a good choice, as 1.7 mm NMR tubes require only 40 μL of supernatant to achieve the minimum filling volume for appropriate filling height in the tube. In comparison, a 5 mm NMR spectrometer probe with 5 mm NMR tubes requires 600 μL of supernatant volume or for 3 mm – 200 μL , which is still 5-fold higher volume, which for small precious tissue amounts leads to dilution, resulting in some metabolite concentrations below the limit of detection.

Spectra acquisition (Figure 6e) is carried out using optimized pulse programs, such as the 1D nuclear Overhauser effect spectroscopy (NOESY) sequence, providing efficient excess water suppression and Carr-Purcell-Meiboom-Gill (CPMG) sequence, that is optimized for efficient water and lipid background suppression⁸⁶. Each sample type requires some optimization to establish a necessary number of scans for appropriate metabolite quantification in spectra related to the necessary time.

Typically, preclinical samples in a 1.7 mm probe require between 1 to 4 h measurement time per sample. While one would consider that longer time equals better spectra, it must be taken into consideration that with more iterations also the background noise gets amplified, and a balance between signal-to-noise ratio is therefore desired.

After the acquisition, spectra are acquired as fid, which then need to be Fourier transformed and processed for further annotation, using Bruker TopSpin software (Figure 6f). Then spectra are imported into Chenomx NMR mixture analysis commercial software and annotated based on the Chenomx reference compound library and human metabolome database (HMDB) ⁸⁷ reference spectra (Figure 6g). These libraries contain reference compound spectra with peak areas under the curve, that in relation to an internal standard allow calculating metabolite absolute concentrations in the mixture. As an output, a spreadsheet with the metabolite list and quantified concentration in each acquired sample is acquired. Similarly, other available software solutions for spectra processing and annotation include MestreNova and Bruker AMIX with an internal reference compound library of around 800 compounds (BioRefCode) ⁸⁸⁻⁸⁹. Other NMR spectra databases include NMRShiftDB, biological magnetic resonance bank, and Birmingham metabolite library (BML-NMR) as publicly available, yet limited in their numbers of compounds and without integrated usage ability ⁹⁰.

Finally, data is evaluated by univariate and multivariate statistical analysis and visualized for interpretation. MetaboAnalyst ⁹¹ is commonly used as an online R-based platform for metabolomics data evaluation (Figure 6e), however, many other R- or Python-based scripts exist. MetaboAnalyst online tool includes features, such as statistical visualization for t-test, volcano plot and analysis of variance (ANOVA), auto-scaled feature heatmap visualization tool, principal component analysis (PCA) and additional regression models of partial least-squares discriminant analysis (PLS-DA), correlations analysis between features, all aiming for appropriate data exploration. Furthermore, additional data visualization and statistical analysis can be performed via Graph Pad Prism (Figure 6h). Altogether, the NMR spectroscopy-based metabolomics pipeline provides a pipeline for obtaining quantitative information on the investigated sample metabolome, illustrates the largest sources of differences and proposes interesting target compounds for further interpretation. In addition, a more

comprehensive analysis can be carried out including information on enriched pathways and metadata integration, such as transcriptomics or proteomics data.

1.6. Inflammation, immunology and immunometabolism in metabolomics

Metabolomics is widely used in preclinical and clinical research as it allows one to obtain an overview of a metabolic profile based on distinct pathways and interactions. In recent years, metabolomics has been successfully applied in inflammatory disease research of immunometabolism.

For example, macrophage energy metabolism is largely affected during bacterial infection ⁹². Moreover, Fuchs, A. L., *et al.* ⁹³ investigated metabolomics differences between pro-inflammatory and anti-inflammatory macrophage cultures and revealed alterations in macrophage energy and growth metabolism as well as reactive oxygen and nitrogen species (RONS) scavenging capacity ⁹³.

Mixed immune cell metabolic alterations have been reported to be a readout of several autoimmune diseases, such as psoriasis and rheumatoid arthritis ⁹⁴. For instance, high-resolution magic angle spinning (HR-MAS) NMR spectroscopy analysis indicated alterations in taurine, ascorbate, and other RONS-related metabolites in relation to inflammatory cytokines in psoriasis patient skin ⁹⁵. In another study, ¹H-NMR spectroscopy was used to investigate metabolic profiles of peripheral spondyloarthritis and reactive arthritis in patient synovial fluid or serum, revealing similar metabolic signatures between the two conditions ⁹⁶. Sufficient immunometabolism characterization is still needed for further therapeutic intervention point determination and biomarker identification for improved disease early-stage diagnostics. The metabolomics approach can not only elucidate the ongoing cellular and molecular alterations but also serve as a platform for characteristic metabolite identification that can be further employed as substrates for novel radiotracer development.

1.7. Gut microbiota and metabolomics

The activity of gut microbiota has been shown to be tightly connected to the immune system of its host and, therefore, potential alterations in the composition of the microbiome can directly affect the host's health ⁹⁷. Common gut microbiota-related disease conditions include neurological disorders ⁹⁸; cardio-metabolic diseases, such as obesity ⁹⁹⁻¹⁰⁰, type 2 diabetes ¹⁰¹⁻¹⁰², or non-alcoholic fatty liver disease ^{99, 103-106};

digestive diseases, such as inflammatory bowel disease ¹⁰⁷ and irritable bowel syndrome ¹⁰⁸; or even breast ¹⁰⁹⁻¹¹² or colon cancer ¹¹³⁻¹¹⁵ and food allergy ^{97, 116}. Routine sample types used to investigate gut microbiota-related metabolic alterations are biofluids ¹¹⁷, such as blood (plasma or serum) ¹⁰⁰, urine ¹¹⁸, and feces ¹¹⁹, as the biofluid collection is the least invasive. Biofluids provide an excellent readout of the general phenotype in health and disease, including microbiota-related alterations. Bacterial metabolism has been shown to involve mainly short-chain fatty acids (SCFA) as a product of a carbohydrate diet ¹¹⁹ and branched short-chain fatty acids as a product of a protein diet, some organic acids (benzoate, phenyl acetate, hydroxyphenyl acetate, hydroxyphenyl propionate), aromatic amino acids ¹²⁰, and vitamins ¹¹⁷ and hence these metabolites are often associated with gut microbiota. Moreover, bacteria are able to transform bile acids, several amino acids, e.g. branched-chain amino acids (BCAA), amines, and even lipid species, e.g. glycerol. All these compounds can be observed and quantified by NMR spectroscopy to further characterize microbiota perturbations related to health and dysbiosis (Figure 7).

Microbiome-related alterations in bile acids are reported of high interest due to their relevance for lipid digestion and antibacterial properties and therefore role in homeostasis maintenance ¹²¹. Yet some probiotic bacteria have the potential to resist bile acid antibacterial activity by altering their energy metabolism ¹²¹.

SCFAs are produced from dietary fiber via bacterial fermentation and play a role in the maintenance of sufficient gut-brain axis signaling ¹²², cognitive performance ¹²³, gut barrier stability and intestinal homeostasis ¹²⁴. It has been also shown that sufficient brain damage reflects in the dysbiotic gut consequently reducing SCFA ¹²⁵⁻¹²⁶. Similarly, dysbiosis and reduction of fiber fermentation were shown in colorectal cancer ¹²⁷.

Common SCFAs include acetate, propionate and butyrate. Acetate has been correlated with decreased visceral fat and therefore lowered risk for cardiac disease ¹²⁸⁻¹²⁹. Cognitive function has been reported impaired in correlation with circulating acetate depletion ¹³⁰. Moreover, butyrate is reported to have an immunomodulatory effect, and role in infection development ¹³¹ via macrophage preconditioning ¹³²⁻¹³³.

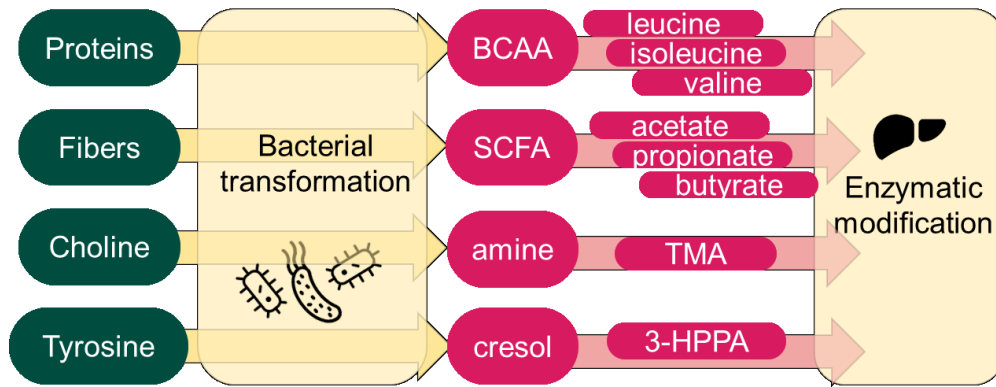


Figure 7: Common substrates and bacterial-origin metabolites. Bacteria produce many important metabolites and intermediates from available protein, fiber and nutrient substrates. Common bacteria metabolites include branched-chain amino acids (BCAA), short-chain fatty acids (SCFA), amines and cresols, which can be transported to the liver for enzymatic modifications and further distributed to other organs. Figure reproduced and based on Brial, F., et al. 2018 ¹³⁴.

Other gut microbiota-produced metabolites, such as inosine and trimethylamine N-oxide (TMAO), are also involved in immunomodulatory pathways and can be used in determining the success of tumor immunotherapy ¹³⁵. Inosine was shown to support intestinal health ¹³⁶ and improve treatment efficacy through adenosine receptor binding ¹³⁷. TMAO improves CD8⁺ T cell-mediated anti-tumor immunity by stimulating pyroptosis¹³⁸ – a programmed cell death of inflammatory cells upon microbial infection ¹³⁹.

Branched short-chain fatty acids, such as isovaleric and isobutyric acids, are produced by BCAA degradation and have an impact on cellular metabolism ¹⁴⁰ and structural integrity ¹⁴¹, interfering with insulin-related glucose and lipid metabolic processes ¹⁴². Increased isovaleric acid concentration has an adverse effect on neurotransmission and has been even linked to depression ¹⁴³.

Circulating leucine, isoleucine, and valine (BCAA) are mostly re-absorbed, crucial for organ development, function and signalling processes, however, accelerated BCAA concentrations in blood have been linked to obesity, insulin resistance and type 2 diabetes ¹⁴⁴⁻¹⁴⁵. Bariatric surgery has been shown capable of reverting excess BCAA accumulation in blood and generally reverting metabolic syndrome ¹⁴⁶. However, bariatric surgery comes with great risks and adverse effects ¹⁴⁷, including malnutrition,

alterations in anatomy, prolonged bleeding risk of infection ¹⁴⁸, and increased risk of colorectal cancer ¹⁴⁹. There is still a need for mechanistic and metabolomic information that characterizes in detail gut microbiota alterations and effects on the host. Mechanistic causes of successful weight loss arising from surgical intervention are not yet entirely understood, and further work towards novel therapeutic targets and approaches that allow avoiding such greatly invasive surgery is needed.

1.8. Key topics of this thesis

Both immunometabolism and neurological disorders are important topics in broader preclinical and clinical research. Molecular findings on the metabolomics level can be further correlated with additional omics layers or, for example, metabolic imaging in vivo for therapeutic target identification and improved treatment development. Herein, precise experimental planning and sampling can provide an important knowledge basis to better understand the dynamic imaging data output and elucidate specific ongoing metabolic events towards advanced medical diagnostics, including the identification of substrates for radiotracer development for medical imaging or even elucidating molecular targets for therapy. Established preclinical research-relevant animal models for immunology and neurology were selected to investigate the link between alterations in tissue, fecal and blood metabolites, and systemic responses to specific manipulation or intervention.

2. Objectives and expected outcome

In this thesis project, we chose two highly-relevant preclinical disease models in the fields of neurology and immunology, that have been previously studied with different imaging approaches established in our department. These models were used to elaborate metabolic profiling and metabolic pathway elucidation by NMR spectroscopy-based metabolomics by applying

- i. a highly reproducible and quantitative analytical chemistry approach (NMR spectroscopy) with a novel ultra-sensitive 1.7 mm room temperature probe, ideal for low quantity and precious sample analysis;
- ii. and optimizing in-house pre-analytical standard operation procedures (SOPs) for tissue homogenization and two-phase metabolite/lipid extraction;
- iii. reproducible and harmonized workflows for spectral acquisition and chemometric analysis (metabolite assignment, quantification) until the statistical evaluation of obtained metabolomics data.

The general hypothesis of this work was that the addition of metabolomics data to existing *in vivo* and *ex vivo* imaging modality data – in the case of this project histopathology, immunohistochemistry, or PET – can provide a deeper insight on a functional biomolecular level. We further hypothesized that the successful implementation of a novel ultrasensitive 1.7 mm microprobe to mass-limited samples, as typically obtained from mice and rats, makes it more feasible to implement quantitative metabolomics data to typical preclinical imaging research projects elucidating metabolic pathway alterations relevant for improved disease diagnostics or therapeutic development.

The two main peer-reviewed publications within this thesis demonstrate the use and value of NMR spectroscopy-based metabolomics in preclinical immunology and neurology research. Neurological and immunological conditions are driven to a major extent by energy metabolism, cell membrane growth, repair and buildup as well as responses in relation to oxidative stress. Measuring such significant alterations in metabolite concentrations can robustly characterize a neurological or immunological disease or condition-related perturbations and display interactions in a larger network of metabolic pathways, providing a detailed insight into the onset, progression and development of a disorder.

In the first project, we set out to investigate the metabolic differences between acute and chronic inflammation in a delayed-type hypersensitivity reaction (DTHR) mouse model, which has been previously established and extensively studied in our imaging department ¹⁵⁰⁻¹⁵². Here, we hypothesized that the characterization of inflammation progression at specific time points, selected based on previous metabolic imaging studies, will result in dynamic metabolomic profile alterations, revealing important metabolic and molecular events crucial for each inflammation stage. We also correlated metabolomics findings with the immune cell activity characterized by immunohistochemistry staining of macrophages, T cells and neutrophils, providing insights into the immunometabolism phenotype in relation to the inflammatory stage progression.

For our second project, we set out to determine how bariatric surgery influences metabolism in a previously under-explored high-liquid sucrose diet model ¹⁵³ in rats. Here, we aimed to characterize biomolecular systemic effects that could lead to novel therapeutic targets, allowing us to avoid currently employed highly invasive RYGB surgery. We hypothesized that by employing metabolomics analysis, we could gain important insight in functional information connecting the surgery-related gut microbiome and metabolome alterations with an altered brain activity post-surgery. We correlated metabolomics findings with the abundance of various microbiota species, related liver lipid metabolites, immune and hormonal parameters, and neuronal activity by PET brain imaging to investigate how gut microbiota-originated metabolites may provoke reduced appetite, weight loss and their systemic effects in surgery animals compared to sham via the gut-brain axis signaling.

Taken together, we propose that the characterization of sample-specific biological metabolomes by NMR spectroscopy might provide detailed and valuable insights into tissue inflammation and high liquid sucrose diet-related gut-brain communication. Such readout can serve for advanced imaging data interpretation by integrating and correlating in vivo findings with the additional metabolomic layer ex vivo. Furthermore, in the case of tissue metabolomics, NMR spectroscopy might aid the identification of novel targets for PET tracer development, hyperpolarized imaging or localized in vivo MR spectroscopy.

3. Results

3.1. Publication I

Acute and chronic inflammation alter immunometabolism in a cutaneous delayed-type hypersensitivity reaction (DTHR) mouse model

Zizmare, L.¹; Mehling, R.¹; Gonzalez-Menendez, I.^{2,3}; Lonati, C.; Quintanilla-Martinez, L.^{2,3}; Pichler, B.J.^{1,2}; Kneilling, M.^{1,2,5}; Trautwein, C.¹

¹ Werner Siemens Imaging Center, Department of Preclinical Imaging and Radiopharmacy, Eberhard Karls University of Tübingen, Röntgenweg 13, 72076, Tübingen, Germany

² Cluster of Excellence iFIT (EXC 2180) "Image-Guided and Functionally Instructed Tumor Therapies", Eberhard Karls University of Tübingen, Röntgenweg 11, 72076, Tübingen, Germany

³ Institute of Pathology and Neuropathology, Comprehensive Cancer Center, Eberhard Karls University of Tübingen, Liebermeisterstraße 8, 72076, Tübingen, Germany

⁴ Center for Preclinical Research, Fondazione IRCCS Ca' Granda Ospedale Maggiore Policlinico, Via Pace 9, 20100 Milan, Italy

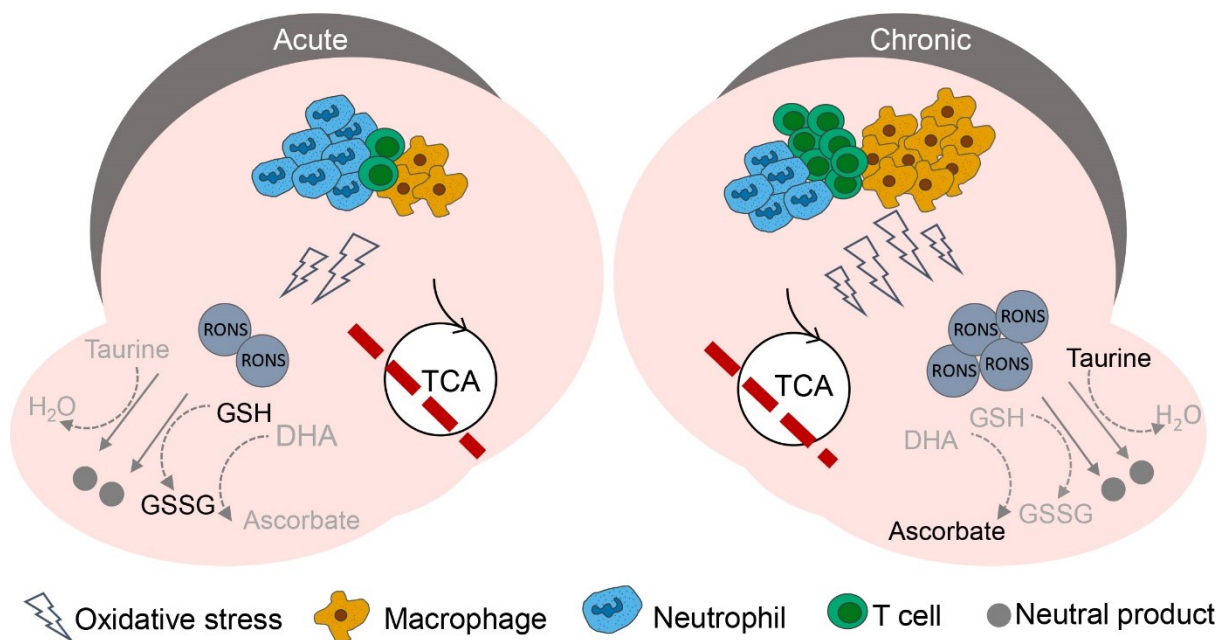
⁵ Department of Dermatology, Eberhard Karls University of Tübingen, Liebermeisterstraße 25, 72076, Tübingen, Germany

Nature Communications Biology

Year 2022, Volume 5, page 1250

<https://doi.org/10.1038/s42003-022-04179-x>

Graphical abstract



Acute and chronic inflammation alter immunometabolism in a cutaneous delayed-type hypersensitivity reaction (DTHR) mouse model

Laimdota Zizmare¹, Roman Mehling¹, Irene Gonzalez-Menendez^{2,3}, Caterina Lonati⁴, Leticia Quintanilla-Martinez^{2,3}, Bernd J. Pichler^{1,2}, Manfred Kneilling^{1,2,5} & Christoph Trautwein¹

T-cell-driven immune responses are responsible for several autoimmune disorders, such as psoriasis vulgaris and rheumatoid arthritis. Identification of metabolic signatures in inflamed tissues is needed to facilitate novel and individualised therapeutic developments. Here we show the temporal metabolic dynamics of T-cell-driven inflammation characterised by nuclear magnetic resonance spectroscopy-based metabolomics, histopathology and immunohistochemistry in acute and chronic cutaneous delayed-type hypersensitivity reaction (DTHR). During acute DTHR, an increase in glutathione and glutathione disulfide is consistent with the ear swelling response and degree of neutrophilic infiltration, while taurine and ascorbate dominate the chronic phase, suggesting a switch in redox metabolism. Lowered amino acids, an increase in cell membrane repair-related metabolites and infiltration of T cells and macrophages further characterise chronic DTHR. Acute and chronic cutaneous DTHR can be distinguished by characteristic metabolic patterns associated with individual inflammatory pathways providing knowledge that will aid target discovery of specialised therapeutics.

¹Werner Siemens Imaging Center, Department of Preclinical Imaging and Radiopharmacy, Eberhard Karls University of Tübingen, Röntgenweg 13, 72076 Tübingen, Germany. ²Cluster of Excellence iFIT (EXC 2180) "Image-Guided and Functionally Instructed Tumor Therapies", Eberhard Karls University of Tübingen, Röntgenweg 11, 72076 Tübingen, Germany. ³Institute of Pathology and Neuropathology, Comprehensive Cancer Center, Eberhard Karls University of Tübingen, Liebermeisterstraße 8, 72076 Tübingen, Germany. ⁴Center for Preclinical Research, Fondazione IRCCS Ca' Granda Ospedale Maggiore Policlinico, Via Pace 9, 20100 Milan, Italy. ⁵Department of Dermatology, Eberhard Karls University of Tübingen, Liebermeisterstraße 25, 72076 Tübingen, Germany. ✉email: Manfred.Kneilling@med.uni-tuebingen.de; Christoph.Trautwein@med.uni-tuebingen.de

Immunometabolism is crucial to fine-tune and modulate inflammatory processes and thus can terminate or promote inflammation directed to the final pathophysiological phenotype¹. Several autoimmune conditions, such as rheumatoid arthritis or psoriasis vulgaris, are characterised as T-cell-driven inflammatory immune responses^{2,3}. Dynamically progressing chronic inflammatory autoimmune processes are also frequently associated with a loss of function, scar formation and permanent tissue damage, such as cartilage and joint destruction.

Inflammation is highly interconnected with reactive oxygen and nitrogen species (RONS) production⁴. RONS are necessary for the appropriate inflammatory response and immune cell signalling. Alternatively, excessive RONS production is extremely toxic not only to pathogens but also to endogenous cells, resulting in increased synthesis of RONS-scavenging metabolites such as ascorbate and glutathione. Triggering inflammation results in metabolic reprogramming, which leads to temporary metabolic changes; some pathways, such as lipid metabolism⁵ and the tricarboxylic acid (TCA) cycle⁶, are disrupted due to the increasing need for RONS scavengers and energy production⁷. If the inflammatory state is prolonged, it can eventually lead to permanent site-specific and systemic dysregulation and tissue damage. Inflammation progression and cellular homeostasis can thus be characterised by metabolite changes, offering a potential wider understanding and points for early intervention⁸.

Recently, we noninvasively characterised the temporal dynamics of RONS⁹ in vivo and the differential impact of different RONS sources⁸ in our T-cell-driven trinitrochlorobenzene (TNCB)-induced acute and chronic contact delayed-type hypersensitivity reaction (DTHR) prototypic preclinical model^{10–13},

which aids in determining the underlying mechanisms of T-cell-driven autoimmune diseases.

Nuclear magnetic resonance (NMR) spectroscopy and mass spectrometry-based metabolomics have been previously broadly applied to characterise inflammation in various models, such as murine tissue^{14,15}, patient blood^{16,17}, urine¹⁸, and biopsy tissue¹⁹, indicating a crucial metabolomics role in inflammation characterisation during disease progression^{20,21}.

We employed the established prototypic cutaneous DTHR model¹³, mediated by IFN- γ -producing CD4⁺ (Th1 cells) and CD8⁺ T cells (Tc1 cells)^{13,22,23}, to characterise the temporal dynamics of the metabolic signature during acute and progressive inflammation and to uncover the underlying mechanisms of T-cell-driven inflammatory diseases.

The focus of this study was to identify the metabolic alterations, pathways and regulators that indicate the switch from acute to chronic inflammation and the related biomolecular events occurring during progressive T-cell-driven inflammation. Hereby it was found that acute and chronic DTHR yielded significantly different metabolite concentration profiles related to tricarboxylic acid (TCA) cycle activity, energy metabolism, redox metabolism, nucleotide and growth metabolism, and immune cell activity. These findings help to better understand the underlying metabolic events of acute and chronic T-cell-driven inflammatory immune responses and serve as a prerequisite for the development of novel therapeutics.

Results

Ear swelling progresses during acute and chronic cutaneous DTHR. Experimental setup of the acute and chronic TNCB-specific cutaneous DTHR model is illustrated in Fig. 1a. The course of the ear swelling response represents a clinical measure of the severity of inflammation (Fig. 1b), characterising the temporal dynamics of the ear swelling response at the point in time of metabolite analysis of the ear tissue of naive mice, mice with acute (1st TNCB ear challenge) and chronic (5th TNCB ear challenge) cutaneous DTHR. During acute cutaneous DTHR, ear thickness significantly increased ($P = 0.048$) from 4 h (0.24 mm \pm 0.02 mm) to 24 h (0.42 mm \pm 0.03 mm) after the 1st TNCB ear challenge, which is the peak of acute inflammation. At 0 h of chronic cutaneous DTHR, 48 h after the 4th TNCB ear challenge, the ear thickness (0.48 mm \pm 0.06 mm) was slightly above the peak of acute cutaneous DTHR. During chronic cutaneous DTHR, the swelling peaked 4 h and 24 h after the 5th TNCB challenge. In fact, ear thickness increased significantly during the course of chronic cutaneous DTHR from 0 h to 4 h ($P = 0.003$) and from 0 h to 24 h ($P = 0.0007$) after the 5th TNCB ear challenge (Fig. 1b).

Inflamed ears with acute and chronic cutaneous DTHR exhibit a distinct metabolic profile.

Inflamed ears with acute and chronic cutaneous DTHR were further characterised by their unique metabolite concentration patterns, as shown by the group separation and 95% confidence interval clouds in principal component analysis (PCA) (Fig. 2a). Here, the naive control ears were clearly separated from the inflamed ears with acute and chronic cutaneous DTHR. In addition, PCA also separated inflamed ears with acute DTHR from those with chronic cutaneous DTHR. Interestingly, PCA identified the peaks of acute and chronic cutaneous DTHR (acute, 24 h; chronic, 4 h) in a similar direction in principal component 2. Inflamed ears with chronic cutaneous DTHR, collected 12 h and 24 h after the 5th TNCB ear challenge, exhibited the strongest similarities in metabolite concentration patterns, illustrated by the slight overlap of the 95% confidence interval cloud (Fig. 2a).

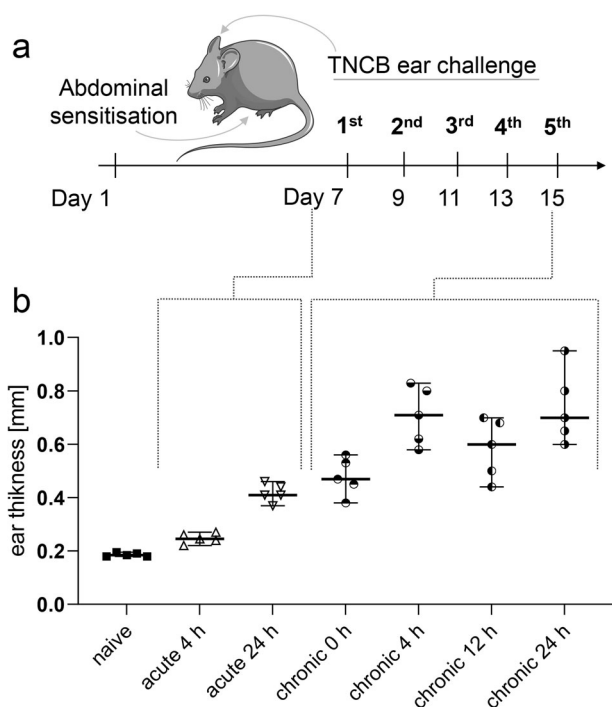


Fig. 1 Experimental setup, course of ear swelling response and metabolite concentration profiling. **a** Experimental timeline: Sensitisation with 5% trinitrochlorobenzene (TNCB) at the abdomen on Day 1, followed by TNCB ear challenges (1% TNCB) at the right ear on Day 7 (acute DTHR) and repetitive TNCB ear challenges at Days 9, 11, 13 and 15 (chronic DTHR). **b** Ear thickness of naive mice and mice with acute (4 h and 24 h after the 1st TNCB challenge) and chronic (0 h – 48 h after the 4th challenge – and 4 h, 12 h and 24 h after the 5th TNCB challenge) cutaneous DTHR ($n = 4$ animals).

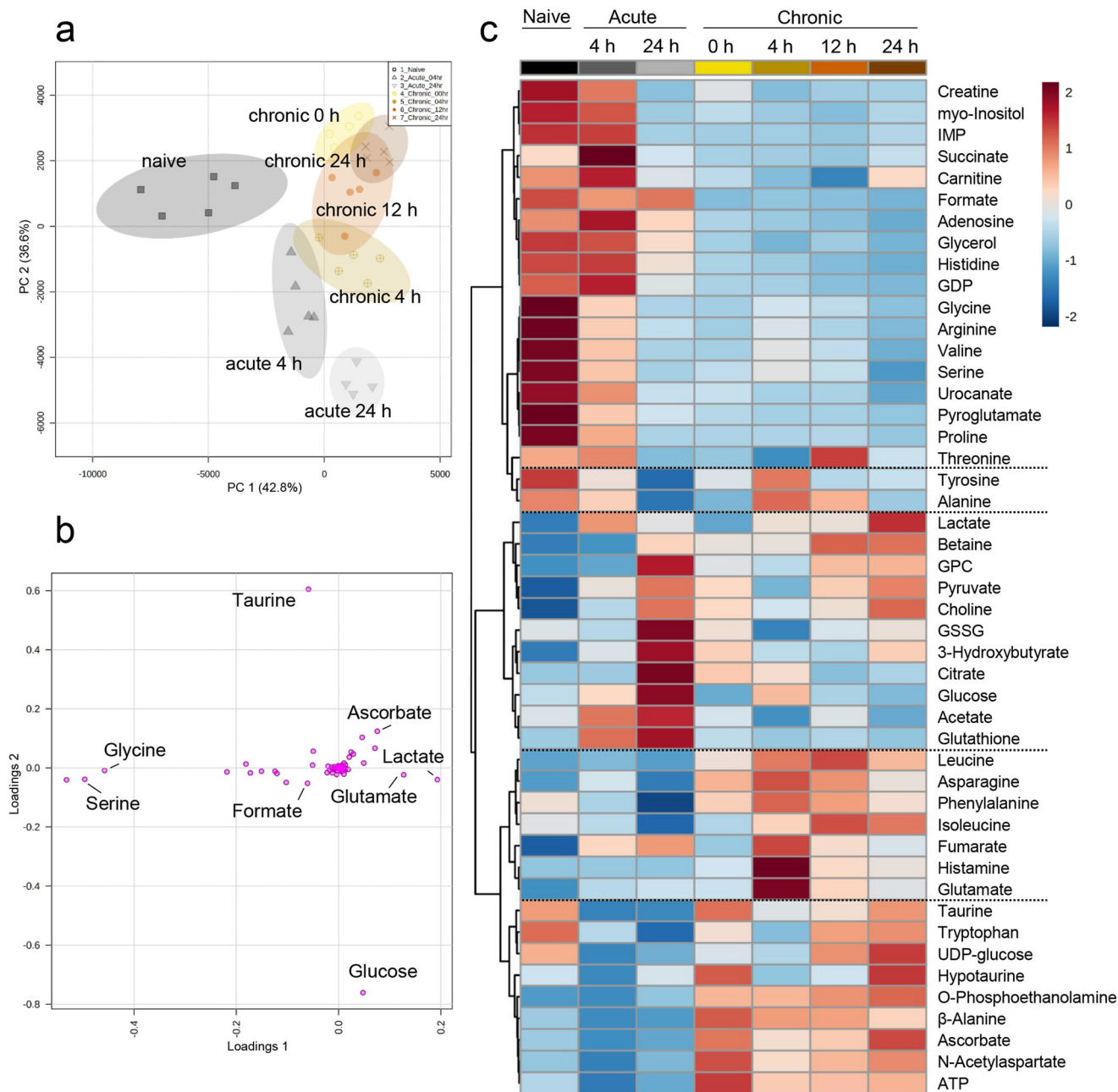


Fig. 2 Metabolomics overview of metabolite concentrations in healthy ears and in inflamed ears with acute and chronic cutaneous DTHR. **a** Principal component analysis (PCA) of the first two principal components (PC 1 (42.8%), PC 2 (36.6%)) scores plot illustrating the group separation based on the metabolite concentrations. Naive—dark grey squares, acute 4 h—medium grey upward triangles, acute 24 h—downward light grey triangles, chronic 0 h—yellow empty circles, chronic 4 h—beige dots with cross, chronic 12 h—orange full dots, chronic 24 h—brown exes. **b** PCA loadings plot illustrating the most significant metabolites that drive the principal component separation. **c** Averaged group heatmap illustrating normalised and autoscaled (-2; 2) metabolite concentration changes during acute and chronic cutaneous DTHR, red—relatively high concentration, blue—relatively low concentration. Metabolite list organised by Ward hierarchical clustering using Euclidean distance measure ($n = 5$ animals, except acute 24 h $n = 4$ animals). GDP guanosine diphosphate, IMP inosine monophosphate, GPC sn-glycero-3-phosphocholine, GSSG glutathione disulfide, UMP uracil monophosphate, ATP adenosine triphosphate.

When comparing naive ear tissue with acute and chronic DTHR-affected ear tissue in detail, we observed chronic inflammation-dependent specific changes in the metabolic profile, as illustrated in the PCA loadings plot (Fig. 2b) and the heatmap (Fig. 2c and Supplementary Fig. 1). The healthy naive condition was characterised by active amino acid metabolism, nucleotide metabolism and relatively low RONS scavenger concentrations. During the irritative toxic peak of acute cutaneous DTHR, 4 h after the 1st TNCB ear challenge, slight changes towards downregulation of several amino

acid concentrations, such as glycine, arginine, valine, serine and proline, were observed. Here, the initial innate immune response was characterised by increased glutathione (GSH), glutathione disulfide (GSSG), acetate, glucose, citrate and fumarate concentrations (Fig. 2b, c). During the peak of the ear swelling response, 24 h after the 1st TNCB ear challenge, we identified increased pyruvate, 3-hydroxybutyrate, choline, sn-glycero-3-phosphocholine (GPC), citrate and glucose concentrations. Meanwhile, amino acids, such as glycine, arginine, valine, serine, proline, isoleucine, and tryptophan, were

continuously downregulated during the acute phase of cutaneous DTHR (Fig. 2c).

Chronic cutaneous DTHR was distinctively characterised by increased β -alanine, ascorbate, ATP and taurine concentrations (Fig. 2c and Supplementary Fig. 2). Concentrations of histamine, glutamate, leucine, phenylalanine, alanine and tyrosine in inflamed ears peaked simultaneously with the peak of chronic cutaneous DTHR at 4 h after the 5th TNCB ear challenge, followed by a constant decrease at 12 h and 24 h. During the chronic phase of cutaneous DTHR, glucose, GSH, GSSG and TCA cycle metabolites citrate and succinate remained at low concentrations similar to healthy ears of the naive group (Fig. 2c).

Histopathological and immunohistochemical characterisation of acute and chronic cutaneous DTHR. Histopathological analysis of haematoxylin and eosin (H&E)-stained slices from inflamed ears with acute cutaneous DTHR revealed pronounced oedema with dilated blood vessels and extravasation of PMN, moderate neutrophilic infiltrate, subepidermal neutrophilic abscesses (Munro's microabscesses) and small crusts at 24 h after the 1st TNCB ear challenge (Fig. 3a, b). Meanwhile, H&E analysis of inflamed ears with chronic cutaneous DTHR showed a pronounced leucocyte infiltrate, hyperkeratosis, acanthosis, dilated blood vessels and an increased number of blood vessels (Fig. 3c).

To further characterise the immune cell infiltrate throughout acute and chronic cutaneous DTHR, we performed immunohistochemistry (IHC), focusing on cells expressing CD3 (T cells), MPO (neutrophils, macrophages) and Iba1 (phagocytes, mainly macrophages). No T cells or neutrophils were present in healthy naive ears, while Iba1 staining revealed the presence of some resident macrophages (Fig. 3a, d–f). During acute cutaneous DTHR, 4 h after the 1st TNCB ear challenge, we observed some MPO- and CD3-positive cells within the vessels but not in the surrounding tissue, indicating an initial infiltration of neutrophils and T cells into the inflamed ears (Fig. 3b, d–f). Notably, 24 h after the 1st challenge, we observed a strongly pronounced infiltration of neutrophils with neutrophil abscesses and crusts in the epidermis, reflecting the characteristics of an early acute inflammatory immune response. In addition, a mild increase in CD3⁺ T cells and macrophages was observed (Fig. 3b, d–f).

At 48 h after the 4th challenge (0 h), the point in time of the 5th TNCB ear challenge, some CD3⁺ T cells together with scarce MPO⁺ cells and a massive accumulation of macrophages in the dermis (Fig. 3c–f) were observed. The infiltration of CD3⁺ T cells and MPO⁺ neutrophils steadily increased from 4 h to 24 h after the 5th TNCB ear challenge, while the presence of macrophages remained at an identical level (Fig. 3c–f).

Individual metabolites correlate with the severity of the ear swelling response and the specific immune cell subtype infiltration. Our investigations focused on potential correlations between individual metabolite alterations, the degree of ear swelling response, reflecting the severity of inflammation, and the presence of immune cells within the inflamed ears with acute and chronic cutaneous DTHR.

Positive correlations were observed between the degree of ear swelling response and betaine, O-phosphocholine, ascorbate, leucine, and glutamate concentrations in inflamed ears with acute and chronic cutaneous DTHR (Fig. 4a). In contrast, we observed a negative correlation between the severity of ear swelling and the metabolites creatine, myo-inositol, IMP, formate, GDP and several amino acids, such as glycine, valine, arginine, serine, proline and histidine (Fig. 4b).

Enhanced neutrophil recruitment showed a distinctive metabolic signature compared to the degree of ear swelling as well as

to the other leucocyte subtypes. In fact, increased concentrations of AMP, 3-hydroxybutyrate, choline, pantothenate, quinone, lysine, GSSG, and citrate were specifically associated with neutrophil infiltration, while the opposite trend was observed for ATP, β -alanine, ascorbate and N-acetylaspartate (NAA), which did not correlate with enhanced neutrophil recruitment (Fig. 4a).

Regarding negative correlations (Fig. 4b), carnitine, O-acetylcarnitine, formate, adenosine and acetate were negatively associated with all inflammatory variables except for neutrophil infiltration. Taurine, hypotaurine and GTP were positively associated only with macrophages. In addition, the abundance of T cells and macrophages was negatively correlated with succinate, carnitine, O-acetylcarnitine, formate, glycerol, adenosine, and acetate concentrations in inflamed ears with acute and chronic cutaneous DTHR (Fig. 4b).

Acute and chronic inflammation is associated with changes in redox and immune metabolism. Redox metabolism is an interconnected network of several cascade reactions, simplified in Fig. 5a. GSH and GSSG were significantly increased during the peak of acute cutaneous DTHR, while in the chronic phase, the concentrations of GSH and GSSG were similar to the baseline measurements of healthy ears derived from naive mice (Fig. 5b and Supplementary Fig. 3a). We observed a further constant downregulation of the folate and methionine cycle metabolites serine, glycine and 5-oxoproline (pyroglutamate), which are also precursors for GSH synthesis (Supplementary Fig. 3a), in inflamed ears with both acute and chronic cutaneous DTHR.

The overall GSH and GSSG concentration pattern of inflamed ears with acute and chronic cutaneous DTHR positively correlated with acetate, glucose, and lysine, while ascorbate and taurine revealed a negative correlation together with phenylalanine, UDP-glucose and β -alanine (Fig. 5c and Supplementary Figs. 3 and 4).

Ascorbate concentrations were increased during chronic compared to acute cutaneous DTHR (Fig. 5b), similar to ATP and N-acetylaspartate (Supplementary Fig. 3b). Although the results above show significant changes in the common redox metabolites, we did not observe any significant changes in the overall NAD⁺, which is crucial for redox metabolism, over the investigated period (Supplementary Fig. 3b). Furthermore, taurine, which can act as a RONS scavenger, was consumed during acute cutaneous DTHR peaking 24 h after the 1st TNCB ear challenge (Fig. 5b). At 48 h after the 4th challenge, the point in time shortly before the 5th TNCB ear challenge, the taurine concentration within the inflamed ear was similar to that in the naive control ear, while taurine was depleted at 4 h after the 5th TNCB ear challenge, the peak in the ear swelling response of chronic cutaneous DTHR. Together with taurine, we detected increased β -alanine, betaine and hypotaurine concentrations in the chronic phase of cutaneous DTHR (Supplementary Fig. 3c). However, histidine and its downstream metabolite urocanate were significantly downregulated during the course of chronic cutaneous DTHR while histamine concentration peaked 4 h after the 5th TNCB ear challenge (Supplementary Fig. 3d).

Inflammation and oxidative stress are associated with metabolic responses in energy, growth and nucleotide metabolism. Next, we investigated the metabolites related to energy, growth, and cellular renewal metabolism (Fig. 6a and Supplementary Figs. 4 and 5). As early as 4 h after the 1st TNCB ear challenge, a significant accumulation of succinate was detected (Fig. 6b). Furthermore, we quantified increased concentrations of pyruvate, lactate, fumarate, glutamate, citrate, and glucose that peaked in

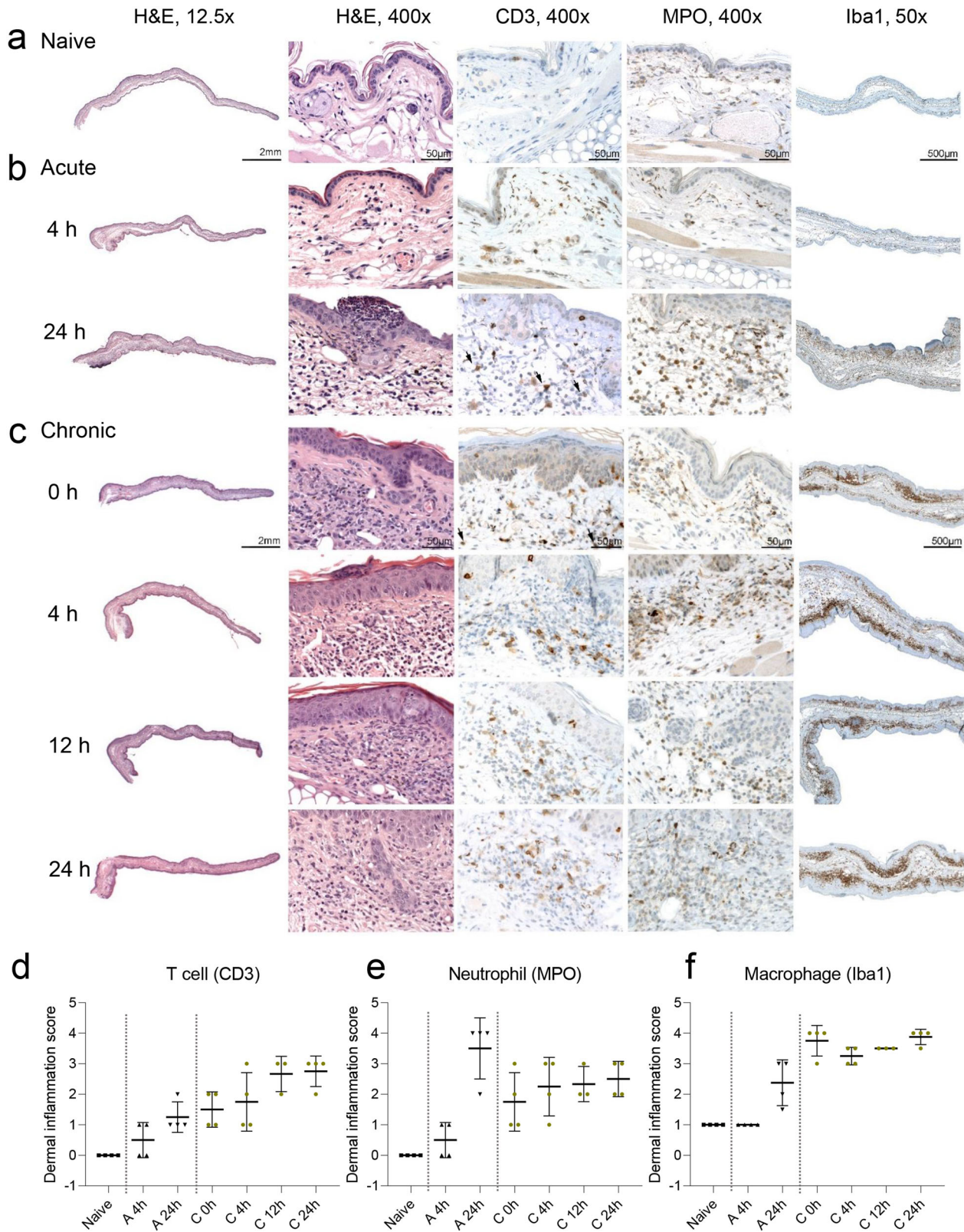


Fig. 3 Histopathological (H&E) and immunohistochemical (IHC) characterisation of the inflammatory immune cell infiltrate during acute and chronic cutaneous DTHR. Naive ears (a), inflamed ears with acute (b) cutaneous DTHR (4 h and 24 h) and (c) chronic cutaneous DTHR (0 h, 4 h, 12 h, and 24 h) H&E staining (magnification $\times 12.5$ and $\times 400$, at the scale of 2 mm), CD3, MPO IHC (magnification $\times 400$, at scale of 50 μm), and Iba1 IHC (magnification $\times 50$ and scale of 500 μm). Scoring of dermal CD3 (d), MPO (e) and Iba1 (f) immune cell infiltration presented as a scatter plot: mean \pm SD (0 = no inflammatory infiltrate, 1 = minimal, 2 = mild, 3 = moderate, 4 = severe presence of inflammatory cells, $n = 4$ animals, except chronic 12 h $n = 3$ animals). Grey dashed lines aid visual separation between naive, acute and chronic DTHR.

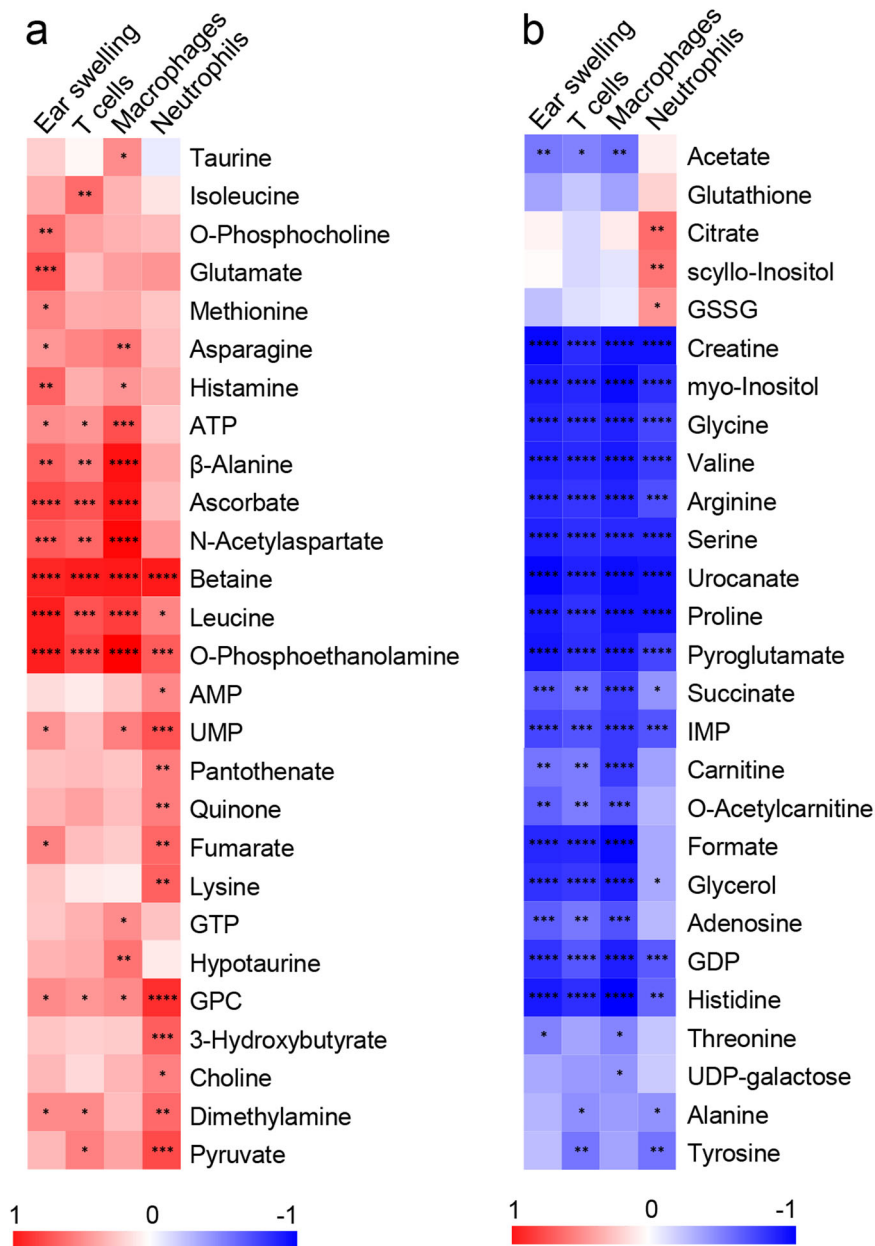


Fig. 4 Ear swelling and immune parameters correlated to the metabolite concentrations during acute and chronic cutaneous DTHR. Ear swelling thickness, T cell (CD3), macrophage and neutrophil epidermal inflammation scores were correlated to metabolite concentration changes over the whole experimental setup, showing autoscaled (−1; 1) (a) positive (red) and (b) negative (blue) correlation with correlation coefficient statistical significance *P* values: ****<0.0001, ***<0.001, **<0.01, *<0.05, based on Pearson *r* distance measure ($n = 5$ animals).

inflamed ears with acute cutaneous DTHR 24 h after the 1st TNCB ear challenge. Meanwhile, anaplerotic TCA cycle substrates of fumarate (phenylalanine and tyrosine), succinyl-CoA (isoleucine, valine) and pyruvate (serine, glycine, alanine) were downregulated in inflamed ears with acute cutaneous DTHR compared to naive control ears (Supplementary Figs. 3 and 4). Most of these metabolites were permanently downregulated without recovering their baseline concentrations even in the chronic state of cutaneous DTHR. Furthermore, cataplerotic substrates of α -ketoglutarate (arginine, proline) showed similar concentration decay in inflamed ears with initially acute but also with chronic cutaneous DTHR. Creatine was similarly consumed as its metabolic precursors arginine, proline, glycine and serine, once again stressing the downregulation of these metabolic pathways during chronic cutaneous DTHR (Supplementary

Fig. 4a). In addition, the moderate irritative toxic peak of the ear swelling response at 4 h after the 1st TNCB ear challenge was further characterised by the build-up of choline, GPC and UMP (Supplementary Fig. 5a, b). Conversely, we observed decay of IMP and GDP in inflamed ears with chronic cutaneous DTHR (Supplementary Fig. 5c).

During chronic cutaneous DTHR, an accumulation of phenylalanine, tyrosine and glutamate was observed 4 h after the 5th TNCB ear challenge, suggesting disrupted substrate uptake (Supplementary Fig. 4a) at the peak of chronic inflammation. We also identified an increase in the fumarate and glucose concentrations at 4 h during chronic cutaneous DTHR (Fig. 6). Similarly, we observed an increase in methionine (Supplementary Fig. 3), isoleucine, alanine, lysine, asparagine concentrations, glutamate/serine ratio (Supplementary Fig. 4a, b),

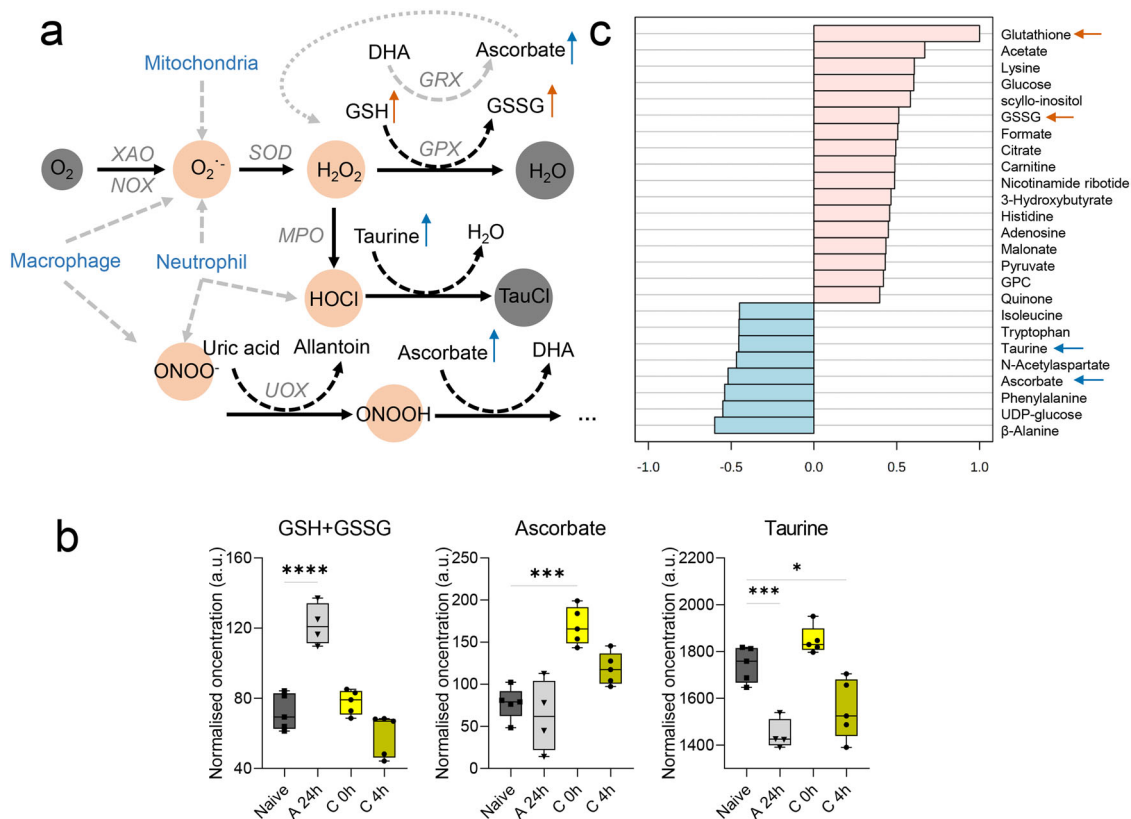


Fig. 5 Redox and immune metabolism during acute and chronic cutaneous DTHR. **a** Overview of reactive oxygen and nitrogen species (RONS) production by resident and infiltrating immune cells during an immune response initiating the RONS cascade and their scavengers. The most important small molecule RONS scavengers, such as glutathione (GSH), ascorbate and taurine, are illustrated at their site of action. The ear swelling response during the acute cutaneous DTHR peak at 24 h is illustrated by the orange arrow, and the chronic cutaneous DTHR peak at 4 h is illustrated by the blue arrow. **b** Normalised concentration changes illustrated as box plots with max. to min. whisker, individual replicate points and median of GSH and glutathione disulfide (GSSG) concentration sum, ascorbate and taurine changes during acute 24 h (grey, downward triangle) and chronic 0 h (bright yellow, dot) and 4 h (dark yellow, dot) cutaneous DTHR (compared to naive control (grey, square), P values **** <0.0001 , *** <0.001 , ** <0.01 , * <0.05 , one-way ANOVA). **c** Correlation pattern hunter graph of the top 25 most significantly correlated metabolites to glutathione (GSH) concentration changes over time, based on Pearson r distance measure ($n = 5$ animals, except A 24 h $n = 4$ animals). DHA dehydroascorbate, GPC sn-glycero-3-phosphocholine, GPX glutathione peroxidase, GRX glutaredoxin, GSSG glutathione disulfide, MPO myeloperoxidase, NADPH reduced nicotinamide adenine dinucleotide phosphate, NOX NADPH oxidase, SOD superoxide dismutase, TauCl taurine chloramine, UDP uridine diphosphate, UOX urate oxidase, XAO xanthine oxidase.

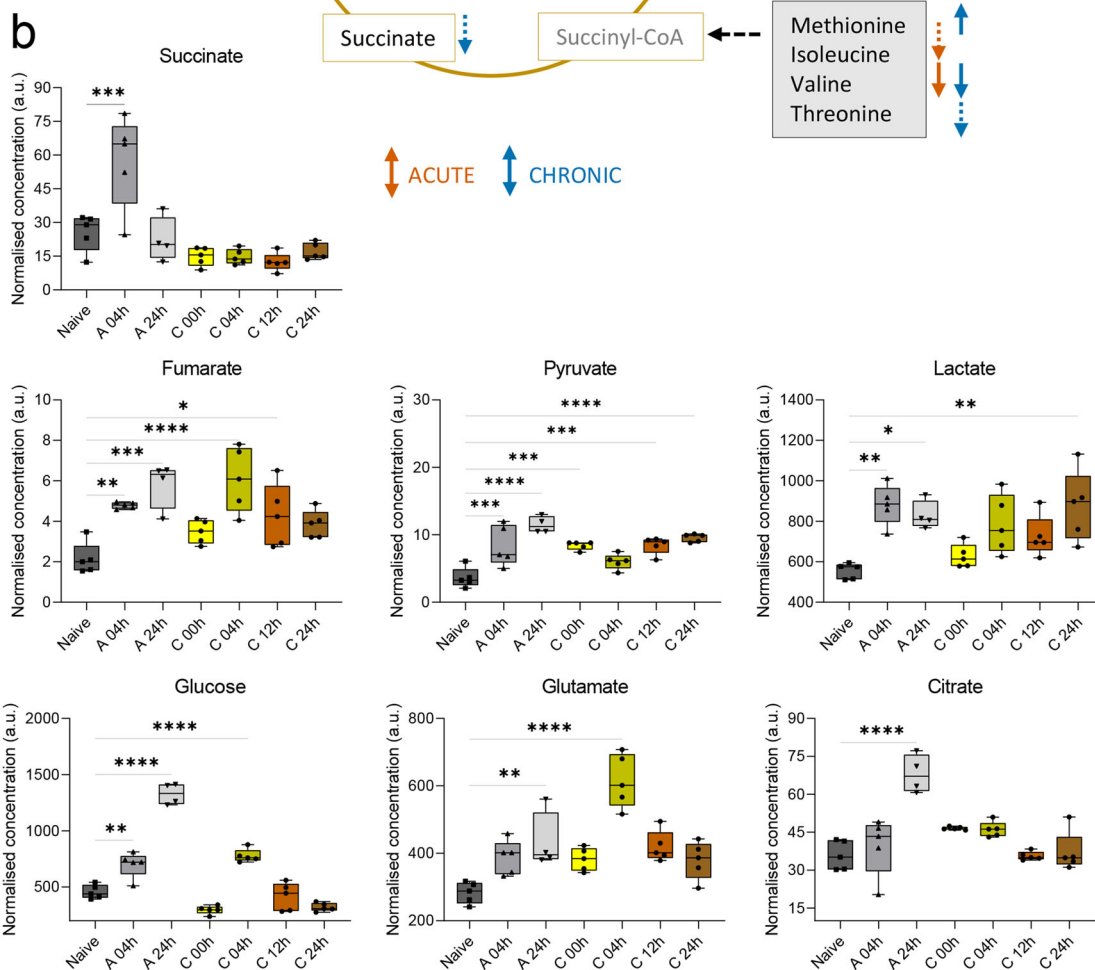
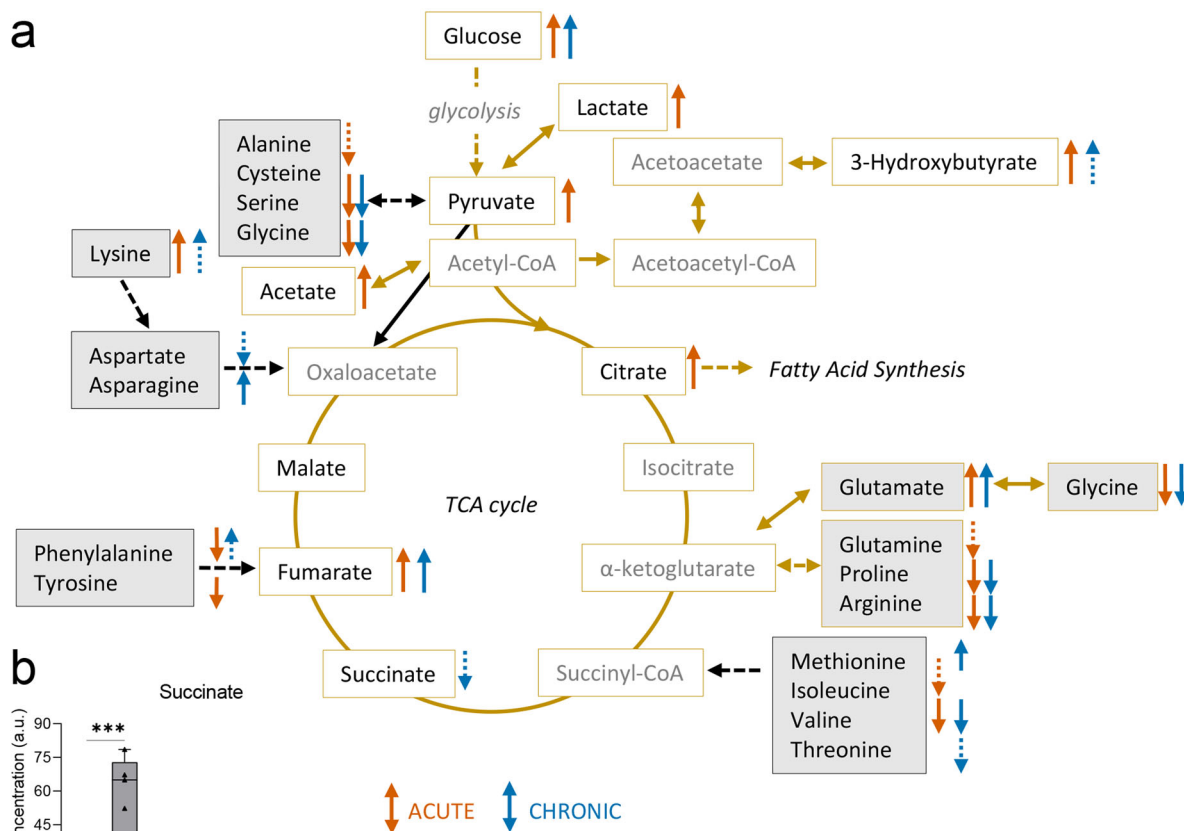
O-phosphocholine and O-phosphoethanolamine concentrations (Supplementary Fig. 5b), while myo-inositol and glycerol concentrations decreased during chronic cutaneous DTHR (Supplementary Fig. 5d).

Discussion

We identified specific metabolite patterns for ear swelling and the immune response during acute and chronic cutaneous DTHR. Acute cutaneous inflammation was associated with early succinate accumulation, disrupted energy metabolism with alterations in the TCA cycle, increased glutathione metabolism, and a switch to ketone body production and β -oxidation, while the chronic phase is characterised by increased ascorbate and taurine as RONS scavengers, indicating a switch in redox metabolism. Both types of inflammation showed alterations in metabolic precursors of membrane lipid synthesis, turnover and the Kennedy pathway. These metabolite signatures correlated well with the characteristic inflammatory response peaks of acute DTHR at 24 h after the 1st TNCB ear challenge and chronic cutaneous DTHR at 4 h after the 5th TNCB challenge, as reported in the previous studies^{8,9}. Our data confirm that acute and chronic inflammation leads to differences in the immune cell composition, illustrated by the

changes in the concentration of metabolites involved in redox, immune, energy, cell growth and nucleotide metabolism.

Resident macrophages are the predominant immune cell type in naive ear tissue, also previously shown in a psoriatic mouse model²⁴. Acute inflammation is characterised by a strong influx of neutrophils and activation of resident macrophages; however, this influx of neutrophils peaks at 24 h post 1st challenge, as discussed in the previous work⁹. Changes observed in samples collected 4 h post 1st TNCB challenge reflect the innate immune response of the resident cells, as no infiltrated immune cells were detected at this time. Furthermore, acute inflammation is accompanied by strong oedema and neutrophil recruitment, resulting in increased ear swelling. In our dataset, we quantified a significant elevation of succinate 4 h after the 1st TNCB ear challenge during acute inflammation. Succinate accumulation reportedly signifies a disruption in the TCA cycle²⁵. This disruption was later confirmed by subsequent citrate, pyruvate, lactate and fumarate accumulation at the acute phase 24 h after the 1st TNCB challenge. Succinate is also a pleiotropic signalling molecule responsible for HIF-1 α stabilisation and continuation of proinflammatory signalling²⁶. Succinate was further reduced to baseline 24 h after the 1st challenge and remained at low levels throughout the course of chronic inflammation, further



confirming its unique role as an early inducer in the innate immune reaction.

GSH is a major physiological antioxidant, and it plays a crucial role in redox signalling and inflammatory immune cascades. GSH controls the innate immune response in the context of infection²⁵. Amino acids such as serine, glycine and threonine are precursors for the folate cycle, while glycine, together with

cysteine and glutamate, is also a precursor for GSH synthesis. We quantified the highest GSH and GSSG concentrations at the acute inflammatory response peak 24 h after the 1st TNCB challenge, correlating to the infiltrating neutrophil peak.

Short-chain fatty acids have been reported in inflammation-regulatory processes as anti-inflammatory agents^{27,28}. We quantified acetate upregulation during the acute cutaneous DTHR,

Fig. 6 Energy metabolism during acute and chronic cutaneous DTHR. **a** Simplified illustration of the tricarboxylic acid (TCA) cycle with additional information of amino acid entry as anaplerotic (black frame, grey background) and cataplerotic substrates. Dashed line for indirect reactions with multiple steps. **b** Metabolite normalised concentration changes (in arbitrary unit (a.u.)) illustrated as box plots with max. to min. whisker, individual replicate points and median within the inflamed ears during acute 4 h (medium grey, upward triangle), 24 h (light grey, downward triangle) and chronic 0 h (bright yellow, dot), 4 h (dark yellow, dot), 12 h (orange, dot) and 24 h (brown, dot) cutaneous DTHR (compared to naive control (dark grey, square), P value $^{***}<0.0001$, $^{**}<0.001$, $^{*}<0.01$, $^{<0.05}$, $n = 5$ animals, except A 24 h $n = 4$ animals). Statistical significance test stars shown for comparisons to naive control by one-way ANOVA. The ear swelling response during the acute cutaneous DTHR peak at 24 h is illustrated by the orange arrow, and the chronic cutaneous DTHR peak at 4 h is illustrated by the blue arrow. The dashed lines show a non-significant trend.

which was later reduced to baseline levels in the chronic phase of cutaneous DTHR, similar to the naive control. Acetate concentration changes negatively correlated with macrophage and T-cell infiltration patterns during acute and chronic inflammation progression.

Furthermore, the 3-hydroxybutyrate concentration was increased in the acute phase of cutaneous DTHR, indicating a response to increased energy consumption and reduced fatty acid stock²⁹. Switching to alternative energy substrates, such as fatty acid β -oxidation, can be seen as a result of a decreased TCA cycle, as indicated by the accumulation of the TCA cycle-related metabolites fumarate, pyruvate, lactate, glutamate, citrate and even glucose during the acute inflammation peak.

The histopathological analysis confirmed that acute inflammation was dominated by the infiltration of neutrophils, while chronic cutaneous DTHR was associated with an influx of T cells, a dense accumulation of macrophages, hyperkeratosis and acanthosis. The influx and activation of immune cells peaked at 4 h after the 5th TNCB ear challenge, as shown previously⁹. Different leucocytes are recruited to the site of inflammation, including macrophages, CD4⁺ and CD8⁺ T cells, B cells and neutrophils. Resident macrophages and mast cells proliferate during chronic inflammation. While neutrophils are still present, their percentage is lower than that in the acute state due to the presence of other recruited cell types confirmed by immunohistochemistry. Neutrophils highly express NADPH oxidase 2 (NOX2), producing excess superoxide, which is quickly converted to hydrogen peroxide (H₂O₂) and further downstream to hypochlorous acid (HOCl) by MPO. Furthermore, the iNOS enzyme facilitates nitric oxide (NO) production, which is further converted to peroxynitrite (ONOO⁻)³⁰. Moreover, fibrosis, angiogenesis, an increase in connective tissue and vascularisation are additional consequences of a chronic inflammatory state³¹.

We observed increased ascorbate and taurine 48 h after the 4th challenge, the time point of the 5th TNCB ear challenge, which was reduced at 4 h after the 5th TNCB ear challenge. GSH and GSSG concentrations in inflamed ears were restored back to similar concentrations as those determined in naive control ears. In mouse liver, GSH is consumed during oxidation to produce ascorbate from dehydroascorbate (DHA)^{32,33}. This reaction, however, also produces additional hydrogen peroxide (H₂O₂). However, in humans, ascorbate cannot be synthesised, though it still participates in RONS scavenging³⁴.

In addition, serine was depleted during chronic cutaneous DTHR. A previous report demonstrated that supplementation with serine can re-establish methionine cycle activity and GSH synthesis due to a shift from glycolysis to GSH production and one-carbon metabolism³⁵. Therefore, depletion of serine could lead to the downregulation of the methionine cycle and eventually to GSH depletion during the chronic phase of cutaneous DTHR.

Taurine, a common HOCl scavenger³⁶ that accumulates in tissues exposed to oxidative stress³⁷, was consumed during the acute phase, thereby negatively correlating to the GSH and GSSG concentrations. Taurine build-up has been previously quantified in M1-type macrophages when GSH is depleted³⁸, potentially indicating the redox-dependent balance between the two

scavengers. In addition, alterations of the taurine concentration have been previously reported in psoriatic skin lesions³⁹, similar to our studies related to oxidative stress and ROS scavenging well correlating to the alterations in taurine activity within inflamed ears during the course of chronic DTHR.

Furthermore, β -alanine was highly upregulated in inflamed ears during chronic cutaneous DTHR. β -Alanine is linked to the activation of T and B cells⁴⁰. The progression from acute to chronic inflammation in our model is associated with increased infiltration of T and B cells in the inflamed ears could explain the increased concentrations of β -alanine. A study in a cardiac model stated that β -alanine and taurine oppose each other, indicating that β -alanine caused taurine level reduction, mitochondrial superoxide accumulation, and eventual apoptosis and reduced ATP generation⁴¹. This fact is consistent with our observations of increased ATP in inflamed ears with chronic cutaneous DTHR when compared to inflamed ears with acute cutaneous DTHR or naive control ears.

Together with ascorbate, N-acetylaspartate (NAA) was increased at 48 h after the 4th TNCB ear challenge, the time point shortly before the 5th TNCB ear challenge, possibly as a consequence of a metabolic adaptation mechanism. NAA was then consumed at the peak of chronic cutaneous DTHR 4 h after the 5th TNCB ear challenge for a short period with a trend of regeneration until 24 h. NAA is believed to mainly be a central nervous system-characteristic metabolite; however, it is linked to de novo lipogenesis and plays an important role in histone acetylation^{42,43}. NAA accumulation has also been previously observed in tumours⁴², linking the inflammatory process to further cancer development.

Energy consumption, RONS production and cell influx are highly increased due to the progression of inflammation. RONS production during the oxidative burst leads to a switch from oxidative phosphorylation to aerobic glycolysis⁴⁴, also known as the Warburg effect. Peaks of the ear swelling response are characterised by maximal oedema and dilated blood vessels. Glucose is one of the most abundant blood metabolites. The glucose concentration increases when the blood vessels expand. We observed an increased concentration of glucose at peaks of the acute and chronic inflammatory immune response (acute, 24 h; chronic, 4 h), followed by its rapid consumption in the later phase of chronic inflammation. Meanwhile, glutamine, which is the most abundant amino acid in the blood, was not significantly changed during the chronic cutaneous DTHR, potentially due to its multiple roles and involvement in several metabolic pathways.

Lactate accumulation was observed during both acute and chronic cutaneous DTHR. During acute cutaneous DTHR, we also determined an accumulation of pyruvate and succinate, indicating disruption of the TCA cycle and the preferential use of glucose in aerobic glycolysis. During chronic cutaneous DTHR, we observed the consumption of pyruvate at the peak of chronic inflammation (chronic, 4 h) relative to 0 h, 12 h and 24 h after the 5th TNCB ear challenge. Lactate concentrations in inflamed ears were increased, potentially suggesting pyruvate conversion to lactate due to the inflammatory peak and necessary acidic environment stabilisation for recruitment of additional

inflammatory cells⁴⁵. Consistent with the changes in TCA metabolites, a slight increase in ATP consumption was determined at 4 h after the 1st TNCB ear challenge (acute cutaneous DTHR), while the energy pool was later restored upon chronic cutaneous DTHR.

Disruption of the TCA cycle during acute cutaneous DTHR was further suggested by the downregulation of its anaplerotic substrates⁴⁶. Some amino acids, such as phenylalanine, methionine and asparagine, further accumulated in the chronic phase. Phenylalanine accumulation has been previously linked to an acute inflammatory state due to disrupted metabolism^{47,48}. However, in our dataset, we quantified the reduction in phenylalanine upon acute cutaneous DTHR, while it tended to increase during the peak of chronic cutaneous DTHR at 4 h after the 5th TNCB ear challenge.

The effector phase of TNCB-induced cutaneous DTHR does not entirely reflect the pathology of clinical allergic contact dermatitis as the T-cell-driven immune response is associated with pronounced immigration of neutrophils, including subepidermal abscesses which are not evident in human contact dermatitis. However, TNCB-induced cutaneous DTHR shares a lot of similarities with clinical psoriasis vulgaris, an antigen-specific T-cell-driven autoimmune disease.

Psoriatic skin lesions have been characterised as highly metabolically active with upregulated cell proliferation⁴⁸. Phenylalanine, glutamate concentrations and glutamate/serine ratios were upregulated in lesional skin when compared to nonlesional skin or the skin of healthy patients⁴⁹, which is consistent with our findings in the preclinical acute and chronic DTHR model.

Moreover, glucose, myo-inositol and branched-chain amino acid (BCAA, valine-leucine/isoleucine) levels were reduced in psoriatic skin lesions compared to nonlesional skin⁴⁹. In our study, inflamed ears displayed increased glucose concentrations during acute and chronic inflammation, peaking at 24 h after 1st TNCB challenge and 4 h after 5th TNCB ear challenge. However, we also observed strongly reduced glucose levels during chronic cutaneous DTHR reaching baseline levels determined in healthy ears. Within our studies, myo-inositol and valine followed the trend described in human psoriasis with a significant reduction during both acute and chronic DTHR⁴⁹.

We also observed alterations in the histidine metabolism during chronic cutaneous DTHR. Thus, histidine and urocanate in inflamed ears were significantly downregulated while histamine concentration peaked 4 h after the 5th TNCB ear challenge. In line with our data, alterations in histidine metabolism have been previously reported in the context of human psoriasis skin inflammation, highlighting the histidine metabolic pathway as a potential therapeutic target⁵⁰.

We observed increased tryptophan consumption during the peak of acute cutaneous DTHR at 24 h after the 1st TNCB ear challenge as a potential indicator of the anti-inflammatory capacity of the system. Tryptophan has been linked to the immune response via the kynurenine pathway⁵¹, further connecting chronic inflammation to downstream systemic effects, such as gut dysbiosis and autoimmune disease⁵². Its degradation is a marker for immunoregulatory effects toward reduced lipid peroxidation⁵³, antioxidant activity⁵⁴, antimicrobial activity of skin inflammation⁵⁵.

Proinflammatory cytokines, which are upregulated during inflammation progression, induce changes in phospholipid species together with overall mitochondrial mass reduction¹⁷. While we quantified increased choline and GPC during acute cutaneous DTHR, they were restored to baseline levels during chronic cutaneous DTHR, leading to a build-up of O-phosphoethanolamine. These glycerophospholipid changes have been associated with pro- and anti-inflammatory activity via plasmalogen hydrolysis, cell membrane property changes, and inflammatory cascade triggering⁵⁶. A switch from choline to

ethanolamine metabolism has been previously shown as part of rapid cell growth and repair in environments such as tumour^{57,58}. Moreover, a recent study by Fuchs et al.³⁸ showed a similar build-up of O-phosphoethanolamine in M1 macrophages, resulting in reduced mitochondrial respiration and a reduced inflammatory response³⁸.

Overall, ¹H-NMR spectroscopy-based metabolomics investigation has been shown to be a useful tool for a deeper metabolic characterisation of the immune response during acute and chronic T-cell-driven inflammation. Our findings of GSH and GSSG alterations suggest a systemic response to local inflammation, as GSH is mainly synthesised in the liver⁵⁹. Because acute inflammation is driven by resident cells and infiltrating neutrophils, while the chronic phase is characterised by an increased accumulation of T cells and macrophages, we could correlate common metabolites acting as RONS scavengers to the corresponding immune cell infiltration relative to the inflammation progression stage. Fuchs et al.³⁸ *in vitro* studies recently reported that changes in taurine and tryptophan concentrations were associated with the activation state of macrophages³⁸, supporting the results of our immune cell–metabolite correlation analysis. Meanwhile, an *ex vivo* study by Chokesuwattanaskul et al.⁶⁰ has previously connected alterations in N-acetylaspartate concentrations to the activation state of neutrophils⁶⁰. These findings are also relevant towards a better understanding of how different inflammatory stages can be involved in the tumour-promoting inflammatory response and how immunometabolomics could emerge as a novel diagnosis and therapy monitoring tool.

Methods

Animals. C57BL/6J mice were purchased from Jackson Laboratory (Bar Harbor, USA). Eight-week-old female mice were used for *in vivo* experiments. All mice were held in individually ventilated cages under the same conditions in the animal housing facility at Werner Siemens Imaging Center, Eberhard Karls University of Tübingen. This study received an ethical approval and experimental protocol approval by the German Regional Authority Committee of Tübingen (Regierungspräsidium Tübingen).

Cutaneous delayed-type hypersensitivity reaction (DTHR) and ear sample collection

Mice were sensitised with 5% trinitrochlorobenzene (TNCB) at the abdomen and challenged after 1 week on the right ear with 1% TNCB to elicit acute DTHR ($n = 5$). Chronic DTHR was induced by repetitive challenges with 1% TNCB every 2 days up to five times (1st TNCB challenge: Day 7; 2nd: Day 9; 3rd: Day 11; 4th: Day 13, 5th: Day 15, Fig. 1a). Mice were anaesthetised by inhalation of isoflurane-O₂ (1.5% Forane, Abbott GmbH, Wiesbaden, Germany), and the ear thickness was measured with a micrometre (Kroeplin, Schlüchtern, Germany) before (naive), 4 h, 12 h and 24 h after the 1st and 5th TNCB challenge to monitor the course of the ear swelling response.

Ear tissue ($n = 5$) was cut with scissors immediately after sacrificing experimental mice and snap-frozen in liquid nitrogen at the following time intervals (Fig. 1a): (1) naive, immediately before the 1st TNCB challenge; (2) acute inflammation: at 4 h and 24 h after the 1st TNCB challenge, referred to as A 4 h and A 24 h, respectively; (3) chronic inflammation: at 48 h after the 4th and at 4 h, 12 h and 24 h after the 5th TNCB challenge, referred to as C 0 h, C 4 h, C 12 h, and C 24 h, respectively.

Histopathology and immunohistochemistry. Ear tissue samples ($n = 4$) were fixed in 4.5% formalin and further embedded in paraffin. Three to five micrometre-thick sections were cut from distinct samples and stained with haematoxylin and eosin (H&E) for histology. Immunohistochemistry was performed with an automated immunostainer (Ventana Medical Systems, Inc., Oro Valley, USA). The slides were stained with antibodies against the cluster of differentiation 3 protein complex (CD3, Clone SP7, DCS Innovative Diagnostik-Systeme GmbH u. Co. KG, Hamburg, Germany), myeloperoxidase (MPO, Anti-Myeloperoxidase Ab-1, Lab Vision UK, Ltd., Newmarket, Suffolk) and ionised calcium-binding adaptor molecule 1 (Iba1, Abcam, Cambridge, UK). Appropriate positive and negative controls were used to confirm the adequacy of the staining. Photomicrographic images were acquired with an Axioskop 2 plus Zeiss microscope with a Jenoptik ProgRes C10 plus camera and software (Laser Optik System, Jena, Germany). Final image preparation was performed with Adobe Photoshop CS6.

The epidermal inflammation score was based on the presence and number of epidermal abscesses and crusts per section (0 = no damage, 1 = presence of abscesses, 2 = between 1 and 5 crusts, 3 = between 6 and 10 crusts, 4 = more than 11 crusts). In addition, a semiquantitative analysis of dermal inflammation was

performed (“–” = no inflammatory infiltrate, “+” = minimal inflammatory cells, “++” = mild inflammation, “+++” = moderate inflammation, “++++” = severe amount of inflammatory cells). Due to a technical issue, one sample of the chronic 12 h group had to be excluded from further analysis. Therefore, chronic 12 h group $n = 3$ animals, while all the other sample conditions, naive, acute 4 h and 24 h, chronic 0 h, 4 h, and 24 h were $n = 4$ animals.

Ear tissue preparation for metabolomics. Deep-frozen ear tissue ($n = 5$) was cryogenically pulverised (Covaris cryoPREP CP02, Woburn, MA, USA) using liquid nitrogen and transferred to adaptive focused acoustics (AFA)-compatible glass tubes. A two-phase metabolite extraction protocol was applied to remove lipid signals from the $^1\text{H-NMR}$ spectra. Therefore, 300 μL of methanol (LC-MS grade, Sigma Aldrich, Taufkirchen, Germany) and 1000 μL of *tert*-butyl methyl ether (MTBE, Sigma Aldrich, Taufkirchen, Germany) were added to the homogenous tissue powder and gently vortexed. A 5 min ultrasonication programme was employed for metabolite extraction (Covaris E220 Evolution, Woburn, MA, USA). Then, 250 μL of ultrapure water was added for two-layer phase separation. After dividing the layers, the polar phase was evaporated to dryness and used for subsequent metabolomics analysis.

Sample preparation and $^1\text{H-NMR}$ spectroscopy acquisition. Dry metabolite pellets were resuspended in a deuterated phosphate buffer (pH corrected to 7.4) containing 1 mM 3-(trimethylsilyl) propionic-2,2,3,3- d_4 acid sodium salt (TSP) as an internal standard (Sigma Aldrich Chemie, Taufkirchen, Germany). NMR spectra were recorded from distinct samples at 298 K on a 14.1 Tesla ultrashielded NMR spectrometer (600 MHz proton frequency, Avance III HD, Bruker BioSpin, Ettlingen, Germany) equipped with a triple resonance 1.7 mm room temperature microprobe. Short zero-go (zg), 1D nuclear Overhauser effect spectroscopy (NOESY) and Carr-Purcell-Meiboom-Gill (CPMG, 1024 scans) pulse programmes were used for spectral acquisition. Bruker TopSpin 3.6.1 software was used for spectral preprocessing, and ChenomX NMR Suite 8.5 was used for metabolite assignment and quantification. Supplementary Fig. 2 illustrates metabolite spectra assignment examples.

Statistics and reproducibility. Most statistical analyses were performed with the MetaAnalyst 5.0 web server⁶¹. Here, data were normalised for dilution effects by the probabilistic quotient normalisation (PQN) approach on a reference sample. Heatmaps were produced using non-parametric one-way ANOVA, Fischer’s least significant difference (LSD) was applied in the post hoc analysis, and unsupervised clustering was achieved by the Ward clustering algorithm employing the Euclidean distance measure. Heatmaps show autoscaled and normalised metabolite concentration values. For visualisation and further statistical analysis, we used Graph Pad Prism (Version 9.1.0, Graph Pad Software, San Diego, CA, USA) and R version 1.4.11.06. The individual metabolite concentrations were visualised as box plots with max. to min. whiskers with individual data points, and P values illustrated statistically significant metabolites compared to the naive baseline control: **** <0.0001 , *** <0.001 , ** <0.01 , * <0.05 .

Due to the technical issue of poor spectral resolution, one sample of the acute 24 h group had to be excluded from further analysis. Therefore, acute 24 h is $n = 4$ animals, while all the other sample conditions, naive, acute 4 h, chronic 0 h, 4 h, 12 h and 24 h were $n = 5$ animals. The number of replicates was defined by minimum necessary replicates for metabolomics studies for efficient statistical power of metabolite concentration data and available number of animals as defined by the ethical approval.

Reporting summary. Further information on research design is available in the Nature Portfolio Reporting Summary linked to this article.

Data availability

Supplementary data with the source data are provided. Supplementary Data 1: ear thickness measurement data for Fig. 1b dot plot. Supplementary Data 2: normalised source data for metabolite dot/box plots, heatmaps, correlation graphs, and principal component analysis. Supplementary Data 3: the source data for Fig. 3 histopathology scoring and correlation analysis. $^1\text{H-NMR}$ spectra data are available upon request.

Received: 31 May 2022; Accepted: 27 October 2022;

Published online: 15 November 2022

References

1. Qiu, J. T. et al. Metabolic control of autoimmunity and tissue inflammation in rheumatoid arthritis. *Front. Immunol.* **12**, 652771 (2021).
2. Kapoor, S. R. et al. Metabolic profiling predicts response to anti-tumor necrosis factor alpha therapy in patients with rheumatoid arthritis. *Arthritis Rheumatism* **65**, 1448–1456 (2013).

3. Casciano, F., Pigatto, P. D., Secchiero, P., Gambari, R. & Reali, E. T cell hierarchy in the pathogenesis of psoriasis and associated cardiovascular comorbidities. *Front. Immunol.* **9**, 1390 (2018).
4. Quijano, C., Trujillo, M., Castro, L. & Trostchansky, A. Interplay between oxidant species and energy metabolism. *Redox Biol.* **8**, 28–42 (2016).
5. Vogel, A., Brunner, J. S., Hajto, A., Sharif, O. & Schabbauer, G. Lipid scavenging macrophages and inflammation. *Biochimica Et Biophysica Acta-Molecular Cell Biol. Lipids* **1867**, 159066 (2022).
6. Collins, J. M. et al. TCA cycle remodeling drives proinflammatory signaling in humans with pulmonary tuberculosis. *PLoS Pathogens* **17**, e1009941 (2021).
7. Chimentì, M. S. et al. The interplay between inflammation and metabolism in rheumatoid arthritis. *Cell Death Dis.* **6**, e1887 (2015).
8. Mehling, R. et al. Immunomodulatory role of reactive oxygen species and nitrogen species during T cell-driven neutrophil-enriched acute and chronic cutaneous delayed-type hypersensitivity reactions. *Theranostics* **11**, 470–490 (2021).
9. Schwenck, J. et al. Temporal dynamics of reactive oxygen and nitrogen species and NF-kappa B activation during acute and chronic T cell-driven inflammation. *Mol. Imaging Biol.* **22**, 504–514 (2020).
10. Kneilling, M. et al. Direct crosstalk between mast cell-TNF and TNFR1-expressing endothelia mediates local tissue inflammation. *Blood* **114**, 1696–1706 (2009).
11. Pichler, B. J. et al. Imaging of delayed-type hypersensitivity reaction by PET and F-18-Galacto-RGD. *J. Nucl. Med.* **46**, 184–189 (2005).
12. Thunemann, M. et al. Cre/lox-assisted non-invasive in vivo tracking of specific cell populations by positron emission tomography. *Nat. Commun.* **8**, 1–12 (2017).
13. Schwenck, J. et al. Cysteine-type cathepsins promote the effector phase of acute cutaneous delayed-type hypersensitivity reactions. *Theranostics* **9**, 3903–3917 (2019).
14. Lonati, C. et al. Quantitative metabolomics of tissue, perfusate, and bile from rat livers subjected to normothermic machine perfusion. *Biomedicine* **10**, 538 (2022).
15. Viola, A., Munari, F., Sanchez-Rodriguez, R., Sclaro, T. & Castegna, A. The metabolic signature of macrophage responses. *Front. Immunol.* **10**, 1462 (2019).
16. Shommu, N. S. et al. Metabolomic and inflammatory mediator based biomarker profiling as a potential novel method to aid pediatric appendicitis identification. *PLoS ONE* **13**, e0193563 (2018).
17. Mendes-Frias, A. et al. Dysregulation of glycerophospholipid metabolism during Behcet’s disease contributes to a pro-inflammatory phenotype of circulating monocytes. *J. Transl. Autoimmun.* **3**, 100056–100056 (2020).
18. Pietzner, M. et al. Comprehensive metabolic profiling of chronic low-grade inflammation among generally healthy individuals. *BMC Med.* **15**, 1–12 (2017).
19. Ekici, S., Risk, B. B., Neill, S. G., Shu, H.-K. & Fleischer, C. C. Characterization of dysregulated glutamine metabolism in human glioma tissue with H-1 NMR. *Sci. Rep.* **10**, 1–10 (2020).
20. Tanimine, N., Turka, L. A. & Priyadarshini, B. Navigating T-cell immunometabolism in transplantation. *Transplantation* **102**, 230–239 (2018).
21. Jutley, G. S. & Young, S. P. Metabolomics to identify biomarkers and as a predictive tool in inflammatory diseases. *Best. Pract. Res. Clin. Rheumatol.* **29**, 770–782 (2015).
22. Pease, C. K. S., Basketter, D. A. & Patlewicz, G. Y. Contact allergy: the role of skin chemistry and metabolism. *Clin. Exp. Dermatol.* **28**, 177–183 (2003).
23. Silvestre, M. C., Sato, M. N. & Silva dos Reis, V. M. Innate immunity and effector and regulatory mechanisms involved in allergic contact dermatitis. *An. Brasilienses De. Dermatologia* **93**, 242–250 (2018).
24. Qie, C. X. et al. Single-cell RNA-Seq reveals the transcriptional landscape and heterogeneity of skin macrophages in Vsr(–/–) murine psoriasis. *Theranostics* **10**, 10483–10497 (2020).
25. Mills, E. L. et al. Succinate dehydrogenase supports metabolic repurposing of mitochondria to drive inflammatory macrophages. *Cell* **167**, 457–45 (2016).
26. Tannahill, G. M. et al. Succinate is an inflammatory signal that induces IL-1 beta through HIF-1 alpha. *Nature* **496**, 238–243 (2013).
27. Xu, M. et al. Acetate attenuates inflammasome activation through GPR43-mediated Ca²⁺-dependent NLRP3 ubiquitination. *Exp. Mol. Med.* **51**, 1–13 (2019).
28. Tedelind, S., Westberg, F., Kjerrulf, M. & Vidal, A. Anti-inflammatory properties of the short-chain fatty acids acetate and propionate: a study with relevance to inflammatory bowel disease. *World J. Gastroenterol.* **13**, 2826–2832 (2007).
29. Fitzpatrick, M. A. & Young, S. P. Metabolomics—a novel window into inflammatory disease. *Swiss Medical Weekly* **143**, w13743 (2013).
30. Mittal, M., Siddiqui, M. R., Tran, K., Reddy, S. P. & Malik, A. B. Reactive oxygen species in inflammation and tissue injury. *Antioxid. Redox Signal.* **20**, 1126–1167 (2014).
31. Wynn, T. A. Cellular and molecular mechanisms of fibrosis. *J. Pathol.* **214**, 199–210 (2008).

32. Banhegyi, G., Csala, M., Braun, L., Garzo, T. & Mandl, J. Ascorbate synthesis-dependent glutathione consumption in mouse liver. *Febs Lett.* **381**, 39–41 (1996).
33. Miller, C. G. et al. Supplemental ascorbate diminishes DNA damage yet depletes glutathione and increases acute liver failure in a mouse model of hepatic antioxidant system disruption. *Antioxidants* **10**, 359 (2021).
34. Padayatty, S. J. & Levine, M. Vitamin C: the known and the unknown and goldilocks. *Oral Dis.* **22**, 463–493 (2016).
35. Zhou, X. et al. Serine alleviates oxidative stress via supporting glutathione synthesis and methionine cycle in mice. *Mol. Nutr. Food Res.* **61**, 1700262 (2017).
36. Piao, S., Cha, Y.-N. & Kim, C. Taurine chloramine protects RAW 264.7 macrophages against hydrogen peroxide-induced apoptosis by increasing antioxidants. *J. Clin. Biochem. Nutr.* **49**, 50–56 (2011).
37. Marcinkiewicz, J. & Kontny, E. Taurine and inflammatory diseases. *Amino Acids* **46**, 7–20 (2014).
38. Fuchs, A. L. et al. Quantitative H-1 NMR metabolomics reveal distinct metabolic adaptations in human macrophages following differential activation. *Metabolites* **9**, 248 (2019).
39. Sitter, B., Johnsson, M. K., Jostein, H. & Bathen, T. F. Metabolic changes in psoriatic skin under topical corticosteroid treatment. *BMC Dermatol.* **13**, 1–7 (2013).
40. Nagai, K. & Suda, T. IMMUNOREGULATIVE EFFECTS OF CARNOSINE AND BETA ALANINE. *J. Physiological Soc. Jpn.* **48**, 564–571 (1986).
41. Shetwky, A. et al. Mitochondrial defects associated with beta-alanine toxicity: relevance to hyper-beta-alaninemia. *Mol. Cell. Biochem.* **416**, 11–22 (2016).
42. Bogner-Strauss, J. G. N-acetylaspartate metabolism outside the brain: lipogenesis, histone acetylation, and cancer. *Front. Endocrinol.* **8**, 240 (2017).
43. Williams, N. C. & O'Neill, L. A. J. A Role for the Krebs cycle intermediate citrate in metabolic reprogramming in innate immunity and inflammation. *Front. Immunol.* **9**, <https://doi.org/10.3389/fimmu.2018.00141> (2018).
44. Chang, C. H. et al. Posttranscriptional control of T cell effector function by aerobic glycolysis. *Cell* **153**, 1239–1251 (2013).
45. Jha, M. K. et al. Metabolic connection of inflammatory pain: pivotal role of a pyruvate dehydrogenase kinase-pyruvate dehydrogenase-lactic acid axis. *J. Neurosci.* **35**, 14353–14369 (2015).
46. Bequette, B. J., Sunny, N. E., El-Kadi, S. W. & Owens, S. L. Application of stable isotopes and mass isotopomer distribution analysis to the study of intermediary metabolism of nutrients. *J. Anim. Sci.* **84**(Suppl), E50–E59 (2006).
47. Neurauter, G. et al. Chronic immune stimulation correlates with reduced phenylalanine turnover. *Curr. Drug Metab.* **9**, 622–627 (2008).
48. Yan, D. et al. The metabolomics of psoriatic disease. *Psoriasis-Targets Ther.* **7**, 1–15 (2017).
49. Dutkiewicz, E. P., Hsieh, K. T., Wang, Y. S., Chiu, H. Y. & Urban, P. L. Hydrogel micropatch and mass spectrometry-assisted screening for psoriasis-related skin metabolites. *Clin. Chem.* **62**, 1120–1128 (2016).
50. Wu, X. et al. Integrated metabolomics and transcriptomics analyses reveal histidine metabolism plays an important role in imiquimod-induced psoriasis-like skin inflammation. *DNA Cell Biol.* **40**, 1325–1337 (2021).
51. Le Floch, N., Otten, W. & Merlot, E. Tryptophan metabolism, from nutrition to potential therapeutic applications. *Amino Acids* **41**, 1195–1205 (2011).
52. Bae, H. R. et al. Multi-omics: differential expression of IFN-gamma results in distinctive mechanistic features linking chronic inflammation, gut dysbiosis, and autoimmune diseases. *J. Autoimmunity* **111**, 102436 (2020).
53. Wang, Q., Liu, D., Song, P. & Zou, M.-H. Tryptophan-kynurenine pathway is dysregulated in inflammation, and immune activation. *Front. Biosci.-Landmark* **20**, 1116–1143 (2015).
54. Zaher, S. S., Germain, C., Fu, H., Larkin, D. F. P. & George, A. J. T. 3-Hydroxykynurenine suppresses CD4(+) T-cell proliferation, induces T-regulatory-cell development, and prolongs corneal allograft survival. *Investig. Ophthalmol. Vis. Sci.* **52**, 2640–2648 (2011).
55. Liu, X. et al. Activation of aryl hydrocarbon receptor in Langerhans cells by a microbial metabolite of tryptophan negatively regulates skin inflammation. *J. Dermatological Sci.* **100**, 192–200 (2020).
56. Bozelli, J. C., Azher, S. & Epand, R. M. Plasmalogens and chronic inflammatory diseases. *Front. Physiol.* **12**, <https://doi.org/10.3389/fphys.2021.730829> (2021).
57. Esmaeili, M. et al. IDH1 R132H mutation generates a distinct phospholipid metabolite profile in glioma. *Cancer Res.* **74**, 4898–4907 (2014).
58. Trautwein, C. et al. Tissue metabolites in diffuse glioma and their modulations by IDH1 mutation, histology, and treatment. *JCI Insight* **7**, <https://doi.org/10.1172/jci.insight.153526> (2022).
59. Lu, S. C. Glutathione synthesis. *Biochimica Et. Biophysica Acta-Gen. Subj.* **1830**, 3143–3153 (2013).
60. Chokesuwattanasakul, S., Phelan, M. M., Edwards, S. W. & Wright, H. L. A robust intracellular metabolite extraction protocol for human neutrophil metabolic profiling. *PLoS ONE* **13**, e0209270 (2018).
61. Chong, J., Wishart, D. S. & Xia, J. Using MetaboAnalyst 4.0 for comprehensive and integrative metabolomics data analysis. *Curr. Protoc. Bioinforma.* **68**, e86–e86 (2019).

Acknowledgements

The authors acknowledge support by Open Access Publishing Fund of University of Tübingen. The authors would like to thank Rebecca Rock, Maren Harant, Natalie Hermann, Funda Cay, Miriam Owczorz, Georgy Berezhnoy and Aditi Kulkarni for excellent technical support, and Jonathan Cotton for language edit support. Art for Fig. 1 is adapted from CC-BY SMART Servier Medical Art <https://smart.servier.com> (accessed on 4 October 2022), under license CC-BY 3.0. This work was funded by the German Research Foundation (SFB TRR156, TP C03 to M.K. & B.P. and the Germany's Excellence Strategy – EXC 2180 – 390900677) and the Werner Siemens Foundation (Zug, Switzerland).

Author contributions

Conception: M.K. and C.T.; design of the work: L.Z., R.M., M.K. and C.T.; data acquisition: L.Z., R.M. and I.G.M.; data analysis: L.Z., R.M. and I.G.M.; interpretation of data: L.Z., R.M., I.G.M., C.L., L.Q.M., B.J.P., M.K. and C.T.; figure preparation: L.Z. and I.G.M.; manuscript draft: L.Z., R.M., M.K. and C.T.; manuscript editing: L.Z., R.M., I.G.M., C.L., L.Q.M., B.J.P., M.K. and C.T. All authors have approved the submitted version.

Funding

Open Access funding enabled and organized by Projekt DEAL.

Competing interests

The authors declare no competing interests.

Additional information

Supplementary information The online version contains supplementary material available at <https://doi.org/10.1038/s42003-022-04179-x>.

Correspondence and requests for materials should be addressed to Manfred Kneilling or Christoph Trautwein.

Peer review information *Communications Biology* thanks the anonymous reviewers for their contribution to the peer review of this work. Primary Handling Editors: Damon Tumes and Joao Valente.

Reprints and permission information is available at <http://www.nature.com/reprints>

Publisher's note Springer Nature remains neutral with regard to jurisdictional claims in published maps and institutional affiliations.



Open Access This article is licensed under a Creative Commons Attribution 4.0 International License, which permits use, sharing, adaptation, distribution and reproduction in any medium or format, as long as you give appropriate credit to the original author(s) and the source, provide a link to the Creative Commons license, and indicate if changes were made. The images or other third party material in this article are included in the article's Creative Commons license, unless indicated otherwise in a credit line to the material. If material is not included in the article's Creative Commons license and your intended use is not permitted by statutory regulation or exceeds the permitted use, you will need to obtain permission directly from the copyright holder. To view a copy of this license, visit <http://creativecommons.org/licenses/by/4.0/>.

© The Author(s) 2022

Supplementary Figures

Acute and chronic inflammation alter immunometabolism in a cutaneous delayed-type hypersensitivity reaction (DTHR) mouse model

Laimdota Zizmare¹, Roman Mehling¹, Irene Gonzalez-Menendez^{2,3}, Caterina Lonati⁴, Leticia Quintanilla-Martinez^{2,3}, Bernd J. Pichler^{1,2}, Manfred Kneilling^{1,2,5,#}, Christoph Trautwein^{1,#}

¹ Werner Siemens Imaging Center, Department of Preclinical Imaging and Radiopharmacy, Eberhard Karls University of Tübingen, Röntgenweg 13, 72076, Tübingen, Germany

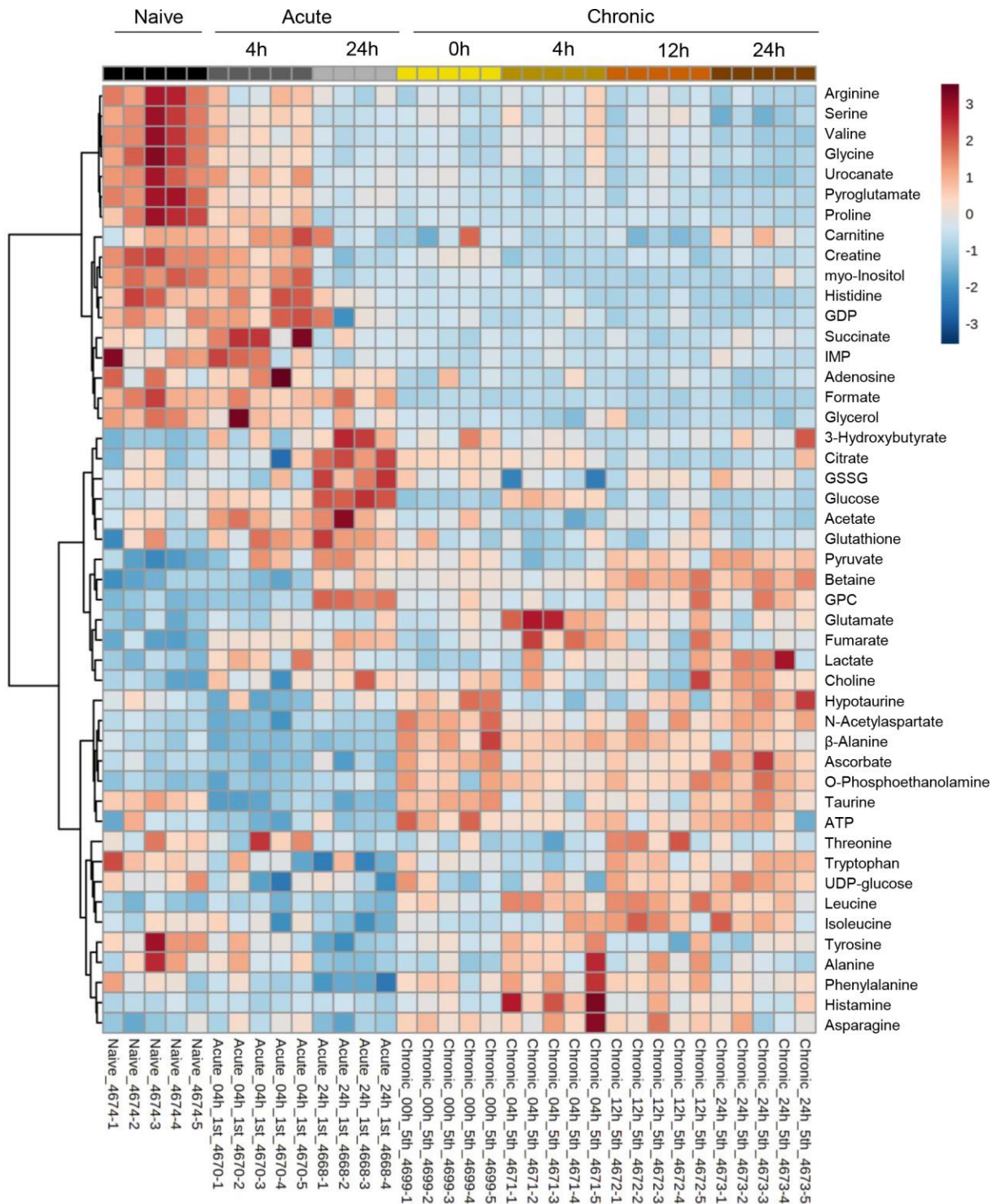
² Cluster of Excellence iFIT (EXC 2180) "Image-Guided and Functionally Instructed Tumor Therapies", Eberhard Karls University of Tübingen, Röntgenweg 11, 72076, Tübingen, Germany

³ Institute of Pathology and Neuropathology, Comprehensive Cancer Center, Eberhard Karls University of Tübingen, Liebermeisterstraße 8, 72076, Tübingen, Germany

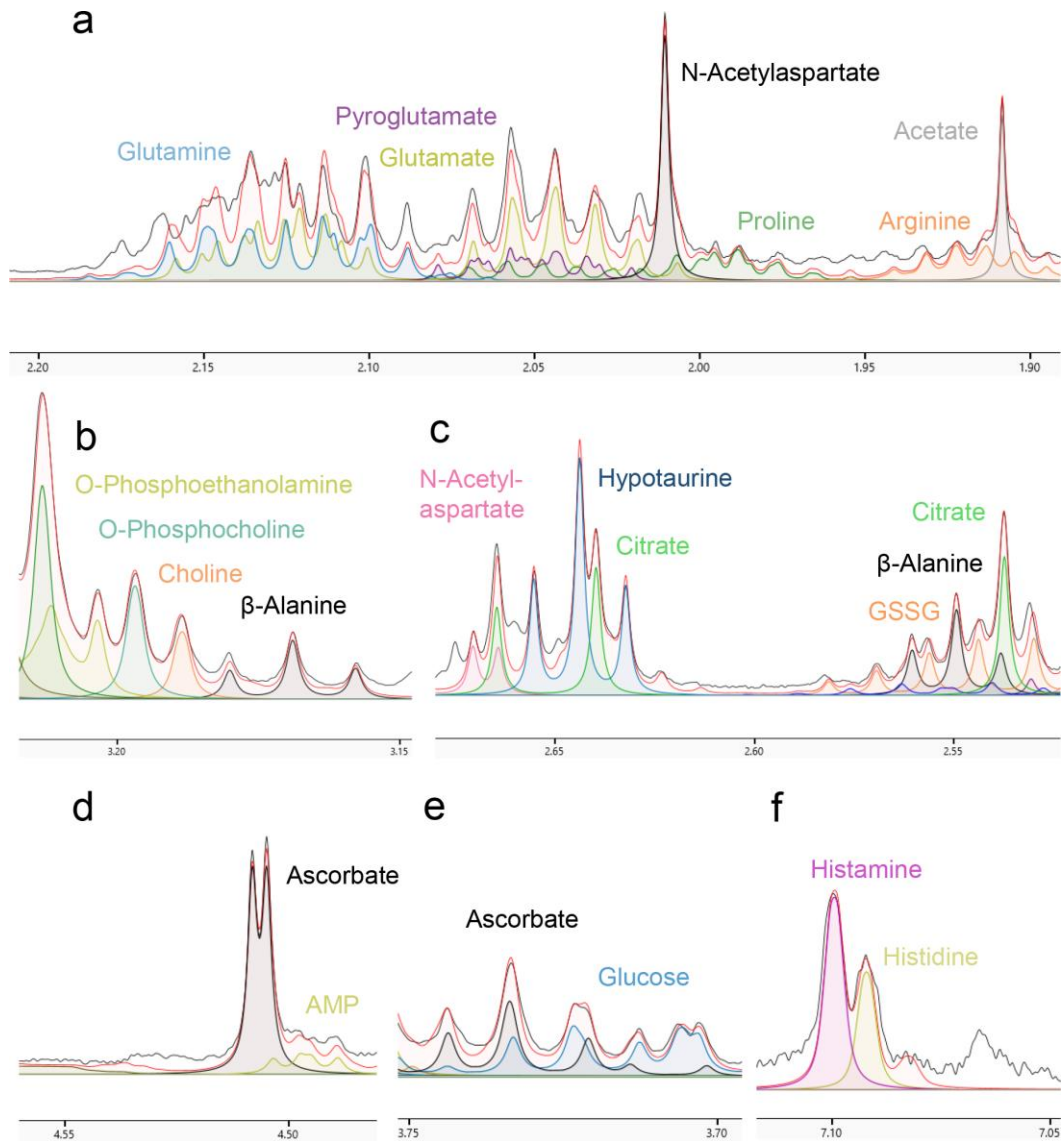
⁴ Center for Preclinical Research, Fondazione IRCCS Ca' Granda Ospedale Maggiore Policlinico, Via Pace 9, 20100 Milan, Italy

⁵ Department of Dermatology, Eberhard Karls University of Tübingen, Liebermeisterstraße 25, 72076, Tübingen, Germany

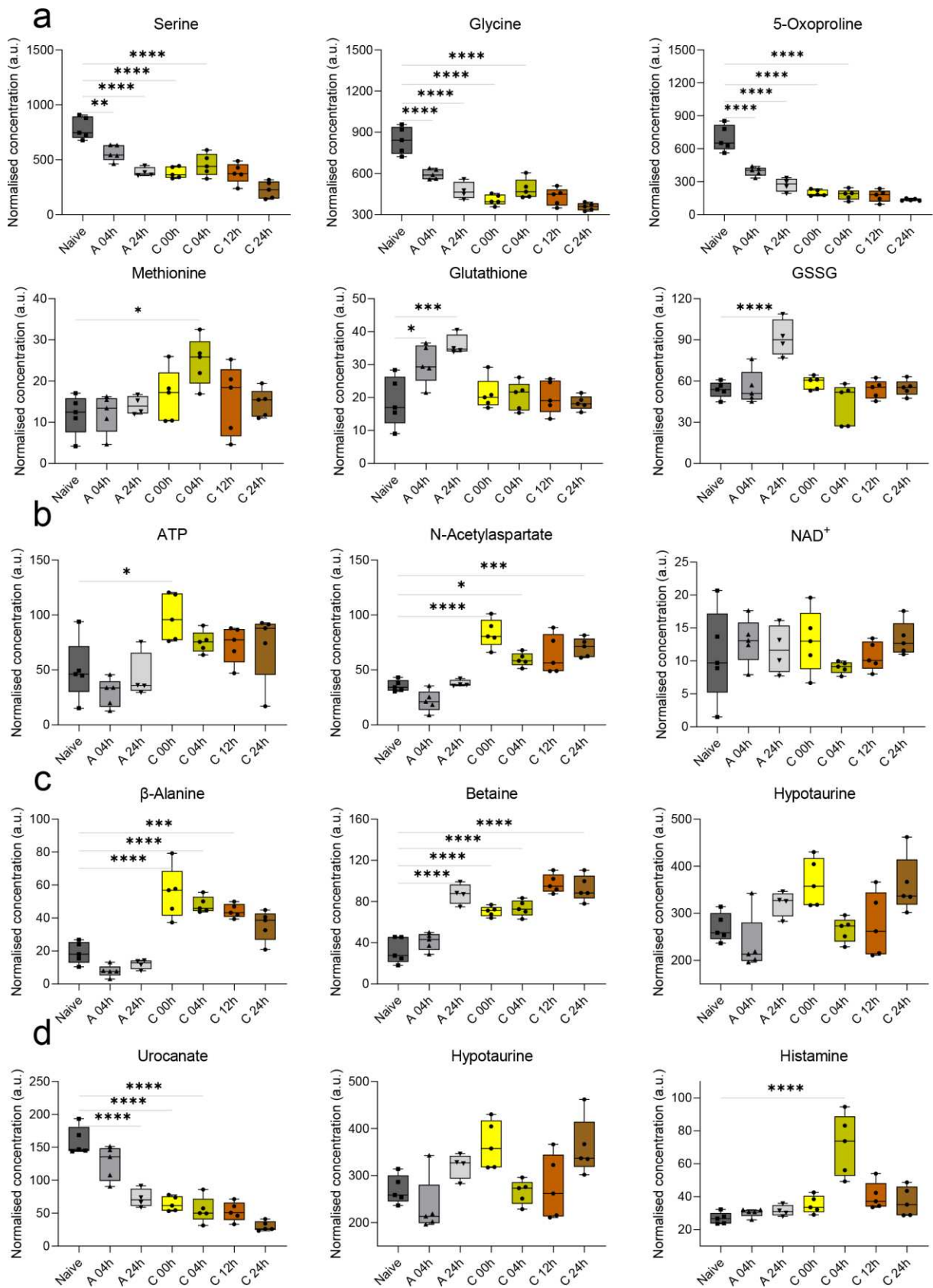
#Corresponding authors: Manfred Kneilling Manfred.Kneilling@med.uni-tuebingen.de and Christoph Trautwein Christoph.Trautwein@med.uni-tuebingen.de.



Supplementary figure 1: Overview of ¹H-NMR spectroscopy-based metabolomics analysis quantified metabolites during acute and chronic cutaneous DTHR. Heatmap of 54 statistically significant quantified metabolites showing each sample individual metabolite changes as auto-scaled (-4; 4) normalised concentration values, further clustered with Ward clustering method and hierarchical clustering algorithm. Red indicating relatively high concentration and blue – relatively low concentration (n=5 animals, except acute 24 h n=4 animals).

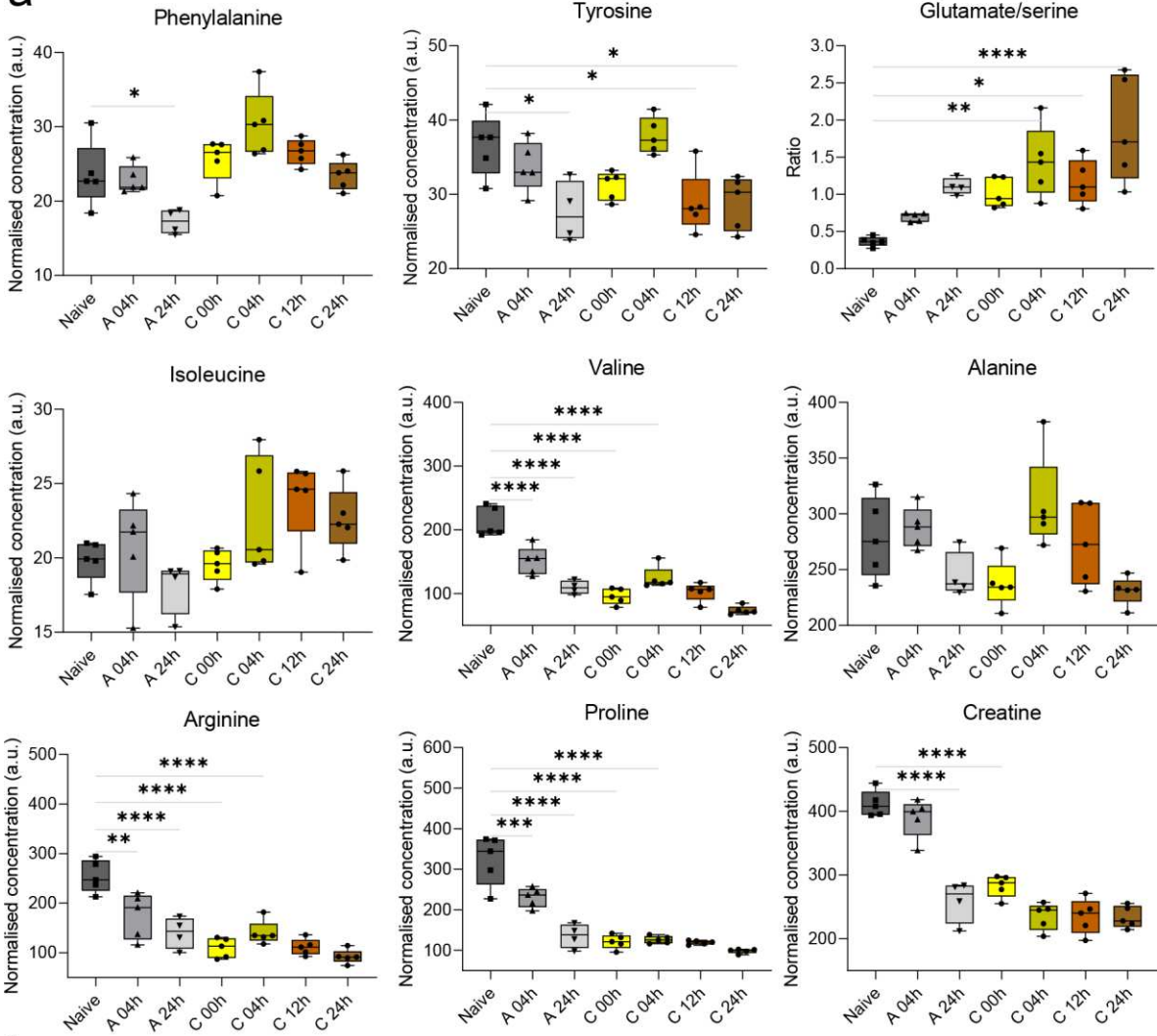
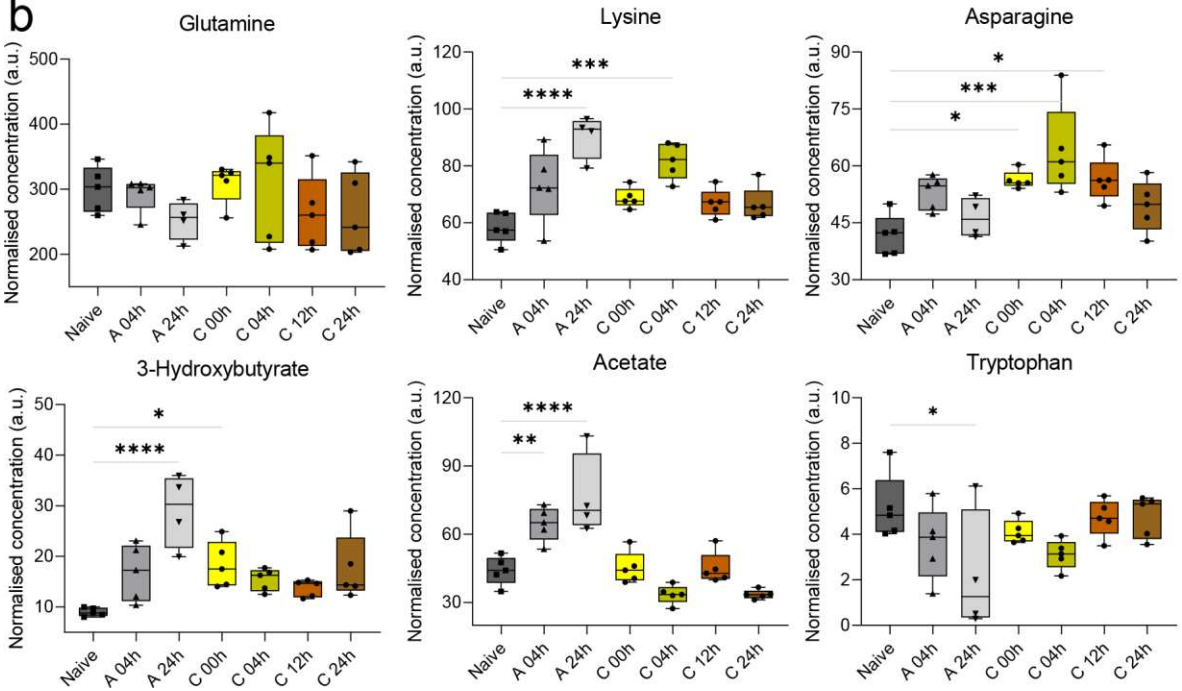


Supplementary figure 2: $^1\text{H-NMR}$ spectroscopy chronic 0 h DTHR (48 h after the 4th challenge) example spectra assignment. Example characteristic resonance regions are shown for (a) N-acetylaspartate, (b) β -alanine, (c) hypotaurine, (d, e) ascorbate and (f) histamine among other metabolite neighbouring peak resonances. All metabolites, that have multiple resonances in spectra were further confirmed in other regions for complete spectra assignment and quantification. Red line indicates sum spectra outline considering all overlapping peaks. Black thin line indicates original spectra. Coloured peak areas with bold outline show metabolite assignment according to the typed metabolite name in corresponding colour.

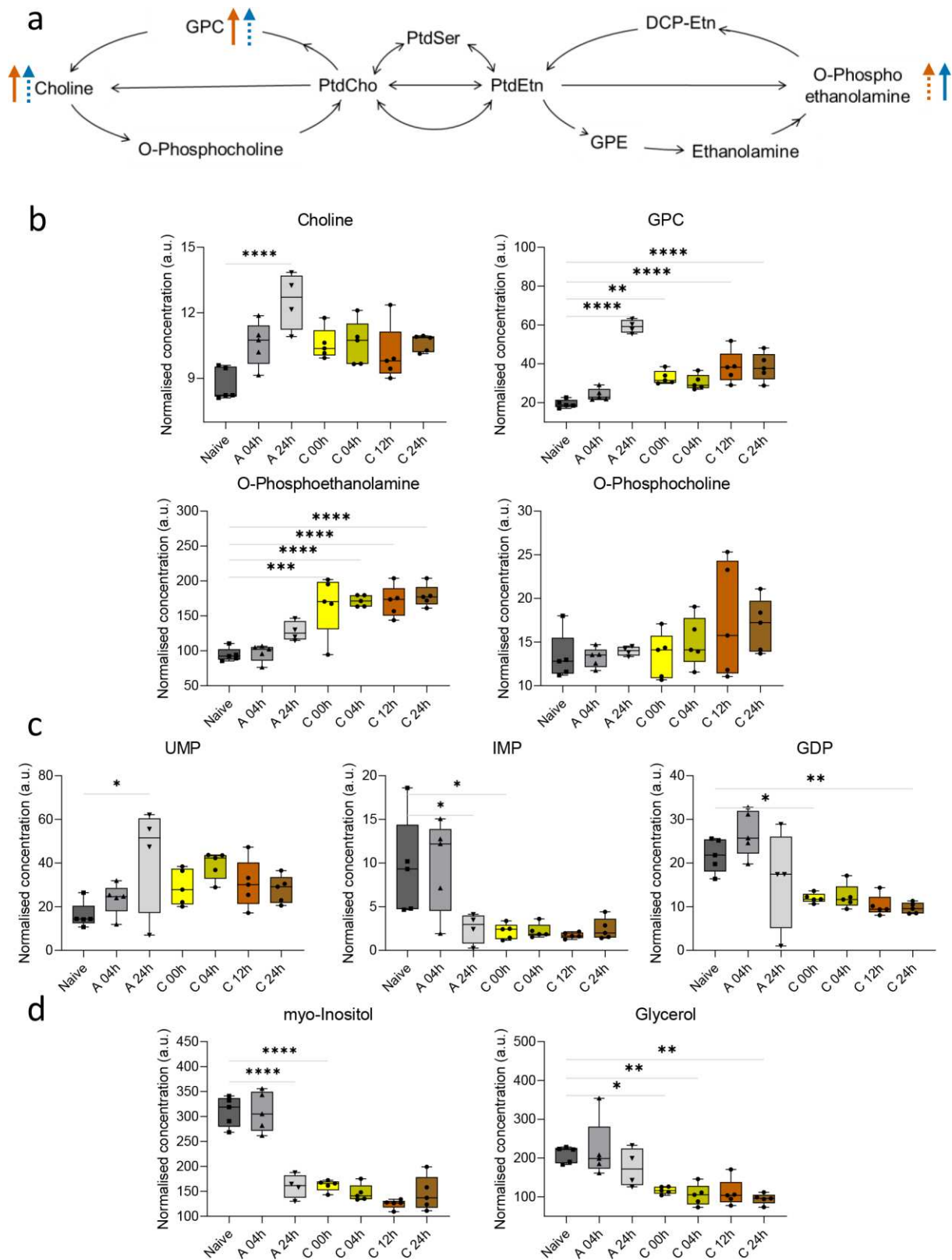


Supplementary Figure 3: Redox and immune metabolism additional metabolite box plots during acute and chronic cutaneous DTHR. (a) Redox-related metabolites serine, glycine and 5-oxoproline were downregulated during acute and chronic DTHR, while

methionine was slightly increased at the chronic inflammation peak; glutathione and glutathione disulfide (GSSG) show increased concentrations during acute DTHR; **(b)** ATP and N-acetylaspartate were increased during chronic DTHR, while NAD⁺ concentration was not significantly affected; **(c)** taurine-related metabolites β-alanine, betaine and hypotaurine were increased during chronic DTHR; **(d)** histidine, fatty acid and galactose metabolic pathway-related metabolites urocanate and histidine were reduced during acute and chronic cutaneous DTHR while histamine peaked at chronic 4 h. Individual metabolite box plots illustrating normalised concentration in arbitrary unit (a.u.) with max. to min. whisker, individual replicate points and median with p values **** < 0.0001, *** < 0.001, ** < 0.01 * < 0.05, one-way ANOVA statistical test, n=5 animals, except acute 24 h n=4 animals). Statistically significant stars shown for comparisons to naive control.

a**b**

Supplementary Figure 4: Energy metabolism during acute and chronic cutaneous DTHR. (a) Phenylalanine, isoleucine, glutamate/serine ratio, tyrosine and alanine follow similar concentration change patterns, while valine, arginine, proline and creatine concentrations are reduced during DTHR progression. (b) Glutamine concentrations were not significantly changed over the course of acute and chronic cutaneous DTHR; lysine, 3-hydroxybutyrate and acetate follow similar concentration change patterns; asparagine concentration increased during chronic cutaneous DTHR; tryptophan concentrations were reduced in acute and chronic cutaneous DTHR compared to the naive control. Normalised concentration changes are illustrated as box plots with max. to min. whisker, individual replicate points and median (p value **** < 0.0001, *** < 0.001, ** < 0.01 * < 0.05) (n = 5). Statistically significant stars shown for comparisons to naive control, by one-way ANOVA, n=5 animals, except acute 24 h n=4 animals.



Supplementary Figure 5: Growth and nucleotide metabolism-related metabolite normalised concentration changes during acute and chronic cutaneous DTHR. (a) Kennedy pathway adapted from Esmaeli *et al.*, 2014; **(b)** Kennedy pathway-related metabolites; **(c)** nucleotide metabolism-related metabolites; **(d)** myo-inositol and glycerol were

reduced during acute and chronic cutaneous DTHR. Concentration changes illustrated as box plots with max. to min. whisker, individual replicate points and median (p value **** < 0.0001, *** < 0.001, ** < 0.01 * < 0.05). Statistically significant stars shown for comparisons to naive control, one-way ANOVA, n=5 animals, except acute 24 h n=4 animals. Orange arrows indicate concentration increase or decrease compared to naive control at acute inflammation peak at 24 h, blue – chronic inflammation peak at 4 h, dashed lines show a non-significant concentration trend.

3.2. Publication II

Roux-en-Y gastric bypass (RYGB) surgery during high liquid sucrose diet leads to gut microbiota-related systematic alterations

Zizmare, L.¹; Boyle, C. N.²; Buss, S.¹; Louis, S.³; Kuebler, L.¹; Mulay, K.⁴; Krüger, R.³; Steinhauer, L.³; Mack, I.⁵; Rodriguez Gomez, M.³; Herfert, K.¹; Ritze, Y.⁴; Trautwein, C.¹

¹ Werner Siemens Imaging Center, Department of Preclinical Imaging and Radiopharmacy, Eberhard Karls University of Tübingen, University Hospital Tübingen, Röntgenweg 13, 72076 Tübingen, Germany

² Institute of Veterinary Physiology, University of Zurich, Winterthurerstraße 260, CH-8057 Zurich, Switzerland

³ Department of Physiology and Biochemistry of Nutrition, Max Rubner-Institut, Haid-und-Neu-Straße 9, 76131 Karlsruhe, Germany

⁴ Department of Medical Psychology and Behavioral Neurobiology, Eberhard Karls University of Tübingen, Silcherstraße 5, 72076 Tübingen, Germany

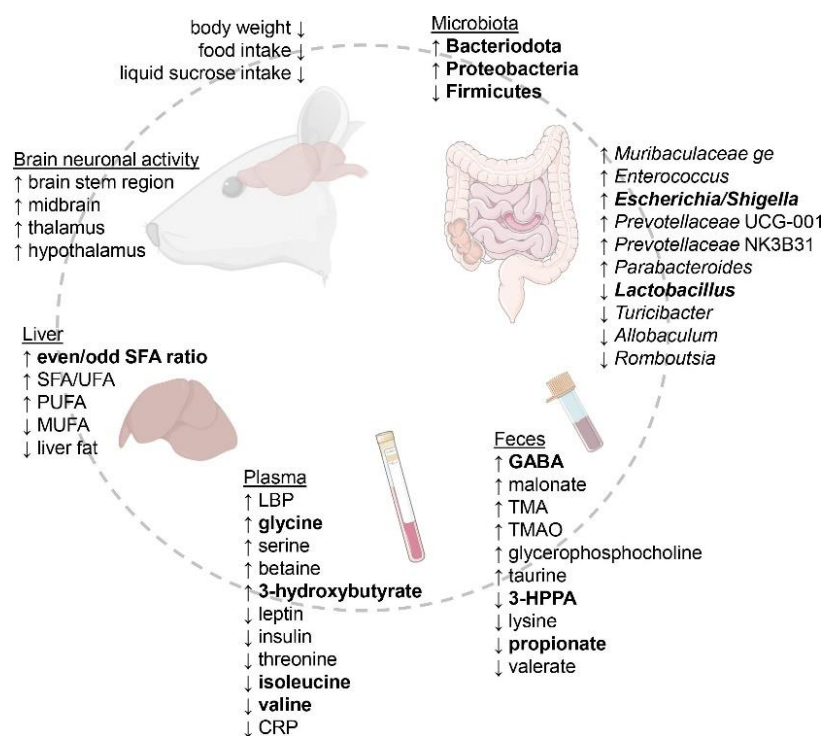
⁵ Department of Psychosomatic Medicine and Psychotherapy, University Hospital Tübingen, Osianderstraße 5, 72076 Tübingen, Germany

International Journal of Molecular Science

Year 2022, Volume 23, Issue 3, page 1126

<https://doi.org/10.3390/ijms23031126>

Graphical Abstract





Article

Roux-En-Y Gastric Bypass (RYGB) Surgery during High Liquid Sucrose Diet Leads to Gut Microbiota-Related Systematic Alterations

Laimdota Zizmare ¹, Christina N. Boyle ², Sabrina Buss ¹, Sandrine Louis ³, Laura Kuebler ¹, Ketki Mulay ⁴, Ralf Krüger ³, Lara Steinhauer ³, Isabelle Mack ⁵, Manuel Rodriguez Gomez ³, Kristina Herfert ¹, Yvonne Ritze ^{4,*} and Christoph Trautwein ¹

- ¹ Werner Siemens Imaging Center, Department of Preclinical Imaging and Radiopharmacy, University Hospital Tübingen, Eberhard Karls University of Tübingen, Röntgenweg 13, 72076 Tübingen, Germany; Laimdota.Zizmare@med.uni-tuebingen.de (L.Z.); Sabrina.Buss@med.uni-tuebingen.de (S.B.); Laura.Kuebler@med.uni-tuebingen.de (L.K.); Kristina.Herfert@med.uni-tuebingen.de (K.H.); Christoph.Trautwein@med.uni-tuebingen.de (C.T.)
- ² Institute of Veterinary Physiology, University of Zurich, Winterthurerstraße 260, CH-8057 Zurich, Switzerland; boyle@vetphys.uzh.ch
- ³ Department of Physiology and Biochemistry of Nutrition, Max Rubner-Institut, Haid-und-Neu-Straße 9, 76131 Karlsruhe, Germany; Sandrine.Louis@mri.bund.de (S.L.); Ralf.Krueger@mri.bund.de (R.K.); Lara.Steinhauer@mri.bund.de (L.S.); Manuel.RodriguezGomez@mri.bund.de (M.R.G.)
- ⁴ Department of Medical Psychology and Behavioral Neurobiology, Eberhard Karls University of Tübingen, Silcherstraße 5, 72076 Tübingen, Germany; mulay.ketki@yahoo.co.in
- ⁵ Department of Psychosomatic Medicine and Psychotherapy, University Hospital Tübingen, Osianderstraße 5, 72076 Tübingen, Germany; Isabelle.Mack@uni-tuebingen.de
- * Correspondence: contact@yvonne-ritze.com



Citation: Zizmare, L.; Boyle, C.N.; Buss, S.; Louis, S.; Kuebler, L.; Mulay, K.; Krüger, R.; Steinhauer, L.; Mack, I.; Rodriguez Gomez, M.; et al. Roux-En-Y Gastric Bypass (RYGB) Surgery during High Liquid Sucrose Diet Leads to Gut Microbiota-Related Systematic Alterations. *Int. J. Mol. Sci.* **2022**, *23*, 1126. <https://doi.org/10.3390/ijms23031126>

Academic Editors: Federica Laudisi and Carmine Stolfi

Received: 23 December 2021

Accepted: 17 January 2022

Published: 20 January 2022

Publisher's Note: MDPI stays neutral with regard to jurisdictional claims in published maps and institutional affiliations.



Copyright: © 2022 by the authors. Licensee MDPI, Basel, Switzerland. This article is an open access article distributed under the terms and conditions of the Creative Commons Attribution (CC BY) license (<https://creativecommons.org/licenses/by/4.0/>).

Abstract: Roux-en-Y gastric bypass (RYGB) surgery has been proven successful in weight loss and improvement of co-morbidities associated with obesity. Chronic complications such as malabsorption of micronutrients in up to 50% of patients underline the need for additional therapeutic approaches. We investigated systemic RYGB surgery effects in a liquid sucrose diet-induced rat obesity model. After consuming a diet supplemented with high liquid sucrose for eight weeks, rats underwent RYGB or control sham surgery. RYGB, sham pair-fed, and sham ad libitum-fed groups further continued on the diet after recovery. Notable alterations were revealed in microbiota composition, inflammatory markers, feces, liver, and plasma metabolites, as well as in brain neuronal activity post-surgery. Higher fecal 4-aminobutyrate (GABA) correlated with higher Bacteroidota and *Enterococcus* abundances in RYGB animals, pointing towards the altered enteric nervous system (ENS) and gut signaling. Favorable C-reactive protein (CRP), serine, glycine, and 3-hydroxybutyrate plasma profiles in RYGB rats were suggestive of reverted obesity risk. The impact of liquid sucrose diet and caloric restriction mainly manifested in fatty acid changes in the liver. Our multi-modal approach reveals complex systemic changes after RYGB surgery and points towards potential therapeutic targets in the gut-brain system to mimic the surgery mode of action.

Keywords: RYGB; metabolomics; microbiome; inflammation; gut-brain axis; GABA; 3-hydroxybutyrate

1. Introduction

Obesity is a metabolic and inflammatory health condition characterized by excess accumulation of body fat, which increases the risk of developing an unbalanced, unresolved metabolic inflammation within adipose tissue and in metabolic organs such as the liver, pancreas and, brain [1,2]. A chronic, whole-body meta-inflammatory state during obesity can further lead to cardiovascular disease, type 2 diabetes, dysregulation of the immune system, and impaired cognitive and mental capabilities [3–8]. Prolonged intake of high

sugar foods, a principal component of the Western diet, promoted excess energy intake and gain of body weight [9]. Moreover, increased sugar intake leads to gut microbiota adaptations and dysbiosis [10]. Alongside cardiovascular complications, obesity and type 2 diabetes are important risk factors in the pathogenesis of cognitive dysfunction [11–13]. On the cellular level, a Western diet is associated with reduced expression of brain-derived neurotrophic factors, elevated levels of oxidative stress, and pro-inflammatory processes in neurons, and affects the whole-body immune response [14].

Considering that obesity has become a global pandemic [15], effective prevention and treatment strategies are needed. This is especially urgent for the 39 million children under the age of five diagnosed as overweight or obese in 2020 [16]. Beyond classical dietary and drug treatment [17,18], currently available approaches to treat morbid obesity and type 2 diabetes include bariatric surgery [19].

Roux-en-Y gastric bypass (RYGB) surgery is the most frequently employed bariatric technique in Western countries [20]. The surgical intervention consists of transection of the stomach, leaving a small gastric pouch, which is anastomosed to a distal part of the small intestine, creating a Roux (dietary) limb [21]. The rearrangement of the gut allows ingested food direct access to the small intestinal lumen, where it is eventually joined with the biliopancreatic limb, from which point the common channel is formed. After RYGB surgery, patient preferences for high-carbohydrate and high-fat foods decreased [22,23], and patients reportedly lost the motivation to eat [22]. Similarly, the preference for a high-fat diet steadily decreased, and the preference for a standard low-fat chow increased over a five-month post-surgical period in a rat model of RYGB [24].

RYGB surgery improves metabolic health and diabetes remission more effectively than other treatment strategies, including pharmacotherapy and lifestyle interventions [25,26]. Several murine RYGB studies show a positive impact of the surgery on various metabolic parameters reducing the risk of type 2 diabetes mellitus [27–29] and hyperlipidemia [30]. RYGB surgery leads to reduced glycemia, as shown by functional studies of the liver and brain. Surgery led to an improvement in liver health and glycemic control, further reducing the risk of hepatic steatosis [31]. RYGB surgery was also reported to lower lipogenesis and increase fatty acid beta-oxidation in the type 2 diabetes rat model [31]. Moreover, indications of lowered glycemia were also reported by a positron emission tomography (PET) imaging study where increased neuronal activity was shown in the hypothalamic and thalamic brain regions [13].

Fundamental changes in the gut microbiota and related metabolites are another common RYGB surgery downstream effect. *Escherichia coli*, *Klebsiella pneumoniae*, *Streptococcus*, *Bifidobacterium dentium*, and *Akkermansia muciniphila* have been reported in an increased abundance in patient feces after RYGB surgery [32]. Murine model studies have revealed a highly affected microbiome by RYGB surgery and have further shown a direct microbiota impact on weight and fat reduction after feces transplantation due to maintained increase of *Escherichia* and *Akkermansia* species abundance [33]. Gut microbiota dysbiosis has also been previously linked to obesity and food addiction due to interactions along the gut-brain axis via altered inflammatory signals such as tumor necrosis factor (TNF), interleukin (IL)-6, IL-1 beta, plasma lipopolysaccharide (LPS) [34], and neuroactive metabolites [35].

Metabolic profiling of RYGB surgery patients is a prospectively valuable tool for identifying subjects with type 2 diabetes that would have the most beneficial surgery outcome [36]. Murine metabolomics studies in RYGB models and patients have reported common altered fecal metabolite patterns such as upregulated trimethylamine (TMA), trimethylamine N-oxide (TMAO), glycine, 4-aminobutyrate (GABA), and downregulated plasma branched-chain amino acids (BCAA), arginine, and the tryptophan-kynurenine pathway [37,38]. However, further studies in animal models are crucial for appropriate biomarker discovery and their translation to clinically relevant sampling such as plasma or serum, feces, and urine [39].

A significant portion of currently available publications has investigated the impact of RYGB in genetic models of obesity or diet-induced obesity models resulting from high-fat

solid diets. Excessive caloric intake, often in a form of artificial sweetened soft drinks and juices, is one of the causes leading to obesity among children and adolescents [40]. Similarly, access to a liquid high sucrose diet increases caloric intake in mice [41] and, therefore, enhances obesity progression and alters the body's metabolism. It has also been shown that a high solid sucrose diet, similarly to a high-fat diet, promoted liver damage and affected insulin signaling even when the serum insulin levels were not changed [31]. However, the metabolic impact of RYGB surgery in an obesity model resulting from liquid high sucrose intake has not yet been described.

In this exploratory study, we examined the effects of surgery, caloric restriction, and liquid sucrose diet in RYGB-operated (RYGB group) versus sham-operated pair-fed (PF) and *ad libitum*-fed (AdLib) rats. We investigated gut microbiota dysbiosis, fecal and plasma metabolites, liver fatty acid composition, inflammatory immune marker correlations, and brain glucose metabolism for a comprehensive, multi-modal characterization of liquid sucrose-induced obesity. This systemic multi-modal characterization of the detailed molecular effects following RYGB surgery will help develop novel potential therapeutics that mimic the invasive surgical approach.

2. Results

2.1. RYGB Surgery Leads to Reduced Body Weight, Food, and Liquid Sucrose Intake

After an initial eight-week period of liquid sucrose diet and weight gain, rats underwent RYGB or sham surgery, followed by a second eight-week phase of liquid sucrose feeding after recovery (Figure 1a). We monitored the development of body weight, food, and liquid sucrose intake (Figure 1b–d). RYGB group sustained a significant weight loss compared to AdLib animals ($p < 0.05$) (Figure 1b). PF and RYGB animals showed similar weight loss at week 10 of the experiment (week 2 post-surgery). By week 11, PF animals had gained weight similar to the AdLib rats, while RYGB rats remained lean. RYGB animals had heterogeneous eating habits consuming between 84–105 kcal/day for the final six weeks before euthanasia, from which 42–80% (median 65.3%) was liquid sucrose (Figure 1c,d). Solid food and liquid sucrose intake were significantly reduced in RYGB and consequently PF groups post-surgery compared to the AdLib group (Figure 1c,d). PF animals were fed 100–106 kcal/day, of which 62–63% (median 62.7%) corresponded to the liquid sucrose diet. AdLib animals consumed 126–177 kcal/day, 62–73% (median 69.3%) derived from a liquid sucrose diet. The total energy consumed by AdLib animals was significantly higher than by RYGB and PF, while the percentage of median energy consumption via liquid sucrose was not significantly different between the RYGB and sham.

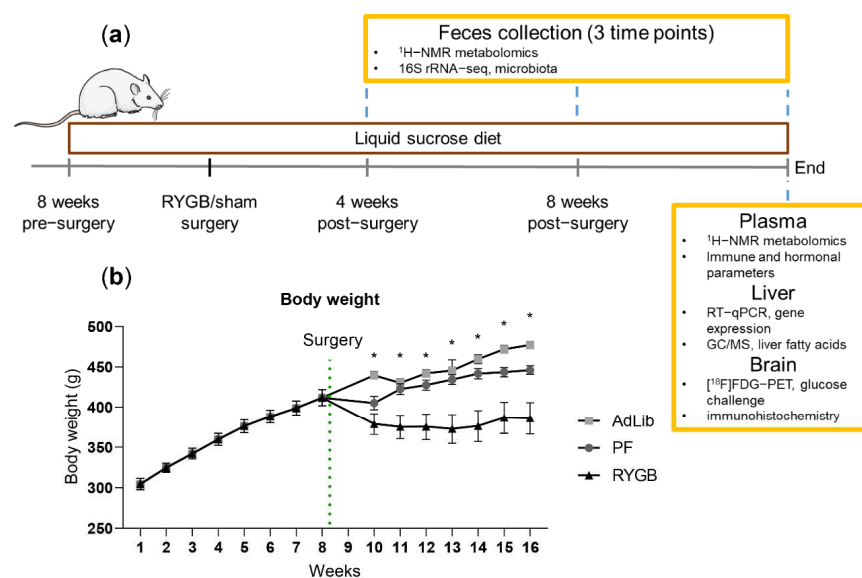


Figure 1. Cont.

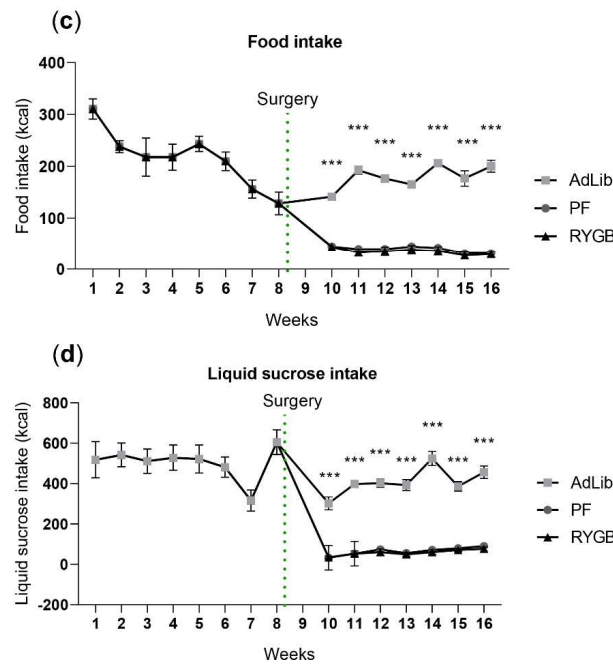


Figure 1. Overview of the experimental setup before and after the Roux-en-Y gastric bypass (RYGB) surgery. The timeline of the experiments, including sample collection points and analytical techniques (a). Average body weight (b), food intake (kcal) (c), and liquid sucrose intake (kcal) (d) are shown for *ad libitum* (AdLib), pair-fed (PF), and Roux-en-Y gastric bypass-operated (RYGB) rats. Data shown as mean ± SEM, *p*-values shown for RYGB vs. AdLib comparison. *** < 0.001, * < 0.05, two-way ANOVA, Tukey’s multiple comparisons test. RYGB (*n* = 5) black triangles, PF (*n* = 8) dark grey dots, AdLib (*n* = 7) light grey squares.

2.2. RYGB Surgery Leads to Reduced Relative Abundance of Firmicutes and Increased Bacteroidota and Proteobacteria Species

RYGB animals displayed a higher abundance of Bacteroidota (particularly *Muribaculaceae*) and Proteobacteria (Enterobacteriaceae, genera *Escherichia/Shigella*) and a lower abundance of Firmicutes compared to sham (Figure 2a,b). RYGB had increased Enterococcus species compared to the sham animals with more *Lactobacillus* species in their microbiota.

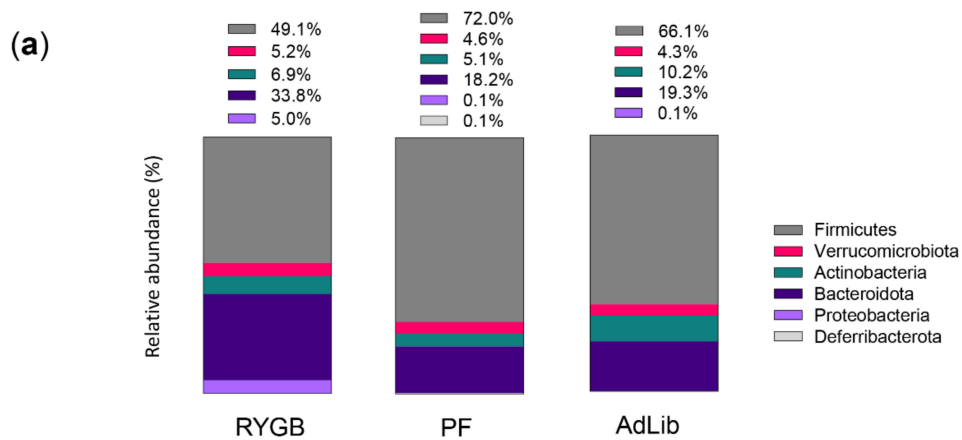


Figure 2. Cont.

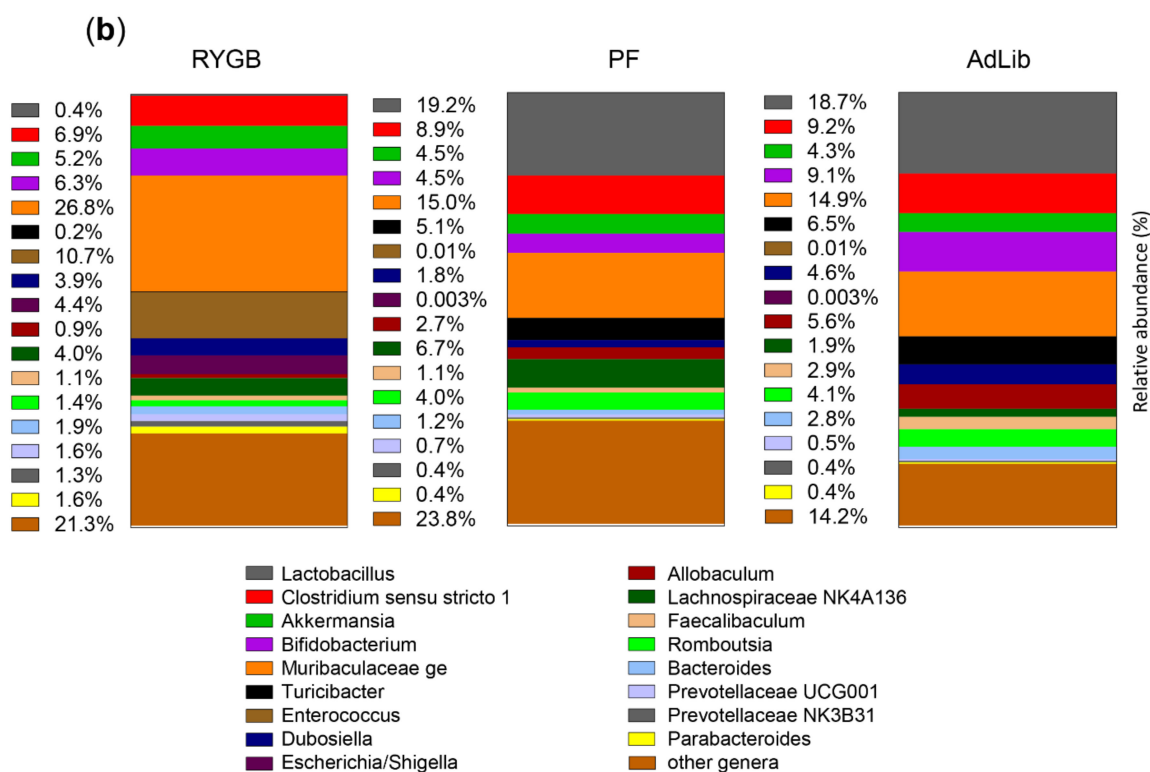


Figure 2. Gut microbiota composition. Bar graph representation of the most abundant taxa at the phylum (a) and genus (b) levels, illustrating a different microbiota composition between the groups with the RYGB animals displaying a higher abundance of Bacteroidota (particularly *Muribaculaceae*) and Proteobacteria (assigned to the family *Enterobacteriaceae*, genera *Escherichia/Shigella*), and a lower abundance of Firmicutes, even if more *Enterococcus* were found in this group, than in the Sham (PF and AdLib) animals, which had more *Lactobacillus* in their microbiota. Data from the three feces collection times are pooled. Mean relative abundance as % of the whole community is shown.

Considering feces microbiome at four and eight weeks after surgery and on the day of euthanasia together, a significant difference in alpha-diversity between the different groups ($p < 0.01$ for all three diversity types) was observed with AdLib animals showing the lowest diversity (Supplementary Figure S1). There were no significant changes in alpha-diversity over time within each condition, indicating relatively stable bacterial communities over the study period (data not shown).

Principal coordinate analysis based on the Bray–Curtis distance, Jenson–Shannon, and weighted UniFrac of all samples showed a clear separation between RYGB and sham animals, of which the two sham groups (AdLib and PF) had a visible overlap (Supplementary Figure S1b).

The permutational multivariate analysis of variance (PERMANOVA) with the Bray–Curtis distance showed a highly significant effect of surgery ($p = 0.001$), time ($p = 0.003$), without interaction between surgery and time effects ($p = 0.3$). The linear discriminant analysis effect size (LefSe) led to 16 significant taxa discriminating between groups: 5 for the PF animals, 5 for the AdLib, and 6 for the RYGB rats (Supplementary Figure S1c), represented in a cladogram (Supplementary Figure S2d). As shown above, *Enterococcaceae* was a significant marker of the RYGB animals. A potential marker for the PF animals was *Lactobacillus* and *Bifidobacterium* species up to their phylum of Actinobacteria for the AdLib animals, all with a linear discriminant analysis (LDA) score > 4 .

2.3. Fecal Metabolomics Show Altered Metabolite Production Post-Surgery

Eight weeks post-surgery, we identified significantly downregulated 3-hydroxyphenylpropionate (3-HPPA) and lysine in RYGB compared to sham (PF and AdLib) in animal

feces (Figure 3a,b). On the contrary, GABA, malonate, TMA, TMAO, and sn-glycero-3-phosphocholine (GPC) concentrations were significantly upregulated in RYGB compared to PF and AdLib (Figure 3b). These metabolite changes were already observed four weeks post-surgery (Supplementary Figure S2b).

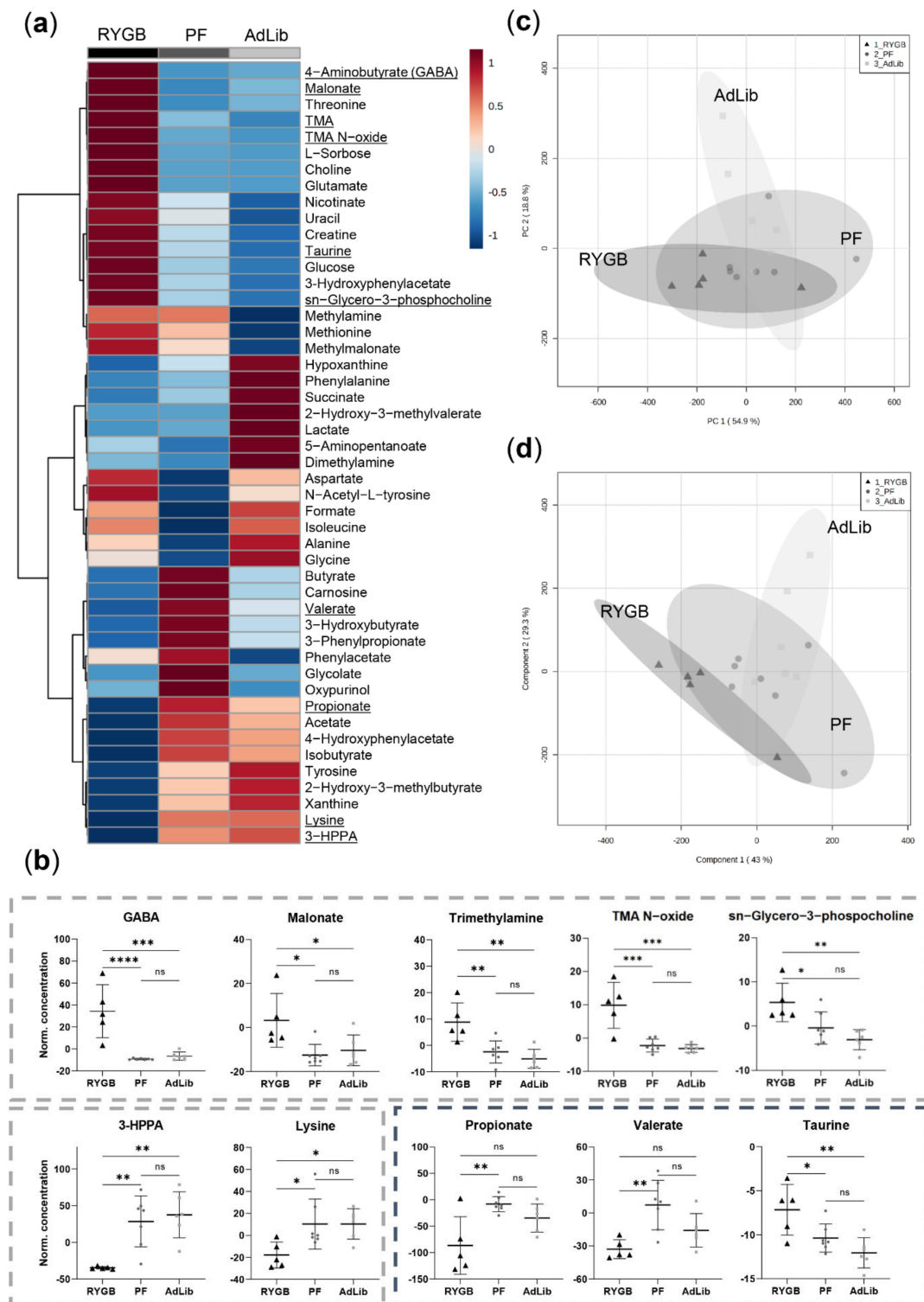


Figure 3. Feces metabolomics analysis eight weeks post-surgery. (a) Averaged heat map representing all the quantified metabolites with their relatively elevated (red) or lowered (blue) concentration differences between the groups. Metabolites significantly different between groups (one-way ANOVA)

are underlined and represented as box plots (b): upregulated 4-aminobutyrate (GABA), malonate, trimethylamine (TMA), TMA N-oxide and sn-glycero-3-phosphocholine, and downregulated 3-hydroxyphenylpropionate (3-HPPA) and lysine in the RYGB animal group (grey dashed border signifies the metabolites that exhibited the same pattern already at four weeks post-surgery). Further, eight weeks post-surgery propionate and valerate were significantly downregulated, and taurine was upregulated in RYGB. Individual samples are represented as RYGB ($n = 5$) black triangles, PF ($n = 8$) dark grey dots, AdLib ($n = 6$) light grey squares with mean and standard deviation. p -values: **** < 0.0001 , *** < 0.001 , ** < 0.01 , * < 0.05 . (c) Principal component analysis (PCA) and (d) partial least squares discriminant analysis (PLSDA) regression model illustrate an overall sample cluster overlap. 95% confidence interval is represented as grey clouds.

Moreover, significantly lower propionate, valerate, and upregulated taurine concentrations were quantified in RYGB compared to sham groups eight weeks post-surgery (Figure 3b). All three group clusters, however, did not completely separate in principal component analysis (PCA), and partial least squares discriminant analysis (PLSDA) illustrated a general overlap (Figure 3c,d).

At the end of the study period, RYGB compared to PF, but not to AdLib, exhibited lowered short-chain fatty acids (SCFA) butyrate, acetate, and formate in feces from the colon (Supplementary Figure S3a,b). We further observed an increased sample scattering in the RYGB group in PCA and PLSDA (Supplementary Figure S3c,d).

2.4. RYGB Surgery-Altered Microbiota Composition Correlates with the Feces Metabolite Changes

Next, we performed correlation analyses between the gastrointestinal microbiota and their metabolites in feces four and eight weeks after the surgery (Figure 4) and at the end of the study (Supplementary Figure S4). This analysis focused on the most significant feature differences between RYGB and both sham groups pooled. The main correlation patterns were present already four weeks post-surgery (Figure 4a, and remained at the eight weeks post-surgery (Figure 4b: GABA, malonate, taurine, TMA, TMAO, and GPC concentrations positively correlated with the relative abundance of the Proteobacteria *Escherichia/Shigella* and the Bacteroidota *Muribaculaceae*, *Parabacteroides*, *Prevotellaceae* NK3B3, *Prevotellaceae* UCG001 as well as the Firmicutes *Enterococcus* species while propionate, valerate, and 3-hydroxyphenylpropionate (3-HPPA) negatively correlated to the abundance of these taxa. Furthermore, negative correlations were observed between GABA, malonate, taurine, TMA, TMAO, and GPC and the Firmicutes *Clostridium sensu stricto* 1, *Romboutsia*, *Turicibacter*, *Lactobacillus*, and the Bacteroidota *Bacteroides* species (Figure 4 and Figure S4).

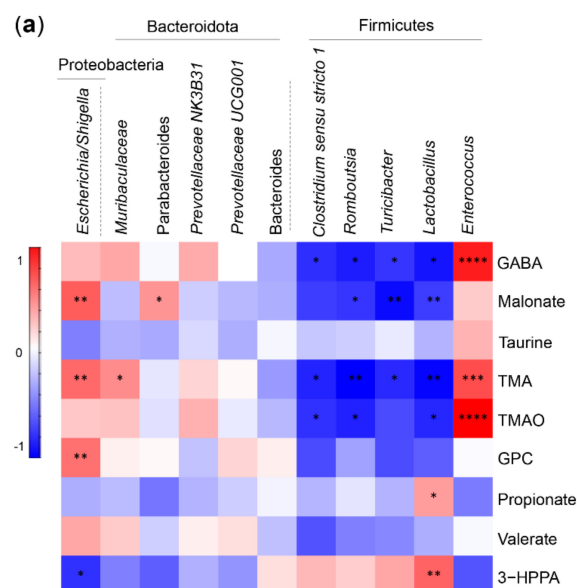


Figure 4. Cont.

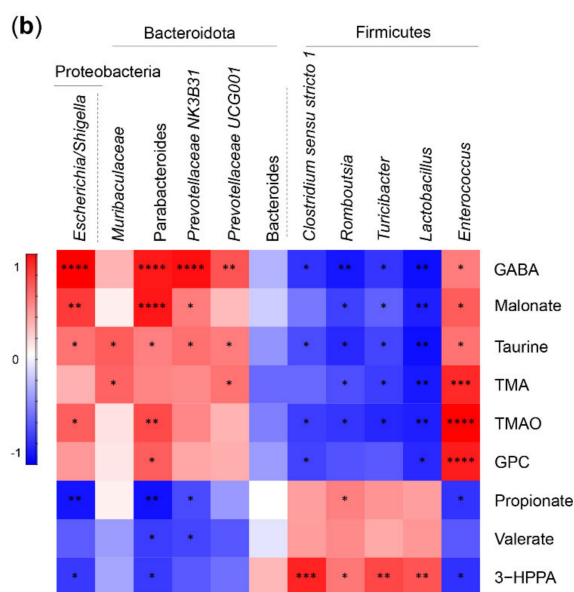


Figure 4. Fecal microbiota and metabolomics correlation analysis. (a) Four weeks and (b) eight weeks post-surgery. The color scheme illustrates the correlation values scaled between -1 and 1 . The red color indicates a positive correlation, blue—negative correlation. Statistical significance of these correlations illustrated as p -values: **** < 0.0001 , *** < 0.001 , ** < 0.01 , * < 0.05 . Correlation analysis involves all three group values (RYGB, PF, and AdLib pooled), correlation coefficients from the Pearson r distance measure. Abbreviations: GABA—4-aminobutyrate, TMA—trimethylamine, TMAO—trimethylamine N-oxide, GPC—sn-glycero-3-phosphocholine, and 3-HPPA—3-hydroxyphenyl propionate.

At the end of the study, the concentrations of fecal metabolites isoleucine and 3-hydroxybutyrate positively correlated with the relative abundance of some Bacteroidota, Parabacteroides, *Prevotellaceae NK3B31*, *Prevotellaceae UCG001*, and also with the abundance of the genera *Enterococcus* and *Escherichia/Shigella* (Supplementary Figure S4). Acetate, propionate, butyrate, and valerate concentrations correlated negatively with the abundance of the same species. Isoleucine showed a negative correlation with *Lactobacillus* species.

2.5. RYGB Surgery Changes the Branched-Chain Amino Acid, Serine, and Glycine Metabolism in Plasma

Plasma metabolomics revealed different metabolic patterns between the RYGB, AdLib, and the PF animal groups (Figure 5a and Figure S5a). Serine and glycine were increased in the RYGB group compared to the PF animals, but not AdLib (Figure 5b and Figure S5b). Creatine levels in RYGB rat plasma were elevated compared to sham animals. Moreover, isoleucine and valine were downregulated in RYGB. These metabolites are connected via glycine, serine & threonine, and glyoxylate & dicarboxylate metabolic pathways. Furthermore, downregulated threonine, valine, and isoleucine further indicated an affected glycine, serine & threonine metabolism pathway and valine, leucine & isoleucine (BCAA) biosynthesis pathway. We also saw downregulated betaine in the AdLib group compared to PF and RYGB. All three groups had many unchanged metabolite concentrations leading to a general group confidence region overlap in PCA (Supplementary Figure S5c). Several metabolites had highly variable concentrations within a group. PLSDA regression model revealed an increased sample scattering in RYGB compared to sham groups (Supplementary Figure S5d).

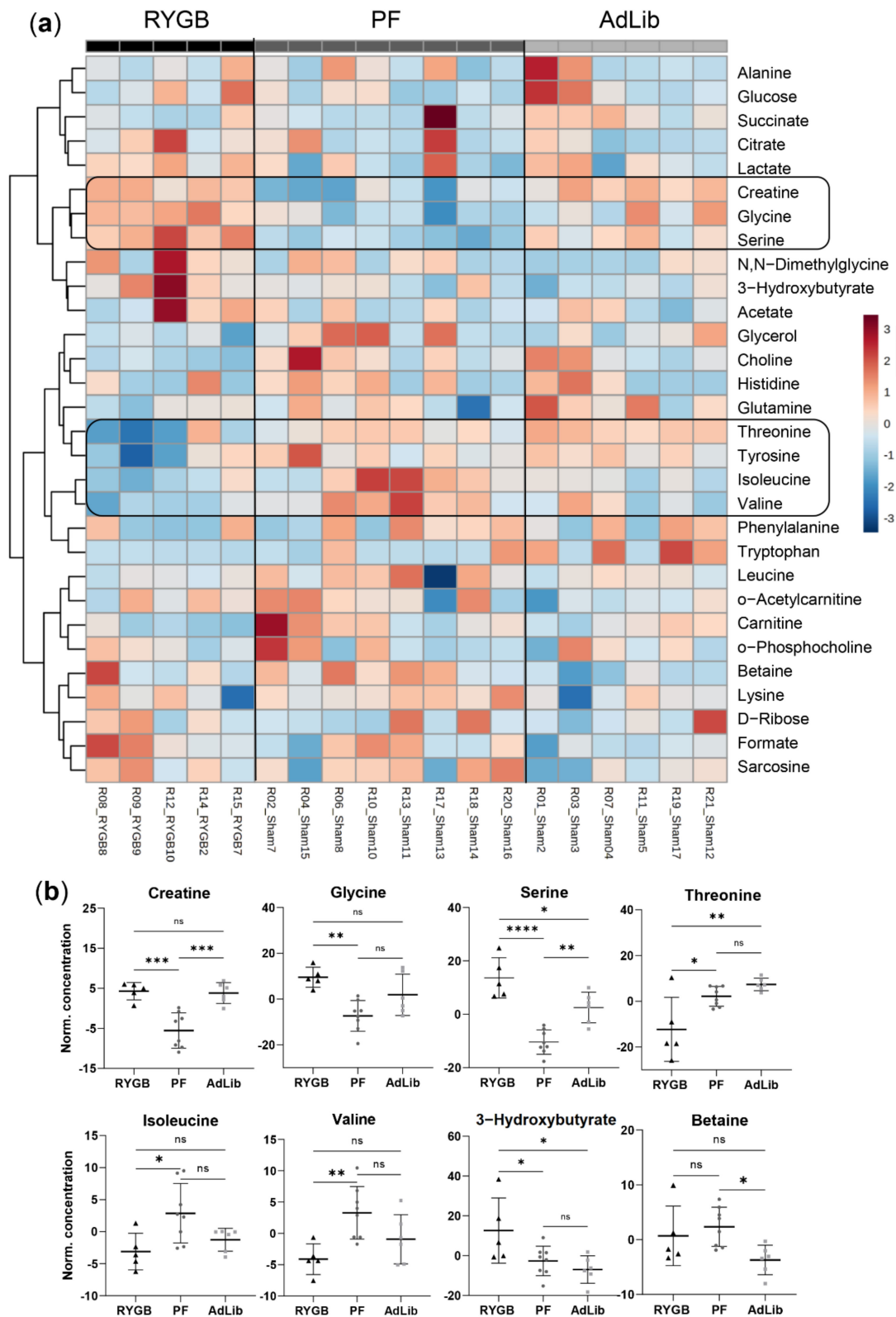


Figure 5. Plasma metabolite quantification analysis at the day of euthanasia. **(a)** Heat map illustration of all the metabolites profiled in all plasma samples, with unsupervised clustering towards similar metabolic patterns. **(b)** Individual box plots of one-way ANOVA significant metabolites: RYGB ($n = 5$) black triangles, PF ($n = 8$) dark grey dots, AdLib ($n = 6$) light grey squares, mean and standard deviation, p -values: **** < 0.0001 , *** < 0.001 , ** < 0.01 , * < 0.05 .

2.6. RYGB Animals Have Reduced C-Reactive and Increased Lipopolysaccharide-Binding Proteins in Plasma

We quantified the concentrations of the acute-phase protein C-reactive protein (CRP), the lipopolysaccharide-binding protein (LBP), the appetite-reducing hormone leptin, and different cytokines in plasma from the three animal groups (Figure 6 and Figure S6). CRP plasma levels were significantly reduced in the RYGB group compared to the PF and the AdLib group (Figure 6a). On the other hand, LBP was significantly increased in RYGB plasma compared to PF (Figure 6b). Leptin levels were also significantly increased in the AdLib compared to the PF and RYGB (Figure 6c). Insulin concentrations were constant across the groups, with a large variation observed in the AdLib group (Figure 6d). Similarly, no differences were detected for monocyte chemoattractant protein (MCP) 1, interleukin (IL) 6, IL-10 (Supplementary Figure S6a). Chemokine ligand (CXCL) 2, IL-1 α , tumor necrosis factor (TNF)- α , and interferon (IFN)- γ were below the limit of detection (Supplementary Figure S6b).

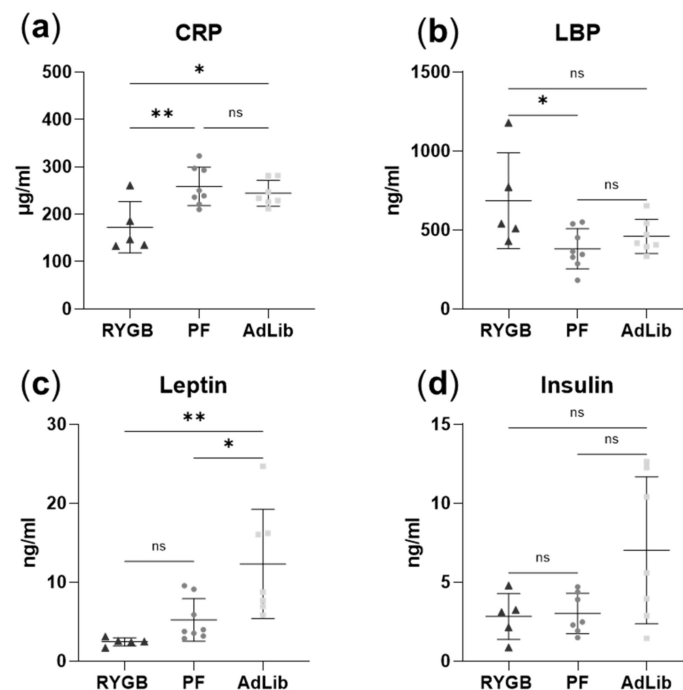


Figure 6. Immune and hormonal parameter profiling. Box plots visualizing the downregulated C-reactive protein (CRP) (a) and upregulated lipopolysaccharide-binding protein (LBP) (b) in RYGB compared to PF. Leptin was downregulated both in RYGB and PF animals compared to AdLib (c). No significant changes in insulin concentration were detected between groups (d). One-way ANOVA statistical significance, individual values illustrated for RYGB as black triangles ($n = 5$), PF dark grey dots ($n = 8$), AdLib light grey squares ($n = 7$), with mean and standard deviation, p -values: ** < 0.01 , * < 0.05 .

2.7. The Hepatic Fatty Acid Profile Changes with Liquid Sucrose Diet after RYGB Surgery

As both diet and microbiota can influence the liver lipid metabolism, we quantified the lipid fraction in the liver and its fatty acid (FA) composition. The overall lipid profile was influenced by both the surgery and food intake. Even/odd chain saturated FA ratio (C15:0, pentadecylic acid; C17:0, margaric acid) was significantly higher in hepatic fat of the RYGB animals compared to the PF group (Figure 7a and Figure S7a,b). Moreover, the hepatic omega 6 to omega 3 FA ratio was significantly higher in the PF animals compared to AdLib and RYGB (Figure 7b). Omega 6/3 ratio of the RYGB group was not significantly different compared to the AdLib group even though C22:5(4,7,10,13,16)

(docosapentaenoic acid, (PUFA, omega-6)) was increased in RYGB compared to the sham groups (Supplementary Figure S7c).

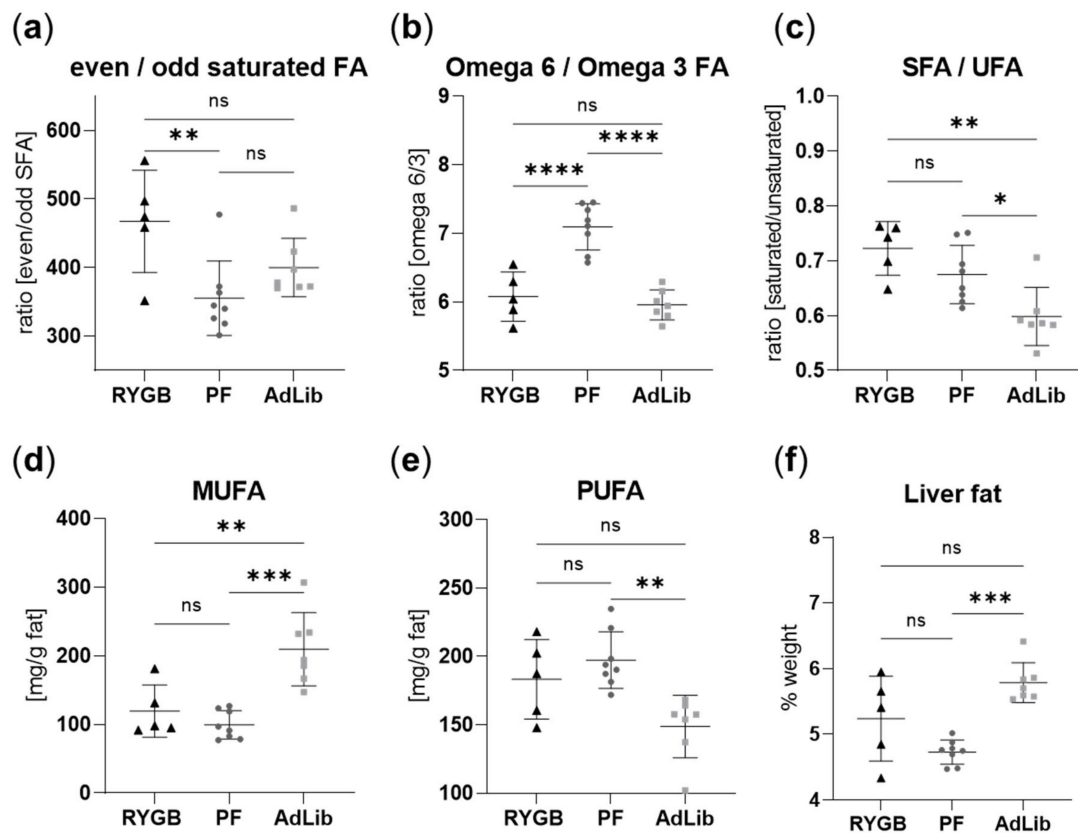


Figure 7. Hepatic fatty acid composition in RYGB and sham-operated animal groups. (a) Even to odd chain fatty acid (FA) ratio (*w/w*), (b) omega 6 to omega 3 FA ratio (*w/w*), (c) saturated (SFA) to unsaturated FA (UFA) ratio (*w/w*), (d) mono-unsaturated fatty acid (MUFA) concentration (mg/g fat), (e) poly-unsaturated fatty acid (PUFA) concentration (mg/g fat), (f) liver fat (% weight of liver). One-way ANOVA statistical significance, individual values illustrated for RYGB as black triangles ($n = 5$), PF dark grey dots ($n = 8$), AdLib light grey squares ($n = 7$), with mean and standard deviation, p -values: **** < 0.0001 , *** < 0.001 , ** < 0.01 , * < 0.05 .

Independent from the surgery-specific observations, food intake restriction and liquid sucrose diet changed FA liver profiles. The most notable differences in the AdLib group were related to the FA saturation compared to RYGB and PF. The saturated/unsaturated FA ratio was higher in the RYGB and PF when the food was reduced, compared to AdLib (Figure 7c), mainly due to low MUFA concentrations (Figure 7d). In contrast, less poly-unsaturated FA was detected in AdLib animal liver compared to RYGB and PF (Figure 7e).

Corresponding differences in the AdLib group were also clearly visible in the plots of several single FA. Upregulated C16:1(9) (palmitoleic acid, SFA), C18:1(9) (oleic acid, MUFA), lowered C18:0 (stearic acid, SFA) and lowered C20:4(5,8,11,14) (arachidonic acid, PUFA, omega-6) and C22:4(7,10,13,16) (docosatetraenoic acid, PUFA, omega-6) were quantified in AdLib rats to RYGB and PF (Supplementary Figure S7d–h). Consequently, liver fat content (%) was higher in the AdLib group compared to PF yet not statistically significant when compared to RYGB (Figure 7f).

Finally, we observed a higher desaturase activity in the AdLib group compared to PF. A lower elongase activity was quantified in the AdLib rats compared to PF and RYGB (Figure 7g,h and Figure S7f,l,m). Besides the fatty acid distribution in the liver, we also quantified the expression of key genes of hepatic lipid metabolism. Only fatty acid-binding protein 1 (FABP1) had an altered expression between groups in our investigated cohort,

higher in the AdLib animals than in the PF (Supplementary Figure S7k). Total energy intake correlated positively to MUFA but negatively to the C24:0 concentration (Supplementary Figure S7n,o). Expression of fatty acid synthase (FAS) positively correlated to the percentage of energy obtained from the liquid sucrose solution (Supplementary Figure S7p).

2.8. The Correlation of Metabolomics Data with Plasma Metabolomics, Immune, Hormonal, and Liver Parameters Indicates Surgery-Specific and Food-Related Patterns

We correlated plasma and fecal metabolite concentration patterns to investigate further the systemic effects of the RYGB surgery (Figure 8). Fecal GABA had the highest positive correlation with fecal malonate and TMAO, while it had negative correlations with plasma threonine, tyrosine, fecal propionate, and 3-HPPA (Figure 8a). Plasma 3-hydroxybutyrate correlated with fecal TMAO and glutamate and had a negative correlation with plasma tyrosine and threonine, as well as fecal tyrosine, lactate, 3-HPPA, propionate, and acetate (Figure 8b).

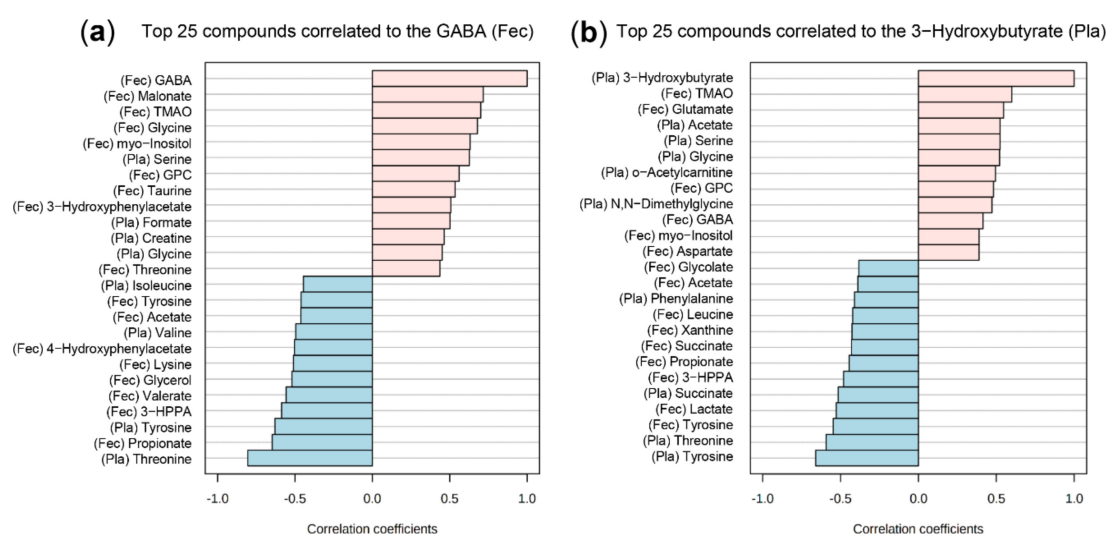


Figure 8. Correlation analysis between the plasma and feces metabolites. Top 25 compounds correlated with (a) GABA and (b) 3-hydroxybutyrate. Correlation coefficients are based on Pearson r distance measure. Abbreviations: Pla—plasma metabolite, Fec—fecal metabolite, GABA—4-aminobutyrate GPC—*sn*-glycero-3-phosphocholine, 3-HPPA—3-hydroxyphenylpropionate, TMAO—trimethylamine N-oxide.

For a cross-platform comparison, we further correlated the significantly differing plasma and feces metabolites with significantly changed immune and hormonal parameters and liver FA concentration changes. Of note, these comparisons correlate between the most prominent feature changes, considering the RYGB group compared to sham. First, we identified a prominent group of features similar between PF and AdLib but significantly different to the RYGB group (Supplementary Figure S8a). Fecal taurine and TMA positively correlated to LBP while fecal TMAO and GABA positively correlated to C22:5(4,7,10,13,16) (docosapentaenoic acid (osbond acid), PUFA, omega-6), and C24:1(15) (nervonic acid, MUFA). C22:5(4,7,10,13,16) also positively correlated to plasma 3-hydroxybutyrate and negatively correlated to plasma threonine. CRP had positive correlations with fecal 3-HPPA, plasma threonine, and a negative correlation with fecal GPC, GABA, and TMAO. Second, we identified similar features between the RYGB and PF groups that were significantly different from the AdLib group (Supplementary Figure S8b). Plasma leptin negatively correlated to C22:4(7,10,13,16) (docosatetraenoic acid, PUFA, omega-6) while it had positive correlations to the sum of MUFA, C16:1(9) (palmitoleic acid, MUFA), and C14:0 (myristic acid, SFA). FABP1 positively correlated to C15:0 (pentadecylic acid, SFA), C16:1(9) (palmitoleic acid, MUFA), and liver fat % content.

2.9. Brain Imaging Reveals Increased Neuronal Activity after RYGB Surgery

Neuronal activity was investigated using [^{18}F]fluorodeoxyglucose (FDG) PET at resting state and after a glucose stimulus. When comparing RYGB to PF rats, [^{18}F]FDG tracer uptake at resting state was increased in the brain stem and midbrain areas, including the central tegmental tract (ctg), dorsal tegmental bundle (dtg), deep mesencephalic nucleus (DpMe), dorsolateral periaqueductal grey (DLPAG), and medial geniculate nucleus dorsal (MGD) (Figure 9a). Similarly, neuronal activation at the resting state in RYGB was increased in the brain stem and midbrain areas, such as retrorubral field (RRF), dtg, and DpMe compared to AdLib (Figure 9b).

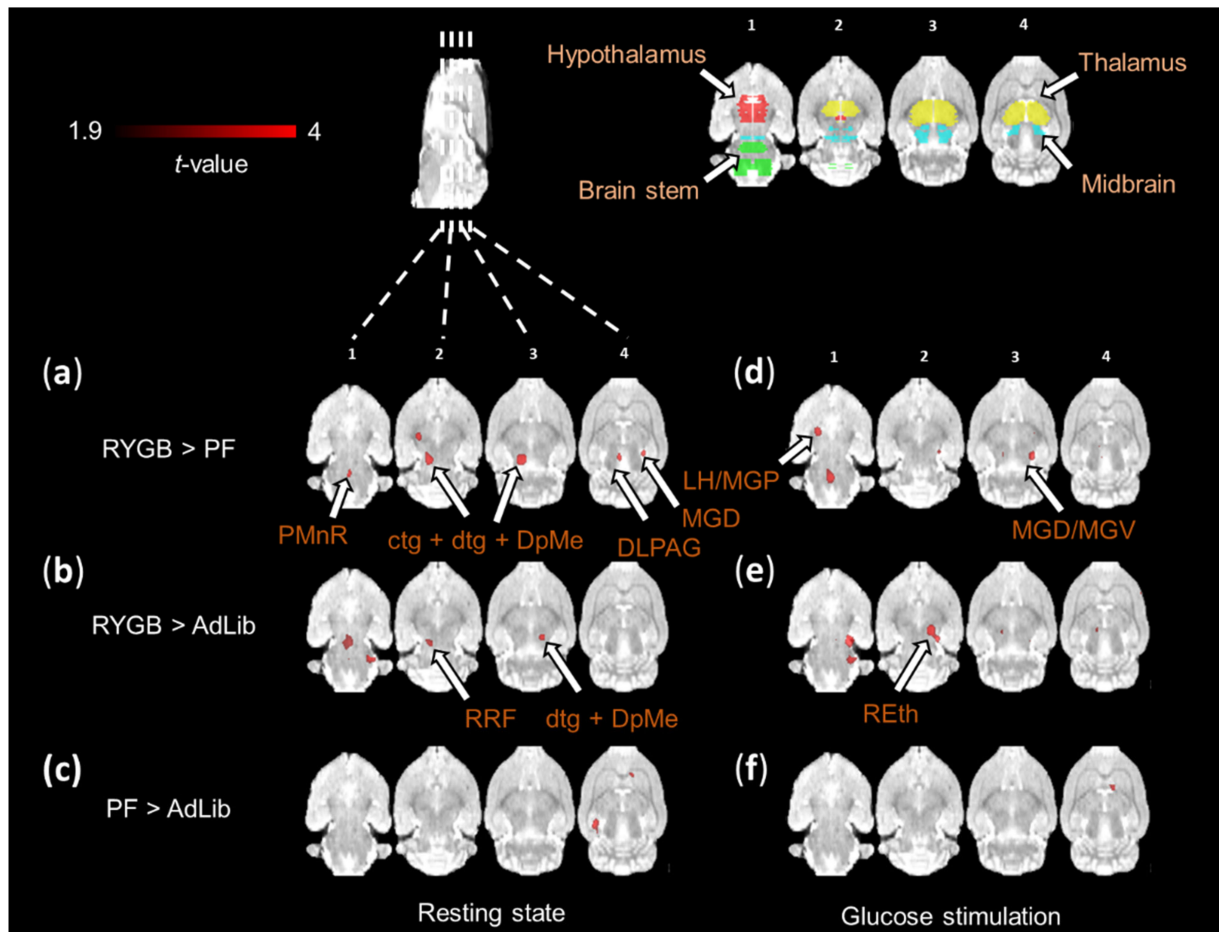


Figure 9. Functional PET brain activation maps at resting state and after glucose stimulation. Coronal brain sections show increase in relative [^{18}F]FDG uptake at resting state and after glucose stimulation. Comparison of (a,d) RYGB > PF rats, (b,e) RYGB > AdLib and (c,f) PF > AdLib at a significance level of $p \leq 0.01$. Brain region color code: red—hypothalamus, green—brain stem, yellow—thalamus, blue—midbrain. RYGB ($n = 5$), PF ($n = 5$) AdLib ($n = 6$). Abbreviations: PMnR—paramedian raphe nucleus, ctg—central tegmental tract, dtg—dorsal tegmental bundle, DpMe—deep mesencephalic nucleus, MGD—medial geniculate nucleus dorsal part, LH—lateral hypothalamus, MGP—medial globus pallidus, MGv—medial geniculate nucleus ventral part, RRF—retrorubral field, REth—retroethmoid nucleus.

Furthermore, increased neuronal activity in response to glucose stimulation was observed in thalamic areas, such as MGD, medial geniculate nucleus ventral (MGV), and the hypothalamic regions, such as the lateral hypothalamus (LH) and medial globus pallidus (MGP) in RYGB animals compared to PF (Figure 9d). The thalamic areas were also activated when comparing RYGB to AdLib (Figure 9e). No specific differences in

tracer uptake were observed in the investigated brain regions before or after the glucose stimulation when comparing AdLib to the PF group (Figure 9c,f).

In addition, the effect of glucose stimulus was analyzed on a cellular level by early gene (c-Fos) histochemical staining. Generally, glucose-induced c-Fos cell counts were low, with no group differences observed in the basolateral amygdala (BLA), layer 2 of the cortex (L2), or paraventricular hypothalamic (PVH) regions (Supplementary Figure S9; Supplementary Tables S1–S3).

3. Discussion

3.1. Liquid Sucrose-Induced Obesity Is Reverted by RYGB Surgery

Our results confirmed the persistent weight reduction in liquid sucrose diet-induced obese rats post-RYGB surgery, similar to other animal studies [20,42] and clinical practice [43]. PF animals had similar body weight to the AdLib group after the sham surgery, suggesting that caloric restriction was not the only driver for the RYGB-induced weight loss. Moreover, caloric restriction efficiently reduced total liver fat content in the PF animals. While the total energy consumption was significantly higher in AdLib compared to RYGB and therefore also PF, the relative percentage of energy consumed via liquid sucrose was not significantly changed between the groups. Therefore, we conclude that the surgery led to a reduced total energy intake in RYGB animals.

3.2. Microbiota Perturbations Lead to Upregulated Fecal GABA and Lower Fiber Fermentation

RYGB surgery causes a persistent environmental change of the gut which has been previously associated with a long-lasting impact on the microbiota composition and metabolism [44]. RYGB has also been shown to promote a change in dietary habits and their associated neuronal processes [45]. Bacteroidetes and Proteobacteria such as *Escherichia* have been reported to actively express the genes necessary for producing the neurotransmitter GABA in human stool [46]. Here we quantified a higher fecal concentration of GABA in RYGB rats, correlating with a higher relative abundance of *Escherichia/Shigella* and *Parabacteroides* in these animals. The regulation of neurotransmitters through the microbiota can affect the host through gut-brain communication (reviewed in [47,48]). GABA is a crucial part of the brain's GABAergic system and the enteric nervous system (ENS), acting as a modulator for the gut signaling processes [49]. It has been reported that GABA can activate gut/intestinal cells and further promote a cascade leading to neuronal cell activation via gut secreted exosomes [50]. GABA receptors also have been shown to influence the liquid secretion processes (GABA-A) and gut motility (GABA-B) [51]. Increased GABA concentrations in feces correlate to the liquid state of the feces and suggest a higher defecation rate in RYGB compared to sham groups.

Further, we quantified a reduced relative abundance of Firmicutes in RYGB compared to AdLib and PF feces, particularly *Lactobacillus*, *Turicibacter*, and *Romboutsia*, which are known to produce SCFA via fiber fermentation [38,52]. Lower levels of fecal SCFA in RYGB and AdLib compared to PF may result from different nutrient availability in the colon. In RYGB, this is a potential side effect of surgery and consequent malabsorption as the macronutrients can escape directly from the small intestine into the large intestine. While in AdLib, similarly lower SCFA was quantified due to the larger amount of food ingested, and thus more macronutrients entered the fermentative section of the gut. As the substrate is different, the readily available macronutrients such as protein and simple carbohydrates might be fermented first and fast by the microbiota, giving the SCFA more time for entering enterocytes and the bloodstream via diffusion, resulting in lower fiber fermentation and therefore less SCFA in RYGB and AdLib feces compared to PF.

Moreover, the higher relative abundance of Bacteroidetes, particularly *Muribaculaceae* species, which are versatile carbohydrate degraders [53], could indicate a shift from fiber fermentation to host-derived carbohydrate utilization in the microbiome of RYGB animals [38,54].

Increased fecal taurine in RYGB has been previously reported in the context of the intestinal NOD-like receptor family pyrin domain containing 6 (NLRP6) inflammasome expression repair leading to gut immune homeostasis [55] and supports our findings of reduced inflammation in RYGB as reflected by decreased CRP plasma levels.

TMA and TMAO were elevated in the feces of RYGB rats and are usually produced from dietary choline and carnitine by gut bacterial enzymes (choline TMA lyase; carnitine oxidoreductase) [56,57]. In our dataset, plasma TMA and TMAO had a significant positive correlation to the relative abundance of *Enterococcus*, most prominent at four and eight weeks post-surgery. *Enterococcus* species have been reported to enable plasma TMAO degradation ex vivo [58], suggesting that bacterial species could be activated with the purpose of TMA and TMAO degradation. TMA and TMAO have been related to increased risk of cardiovascular disease [59–61]. However, we also observed in the RYGB rats a significant decline of TMAO concentrations in feces from four to eight weeks. Furthermore, in feces samples on the day of euthanasia, TMAO was no longer significantly increased in RYGB compared to sham, which indicates a temporary microbiota shift after the surgical intervention that could be resolved during the recovery time after surgery.

3.3. RYGB Surgery Leads to Lowered Plasma BCAA and Increased Glycine

Plasma metabolite profiling confirmed that RYGB surgery alters the valine, leucine, and isoleucine BCAA biosynthesis pathway [62]. BCAA upregulation has been linked to obesity and diabetes [63] and interconnected with glycine downregulation [64]. Reduced solid food intake resulted in less available protein in RYGB and PF. However, quantified BCAA decrease could indicate malabsorption in RYGB.

Furthermore, we identified glycine, serine, and threonine, and glyoxylate and dicarboxylate metabolic pathway upregulation after RYGB surgery. Metabolites such as serine and glycine are known substrates for the folate and methionine cycle [65]. These further participate in one-carbon metabolism, which is crucial for appropriate nucleotide and cofactor synthesis. Obesity and type 2 diabetes have been previously associated with depleted circulating glycine and the potential necessity of therapeutic glycine supplementation [66]. We conclude that RYGB surgery leads to improved plasma metabolite patterns and, therefore, a potentially reduced risk of type 2 diabetes.

3.4. RYGB Surgery Results in Elevated LBP Not as a Result of Inflammation but Possibly from Increased Lipolysis as Seen by Plasma Ketone Body Levels

Although increased LBP in plasma is a known marker for inflammation [67], we did not observe any other signs for an upregulated inflammatory response in the RYGB group compared to the sham. Indeed, plasma CRP levels were decreased in RYGB compared to sham groups, which is in good agreement with previous research [68]. Furthermore, our reported microbial changes of increased gram-negative Bacteroidetes and Proteobacteria, which are known to express the antigen LPS on their cell surface [69], and decreased gram-positive Firmicutes, could lead to a higher LPS concentration within the RYGB gut compared to sham. Increased hepatic even/odd chain fatty acid ratio and reduced leptin levels in RYGB support the hypothesis that RYGB leads to upregulated lipolysis as reflected by increased levels of the ketone body 3-hydroxybutyrate in RYGB animal plasma. 3-Hydroxybutyrate is produced by the liver in lipolysis and serves as the primary energy substrate via beta-oxidation and acetyl-CoA for the TCA cycle when glucose is depleted [70]. During lipolysis, long-chain fatty acids can be transported only within chylomicrons, which are therefore highly upregulated [71]. However, as LPS has a high affinity for chylomicrons, we conclude that chylomicron formation due to increased lipolysis promotes intestinal LPS absorption, as previously described in gut mucosa [68]. We thus hypothesize that due to reduced solid food intake and malabsorption, de novo lipogenesis is enhanced in RYGB animal livers from excess sucrose, particularly from the fructose moiety. However, as too many free fatty acids can be toxic, the body might try to regulate this by simultaneously increasing lipolysis, as seen by elevated 3-hydroxybutyrate levels in RYGB plasma. More-

over, increased lipolysis might contribute to the weight loss in the RYGB group that could not be attributed solely to reduced food intake in PF.

Finally, the decrease of the ketogenic amino acid lysine in RYGB feces and increased 3-hydroxybutyrate in RYGB plasma indicates that lysine could be transformed into 3-hydroxybutyrate. In this context, it is important to note that increased 3-hydroxybutyrate has also been found in humans after one-anastomosis gastric bypass surgery [72].

3.5. The Even/Odd Saturated FA Ratio Is Increased after RYGB Surgery

The RYGB hepatic FA profiles differed from the PF and AdLib animals when considering the hepatic even/odd FA ratio, which was higher in RYGB. Indeed, RYGB animals showed a lower concentration of margaric acid (C17:0) than sham animals, which could be synthesized in the liver from the gut-derived propionate, a metabolite found in reduced concentrations in the RYGB feces. It is well recognized that gut microbiota influences host lipid metabolism [73]. Kindt et al. showed that microbiota-derived dietary fiber acetate leads to the synthesis of FA in the liver, particularly palmitic acid (C16:0) and stearic acid (C18:0). Moreover, fructose triggers de novo lipogenesis in the liver through two mechanisms, both involving its transformation into acetate by the microbiota [73]. Moreover, the liver can use gut-derived propionate to synthesize odd chain FA [74]. As the odd chain FA increases the membrane fluidity and is linked to a lower risk for type 2 diabetes and could help against Alzheimer's disease and cancer [75–77], our observations suggest an unfavorable effect on RYGB associated with high sucrose consumption on the liver FA profile. Kindt et al. showed that changes in FA profiles in the liver were also found in plasma FA profiles and might, therefore, have a systemic effect. It has also been shown that the circulating long-chain FA can be sensed in the hypothalamus, where they regulate glucose homeostasis [78]. Nevertheless, we did not find a direct gut-brain link through our investigation.

3.6. RYGB Surgery Leads to Altered Neuronal Activity in the Rat Brain

We investigated the effect of an RYGB surgery on brain activity by [¹⁸F]FDG-PET. We observed several activated brain areas in rats that underwent RYGB surgery as a possible result of the ketogenic state where 3-hydroxybutyrate replaced glucose as the primary cellular energy source. The highest neuronal activation was observed in RYGB compared to sham rats in the brain stem, midbrain, thalamus, and hypothalamus areas. The midbrain regions of ctg and DpMe are GABAergic cell-rich regions with a high potential for GABAergic signaling processes [79]. They are involved in an exaggerated activation of homeostatic feeding circuits and display enhanced brain serotonergic signaling after RYGB surgery [80].

We also quantified increased 3-HPPA, which is formed through the fermentation of tyrosine by *Clostridium*, *Escherichia*, and *Eubacteria* species or via polyphenol metabolism [54]. 3-HPPA has been reported to be able to cross the blood-brain barrier, further serving as a competitive inhibitor for dopamine synthesis [81]. As we saw a neuronal activation in the hypothalamus and midbrain (ctg, dtg), regions where dopamine is produced, a further investigation would be necessary to confirm this connection. Although a limitation of this study was the relatively low animal number per group, our data shows that the RYGB surgery results in increased neuronal activity in the RYGB animals compared to controls.

3.7. Key Findings and Future Implications

In conclusion, RYGB surgery successfully reversed the weight gain induced by the liquid sucrose diet. In the gut, RYGB rats showed increased Bacteroidota, Pro bacteria, and decreased Firmicutes. Microbiota changes led to notably increased GABA production in the gut, which we further quantified in feces, possibly influencing downstream metabolite and cytokine profiles as well as signaling in GABAergic regions of the ENS and CNS. Lowered plasma BCAA and increased glycine in RYGB suggested a lowered risk of obesity. As we opted to induce obesity using the liquid sucrose diet, most of the changes in the liver

fatty acid profile were related to the diet and caloric restriction effects. We also observed increased brain neuronal activity after the surgery, yet further confirmatory investigations are needed to truly underpin the molecular mechanisms regulating appetite, metabolism, and gut-brain signaling.

4. Materials and Methods

4.1. Animals

Male Lewis rats ($n = 27$, approximately 400 g, (Charles River, Sulzfeld, Germany) were single-housed in IVC cages (1500U) enriched with nesting material and kept on a 12-h day-night cycle at a room temperature of 22 °C and 40–60% humidity. All experimental procedures were performed in accordance with the European Union Directive 2010/63/EU on the protection of animals used for scientific purposes and were approved by the Regierungspraesidium Tuebingen (Tuebingen, Germany regional authorities approval, permit number MPV 3/16, issued 13 May 2019).

4.2. Experimental Design and Surgical Technique

The experimental design is shown in Figure 1a. Rats ($n = 27$) were randomized in cages, housed in groups of four, and had ad libitum access to phytoestrogen-reduced chow (Sniff, Soest, Germany) and a water bottle containing 30% sucrose (Sigma Aldrich Chemie, Taufkirchen, Germany) in water (liquid sucrose) for eight weeks. Subsequently, rats were randomly assigned to undergo RYGB ($n = 10$) or sham surgery ($n = 17$). The details of the RYGB surgery have been described previously [82]. Rats were fasted overnight and were treated with antibiotics (Baytril, 5.7 mg/kg, s.c., Bayer, Leverkusen, Germany) and analgesics (Carprofen, 5 mg/kg, s.c., Bayer, Leverkusen, Germany) prior to anesthesia. Anesthesia was induced in an induction chamber with 4–5% isoflurane (CP-Pharma Handelsgesellschaft mbH, Burgdorf, Germany). When surgical tolerance was reached, anesthesia was maintained with 1–3% isoflurane. The surgical areas were cleaned with Braunol (B Braun SE, Hessen, Germany), and all rats received eye ointment to protect the cornea. Rats were kept on heating pads to avoid hypothermia. Following a midline laparotomy, the RYGB surgical intervention consisted of a transection of the stomach, leaving only a small proximal pouch, a transection of the small bowel, and reanastomosis creating an alimentary (or Roux) limb of approximately 50 cm, a biliopancreatic limb, and a common channel. The esophagogastric junction was anastomosed to a loop of jejunum 8–10 cm distal to the ligament of Treitz in an end-to-side fashion. A 7-mm side-to-side small bowel anastomosis was performed between the biliopancreatic and the alimentary limbs to create a common channel of approximately 25 cm. Anastomoses were performed using prolene 7/0 and the gastric remnant was closed with prolene 5/0. The sham procedure consisted of a laparotomy, a 7-mm gastrotomy on the anterior wall of the stomach, and resuturing of the gastrotomy with 5/0 prolene. At the end of all the procedures, 5 mL of warm 0.9% saline was given i.p. to compensate for fluid loss before the closure of the abdominal wall and skin with vicryl 4/0. Rats were maintained in a warm environment until they were fully awake and mobile. Rats received antibiotics and analgesics (as described in the pre-operative preparation) on postoperative days 1–4, once a day, and single-housed to avoid any additional risk of wounds. Four RYGB rats died shortly after the surgery. During the first week after surgery, wet food was provided in the cages for recovery, and no sucrose was given to avoid inflammation in RYGB animals. Sucrose intake started again one week after surgery. After nine weeks, the RYGB group ($n = 6$) and sham AdLib group ($n = 9$) continued to have ad libitum access to the diet and liquid sucrose, while the sham pair-fed group (PF; $n = 8$) received water ad libitum and were pair-fed chow and liquid sucrose solution calculated from the food and liquid sucrose consumption of the RYGB group. One RYGB rat (RYGB 6) was euthanized 6 weeks after RYGB surgery as weight loss was more than 20% of the average body weight and had reached termination criteria. One AdLib rat (Sham 1) was euthanized as a control to collect data and one AdLib

rat (Sham 9) died shortly before the FDG-PET measurement. The final animal numbers per group were RYGB $n = 5$, PF $n = 8$, AdLib $n = 7$.

4.3. [^{18}F]FDG-PET with Glucose Stimulation

At least eight weeks post-surgery, overnight fasted rats were deeply anesthetized with 3% isoflurane evaporated in the air at a flow rate of 0.8 L/min in an induction chamber. The isoflurane was reduced to 2% for maintenance, and a blood sample was collected from the tail vein to determine the blood glucose concentration. Three catheters were placed into the tail vein for anesthesia, glucose stimulation, and tracer injection, and rats were intubated and connected to a small animal ventilator (DC1 73-3629, Harvard Apparatus, Holliston, MA, USA). Breaths per minute were set to 60 with an inspiration duration of 60% of the ventilation cycle. The end-inspiratory pressure was set to approximately 10 cm H₂O and 500 mL/min flow. During the preparation, animals were warmed by a heating pad. At least 30 min before the start of the PET acquisition, isoflurane anesthesia was replaced by an initial bolus of 16 mg of alpha chloralose, followed by a second bolus containing 5 mg of alpha chloralose and 0.25 mg of pancuronium bromide after five minutes. A constant infusion of alpha chloralose (20 mg/kg/h) (Sigma Aldrich Chemie GmbH, Taufkirchen, Germany) and pancuronium bromide (1 mg/kg/h) (Inresa Arzneimittel GmbH, Freiburg, Germany) was started and maintained for the duration of the imaging experiment.

[^{18}F]FDG was obtained from the radiopharmacy (Department of Preclinical Imaging and Radiopharmacy). PET/MRI experiments were performed on a combined PET/MRI (7T) system (ClinScan, Bruker BioSpin MRI GmbH, Ettlingen, Germany) with an in-house-built PET insert [83]. Using a localizer scan, rats were placed in the center of the field of view (FOV) on a water-heated small animal bed (Medres, Cologne, Germany) connected to a feedback temperature control unit (Medres, Cologne, Germany) set to 37 °C. A 72 mm linearly polarized RF coil (Bruker BioSpin MRI GmbH, Ettlingen, Germany) was used for signal excitation and a transceiver coil for the anatomical sequence. At least 30 min after isoflurane was set to 0%, a bolus plus constant [^{18}F]FDG (injected activity: 87.5 ± 9.2 MBq) infusion was started (bolus: 166 $\mu\text{L}/\text{min}$ for one minute, infusion 8 $\mu\text{L}/\text{min}$ remaining time; 155–165 MBq in 1.1 mL). Dynamic PET data were acquired for 70 min and divided into 70-time frames (60×60 s; 1×30 s). A one-minute glucose stimulation (0.35 g/250 g body weight, 50% Glucose solution B. Braun, Melsungen, Germany) was injected 30 min after the start of the PET acquisition. At the end of the scan, an anatomical T2 image was acquired using a TurboRARE sequence (TE: 67.11 ms, TR: 1800 ms, rare factor: 28, averages: 1, FOV: 40 mm \times 32 mm \times 32 mm, image dimensions: 160 px \times 128 px \times 128 px, voxel size: 0.25 mm \times 0.25 mm \times 0.25 mm).

4.4. [^{18}F]FDG-PET Data Analysis

All [^{18}F]FDG-PET scans were stored as list-mode files and reconstructed dynamically into one-minute time frames using an ordered subset expectation-maximization 2D (OSEM2D) algorithm. Then PET DICOM images were converted into NIfTI files before pre-processing using Statistical Parametric Mapping (SPM12, Wellcome Trust Centre for Neuroimaging, University College London, London, UK) in MATLAB (Mathworks, Natick, MA, USA). First, image realignment was applied to correct the motion artifacts. Then, skull stripping was performed on all PET and anatomical reference images of each rat using binary masks generated in AFNI (Analysis of Functional Neuro Images, Medical College of Wisconsin, Milwaukee, WI, USA). Next, the PET images of each rat were co-registered to their respective anatomical image using SPM12. The anatomical scans were then used to normalize the PET datasets to the Schiffer rat brain atlas [84]. Finally, a $1.5 \times 1.5 \times 1.5$ mm³ full-width-half-maximum (FWHM) Gaussian kernel was applied to all PET images for spatial smoothing [85].

Time-activity curves of each region of interest were normalized to the whole-brain radioactivity. Average normalized PET images were generated for all cohorts between 21 and 30 min and 41 and 50 min for voxel-wise comparison of baseline and glucose-stimulated

conditions. The generated images were loaded into a second-level SPM two-sample analysis to generate contrasts between RYGB and AdLib, RYGB and PF, and PF and AdLib based on *t*-test statistics. R02 (Sham 7), R17 (Sham 13), R04 (Sham15), and R01 (Sham 02) data were excluded from further analysis due to distorted images because of animal movement during the scan or a paravenous [¹⁸F]FDG injection.

4.5. Tissue and Feces Collection

Rat feces were collected at four and eight weeks post-surgery from the cage. After the PET scan, 1–2 mL blood sample was collected and centrifuged for 5 min at 4 °C 3000 rpm after clotting for 20–30 min at room temperature. Plasma was aliquoted, snap-frozen, and stored at –80 °C until further experiments. Rats were transcardially perfused with 50 mL ice-cold PBS followed by 150 mL of 4% paraformaldehyde (PFA). Rat feces were collected from the colon in cryo-vials and snap-frozen in liquid nitrogen. The brains were surgically extracted, post-fixed in 4% PFA overnight, and transferred to PBS the next day for long-term storage at 4 °C. Liver tissue was collected and snap-frozen in liquid nitrogen and kept at –80 °C for long-term storage.

4.6. Immunohistochemistry

Early gene (c-Fos) and NeuN histochemical stainings were performed on free-floating sections. The brains were cut into 60- μ m coronal slices using a Microm (HM 650 V vibratome Thermo Fisher Scientific, Dreieich, Germany). Individual sections were collected in wells filled with 0.1 M PBS (pH 7.4). Per animal, three coronal sections at the level –1.8 mm posterior to bregma, according to the coordinates of the atlas of Paxinos and Watson [86], were chosen for analysis based on brain activity seen in the PET data.

Neural activity on a cellular level was revealed using antibodies against the c-Fos protein, an early transcription factor. In addition, NeuN, a marker for neurons, was applied to detect how many c-Fos positive cells were neuronal. Brain sections were washed three times with 0.1 M PBS (pH 7.4) and blocked for 2 h with 10% goat serum (s-1000, Vector Laboratories, Linaris Biological Products, Mannheim, Germany) in 1X PBS. Sections were incubated with c-Fos antibody (1:1000, mouse monoclonal (C-10), sc-271243, Santa Cruz Biotechnology, Dallas, TX, USA) for 72 h on a shaker at 4 °C in the dark. Sections were then washed three times with 0.1 M PBS and incubated with the secondary antibody (1:2000, Alexa Flour 488, goat anti-mouse IgG H + L, ab150117, Abcam, Cambridge, UK) for 2 h at room temperature (RT). Sections were subsequently washed 0.1 M PBS and incubated with anti-NeuN antibody (Anti-NeuN, clone A60, mouse, Alexa Fluor[®]555 conjugated, Agilent, Santa Clara, CA, USA) in blocking solution for 72 h at 4 °C. After rinsing with 0.1 M PBS, sections were finally stained with DAPI (Thermo Fisher Scientific Inc., Dreieich, Germany) (10 min, RT) and mounted on glass slides using Fluoromount-G (H-100, VECTASHIELD[®] Antifade Mounting Medium, Linaris Biological Products, Mannheim, Germany).

4.7. Confocal Imaging

Images were captured using a confocal microscopy system (Confocal LSM 710, Zeiss, Jena, Germany). The images were post-processed using linear brightness and contrast transformations to improve visibility. For figures, images were further processed with CorelPhotoPaintX6 (CorelPhotoPaintX6, Corel Cooperation, Ottawa, ON, Canada). Experimenters blinded to experimental groups used the DAPI channel and anatomical guidelines described by Paxinos & Watson [86] to determine regions of interest (ROIs). The basolateral amygdaloid nucleus (BLA), central amygdaloid nucleus (CeC), dorsal endopiriform nucleus (DEn), paraventricular nucleus of the hypothalamus (PVN), and layer 2 of the cortex (L2) were examined for c-Fos and NeuN positive cells.

Analysis was performed using ImageJ software (National Institutes of Health). The number of cells labeled for c-Fos and NeuN and their co-localization were counted manually on the Fiji software (National Institutes of Health (NIH), Bethesda, MD, USA) platform

using ImageJ plugin Cell Counter (NIH, Bethesda, MD, USA). The number of counted cells was averaged across three sections per bregma level for each animal and ROI.

4.8. 16S rRNA Gene Sequencing-Based Microbiome Analysis

Genomic DNA was extracted from ~200 mg feces using the Nucleospin Stool Kit according to the manufacturer's recommendation (Macherey Nagel, Düren, Germany) with 1 mL diluted ST1 buffer (1:1 with water), a bead-beating step of 40 s at 6 m/s on a FastPrep 24 G (MP Bio, Illkirch-Graffenstaden, France) instead of step 2. Amplification of 16S RNA gene was performed using a single PCR approach with dual-index V4-region primers (Biomers, Ulm, Germany) [87,88]. The Phusion Hot Start II DNA polymerase (Thermo Fischer Scientific, Walldorf, Germany) was used for 25 cycles on 1 ng of DNA. According to the manufacturer's instructions (Mag-Bind RXNPure Plus, Omega, Norcross, GA, USA), PCR products were checked on agarose gel and purified with magnetic beads. Quantification was then performed on a Quantus Fluorometer (Promega, Walldorf, Germany) with the QuantiFluor One dsDNA System (Promega, Walldorf, Germany), according to the manufacturer's recommendation. Products were then pooled in a library (final concentration 8 pM, with 20% PhiX DNA) and sequenced on a MiSeq (Illumina, San Diego, CA, USA) using a MiSeq Reagent Kit v3 for 2 × 300 cycles as recommended by the manufacturer with additional dual-index sequencing primers [89].

Raw sequences were trimmed and quality filtered before ASVs were defined using the package Dada2 [90]. Phyloseq package was used to determine alpha- and beta-diversity [91]. Adonis from the package vegan was used to perform permanova (<https://cran.r-project.org/web/packages/vegan/index.html>, accessed on 8 October 2020), and the LefSe Server was used to identify significantly discriminative taxa between treatment groups [92].

Raw sequence data have been deposited in the European Nucleotide Archive ENA under the accession number PRJEB49286 (European Nucleotide Archive (ENA)).

The 66 sequenced samples led to 2,618,817 reads in total, corresponding to 1520 amplicon sequencing variants (ASVs). Samples had between 12,704 to 78,082 reads. Removing the negative control (around 700 reads) and mock community samples led to 1461 ASVs in rat samples. All ASVs with less than 10 reads overall were removed, resulting in 1106 ASVs on which further analyses were performed.

4.9. ¹H-NMR Spectroscopy-Based Metabolomics Analysis of Plasma and Feces

45 µL of plasma was mixed with 90 µL of LC-MS grade methanol. 300 mg of rat feces were suspended in 400 µL of methanol and 800 µL of methyl-tert-butyl ether (Sigma Aldrich Chemie, Taufkirchen, Germany). Mixtures were subjected to ultrasound metabolite extraction protocol of 5 min per sample by Covaris E220 ultrasonicator equipped with a water-cooling bath at 8 °C (Covaris, Woburn, MA, USA). Further, 500 µL of ultrapure water was added to the feces sample mixture. Glass tubes were centrifuged at 30,000 × g for 30 min for two-phase separation. The aqueous phase was transferred to a fresh 1.5 mL Eppendorf cup (Eppendorf, Hamburg, Germany). Plasma extract was also transferred to a 1.5 mL Eppendorf cup and centrifuged at 30,000 × g for 30 min. The supernatant of each sample was transferred to another clean 1.5 mL Eppendorf and evaporated to dryness overnight. Metabolite pellets were re-suspended in 45 µL 200 mM phosphate (K₂HPO₄) buffer in deuterated water (D₂O) containing 200 µM NaN₃ (pH 7.4), and containing 1 mM (3-(trimethylsilyl) propionic-2,2,3,3-d₄ acid sodium salt (TSP) internal standard (Sigma Aldrich Chemie, Taufkirchen, Germany). Suspensions were thoroughly mixed (vortexed) and centrifuged at 30,000 × g for 10 min. 40 µL of clear supernatant were used to fill 1.7 mm NMR tubes (Bruker BioSpin, Ettlingen, Germany).

NMR measurements were carried out on a Bruker Avance III 14.10 Tesla, 600 MHz for ¹H with a 1.7 mm triple-resonance room-temperature probe (Bruker BioSpin, Ettlingen, Germany). A short zero-go (zg) measurement was followed by 7-min 1D NOESY and 1-h CPMG (512 scans) experiments. Spectra were pre-processed with Bruker TopSpin 3.6.1 software and later profiled using ChenomX 8.5 Professional NMR Suite. For further

analysis, R01 (Sham 02) and R20 (Sham 16) feces samples and R16 (Sham 06) plasma samples were excluded due to a technical issue of poor NMR spectra resolution.

4.10. Immune and Hormonal Parameter Profiling

Rat interleukin (IL)-10, IL-1 α , interferon-gamma (IFN- γ), and tumor necrosis factor α (TNF α) protein levels were quantitatively measured by cytometric bead array flex sets (CBA) (BD Biosciences, San Diego, CA, USA) according to the manufacturer's protocol. Rat CXCL2, IL-1 β , leptin and C-reactive protein (CRP) (R&D Systems, Minneapolis, MN, USA), IL-6 (BioLegend, London, UK), lipopolysaccharide (LPS) binding protein (LBP) (Hycult Biotech, Uden, The Netherlands), and insulin (Crystal Chem Zaandam, The Netherlands) were quantified by enzyme-linked immunosorbent assay (ELISA) according to the manufacturer's protocol.

4.11. Liver Gene Expression

RNA was extracted from 10–25 mg of the frozen mortar-grounded liver using the RNeasy Plus Mini Kit (Qiagen, Hilden, Germany). Reverse transcription was performed with the GoTaq 2-Step RT-qPCR System according to the manufacturer's recommendation (Promega, Walldorf, Germany), and qPCR was run on a 480 LightCycler (Roche, Basel, Switzerland) with GoTaq qPCR Master Mix 2x (Promega, Walldorf, Germany) for several lipid metabolism-relevant genes and two housekeeping. As beta-actin appears to be highly variable and HPRT highly constant, we kept only HPRT amplification values for the calculation of delta Ct: gene expression values are given relative to this housekeeping gene. Primer sequences are provided in the following Table 1.

Table 1. Liver gene expression selected primer panel.

Primer Name	Target	Sequence
b-Act-F	beta-Actin	5'-ccc gcg agt aca acc ttc t-3'
b-Act-R	beta-Actin	5'-cgt cat cca tgg cga act-3'
HPRT-F	HPRT	5'-tag cac ctc ctc cgc cag-3'
HPRT-R	HPRT	5'-cac taa tca cga cgc tgg ga-3'
FAS-F	FAS	5'-ggc cac ctc agt cct gtt at-3'
FAS-R	FAS	5'-agg gtc cag cta gag ggt aca-3'
rFABP1-F	FABP1	5'-ctt ctc cgg caa gta cca ag-3'
rFABP1-R	FABP1	5'-ttc cct ttc tgg atg agg tc-3'
rLPL-1294-F	LPL	5'-aca gtg gct gag aac a-3'
rLPL-1445-R	LPL	5'-tct gac cag cta gga g-3'
PPARa-180-F	PPAR alpha	5'-CACAGCGTGGTGCATTGG-3'
PPARa-412-R	PPAR alpha	5'-GAGAGAGGACAGATGGGGCT-3'
SREBP1-F	SREBP1	5'-gta cag cgt ggc tgg gaa c-3'
SREBP1-R	SREBP1	5'-ggc tga gcg ata cag ttc aa-3'

4.12. Liver Fatty Acid Composition

Liver fat was extracted starting with 200 mg frozen mortar-grounded material in isopropanol-hexane (2:3 vol. with 0.01% BHT), followed by the addition of sodium sulfate and shaking overnight. After centrifugation, the hexane phase was removed and kept, and the rest was washed with isopropanol-hexane (7:2 vol., 0.01% BHT) by vortexing shortly and centrifuging (2000 rpm for 5 min). The pooled hexane phase was dried under nitrogen gas flow, and residual fat was weighed to determine the percentage of fat in liver tissue. Fatty acids were released and derivatized using acetyl chloride in methanol [93]. The composition of resulting fatty acid methyl esters (FAME) was analyzed by gas chromatography-mass spectrometry (Trace GC 1310 with TSQ Duo, Thermo Fischer Scientific, Waltham, MA, USA) using split injection (1:8) [94]. Briefly, FAME were separated on a 70% cyanopropyl column (TR-FAME, 60 m \times 0.25 mm \times 0.25 μ m, Thermo Fischer Scientific, Waltham, MA, USA) with helium carrier gas (1.2 mL/min) and the following temperature gradient: 50 $^{\circ}$ C (3 min)/50 > 140 $^{\circ}$ C (15 $^{\circ}$ C/min)/140 > 220 $^{\circ}$ C (3 $^{\circ}$ C/min)/220 > 250 $^{\circ}$ C (15 $^{\circ}$ C/min).

Individual FAME were identified and quantified using EI and SIM/Scan mode with time windows and internal calibration (one quantifier, up to two qualifiers).

4.13. Statistical Analysis

All statistics were performed with GraphPad Prism (version 9.2.0 for Windows, GraphPad Software, San Diego, CA, USA). A one-way or two-way analysis of variance (ANOVA) was conducted to examine differences in binding between groups, with a significance level set to $\alpha = 0.05$. Post hoc tests were performed using Tukey's honestly significant difference (HSD) test where appropriate. Statistical analysis for plasma and feces metabolites and correlations between feces, plasma metabolites, cytokines, microbiota, liver parameters were additionally performed using MetaboAnalyst 5.0 online platform [95]. Correlation testing between microbiota parameters, liver weight, fat content, and gene expression was performed using the Spearman test, correcting for multiple testing with the Benjamini–Hochberg test. Kruskal–Wallis test was used to identify differences between treatments for alpha-diversity and liver parameters using an R package.

Supplementary Materials: The following are available online at <https://www.mdpi.com/article/10.3390/ijms23031126/s1>.

Author Contributions: Conceptualization, C.N.B., K.H. and Y.R.; methodology, C.N.B., S.L., M.R.G., K.H., Y.R. and C.T.; formal analysis, L.Z., S.B., S.L., L.K., K.M., L.S. and I.M.; investigation, L.Z., C.N.B., S.B., L.K., K.M., L.S., M.R.G., K.H., Y.R. and C.T.; resources, C.N.B., S.L., R.K., M.R.G., K.H., Y.R. and C.T.; data curation, L.Z., S.B., S.L., K.M., L.S., R.K., I.M. and M.R.G.; writing—original draft preparation, L.Z., S.L., K.M., Y.R. and C.T.; writing—review and editing, L.Z., C.N.B., S.B., S.L., L.K., K.M., L.S., R.K., I.M., M.R.G., K.H., Y.R. and C.T.; visualization, L.Z., S.L., S.B., L.K., K.M., L.S. and M.R.G.; supervision, K.H., Y.R. and C.T. All authors have read and agreed to the published version of the manuscript.

Funding: This research was funded by the German Research Foundation (DFG), grant number RI 2360/2-1, to PI Yvonne Ritze.

Institutional Review Board Statement: All experimental procedures were performed in accordance with the European Union Directive 2010/63/EU on the protection of animals used for scientific purposes and were approved by the Regierungspraesidium Tuebingen (Tuebingen, Germany regional authorities approval, permit number MPV 3/16, issued 13.05.2019).

Informed Consent Statement: Not applicable.

Data Availability Statement: Sequencing data (16S RNA gene, fecal microbiota) will be available from the end of March 2022 on the ENA website (accession number PRJEB49286).

Acknowledgments: L.Z., S.B., L.K., K.H., Y.R. and C.T. would like to thank Bernd Pichler, Werner Siemens Imaging Center, and Werner Siemens Foundation for financial support and Tudor M. Ionescu for the help on brain imaging data analysis. We thank the people at Max Rubner-Institut: Dörte Wiedemann for the excellent performance of FAME analysis, Rebecca Seeger for great technical work and support on the investigation, and Andreas Dötsch for helpful bioinformatics support. L.Z. thanks Andres Eduardo Ortiz Ardila for the support and fruitful discussions. Art for the graphical abstract and Figure 1 is created with BioRender.com (accessed on 22 December 2021) and adapted from CC-BY SMART Servier Medical Art <http://smart.servier.com> (accessed on 22 December 2021), under CC-BY 3.0 license.

Conflicts of Interest: The authors declare no conflict of interest.

References

1. Yang, Y.-J.; Ni, Y.-H. Gut microbiota and pediatric obesity/non-alcoholic fatty liver disease. *J. Formos. Med. Assoc.* **2019**, *118*, S55–S61. [[CrossRef](#)]
2. Singer-Englar, T.; Barlow, G.; Mathur, R. Obesity, diabetes, and the gut microbiome: An updated review. *Expert Rev. Gastroenterol. Hepatol.* **2019**, *13*, 3–15. [[CrossRef](#)] [[PubMed](#)]
3. Pradhan, A.D.; Manson, J.E.; Rifai, N.; Buring, J.E.; Ridker, P.M. C-reactive protein, interleukin 6, and risk of developing type 2 diabetes mellitus. *JAMA-J. Am. Med. Assoc.* **2001**, *286*, 327–334. [[CrossRef](#)] [[PubMed](#)]

4. Jacka, F.N.; Cherbuin, N.; Anstey, K.J.; Sachdev, P.; Butterworth, P. Western diet is associated with a smaller hippocampus: A longitudinal investigation. *BMC Med.* **2015**, *13*, 215. [[CrossRef](#)]
5. Andersen, C.J.; Murphy, K.E.; Fernandez, M.L. Impact of Obesity and Metabolic Syndrome on Immunity. *Adv. Nutr.* **2016**, *7*, 66–75. [[CrossRef](#)] [[PubMed](#)]
6. Gaspar, J.M.; Baptista, F.I.; Paula Macedo, M.; Ambrosio, A.F. Inside the Diabetic Brain: Role of Different Players Involved in Cognitive Decline. *ACS Chem. Neurosci.* **2016**, *7*, 131–142. [[CrossRef](#)]
7. Hotamisligil, G.S. Inflammation, metaflammation and immunometabolic disorders. *Nature* **2017**, *542*, 177–185. [[CrossRef](#)]
8. Pinhel, M.A.S.; Noronha, N.Y.; Nicoletti, C.F.; Pereira, V.A.B.; de Oliveira, B.A.P.; Cortes-Oliveira, C.; Salgado, W., Jr.; Barbosa, F.; Marchini, J.S.; Souza, D.R.S.; et al. Changes in DNA Methylation and Gene Expression of Insulin and Obesity-Related Gene PIK3R1 after Roux-en-Y Gastric Bypass. *Int. J. Mol. Sci.* **2020**, *21*, 4476. [[CrossRef](#)]
9. Hu, F.B.; van Dam, R.M.; Liu, S. Diet and risk of Type II diabetes: The role of types of fat and carbohydrate. *Diabetologia* **2001**, *44*, 805–817. [[CrossRef](#)]
10. Di Rienzi, S.C.; Britton, R.A. Adaptation of the Gut Microbiota to Modern Dietary Sugars and Sweeteners. *Adv. Nutr.* **2020**, *11*, 616–629. [[CrossRef](#)]
11. Shalev, D.; Arbuckle, M.R. Metabolism and Memory: Obesity, Diabetes, and Dementia. *Biol. Psychiatry* **2017**, *82*, e81–e83. [[CrossRef](#)]
12. Graham, L.C.; Harder, J.M.; Soto, I.; de Vries, W.N.; John, S.W.M.; Howell, G.R. Chronic consumption of a western diet induces robust glial activation in aging mice and in a mouse model of Alzheimer’s disease. *Sci. Rep.* **2016**, *6*, 21568. [[CrossRef](#)]
13. Almby, K.E.; Lundqvist, M.H.; Abrahamsson, N.; Kvernby, S.; Fahlstrom, M.; Pereira, M.J.; Gingnell, M.; Karlsson, F.A.; Fanni, G.; Sundbom, M.; et al. Effects of Gastric Bypass Surgery on the Brain: Simultaneous Assessment of Glucose Uptake, Blood Flow, Neural Activity, and Cognitive Function During Normo- and Hypoglycemia. *Diabetes* **2021**, *70*, 1265–1277. [[CrossRef](#)]
14. Khayyat-zadeh, S.S.; Bagherniya, M.; Fazeli, M.; Khorasanchi, Z.; Bidokhti, M.S.; Ahmadinejad, M.; Khoshmohabbat, S.; Arabpour, M.; Afkhamizadeh, M.; Ferns, G.A.; et al. A Western dietary pattern is associated with elevated level of high sensitive C-reactive protein among adolescent girls. *Eur. J. Clin. Investig.* **2018**, *48*, e12897. [[CrossRef](#)] [[PubMed](#)]
15. Swinburn, B.A.; Sacks, G.; Hall, K.D.; McPherson, K.; Finegood, D.T.; Moodie, M.L.; Gortmaker, S.L. Obesity 1 The global obesity pandemic: Shaped by global drivers and local environments. *Lancet* **2011**, *378*, 804–814. [[CrossRef](#)]
16. World Health Organization. Obesity and Overweight. Available online: <https://www.who.int/news-room/fact-sheets/detail/obesity-and-overweight/> (accessed on 20 October 2021).
17. Apovian, C.M.; Aronne, L.J.; Bessesen, D.H.; McDonnell, M.E.; Murad, M.H.; Pagotto, U.; Ryan, D.H.; Still, C.D. Pharmacological Management of Obesity: An Endocrine Society Clinical Practice Guideline. *J. Clin. Endocrinol. Metab.* **2015**, *100*, 342–362. [[CrossRef](#)] [[PubMed](#)]
18. Bauer, K.; Lau, T.; Schwiller-Kiuntke, J.; Schild, S.; Hauner, H.; Stengel, A.; Zipfel, S.; Mack, I. Conventional weight loss interventions across the different BMI obesity classes: A systematic review and quantitative comparative analysis. *Eur. Eat. Disord. Rev.* **2020**, *28*, 492–512. [[CrossRef](#)]
19. Abdeen, G.; le Roux, C.W. Mechanism Underlying the Weight Loss and Complications of Roux-en-Y Gastric Bypass. Review. *Obes. Surg.* **2016**, *26*, 410–421. [[CrossRef](#)] [[PubMed](#)]
20. Lutz, T.A.; Bueter, M. The Use of Rat and Mouse Models in Bariatric Surgery experiments. *Front. Nutr.* **2016**, *3*, 25. [[CrossRef](#)]
21. Olivo, G.; Zhou, W.; Sundbom, M.; Zhukovsky, C.; Hogenkamp, P.; Nikontovic, L.; Stark, J.; Wiemerslage, L.; Larsson, E.M.; Benedict, C.; et al. Resting-state brain connectivity changes in obese women after Roux-en-Y gastric bypass surgery: A longitudinal study. *Sci. Rep.* **2017**, *7*, 6616. [[CrossRef](#)]
22. Näslund, E.; Melin, I.; Grybäck, P.; Hägg, A.; Hellström, P.M.; Jacobsson, H.; Theodorsson, E.; Rössner, S.; Backman, L. Reduced food intake after jejunoileal bypass: A possible association with prolonged gastric emptying and altered gut hormone patterns. *Am. J. Clin. Nutr.* **1997**, *66*, 26–32. [[CrossRef](#)]
23. Olbers, T.; Björkman, S.; Lindroos, A.; Maleckas, A.; Lönn, L.; Sjöström, L.; Lönroth, H. Body composition, dietary intake, and energy expenditure after laparoscopic Roux-en-Y gastric bypass and laparoscopic vertical banded gastroplasty: A randomized clinical trial. *Ann. Surg.* **2006**, *244*, 715–722. [[CrossRef](#)] [[PubMed](#)]
24. Zheng, H.; Shin, A.C.; Lenard, N.R.; Townsend, R.L.; Patterson, L.M.; Sigalet, D.L.; Berthoud, H.R. Meal patterns, satiety, and food choice in a rat model of Roux-en-Y gastric bypass surgery. *Am. J. Physiol. Regul. Integr. Comp. Physiol.* **2009**, *297*, R1273–R1282. [[CrossRef](#)] [[PubMed](#)]
25. Schauer, P.R.; Mingrone, G.; Ikramuddin, S.; Wolfe, B. Clinical Outcomes of Metabolic Surgery: Efficacy of Glycemic Control, Weight Loss, and Remission of Diabetes. *Diabetes Care* **2016**, *39*, 902–911. [[CrossRef](#)]
26. Schauer, P.R.; Bhatt, D.L.; Kirwan, J.P.; Wolski, K.; Aminian, A.; Brethauer, S.A.; Navaneethan, S.D.; Singh, R.P.; Pothier, C.E.; Nissen, S.E.; et al. Bariatric Surgery versus Intensive Medical Therapy for Diabetes—5-Year Outcomes. *N. Engl. J. Med.* **2017**, *376*, 641–651. [[CrossRef](#)]
27. Kwon, I.G.; Kang, C.W.; Park, J.P.; Oh, J.H.; Wang, E.K.; Kim, T.Y.; Sung, J.S.; Park, N.; Lee, Y.J.; Sung, H.J.; et al. Serum glucose excretion after Roux-en-Y gastric bypass: A potential target for diabetes treatment. *Gut* **2021**, *70*, 1847–1856. [[CrossRef](#)]
28. Saeidi, N.; Meoli, L.; Nestoridi, E.; Gupta, N.K.; Kvas, S.; Kucharczyk, J.; Bonab, A.A.; Fischman, A.J.; Yarmush, M.L.; Stylopoulos, N. Reprogramming of Intestinal Glucose Metabolism and Glycemic Control in Rats After Gastric Bypass. *Science* **2013**, *341*, 406–410. [[CrossRef](#)] [[PubMed](#)]

29. Cavin, J.B.; Couvelard, A.; Lebtahi, R.; Ducroc, R.; Arapis, K.; Voitellier, E.; Cluzeaud, F.; Gillard, L.; Hourseau, M.; Mikail, N.; et al. Differences in Alimentary Glucose Absorption and Intestinal Disposal of Blood Glucose After Roux-en-Y Gastric Bypass vs. Sleeve Gastrectomy. *Gastroenterology* **2016**, *150*, 454–464. [[CrossRef](#)]
30. Grayson, B.E.; Schneider, K.M.; Woods, S.C.; Seeley, R.J. Improved Rodent Maternal Metabolism but Reduced Intrauterine Growth after Vertical Sleeve Gastrectomy. *Sci. Transl. Med.* **2013**, *5*, 199ra112. [[CrossRef](#)]
31. Fernandes-Lima, F.; Monte, T.; Nascimento, F.A.D.; Gregorio, B.M. Short Exposure to a High-Sucrose Diet and the First ‘Hit’ of Nonalcoholic Fatty Liver Disease in Mice. *Cells Tissues Organs* **2015**, *201*, 464–472. [[CrossRef](#)]
32. Palleja, A.; Kashani, A.; Allin, K.H.; Nielsen, T.; Zhang, C.; Li, Y.; Brach, T.; Liang, S.; Feng, Q.; Jorgensen, N.B.; et al. Roux-en-Y gastric bypass surgery of morbidly obese patients induces swift and persistent changes of the individual gut microbiota. *Genome Med.* **2016**, *8*, 67. [[CrossRef](#)]
33. Liou, A.P.; Paziuk, M.; Luevano, J.-M., Jr.; Machineni, S.; Turnbaugh, P.J.; Kaplan, L.M. Conserved Shifts in the Gut Microbiota Due to Gastric Bypass Reduce Host Weight and Adiposity. *Sci. Transl. Med.* **2013**, *5*, 178ra41. [[CrossRef](#)]
34. Kirchner, H.; Nylen, C.; Laber, S.; Barres, R.; Yan, J.; Krook, A.; Zierath, J.R.; Naslund, E. Altered promoter methylation of PDK4, IL1 B, IL6, and TNF after Roux-en Y gastric bypass. *Surg. Obes. Relat. Dis.* **2014**, *10*, 671–678. [[CrossRef](#)]
35. Gupta, A.; Osadchiy, V.; Mayer, E.A. Brain-gut-microbiome interactions in obesity and food addiction. *Nat. Rev. Gastroenterol. Hepatol.* **2020**, *17*, 655–672. [[CrossRef](#)] [[PubMed](#)]
36. Luo, P.; Yu, H.; Zhao, X.; Bao, Y.; Hong, C.S.; Zhang, P.; Tu, Y.; Yin, P.; Gao, P.; Wei, L.; et al. Metabolomics Study of Roux-en-Y Gastric Bypass Surgery (RYGB) to Treat Type 2 Diabetes Patients Based on Ultraperformance Liquid Chromatography-Mass Spectrometry. *J. Proteome Res.* **2016**, *15*, 1288–1299. [[CrossRef](#)] [[PubMed](#)]
37. Cerreto, M.; Santopaolo, F.; Gasbarrini, A.; Pompili, M.; Ponziani, F.R. Bariatric Surgery and Liver Disease: General Considerations and Role of the Gut-Liver Axis. *Nutrients* **2021**, *13*, 2649. [[CrossRef](#)] [[PubMed](#)]
38. Seyfried, F.; Phetcharaburanin, J.; Glymenaki, M.; Nordbeck, A.; Hankir, M.; Nicholson, J.K.; Holmes, E.; Marchesi, J.R.; Li, J.V. Roux-en-Y gastric bypass surgery in Zucker rats induces bacterial and systemic metabolic changes independent of caloric restriction-induced weight loss. *Gut Microbes* **2021**, *13*, 1875108. [[CrossRef](#)]
39. Ha, J.; Kwon, Y.; Park, S. Metabolomics in Bariatric Surgery: Towards Identification of Mechanisms and Biomarkers of Metabolic Outcomes. *Obes. Surg.* **2021**, *31*, 4564–4574. [[CrossRef](#)] [[PubMed](#)]
40. Keller, A.; Della Torre, S.B. Sugar-Sweetened Beverages and Obesity among Children and Adolescents: A Review of Systematic Literature Reviews. *Child. Obes.* **2015**, *11*, 338–346. [[CrossRef](#)]
41. Ritze, Y.; Bárdos, G.; D’Haese, J.G.; Ernst, B.; Thurnheer, M.; Schultes, B.; Bischoff, S.C. Effect of High Sugar Intake on Glucose Transporter and Weight Regulating Hormones in Mice and Humans. *PLoS ONE* **2014**, *9*, e101702. [[CrossRef](#)] [[PubMed](#)]
42. Hao, Z.; Townsend, R.L.; Mumphy, M.B.; Morrison, C.D.; Munzberg, H.; Berthoud, H.-R. RYGB Produces more Sustained Body Weight Loss and Improvement of Glycemic Control Compared with VSG in the Diet-Induced Obese Mouse Model. *Obes. Surg.* **2017**, *27*, 2424–2433. [[CrossRef](#)]
43. Baheeg, M.; El-Din, M.T.; Labib, M.F.; Elgohary, S.A.; Hasan, A. Long-term durability of weight loss after bariatric surgery; a retrospective study. *Int. J. Surg. Open* **2021**, *28*, 37–40. [[CrossRef](#)]
44. Guo, Y.; Huang, Z.-P.; Liu, C.-Q.; Qi, L.; Sheng, Y.; Zou, D.-J. Modulation of the gut microbiome: A systematic review of the effect of bariatric surgery. *Eur. J. Endocrinol.* **2018**, *178*, 43–56. [[CrossRef](#)]
45. Cook, J.; Lehne, C.; Weiland, A.; Archid, R.; Ritze, Y.; Bauer, K.; Zipfel, S.; Penders, J.; Enck, P.; Mack, I. Gut Microbiota, Probiotics and Psychological States and Behaviors after Bariatric Surgery—A Systematic Review of Their Interrelation. *Nutrients* **2020**, *12*, 2396. [[CrossRef](#)] [[PubMed](#)]
46. Strandwitz, P.; Kim, K.H.; Terekhova, D.; Liu, J.K.; Sharma, A.; Levering, J.; McDonald, D.; Dietrich, D.; Ramadhar, T.R.; Lekbua, A.; et al. GABA-modulating bacteria of the human gut microbiota. *Nat. Microbiol.* **2019**, *4*, 396–403. [[CrossRef](#)]
47. Strandwitz, P. Neurotransmitter modulation by the gut microbiota. *Brain Res.* **2018**, *1693*, 128–133. [[CrossRef](#)]
48. Chen, O.; Mah, E.; Dioum, E.; Marwaha, A.; Shanmugam, S.; Malleshi, N.; Sudha, V.; Gayathri, R.; Unnikrishnan, R.; Anjana, R.M.; et al. The Role of Oat Nutrients in the Immune System: A Narrative Review. *Nutrients* **2021**, *13*, 1048. [[CrossRef](#)]
49. Krantis, A. GABA in the mammalian enteric nervous system. *News Physiol. Sci.* **2000**, *15*, 284–290. [[CrossRef](#)] [[PubMed](#)]
50. Inotsuka, R.; Uchimura, K.; Yamatsu, A.; Kim, M.; Katakura, Y. Gamma-Aminobutyric acid (GABA) activates neuronal cells by inducing the secretion of exosomes from intestinal cells. *Food Funct.* **2020**, *11*, 9285–9290. [[CrossRef](#)]
51. Auteri, M.; Zizzo, M.G.; Serio, R. The GABAergic System and the Gastrointestinal Physiopathology. *Curr. Pharm. Des.* **2015**, *21*, 4996–5016. [[CrossRef](#)] [[PubMed](#)]
52. Nicholson, J.K.; Holmes, E.; Kinross, J.; Burcelin, R.; Gibson, G.; Jia, W.; Pettersson, S. Host-Gut Microbiota Metabolic Interactions. *Science* **2012**, *336*, 1262–1267. [[CrossRef](#)]
53. Lagkouvardos, I.; Lesker, T.R.; Hitch, T.C.A.; Galvez, E.J.C.; Smit, N.; Neuhaus, K.; Wang, J.; Baines, J.F.; Abt, B.; Stecher, B.; et al. Sequence and cultivation study of Muribaculaceae reveals novel species, host preference, and functional potential of this yet undescribed family. *Microbiome* **2019**, *7*, 28. [[CrossRef](#)]
54. Rowland, I.; Gibson, G.; Heinken, A.; Scott, K.; Swann, J.; Thiele, I.; Tuohy, K. Gut microbiota functions: Metabolism of nutrients and other food components. *Eur. J. Nutr.* **2018**, *57*, 1–24. [[CrossRef](#)]

55. Wang, G.; Wang, Q.; Bai, J.; Zhao, N.; Wang, Y.; Zhou, R.; Kong, W.; Zeng, T.; Tao, K.; Wang, G.; et al. Upregulation of Intestinal NLRP6 Inflammasomes After Roux-en-Y Gastric Bypass Promotes Gut Immune Homeostasis. *Obes. Surg.* **2020**, *30*, 327–335. [[CrossRef](#)] [[PubMed](#)]
56. Zhu, Y.; Jameson, E.; Crosatti, M.; Schaefer, H.; Rajakumar, K.; Bugg, T.D.H.; Chen, Y. Carnitine metabolism to trimethylamine by an unusual Rieske-type oxygenase from human microbiota. *Proc. Natl. Acad. Sci. USA* **2014**, *111*, 4268–4273. [[CrossRef](#)]
57. Craciun, S.; Balskus, E.P. Microbial conversion of choline to trimethylamine requires a glyceryl radical enzyme. *Proc. Natl. Acad. Sci. USA* **2012**, *109*, 21307–21312. [[CrossRef](#)] [[PubMed](#)]
58. Chen, Y.-R.; Fang, S.-T.; Liu, H.-Y.; Zheng, H.-M.; He, Y.; Chen, Z.-W.; Chen, M.-X.; Zhang, G.-X.; Zhou, H.-W. Degradation of trimethylamine in vitro and in vivo by *Enterococcus faecalis* isolated from healthy human gut. *Int. Biodeterior. Biodegrad.* **2018**, *135*, 24–32. [[CrossRef](#)]
59. Liu, Y.; Dai, M. Trimethylamine N-Oxide Generated by the Gut Microbiota Is Associated with Vascular Inflammation: New Insights into Atherosclerosis. *Mediat. Inflamm.* **2020**, *2020*, 15. [[CrossRef](#)]
60. Yang, S.; Li, X.; Yang, F.; Zhao, R.; Pan, X.; Liang, J.; Tian, L.; Li, X.; Liu, L.; Xing, Y.; et al. Gut Microbiota-Dependent Marker TMAO in Promoting Cardiovascular Disease: Inflammation Mechanism, Clinical Prognostic, and Potential as a Therapeutic Target. *Front. Pharmacol.* **2019**, *10*, 1360. [[CrossRef](#)]
61. Rath, S.; Heidrich, B.; Pieper, D.H.; Vital, M. Uncovering the trimethylamine-producing bacteria of the human gut microbiota. *Microbiome* **2017**, *5*, 54. [[CrossRef](#)]
62. Wu, Q.; Li, J.V.; Seyfried, F.; le Roux, C.W.; Ashrafian, H.; Athanasiou, T.; Fenske, W.; Darzi, A.; Nicholson, J.K.; Holmes, E.; et al. Metabolic phenotype-microRNA data fusion analysis of the systemic consequences of Roux-en-Y gastric bypass surgery. *Int. J. Obes.* **2015**, *39*, 1126–1134. [[CrossRef](#)]
63. Siddik, M.A.B.; Shin, A.C. Recent Progress on Branched-Chain Amino Acids in Obesity, Diabetes, and Beyond. *Endocrinol. Metab.* **2019**, *34*, 234–246. [[CrossRef](#)]
64. White, P.J.; Lapworth, A.L.; An, J.; Wang, L.; McGarrah, R.W.; Stevens, R.D.; Ilkayeva, O.; George, T.; Muehlbauer, M.J.; Bain, J.R.; et al. Branched-chain amino acid restriction in Zucker-fatty rats improves muscle insulin sensitivity by enhancing efficiency of fatty acid oxidation and acyl-glycine export. *Mol. Metab.* **2016**, *5*, 538–551. [[CrossRef](#)]
65. Rosenzweig, A.; Blenis, J.; Gomes, A.P. Beyond the Warburg Effect: How Do Cancer Cells Regulate One-Carbon Metabolism? *Front. Cell Dev. Biol.* **2018**, *6*, 90. [[CrossRef](#)]
66. Alves, A.; Bassot, A.; Bulteau, A.-L.; Pirola, L.; Morio, B. Glycine Metabolism and Its Alterations in Obesity and Metabolic Diseases. *Nutrients* **2019**, *11*, 1356. [[CrossRef](#)] [[PubMed](#)]
67. Lim, P.S.; Chang, Y.-K.; Wu, T.-K. Serum Lipopolysaccharide-Binding Protein is Associated with Chronic Inflammation and Metabolic Syndrome in Hemodialysis Patients. *Blood Purif.* **2019**, *47*, 28–36. [[CrossRef](#)] [[PubMed](#)]
68. Parlesak, A.; Schaeckeler, S.; Moser, L.; Bode, C. Conjugated primary bile salts reduce permeability of endotoxin through intestinal epithelial cells and synergize with phosphatidylcholine in suppression of inflammatory cytokine production. *Crit. Care Med.* **2007**, *35*, 2367–2374. [[CrossRef](#)]
69. Lin, T.-L.; Shu, C.-C.; Chen, Y.-M.; Lu, J.-J.; Wu, T.-S.; Lai, W.-F.; Tzeng, C.-M.; Lai, H.-C.; Lu, C.-C. Like Cures Like: Pharmacological Activity of Anti-Inflammatory Lipopolysaccharides From Gut Microbiome. *Front. Pharmacol.* **2020**, *11*, 554. [[CrossRef](#)] [[PubMed](#)]
70. Whipp, A.M.; Vuoksimaa, E.; Korhonen, T.; Pool, R.; But, A.; Ligthart, L.; Hagenbeek, F.A.; Bartels, M.; Bogl, L.H.; Pulkkinen, L.; et al. Ketone body 3-hydroxybutyrate as a biomarker of aggression. *Sci. Rep.* **2021**, *11*, 5813. [[CrossRef](#)]
71. Ghoshal, S.; Witta, J.; Zhong, J.; de Villiers, W.; Eckhardt, E. Chylomicrons promote intestinal absorption of lipopolysaccharides. *J. Lipid Res.* **2009**, *50*, 90–97. [[CrossRef](#)] [[PubMed](#)]
72. Halinski, L.P.; Pakiet, A.; Jablonska, P.; Kaska, L.; Proczko-Stepaniak, M.; Slominska, E.; Sledzinski, T.; Mika, A. One Anastomosis Gastric Bypass Reconstitutes the Appropriate Profile of Serum Amino Acids in Patients with Morbid Obesity. *J. Clin. Med.* **2020**, *9*, 100. [[CrossRef](#)] [[PubMed](#)]
73. Kindt, A.; Liebisch, G.; Clavel, T.; Haller, D.; Hoermannsperger, G.; Yoon, H.; Kolmeder, D.; Sigrüener, A.; Krautbauer, S.; Seeliger, C.; et al. The gut microbiota promotes hepatic fatty acid desaturation and elongation in mice. *Nat. Commun.* **2018**, *9*, 3760. [[CrossRef](#)]
74. Weitkunat, K.; Schumann, S.; Nickel, D.; Hornemann, S.; Petzke, K.J.; Schulze, M.B.; Pfeiffer, A.F.H.; Klaus, S. Odd-chain fatty acids as a biomarker for dietary fiber intake: A novel pathway for endogenous production from propionate. *Am. J. Clin. Nutr.* **2017**, *105*, 1544–1551. [[CrossRef](#)]
75. Yang, X.; Sun, G.Y.; Eckert, G.P.; Lee, J.C.M. Cellular Membrane Fluidity in Amyloid Precursor Protein Processing. *Mol. Neurobiol.* **2014**, *50*, 119–129. [[CrossRef](#)]
76. Vlaeminck, B.; Fievez, V.; Cabrita, A.R.J.; Fonseca, A.J.M.; Dewhurst, R.J. Factors affecting odd- and branched-chain fatty acids in milk: A review. *Anim. Feed. Sci. Technol.* **2006**, *131*, 389–417. [[CrossRef](#)]
77. Fonteh, A.N.; Cipolla, M.; Chiang, J.; Arakaki, X.; Harrington, M.G. Human Cerebrospinal Fluid Fatty Acid Levels Differ between Supernatant Fluid and Brain-Derived Nanoparticle Fractions, and Are Altered in Alzheimer’s Disease. *PLoS ONE* **2014**, *9*, e100519. [[CrossRef](#)]
78. Lam, T.K.T.; Poci, A.; Gutierrez-Juarez, R.; Obici, S.; Bryan, J.; Aguilar-Bryan, L.; Schwartz, G.J.; Rossetti, L. Hypothalamic sensing of circulating fatty acids is required for glucose homeostasis. *Nat. Med.* **2005**, *11*, 320–327. [[CrossRef](#)] [[PubMed](#)]

79. Gonzalez-Hernandez, T.; Barroso-Chinea, P.; de la Cruz, M.A.P.; Valera, P.; Dopico, J.G.; Rodriguez, M. Response of gabaergic cells in the deep mesencephalic nucleus to dopaminergic cell degeneration: An electrophysiological and in situ hybridization study. *Neuroscience* **2002**, *113*, 311–321. [[CrossRef](#)]
80. Hankir, M.K.; Seyfried, F.; Miras, A.D.; Cowley, M.A. Brain Feeding Circuits after Roux-en-Y Gastric Bypass. *Trends Endocrinol. Metab.* **2018**, *29*, 218–237. [[CrossRef](#)]
81. Singh, Y.; Trautwein, C.; Dhariwal, A.; Salker, M.S.; Alauddin, M.; Zizmare, L.; Pelzl, L.; Feger, M.; Admard, J.; Casadei, N.; et al. DJ-1 (Park7) affects the gut microbiome, metabolites and the development of innate lymphoid cells (ILCs). *Sci. Rep.* **2020**, *10*, 16131. [[CrossRef](#)]
82. Bueter, M.; Abegg, K.; Seyfried, F.; Lutz, T.A.; le Roux, C.W. Gastric Bypass Operation in Rats. *J. Vis. Exp.* **2012**, *64*, e3940. [[CrossRef](#)]
83. Wehrl, H.F.; Hossain, M.; Lankes, K.; Liu, C.-C.; Bezrukov, I.; Martirosian, P.; Schickt, F.; Reischl, G.; Pichler, B.J. Simultaneous PET-MRI reveals brain function in activated and resting state on metabolic, hemodynamic and multiple temporal scales. *Nat. Med.* **2013**, *19*, 1184–1189. [[CrossRef](#)]
84. Schiffer, W.K.; Mirrione, M.M.; Biegon, A.; Alexoff, D.L.; Patel, V.; Dewey, S.L. Serial microPET measures of the metabolic reaction to a microdialysis probe implant. *J. Neurosci. Methods* **2006**, *155*, 272–284. [[CrossRef](#)]
85. Ionescu, T.M.; Amend, M.; Hafiz, R.; Biswal, B.B.; Wehrl, H.F.; Herfert, K.; Pichler, B.J. Elucidating the complementarity of resting-state networks derived from dynamic F-18 FDG and hemodynamic fluctuations using simultaneous small-animal PET/MRI. *Neuroimage* **2021**, *236*, 118045. [[CrossRef](#)]
86. Paxinos, G.; Watson, C. *The Rat Brain in Stereotaxic Coordinates*, 4th ed.; Academic Press: Cambridge, MA, USA, 1998.
87. Caporaso, J.G.; Lauber, C.L.; Walters, W.A.; Berg-Lyons, D.; Lozupone, C.A.; Turnbaugh, P.J.; Fierer, N.; Knight, R. Global patterns of 16S rRNA diversity at a depth of millions of sequences per sample. *Proc. Natl. Acad. Sci. USA* **2011**, *108*, 4516–4522. [[CrossRef](#)] [[PubMed](#)]
88. Walters, W.; Hyde, E.R.; Berg-Lyons, D.; Ackermann, G.; Humphrey, G.; Parada, A.; Gilbert, J.A.; Jansson, J.K.; Caporaso, J.G.; Fuhrman, J.A.; et al. Improved Bacterial 16S rRNA Gene (V4 and V4-5) and Fungal Internal Transcribed Spacer Marker Gene Primers for Microbial Community Surveys. *Msystems* **2016**, *1*, e00009-15. [[CrossRef](#)] [[PubMed](#)]
89. Kozich, J.J.; Westcott, S.L.; Baxter, N.T.; Highlander, S.K.; Schloss, P.D. Development of a Dual-Index Sequencing Strategy and Curation Pipeline for Analyzing Amplicon Sequence Data on the MiSeq Illumina Sequencing Platform. *Appl. Environ. Microbiol.* **2013**, *79*, 5112–5120. [[CrossRef](#)] [[PubMed](#)]
90. Callahan, B.J.; McMurdie, P.J.; Holmes, S.P. Exact sequence variants should replace operational taxonomic units in marker-gene data analysis. *ISME J.* **2017**, *11*, 2639–2643. [[CrossRef](#)]
91. McMurdie, P.J.; Holmes, S. phyloseq: An R Package for Reproducible Interactive Analysis and Graphics of Microbiome Census Data. *PLoS ONE* **2013**, *8*, e61217. [[CrossRef](#)]
92. Segata, N.; Izard, J.; Waldron, L.; Gevers, D.; Miropolsky, L.; Garrett, W.S.; Huttenhower, C. Metagenomic biomarker discovery and explanation. *Genome Biol.* **2011**, *12*, R60. [[CrossRef](#)]
93. Ecker, J.; Scherer, M.; Schmitz, G.; Liebisch, G. A rapid GC-MS method for quantification of positional and geometric isomers of fatty acid methyl esters. *Journal of chromatography. B. Anal. Technol. Biomed. Life Sci.* **2012**, *897*, 98–104. [[CrossRef](#)] [[PubMed](#)]
94. Gille, A.; Hollenbach, R.; Trautmann, A.; Gomez, M.R.; Kruger, R.; Bischoff, S.C.; Posten, C.; Briviba, K. Lipophilic compounds, but not fucoxanthin, mediate the genotoxic effect of photoautotrophic grown *Phaeodactylum tricoratum* in Caco-2 and HT-29 cells. *J. Funct. Foods* **2020**, *64*, 103671. [[CrossRef](#)]
95. Chong, J.; Wishart, D.S.; Xia, J. Using MetaboAnalyst 4.0 for Comprehensive and Integrative Metabolomics Data Analysis. *Curr. Protoc. Bioinform.* **2019**, *68*, e86. [[CrossRef](#)] [[PubMed](#)]

Supplementary Material

1. Supplementary figures S1 – S8
2. Supplementary tables ST1 – ST3

Roux-en-Y Gastric Bypass (RYGB) Surgery During High Liquid Sucrose Diet Leads to Gut Microbiota-Related Systematic Alterations

Laimdota Zizmare¹, Christina N. Boyle², Sabrina Buss¹, Sandrine Louis³, Laura Kuebler¹, Ketki Mulay⁴, Ralf Krüger³, Lara Steinhauer³, Isabelle Mack⁵, Manuel Rodriguez Gomez³, Kristina Herfert¹, Yvonne Ritze^{4,*}, Christoph Trautwein¹

¹Werner Siemens Imaging Center, Department of Preclinical Imaging and Radiopharmacy, Eberhard Karls University of Tübingen, University Hospital Tübingen, Röntgenweg 13, 72076, Tübingen, Germany;

² Institute of Veterinary Physiology, University of Zurich, Winterthurerstraße 260, CH-8057, Zurich, Switzerland;

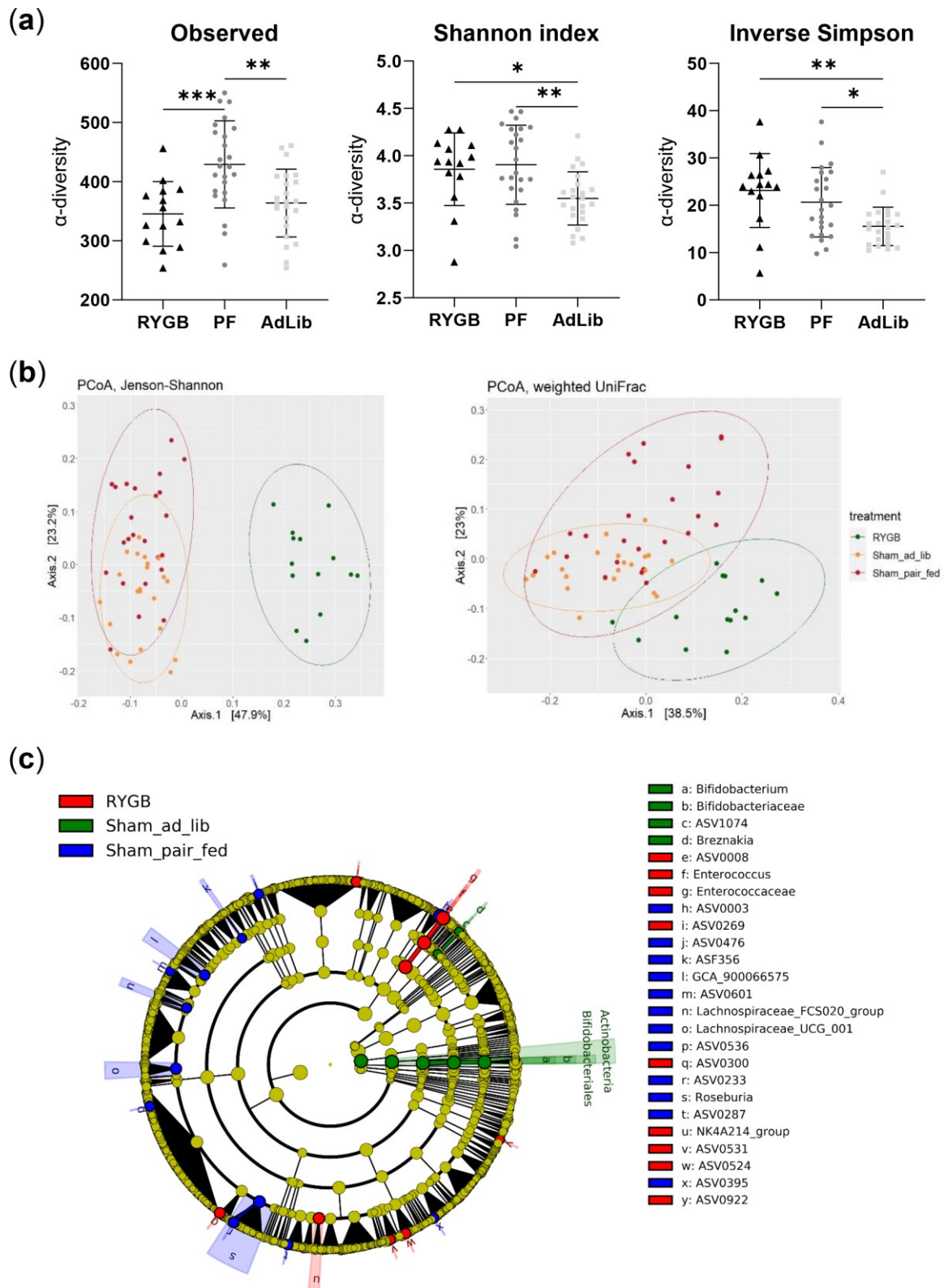
³ Department of Physiology and Biochemistry of Nutrition, Max Rubner-Institut, Haid-und-Neu-Straße 9, 76131, Karlsruhe, Germany;

⁴ Department of Medical Psychology and Behavioral Neurobiology, Eberhard Karls University of Tübingen, Silcherstraße 5, 72076, Tübingen, Germany;

⁵ Department of Psychosomatic Medicine and Psychotherapy, University Hospital Tübingen, Osianderstraße 5, 72076, Tübingen, Germany.

*Corresponding author: Yvonne Ritze, contact@yvonne-ritze.com.

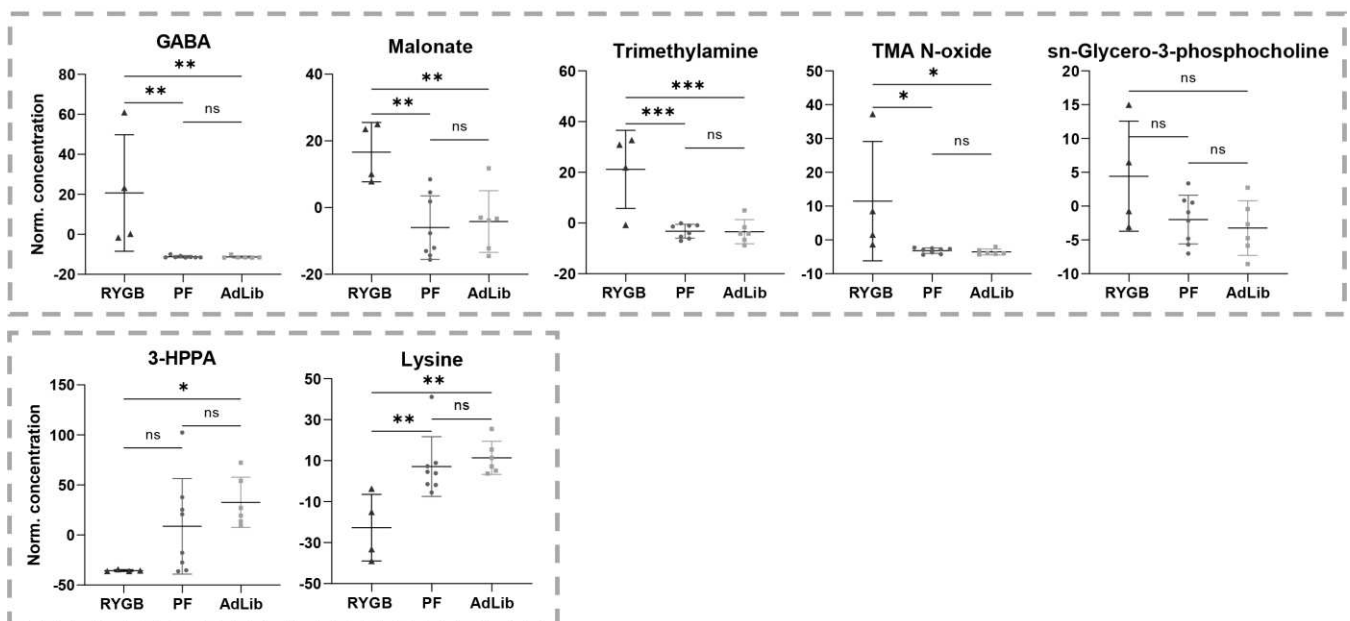
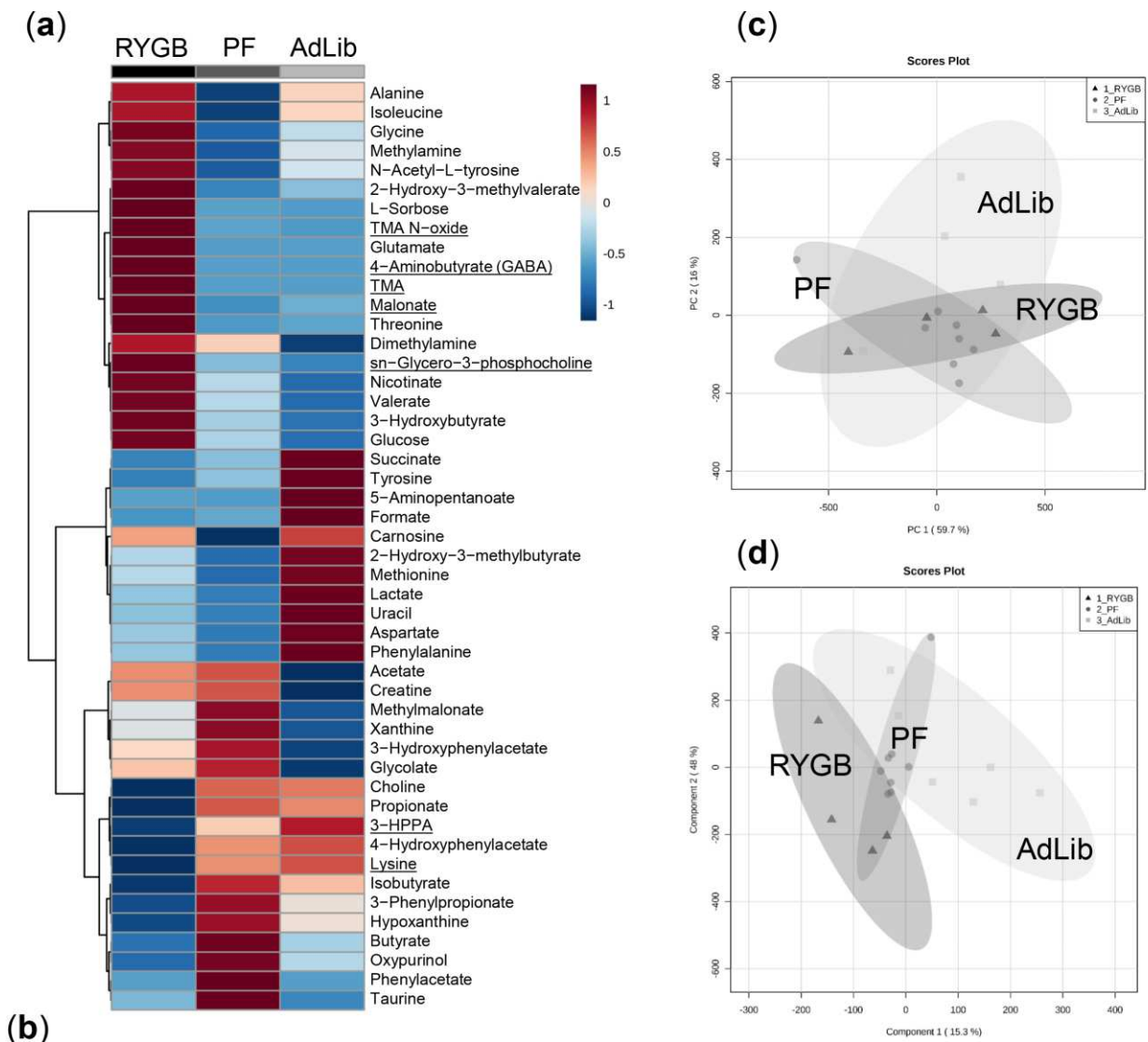
Supplementary Figure S1



Supplementary Figure S1: Microbiota analysis. (a) α -diversity, the microbial community in AdLib animals was less diverse than in the other groups (diversity as the observed number of species, Shannon index and inverse Simpson). (b) β -diversity, principal coordinate analysis

(PCoA) illustrating the separation of RYGB samples from the 2 other groups and showing the changes in the microbiota composition after surgery (PCoA based on either the Jenson-Shannon distance or the weighted UniFrac distance; each dot represents the whole gut microbiota from each animal at feces collection time). (c) LefSe analysis indicates the significant marker of each group represented in a phylogenetic cladogram. Pooled data was used from feces collection at four and eight weeks post-surgery, and at the day of euthanasia.

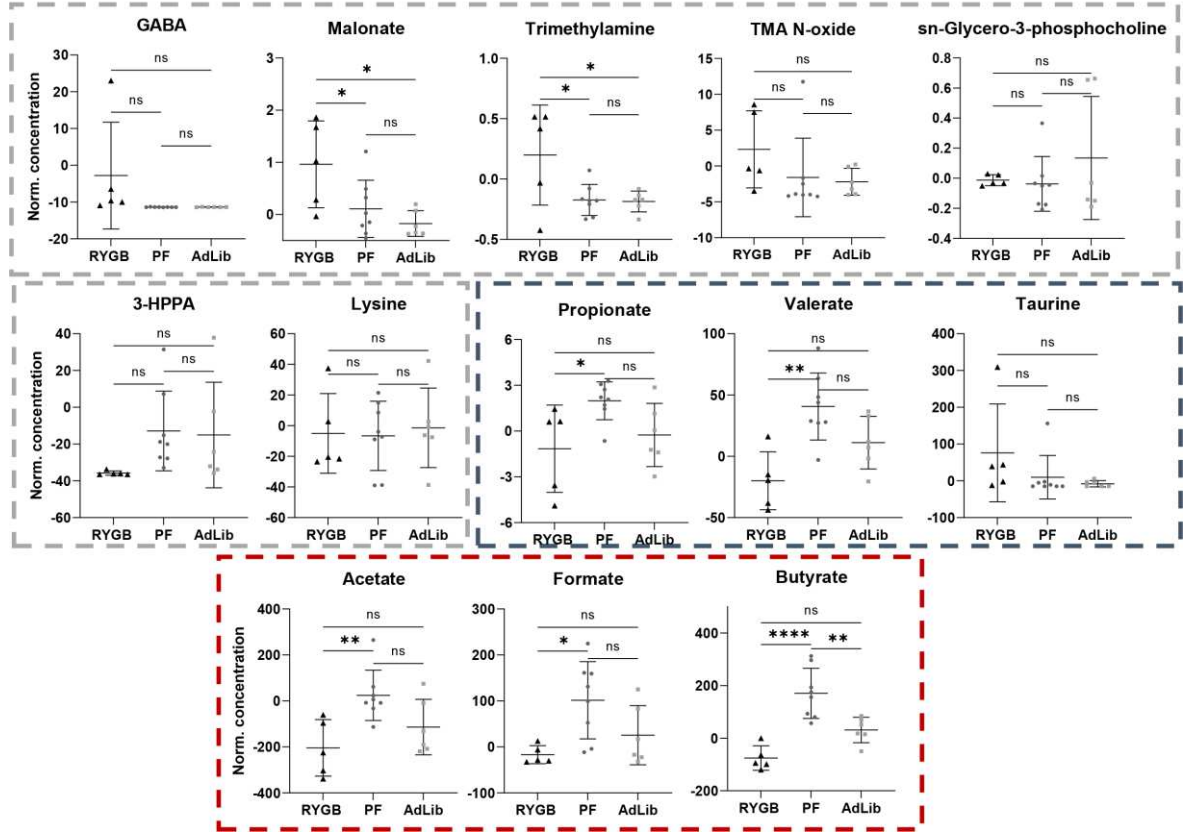
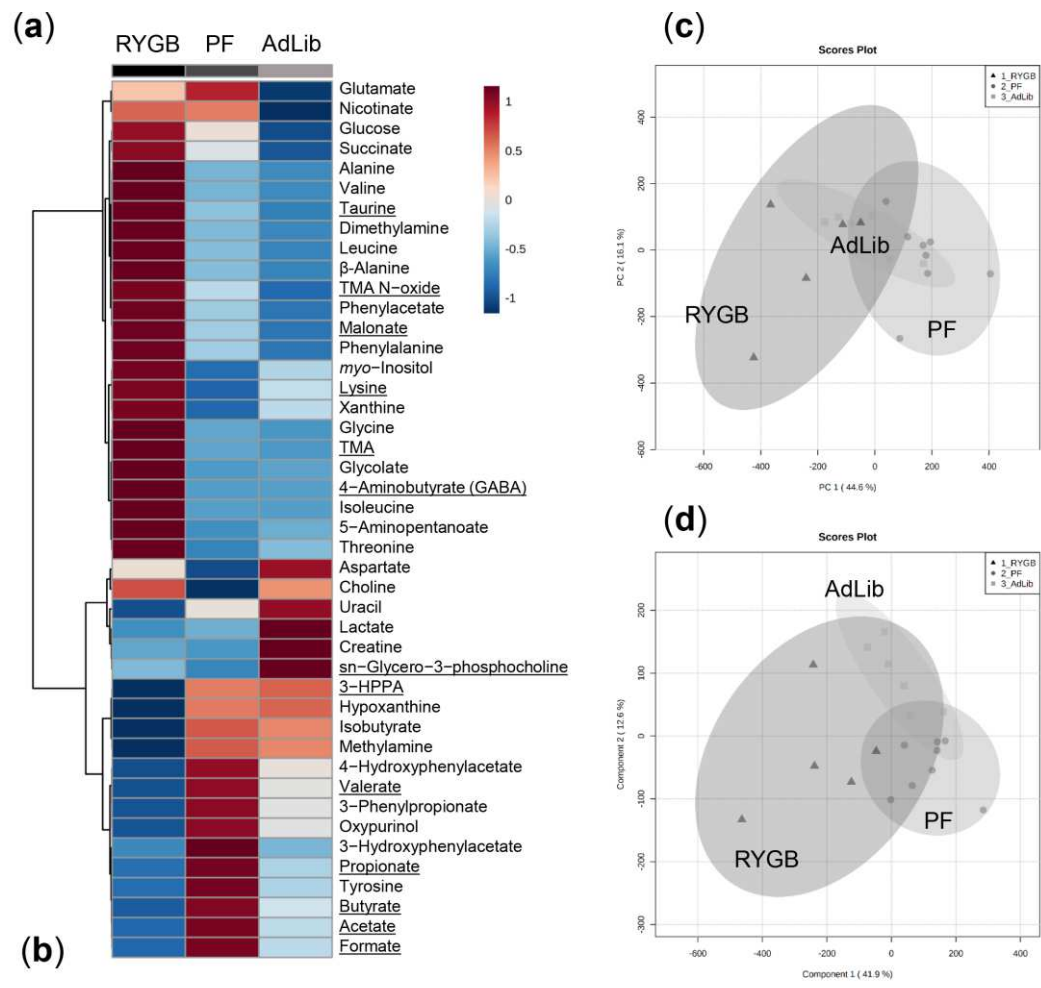
Supplementary Figure S2



Supplementary Figure S2: Feces metabolomics four weeks after RYGB/sham surgery.

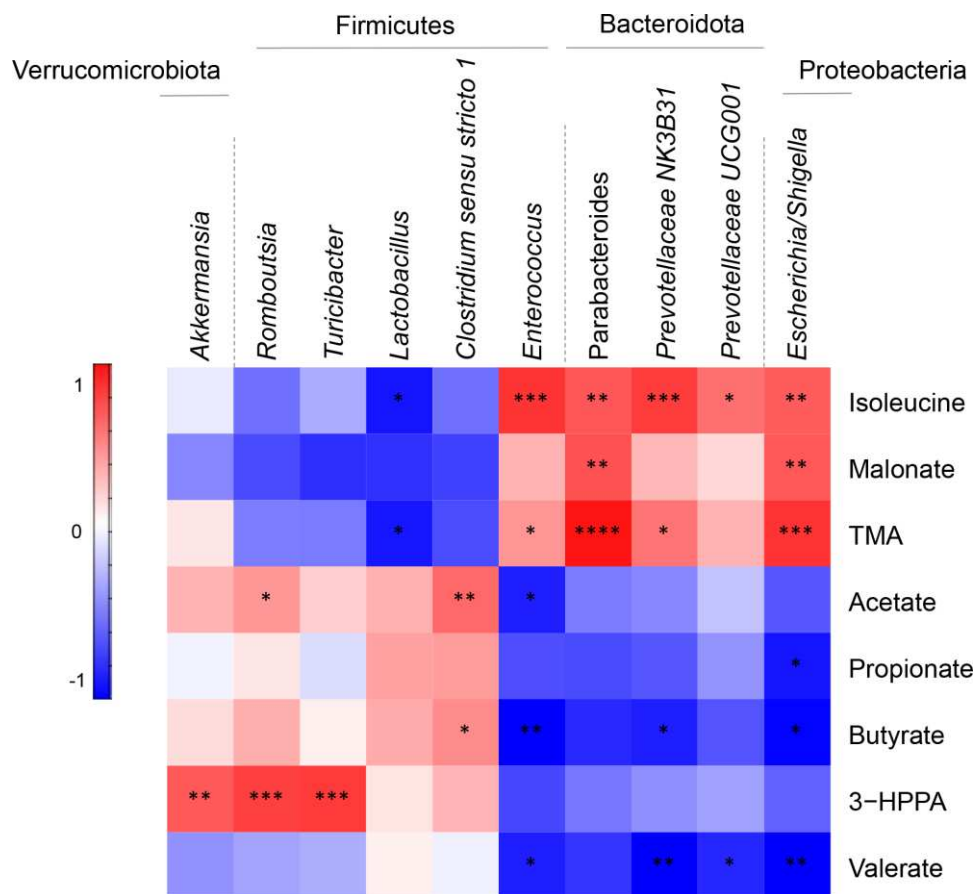
(a) Averaged heat map illustrating all the quantified feces metabolites with their relative concentration increase (red) or decrease (blue). (b) Individual metabolite box plots. Decreased 3-hydroxyphenylpropionate (3-HPPA) and lysine in RYGB. Increased 4-aminobutyrate (GABA), malonate, trimethylamine (TMA) and TMA N-oxide in RYGB. Statistical significance based on one-way ANOVA with illustrated individual animal data points. (c) Principal component analysis (PCA) of feces samples 4 weeks after surgery. (d) Partial least squares discriminant analysis (PLSDA) regression model illustrating the further group cluster separation. 95% confidence regions are illustrated as clouds around the individual data points. RYGB (n = 4) (one animal excluded due to technical limitation of poor spectra resolution) black triangles, PF (n = 8) dark grey circles, AdLib (n = 6) light grey squares, *p*-values: *** < 0.001, ** < 0.01, * < 0.05.

Supplementary Figure S3



Supplementary Figure S3: Metabolite analysis of feces collected on the day of euthanasia from the colon after RYGB/sham surgery. (a) Averaged heat map illustrating all the quantified feces metabolites with their relative concentration increase (red) or decrease (blue). (b) Individual metabolite box plots. Grey box – feces metabolite patterns since week 4. Blue box – feces metabolite changes introduced at week 8. Red box – novel metabolite changes in feces collected on the day of euthanasia: decreased acetate, formate and butyrate in RYGB. Statistical significance based on one-way ANOVA with illustrated individual animal metabolite concentration as points. (c) Principal component analysis (PCA) of feces samples 4 weeks after surgery. (d) Partial least squares discriminant analysis (PLSDA) regression model illustrating the further group cluster separation with the RYGB sample sparsity. 95% confidence regions are illustrated as clouds around the individual data points. RYGB (n = 5) black triangles, PF (n = 8) dark grey dots, AdLib (n = 6) light grey squares, *p*-values: **** < 0.0001, *** < 0.001, ** < 0.01, * < 0.05.

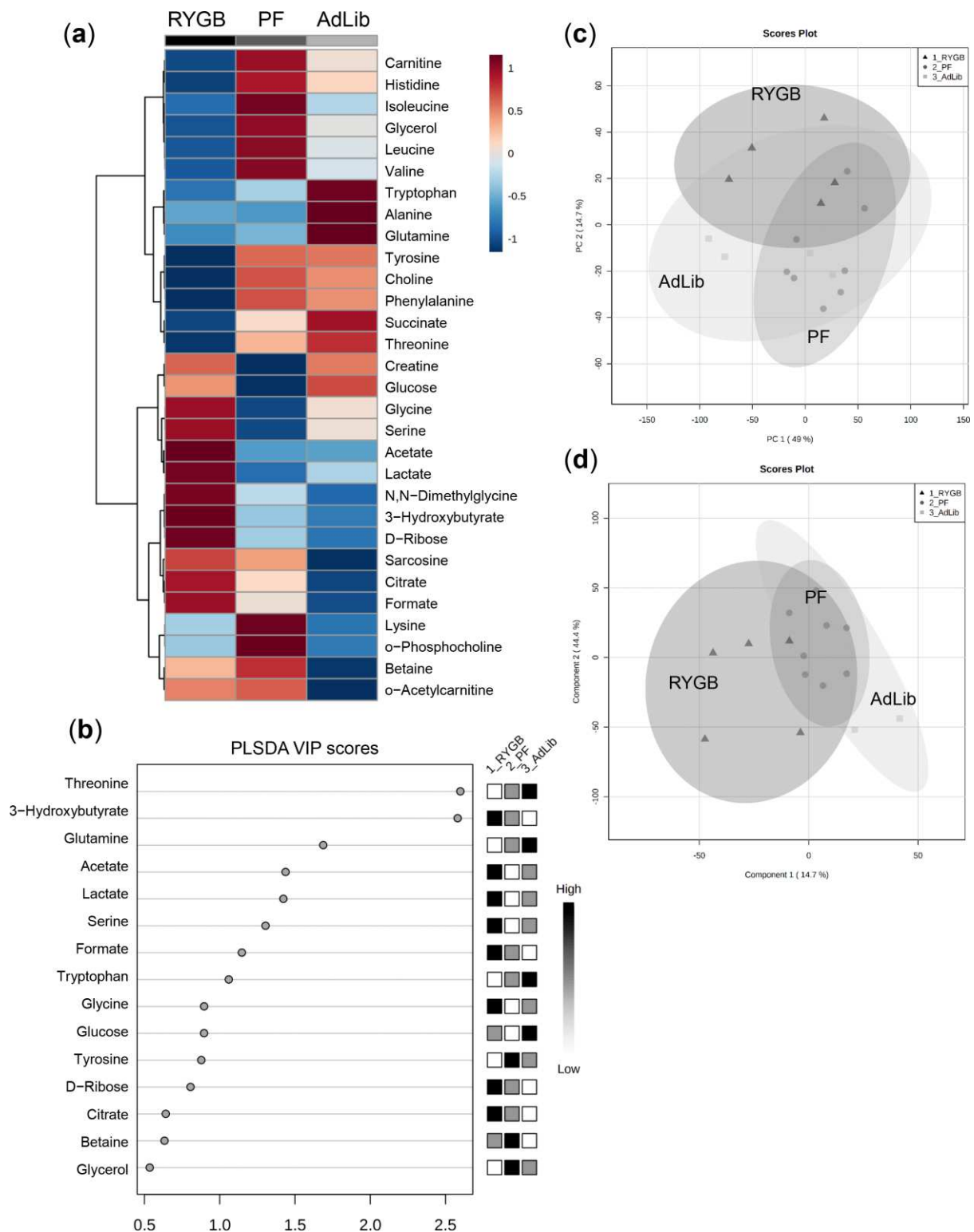
Supplementary Figure S4



Supplementary Figure S4: Feces microbiota and metabolomics correlation analysis.

Feces were collected directly from the colon on the day of euthanasia. 3-HPPA positively correlated with the relative abundance of *Turicibacter* and *Romboutsia*. TMA positively correlated with the relative abundance of *Escherichia/Shigella* and *Parabacteroides*. Isoleucine positively correlated with the relative abundance of *Prevotellaceae NK3B31* and *Enterococcus*. Color scheme illustrates the correlation values scaled between -1 and 1. Red color indicates a positive correlation, blue – negative correlation. Statistical significance of these correlations illustrated as *p*-values: **** < 0.0001, *** < 0.001, ** < 0.01, * < 0.05. Correlation analysis involves all three group (RYGB, PF and AdLib) feature values using Pearson r distance measure for the correlation coefficient determination.

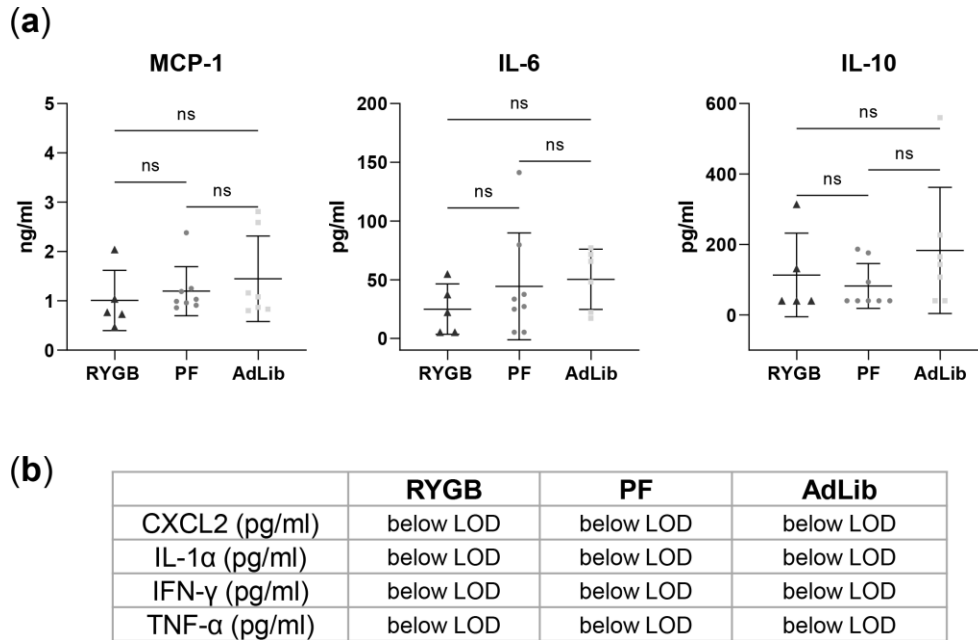
Supplementary Figure S5



Supplementary Figure S5: Plasma metabolomics. (a) Averaged group metabolite concentration heat map illustrating all the quantified plasma metabolites with their relative concentration increase (red) or decrease (blue). (b) Partial least squares discriminant analysis (PLSDA) variable importance in projection (VIP) scores visualisation of most changing

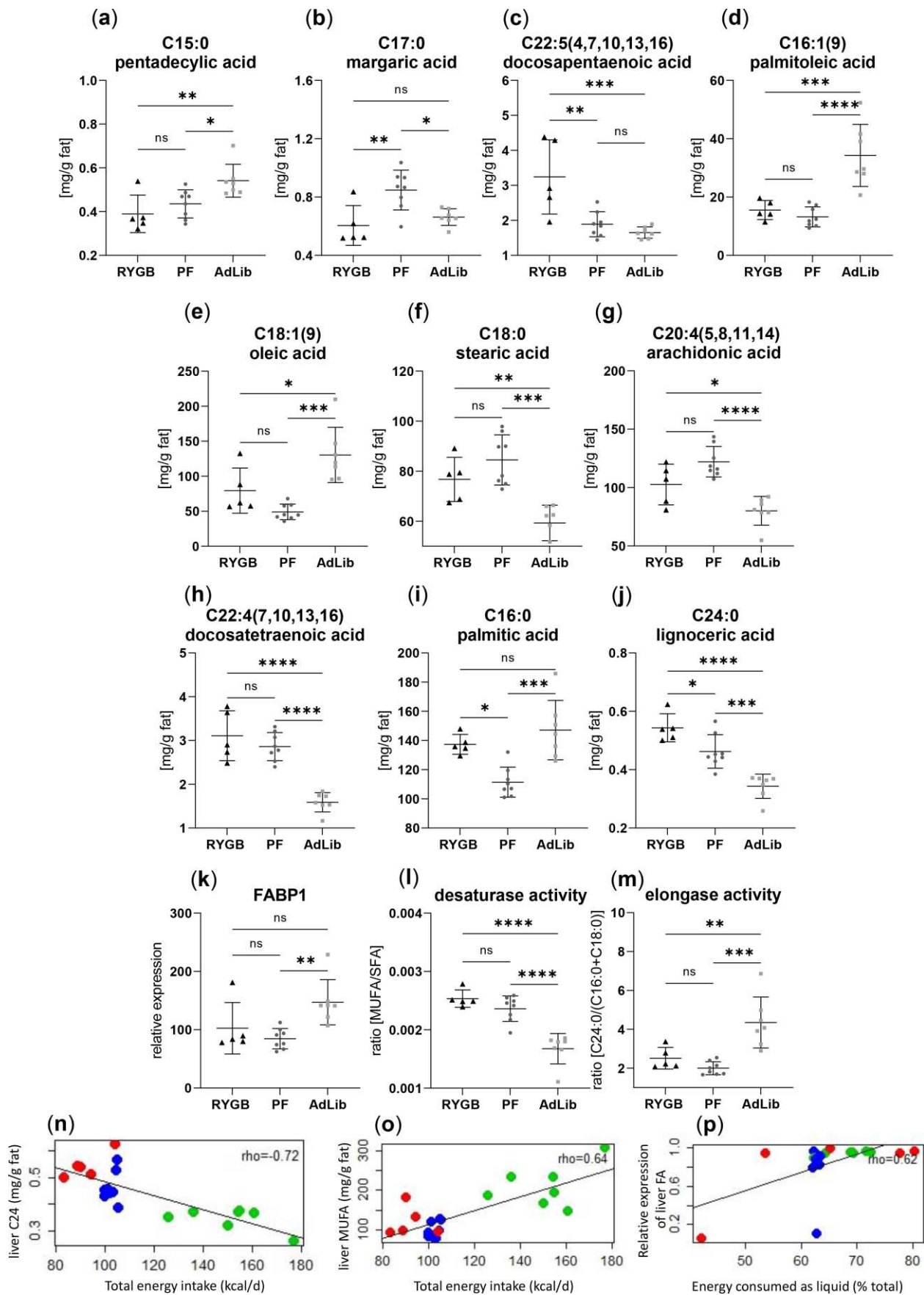
metabolites between the groups. **(c)** Principal component analysis (PCA) of plasma samples. **(d)** PLSDA regression model illustrating the further group cluster separation. 95% confidence regions are illustrated as clouds around the individual data points. RYGB (n = 5), PF (n = 8), AdLib (n = 6).

Supplementary Figure S6



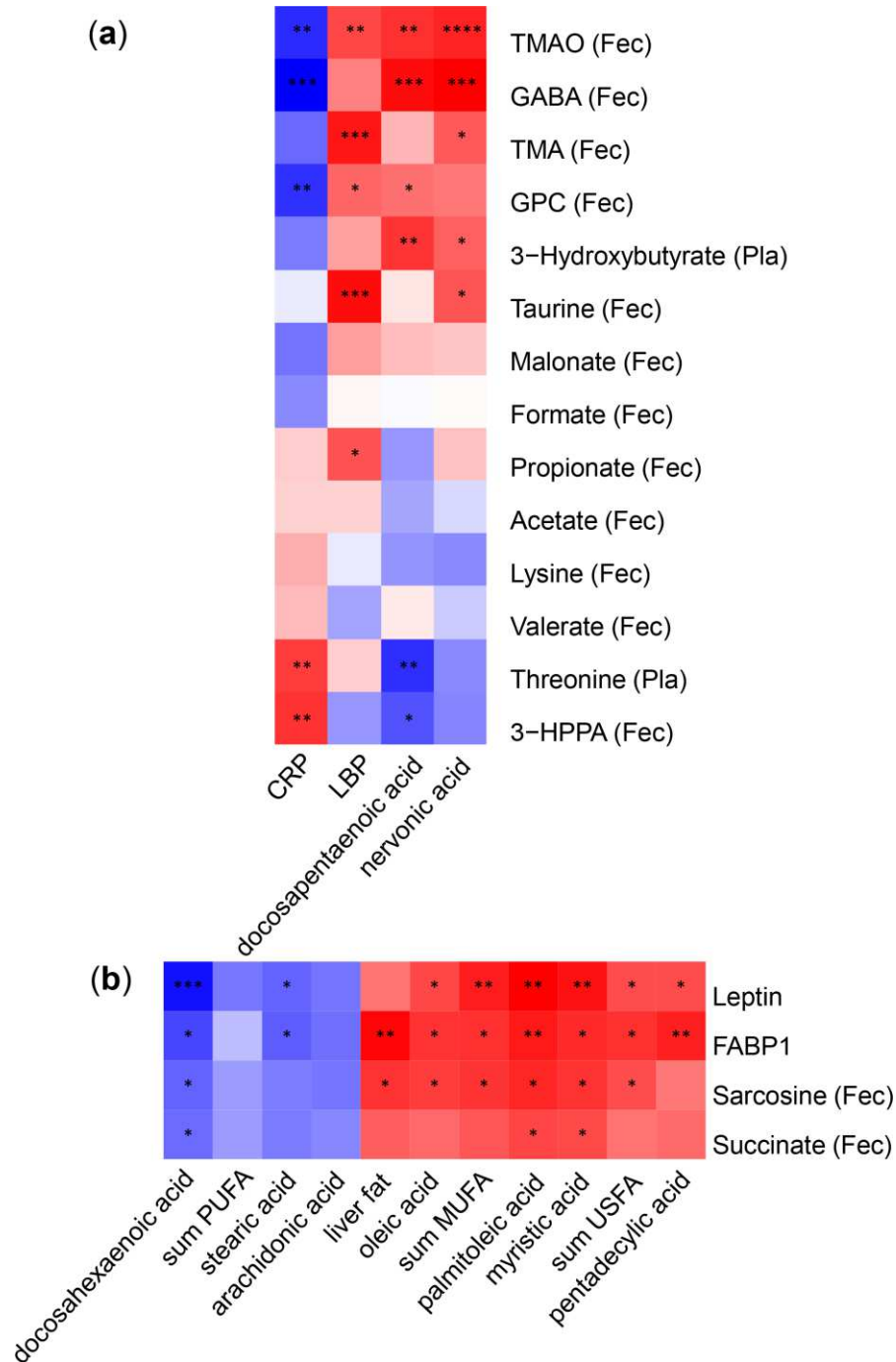
Supplementary Figure S6: Cytokine profiling of rat plasma. **(a)** Quantification of Monocyte Chemoattractant Protein-1 (MCP-1), Interleukin 6 (IL-6) and Interleukin 10 (IL-10), did not pass ordinary one-way ANOVA statistical significance threshold; **(b)** Chemokine ligand 2 (CXCL2), interleukin 1 α (IL-1 α), Interferon gamma (IFN- γ) and Tumour Necrosis Factor (TNF) were below the limit of detection (LOD). RYGB (n = 5) black triangles, PF (n = 8) dark grey dots, AdLib (n = 7) light grey squares.

Supplementary figure S7



Supplementary Figure S7: Hepatic lipid analysis. Mass concentrations (mg/g fat) of hepatic lipid species upregulated in AdLib C14:0 (**a**), C15:0 (**b**), C16:1(9) (**c**), C18:1(9) (**d**); downregulated in AdLib C18:0 (**e**); C20:4(5,8,11,14) (**f**), C22:4(7,10,13,16) (**g**); downregulated in RYGB C18:1(11) (**h**); upregulated in RYGB C22:5(4,7,10,13,16) (**i**), C24:1(15) (**j**); downregulated in AdLib and slightly downregulated in PF C24:0 (**k**); upregulated in PF C17:0 (**l**); downregulated in RYGB C18:1(11) (**m**) compared to the other two groups. One-way ANOVA statistical significance test, RYGB (n = 5) black triangles, PF (n = 8) dark grey dots, AdLib (n = 7) light grey squares, *p*-values: **** < 0.0001, *** < 0.001, ** < 0.01, * < 0.05. (**n**) Correlations between the total energy intake (kcal/d) versus liver C24:0 (mg/g fat) ($p=5.10^{-4}$; rho = -0.72) and (**o**) liver MUFA (mg/g fat) ($p=0.0029$; rho = 0.64); (**p**) correlation between the energy consumed as liquid (% total) versus relative expression of liver FAS ($p= 0.0038$; rho = 0.62). RYGB - red, PF - blue, AdLib - green.

Supplementary figure S8



Supplementary Figure S8: Correlation maps of metabolites, immune, hormonal and liver parameters. (a) Sham vs. RYGB comparison significantly differing parameters, C22:5(4,7,10,13,16) (docosapentaenoic acid (osbond acid), PUFA, omega-6), C24:1(15) (nervonic acid, MUFA), (b) parameters similar between PF and RYGB (reduced food intake) compared to AdLib, C22:4(7,10,13,16) (docosatetraenoic acid, PUFA, omega-6), C16:1(9) (palmitoleic acid, MUFA), C14:0 (myristic acid, SFA), C15:0 (pentadecylic acid, SFA), C16:1(9) (palmitoleic acid, MUFA), *p*-values: **** < 0.0001, *** < 0.001, ** < 0.01, * < 0.05.

Supplementary Tables

Bregma -1.80		RYGB	PF	AdLib	<i>p</i> -value
PVH	Middle	3.00±1.66	8.43± 4.55	5.50±2.88	0.44
CeC	Right	7.33±2.63	2.80±1.01	3.40±1.68	0.16
	Left	10.87±4.60	4.27±1.10	5.47±3.81	0.32
DeN	Right	2.07±1.18	0.93±0.43	2.53±1.28	0.48
	Left	1.20±0.45	0.83±0.40	6.07±2.34	0.02*
BLA	Right	1.27±1.32	1.67±1.26	3.60 ± 1.82	0.44
	Left	0.87±0.60	4.40±3.68	2.87 ±2.45	0.57
layer 2 of cortex	Right	2.00±1.97	14.87±11.63	7.30±3.74	0.39
	Left	2.33±2.25	11.93±9.01	9.73±6.02	0.48

Supplementary Table ST1: Average number of c-Fos labelled cells in different brain areas after eight weeks of high sucrose diet in rats Average numbers were analyzed by counting cells on 3 distinct slices (60 µm thick) for every region. Data were analyzed by ANOVA test followed by a Tukey's post hoc test ($p < 0.05$). Data are means ± SEM (n = 5). PVH – paraventricular hypothalamic nucleus; CeC – central amygdala; DeN – dorsal endopiriform nucleus; BLA – basolateral amygdaloid nucleus, anterior.

Bregma -1.80		RYGB	PF	AdLib	<i>p</i> -value
PVH	Middle	33.73±13.61	55.27± 22.14	35.07±10.10	0.51
CeC	Right	41.20±9.36	33.53±13.12	41.87±14.44	0.84
	Left	39.60±7.69	51.20±14.34	43.53±21.57	0.84
DeN	Right	123.40±23.86	124.53±24.11	91.93±19.55	0.26
	Left	122.87±25.44	159.30±7.05	132.67±32.02	0.48
BLA	Right	161.80±21.55	172.33±52.96	148.47±37.41	0.89
	Left	184.27±14.95	179.93±41.91	182.80±32.78	0.99
layer 2 of cortex	Right	338.67±27.05	314.77±38.82	339.20±37.31	0.82
	Left	318.53±17.72	372.63±30.71	263.13±59.22	0.14

Supplementary Table ST2: Average number of NeuN labeled cells in different brain areas after eight weeks of high sucrose diet in rats. Average numbers were analyzed by counting cells on 3 distinct slices (60 μ m thick) for every region. Data were analyzed by ANOVA test followed by a Tukey's post hoc test if significant (*P<0.05; n.s., non-significant). Data are means \pm SEM (n = 5). PVH – paraventricular hypothalamic nucleus; CeC – central amygdala; DeN – dorsal endopiriform nucleus; BLA – basolateral amygdaloid nucleus, anterior.

Bregma -1.80		Pair-fed	Ad-libitum	RYGB	p-value
PVH	Middle	4.47 \pm 2.74	2.93 \pm 1.78	2.10 \pm 1.25	0.65
CeC	Right	0.87 \pm 0.62	2.13 \pm 1.07	2.93 \pm 0.88	0.21
	Left	1.67 \pm 0.54	2.80 \pm 1.92	4.73 \pm 2.48	0.43
DeN	Right	0.93 \pm 0.43	1.13 \pm 0.83	0.73 \pm 0.38	0.86
	Left	0.60 \pm 0.36	3.87 \pm 2.05	0.40 \pm 0.30	0.08
BLA	Right	1.60 \pm 1.24	2.80 \pm 1.97	0.08 \pm 0.08	0.31
	Left	3.87 \pm 3.12	2.73 \pm 2.31	0.40 \pm 0.45	0.49
layer 2 of cortex	Right	14.60 \pm 11.57	4.33 \pm 3.48	2.00 \pm 1.97	0.36
	Left	11.60 \pm 8.73	7.13 \pm 6.38	2.27 \pm 2.27	0.53

Supplementary Table ST3: Average number of co-localized cells (labeled by both c-Fos and NeuN) in different brain areas after eight weeks of high sucrose diet in rats. Average numbers were analyzed by counting cells on 3 distinct slices (60 μ m thick) for every region. Data were analyzed by ANOVA test followed by a Tukey's post hoc test. Data are means \pm SEM (n = 5). PVH – paraventricular hypothalamic nucleus; CeC – central amygdala; DeN – dorsal endopiriform nucleus; BLA – basolateral amygdaloid nucleus, anterior.

4. Discussion

NMR spectroscopy-based metabolomics provides highly reproducible and quantitative information about the composition and status of a sample-specific metabolome at a specific point in time *ex vivo*, which can be relevant for elucidation and validations of *in vivo* imaging readout. Here, two application examples of inflammation and immunometabolism investigations by ¹H-NMR in the acute and chronic DTHR mouse model¹⁵⁴ and neuro-metabolism characterization in the RYGB surgery rat model¹⁵⁵ (Table 1) illustrate the use of such data to characterize in detail molecular events on the cellular level to be further lined with existing imaging modalities. These findings have a broad application potential towards not only metabolic imaging data correlation and elucidation but also novel diagnostic or therapeutic target discovery, as pathways and interactions identified are important markers for health maintenance or the course of a disease progression.

Table 1: Metabolomics overview of significant metabolite concentration changes and pathway alterations. (a) RYGB surgery feces (F) and plasma (P) metabolomics (blue) and (b) acute and chronic DTHR ear tissue (T) metabolomics (purple) studies, classified in super-pathways and sub-pathways. Only metabolites that had significant concentration changes are shown. Metabolites that are part of more than one metabolic pathway in this table have a grey cell background. Metabolites that overlap in both studies are colored green.

Super-pathway	Sub-pathway	Metabolites quantified by NMR (p<0.05)	Roux-en-Y gastric bypass (a)	Acute and chronic DTHR (b)
Amino acid	taurine & hypotaurine	taurine		T
	alanine, aspartate and glutamate	GABA	F	
		glutamate		T
		NAA		T
	glycine, serine, threonine	betaine	P	T
		serine	P	T
		glycine	P	T
		creatine	P	
	lysine	lysine	F	T
	phenylalanine & tyrosine	tyrosine	P	T
		3-HPPA	F	
	urea cycle, arginine, proline	proline		T
		arginine		T
		creatine	P	T
	valine, leucine, isoleucine (BCAA)	isoleucine	P	
		leucine	P	
valine		P	T	
β-alanine	β-alanine		T	

	glutathione	glutathione		T	
		GSSG		T	
		malonate	F		
Carbo-hydrate	glycolysis, gluconeogenesis	pyrimidine	5-oxoproline	T	
		glucose		T	
		acetate		T	
		pyruvate		T	
Lipid	glycerolipid		lactate	T	
		GPC	F	T	
	Glycerol-phospholipid		O-phosphoethanolamine		T
		inositol	myo-inositol		T
Energy	TCA cycle	ketone bodies	3-hydroxybutyrate	P	
			citrate		
			succinate		
		fumarate			
	OXPPOS	NAD ⁺		T	
Co-factors and vitamins	ascorbate and aldarate	ascorbate		T	
	nicotinate and nicotinamide	propionate	F		
		valerate	F		
		NAD ⁺		T	
Methanogenesis	methane	TMAO	F		
		TMA	F		
	methionine cycle	betaine	P	T	
	Trans-sulfuration pathway	serine	P		
glutathione			T		

4.1. Redox metabolism

NMR metabolomics of acute and chronic delayed-type hypersensitivity reaction (DTHR) challenged ear tissue revealed a distinctive immunometabolism of reactive oxygen and nitrogen species (RONS)-related metabolites (Table 1, a). Indeed, acute DTHR is characterized by neutrophil recruitment at the site of inflammation. These immune cells arrive via the bloodstream and they are responsible for RONS production. Tissue and blood vessel swelling are characteristic of both acute and chronic DTHR to accommodate immune cell infiltration and a molecular influx of substrates to the inflammation site. During acute DTHR, we identified glutathione and glutathione disulfide (GSSG, oxidized form) concentration changes, indicating altered RONS scavenging. Similarly, taurine consumption further indicated RONS activity and scavenging during the acute inflammatory phase ¹⁵⁴.

Further increase in macrophages and T cells, as confirmed by immunohistochemistry, is one of many systemic adaptations characterizing chronic DTHR. Chronic inflammation leads to further angiogenesis, increased fibrosis, higher vascularization

and therefore more connective tissue and further increased tissue swelling. While during acute DTHR, the liver could sufficiently produce the necessary glutathione for RONS scavenging, chronic DTHR possesses additional challenges, such as a lack of important substrates, arising from the prolonged inflammatory response. Thus, during chronic DTHR, additional RONS scavenging support was provided via increased ascorbate synthesis (Table 1, a), an important radical scavenger. Of note, while mice can produce ascorbate (vitamin C), humans cannot produce it and need to solely obtain it as vitamin C via nutrition ¹⁵⁶⁻¹⁵⁷.

We quantified both increased ascorbate and taurine concentrations during chronic DTHR at the 5th ear tissue challenge (48 h post 4th TNCB challenge), which were significantly reduced 4 hours after the 5th ear tissue challenge, during the peak of chronic DTHR (Table 1, a). Increased metabolite concentrations prior to the inflammatory peak indicated metabolomic adaptations on the systemic level as preparations for an upcoming challenge, specific to chronic inflammatory response ¹⁵⁴.

One of the reasons for the observed alterations in redox metabolism between acute and chronic DTHR is the availability of different metabolic substrates. Glutathione is a tripeptide, produced from three amino acids – glutamate, glycine and cysteine – in the presence of ATP. Glutathione production is a high-energy and substrate-demanding process involving cysteine and methionine cycles and transsulfuration pathway ¹⁵⁸. Indeed, we observed the consumption of several amino acid substrates – serine, glycine, pyroglutamate (5-oxoproline), arginine, and proline – during acute DTHR, which were continuously low during the chronic phase. As the inflammation progression leads to a dramatic depletion of substrates, we conclude that RONS scavengers which are demanding less substrate, such as ascorbate and taurine, are further systemically favored during chronic DTHR. Characterization of RONS activity and understanding metabolic adaptations of RONS scavenging is also important for investigations of tumor microenvironment function, adaptations and the development of effective tumor therapies ¹⁵⁹, providing a highly translational value of the dynamic inflammation progression dataset.

4.2. Energy metabolism

Many metabolites are involved in not only one but several metabolic pathways. This is especially the case within energy metabolism. For instance, previously described

amino acids serve as substrates for redox scavenger synthesis, however, some of them are also involved in general energy maintenance metabolic pathways (anaplerotic substrates for the TCA cycle). Redox pathways are highly energy consuming and therefore strictly dependent on ATP and NADPH generation by glycolysis and TCA cycle.

Our first investigated point in time during acute DTHR was 4 h post 1st tissue challenge (Table 1, a). Here, succinate accumulation was the most significant characteristic event indicating macrophage polarization-related disruption of regular TCA cycle function^{154, 160}. Consequently, during the acute inflammation peak^{152, 161}, 24 h post 1st trinitrochlorobenzene (TNCB) ear challenge, the hypothesis of a disrupted TCA cycle function is supported by the accumulation of the TCA cycle metabolites citrate and fumarate. Citrate accumulation has been linked to increased activity of the pentose phosphate pathway, responsible for nucleotide and NADPH production during high exposure to oxidative stress¹⁶⁰.

Pyruvate and lactate concentrations were also increased during acute DTHR, together with high glucose, confirming the loss of full TCA function while glycolysis is actively functioning. Furthermore, glucose, fumarate and glutamate concentrations were the most increased during chronic DTHR peak 4 h post-TNCB challenge, indicating a particular challenge of consuming these substrates when the inflammatory response is at its highest.

A disruption of the TCA cycle does not necessarily result in a complete cycle shutdown. Anaplerotic substrates, such as glutamate or branched chain amino acids, are able to feed the partially-functioning TCA cycle, e.g. as previously described as the mini-TCA cycle in neuronal tissue¹⁶², to carry out the necessary activity to maintain a continuous electron transport chain and OXPHOS in order to provide enough ATP energy for cell survival, proliferation and RONS scavenging²⁷.

We also investigated energy metabolism in the context of liver perfusion and transplantation in a preclinical rat model, where it is particularly important to sustain effective organ function during the ex vivo phase prior to transplantation (Supplementary Table 1, d). Similar to the DTHR inflammation study, here the TCA cycle disruption was characterized by accumulation of succinate in perfused liver tissue, while lactate, pyruvate and also succinate concentrations were increased in the

bile post-perfusion. We also quantified a reduction of glutamate in bile, as it could have been consumed as an alternative energy substrate ¹⁶⁴.

Concerning the mini-TCA cycle function, an accumulation of N-acetylaspartate (NAA) is expected as the end product of this cycle ¹⁶². During chronic DTHR, NAA concentration was significantly increased in the ear tissue compared to the naive ears and acute DTHR, indicating the cellular adaptations of chronic inflammation to continue oxidative phosphorylation despite disrupted TCA ¹⁵⁴. NAA in vivo is mainly considered a healthy tissue metabolite while its excretion indicates brain tissue damage. In a neuropediatric study investigating metachromatic leukodystrophy (MLD) patient urine metabolomics (Supplementary Table 1, e), increased levels of NAA were quantified in the early-onset MLD patient urine as one of the potential neurodegeneration markers ⁶². In a follow-up project, urine NAA in specific patient cases with progressive MLD condition were significantly negatively correlated with clinical MRI brain NAA ¹⁶⁵, demonstrating a direct inverse relation between brain and urine NAA. Such knowledge provides new perspectives for frequent biomonitoring of MLD patients e.g. during therapy, as NMR urine metabolomics is a high-throughput technique and different to MR scanners also less incriminatory to the pediatric patients. Furthermore, some literature also suggest a role of NAA outside the brain ¹⁶⁶, which is in line with our observation of NAA accumulation in the chronically inflamed ear tissues.

4.3. Membrane lipid synthesis and breakdown pathways

Another crucial aspect of metabolism that can be investigated by NMR spectroscopy-based metabolomics is the ethanolamine, inositol and choline-related cell membrane lipid homeostasis. We identified the acute DTHR peak at 24 h post 1st TNCB challenge and marked this with a high increase in glycerophosphocholine (GPC) and choline concentrations and significantly lowered myo-inositol concentrations (Table 1, a). While GPC and choline were restored in the chronic phase to baseline, myo-inositol was continuously reduced throughout chronic DTHR. Moreover, chronic DTHR was characterized by increased O-phosphoethanolamine concentrations compared to naive baseline and acute DTHR ¹⁵⁴. Here, we could observe a switch in the Kennedy pathway involving the synthesis and breakdown of membrane lipids. Esmaeili, M. *et al.*, in 2014 underlined that choline – ethanolamine pathway alterations are important

markers for rapidly growing and expanding cell environments, similar in the case with tumors ⁴⁵. Further, O-phosphoethanolamine accumulation has been also reported together with a lowered inflammatory response and mitochondrial respiration in an M1 macrophage study ⁹³, highlighting the metabolic connectivity and far-reaching effects of RONS activity and inflammation.

4.4. Identical metabolites but different conditions

Of note, several metabolic pathways are altered and play a role in different disease conditions, e.g. altered glucose metabolism is characteristic both for diabetes and also cancer. In our research, alterations in membrane lipid buildup and degradation have been described for inflammatory progression and a switch between acute and chronic DTHR has been observed (Table 1, a). However, significant changes in membrane lipid-related metabolite activity have been also characterized in the second thesis project focusing on the RYGB surgery outcome and impact on the metabolomic readout (Table 1, b).

Herein, GPC and choline were highly concentrated in the animal feces compared to pair-fed and ad libitum-fed animal feces of RYGB surgery animals ¹⁵⁵. Feces as a matrix for metabolomics investigations is tightly connected to the activity of the gut microbiome. Hence, we could speculate that the reason for the accumulation of these two specific metabolites in the case of RYGB surgery animals is due to the alterations in the abundance of specific microbiota species and the consecutive animal lack of absorption of nutrients ¹⁶⁷ as a consequence of the surgery.

4.5. Ketone bodies and metabolomics

Both metabolomics studies – acute and chronic DTHR and RYGB surgery – displayed energy metabolism adaptations as well as an increase in ketone bodies (Table 1, a – b). 3-Hydroxybutyrate is normally produced in the liver as a result of lipolysis triggered by empty glycogen stocks. Acute DTHR showed increased 3-hydroxybutyrate concentrations in the TNCB-challenged ear tissue, potentially as a result of a lack of glucose. Hence 3-hydroxybutyrate production indicates a switch to an alternative energy production pathway when there is a lack of carbohydrate sources to maintain glycolysis ¹⁶⁸.

In the context of RYGB surgery, we quantified increased plasma 3-hydroxybutyrate concentration, a marker for fasting and low glycogen stocks, as it is an energy source for acetyl-CoA production and beta-oxidation in case of glucose depletion ¹⁶⁹. 3-hydroxybutyrate is a product of liver lipolysis and hence upregulated lipolysis can lead to weight loss, together with low nutrient absorption, which has been also reported in clinical bypass surgery patients ¹⁷⁰.

Glucose deprivation-related ketogenesis and upregulated fatty acid metabolism is commonly observed in highly catabolic and anabolic active tissues and biofluids. This fits in line with liver perfusion effect investigatory work, where significantly increased 3-hydroxybutyrate concentrations were shown in perfused livers compared to native tissues (Supplementary Table 1, d) ¹⁶⁴. Moreover, MLD patient urine metabolomics revealed increased ketone bodies, including 3-hydroxybutyrate and acetone as a result of impaired liver and renal function during the early onset of the disease (Supplementary Table 1, e) ¹⁶⁴.

Together, 3-hydroxybutyrate demonstrates how one specific metabolite can hint towards a specific pathway activity in different diseases and conditions, including alterations of energy metabolism in the liver or inflamed tissue, and serve as a marker in circulating bloodstream and even excreted in the urine. A wide range of neurological health benefits of 3-hydroxybutyrate has been discussed in the literature, focusing on the preservation of tissue during inflammation, defense during insulin-induced hypoglycemia, and the beneficial effects of a ketogenic diet ¹⁷¹.

4.6. One-carbon metabolism: folate and methionine cycle

Besides the maintenance of redox defense, one-carbon metabolism is crucial for many physiological activities, including amino acid homeostasis and purine biosynthesis. It is also a commonly used pathway by developmental cells and therefore often dysregulated and hijacked during tumor progression ¹⁷². Glycine, serine and threonine metabolism is a crucial part of the one-carbon metabolism, providing valuable amino acid substrates.

Plasma serine and glycine concentrations in RYGB surgery animals were increased compared to pair-fed and ad libitum-fed animal groups (Table 1, b). Of note, reduction of serine and glycine pools have been reported in obese and type-2 diabetes patients ¹⁷³. Therefore, increased pools of circulating amino acids point towards a beneficial

surgery outcome. Alterations in amino acid concentrations have been also linked to tumor ability to employ and dysregulate one-carbon metabolism in its benefit to sustain the malignant proliferation and activity via oncogenic signaling ¹⁷⁴. In particular, serine and glycine concentrations have been shown to decrease in IDH-1 mutated gliomas, compared to wildtype gliomas (Supplementary Table 1, c) ⁶⁹, indicating specific mutation capability to dysregulate amino acid usage and general availability.

4.7. Gut microbiota, dysbiosis and metabolomics

Radical alterations in microbiota abundances of RYGB surgery animals lead to an altered microbiota-related metabolite production. Together with glycine, an increase of branched-chain amino acids (BCAA) valine, leucine and isoleucine in the circulating blood plasma are considered negative markers for some diseases, such as insulin resistance and diabetes ¹⁵⁵. Hence our observation of BCAA reduction in RYGB surgery animals compared to control groups (Table 1, b), also observed in a clinical setting ¹⁷⁵, can be seen as a positive surgery outcome. BCAA are not only an energy substrate but also important structural building blocks of proteins ¹⁷⁶ and involved in molecular signaling pathways ¹⁷⁷. As BCAA are produced and degraded by the gut microbiota, characterization of host-microbiome interactions is of great interest for novel therapeutic targets that could be altered via diet ¹⁴⁴.

Host-microbiome interactions and gut microbiota-related alterations in metabolism are involved in the progression of several other neurological diseases, such as Parkinson's disease ¹⁷⁸⁻¹⁷⁹ and Alzheimer's disease ¹⁸⁰⁻¹⁸¹. For example, several adverse molecular events arise from the lack of Parkinson's disease-related protein 7 (protein deglycase DJ-1) (Supplementary table 1, f) ⁵¹. DJ-1 knockout results in an altered microbiome and significantly reduced valine, leucine and isoleucine (BCAA) concentrations both in animal plasma and feces. Lowered BCAA levels hence point towards microbiota alterations that lead to neurodegenerative effects and dysfunctional gastrointestinal processes ¹⁸². In fact, BCAA supplementation has been suggested for neurodegenerative disease patients ¹⁸³, however, the long-term efficacy and true therapeutic effects of such supplementation are yet to be investigated. Moreover, the gut microbiota has an influence on metabolic readout beyond BCAA.

Further, we quantified increased 3-(3-hydroxyphenyl) propionate (3-HPPA) and GABA in RYGB surgery animal feces as two potential gut microbiota-related neurological

activators post-RYGB surgery (Table 1, b). 3-HPPA has been previously reported as a potential competitive inhibitor in dopamine synthesis pathway⁵¹ and to have an inhibitory effect on atherosclerosis progression¹⁸⁴. Meanwhile, increased GABA concentrations indicate potentially increased gut-brain signaling via GABAergic¹⁸⁵ and enteric nervous systems¹⁸⁶.

Finally, microbiota-originating fecal trimethylamine (TMA) and TMA N-oxide (TMAO) increase in RYGB animal feces indicated rapid choline and carnitine degradation (Table 1, b). TMAO has been previously linked to endothelial inflammation and cardiovascular risk¹⁸⁷, and, therefore, could be seen as a negative outcome of the RYGB surgery. TMA has been also reported to increase in Parkinson's disease DJ-1 gene knockout mice plasma (Supplementary table 1, f)⁵¹ and MLD patient urine as a sign of disease-related leaky gut (Supplementary table 1, e)⁶². TMA concentration change examples in different studies illustrate how a specific gut microbiota-originated metabolite can lead to systemic effects and be transferred from the gut to other biofluids and tissues.

4.8. Conclusions and outlook

The novelty of this doctoral thesis includes aspects of both the analytical setup and scientific output levels. NMR spectroscopy-based metabolomics was employed with an ultra-sensitive 1.7 mm probe that requires generally less sample material compared to conventional approaches. This allows us to characterize different preclinical and limited clinical-origin specimens which were not amenable to NMR before. Therefore, comprehensive metabolite datasets were obtained and analyzed in two example studies, that have been previously identified as of high relevance for preclinical metabolic imaging. A broad insight was provided into different metabolic pathways depending on the sample matrix and disease condition.

In the DTHR model study for inflammation progression, unique metabolic events were characterized for specific points in time in accordance with imaging data of acute and chronic inflammatory peaks. For the first time, we present DTHR metabolic alterations on the longitudinal scale which helps to understand the complex dynamics of metabolism and immune-cell infiltration. The most important findings include oxidative stress-related metabolic events leading to a switch between glutathione as the preferred scavenger substrate during the acute phase, while taurine and ascorbate

activity was characteristic during chronic DTHR. Some metabolites, including tryptophan, hypotaurine, ATP followed taurine metabolic pattern of increased concentrations prior to the chronic DTHR peak. The identified metabolites could be of future interest as targets for diagnostic radiotracer development, as well as interventional drug discovery. Furthermore, existing large imaging data sets of previous DTHR cohorts could be used for extended metabolite activity mapping. Finally, as immune cells obtain their metabolic substrates directly from the bloodstream, future investigations could try to assess the impact of the blood serum metabolome upon the different stages of acute and chronic inflammation.

In the RYGB surgery study, the gut-brain axis communication was hypothesized to be triggered by a successful surgery outcome. While surgery provokes adverse systemic long-term effects, there is a need to further investigate possibilities of therapeutic development that could mimic the surgery effect, but allow avoiding the invasive procedure. We found increased concentrations of the gut-produced metabolites GABA and 3-HPPA. Altered brain neuronal activity in the hypothalamus and midbrain regions was identified by metabolically-active tissue tracer uptake imaging of [¹⁸F]FDG-PET. As these brain areas are reported to be GABAergic cell-rich, our preliminary results point towards promising metabolically-quantifiable substrates which should be further explored in detail to fully elucidate their role and mode of action. Especially the investigation of how a manipulated gut microbiome which lacks GABA-producing microbiota, affects the surgery outcome, remains to be elucidated.

Overall, this thesis project demonstrates high-resolution NMR spectroscopy metabolomics ability to generate additional layers of metabolic information from different specimens. This can help to better interpret low-resolution imaging data and opens new perspectives towards diagnostics, therapeutics and mechanistic investigations in preclinical research and its translation to humans.

5. References

1. Freidel, L.; Li, S.; Choffart, A.; Kuebler, L.; Martins, A. F., *Imaging Techniques in Pharmacological Precision Medicine*. Springer: Berlin, Heidelberg, **2023**.
2. Trautwein, N. F.; Reischl, G.; Seitz, C.; Dittmann, H.; Seith, F.; Scheuermann, S.; Feuchtinger, T.; Dombrowski, F.; Handgretinger, R.; Fuchs, J.; Pichler, B.; la Fougère, C.; Schwenck, J., First-in-Humans PET/MRI of In Vivo GD2 Expression in Osteosarcoma. *Journal of Nuclear Medicine* **2023**, *64* (2), 337-338.
3. Herfert, K.; Mannheim, J. G.; Kuebler, L.; Marciano, S.; Amend, M.; Parl, C.; Napieczynska, H.; Maier, F. M.; Vega, S. C.; Pichler, B. J., Quantitative Rodent Brain Receptor Imaging. *Molecular Imaging and Biology* **2020**, *22* (2), 223-244.
4. Liu, R.; Bao, Z. X.; Zhao, P. J.; Li, G. H., Advances in the Study of Metabolomics and Metabolites in Some Species Interactions. *Molecules* **2021**, *26* (11).
5. Bhinderwala, F.; Powers, R., NMR Metabolomics Protocols for Drug Discovery. *Nmr-Based Metabolomics: Methods and Protocols* **2019**, *2037*, 265-311.
6. Krumsiek, J.; Bartel, J.; Theis, F. J., Computational approaches for systems metabolomics. *Current Opinion in Biotechnology* **2016**, *39*, 198-206.
7. Yelamanchi, S. D.; Jayaram, S.; Thomas, J. K.; Gundimeda, S.; Khan, A. A.; Singhal, A.; Prasad, T. S. K.; Pandey, A.; Somani, B. L.; Gowda, H., A pathway map of glutamate metabolism. *Journal of Cell Communication and Signaling* **2016**, *10* (1), 69-75.
8. Frigerio, F.; Casimir, M.; Carobbio, S.; Maechler, P., Tissue specificity of mitochondrial glutamate pathways and the control of metabolic homeostasis. *Biochimica Et Biophysica Acta-Bioenergetics* **2008**, *1777* (7-8), 965-972.
9. Alarcon-Barrera, J. C.; Kostidis, S.; Ondo-Mendez, A.; Giera, M., Recent advances in metabolomics analysis for early drug development. *Drug Discovery Today* **2022**, *27* (6), 1763-1773.
10. Gomez-Cebrian, N.; Ferreiro, P. V.; Hueso, F. J. C.; Andres, J. L. P.; Puchades-Carrasco, L.; Pineda-Lucena, A., Pharmacometabolomics by NMR in Oncology: A Systematic Review. *Pharmaceuticals* **2021**, *14* (10).
11. Tolstikov, V., Metabolomics: Bridging the Gap between Pharmaceutical Development and Population Health. *Metabolites* **2016**, *6* (3).
12. Colet, J.-M., Metabonomics in the preclinical and environmental toxicity field. *Drug Discovery Today: Technologies* **2015**, *13*, 3 - 10.

13. Wilkinson, G. R., Drug therapy - Drug metabolism and variability among patients in drug response. *New England Journal of Medicine* **2005**, 352 (21), 2211-2221.
14. Organization, B. I. New Clinical Development Success Rates 2011-2020 Report. <https://www.bio.org/clinical-development-success-rates-and-contributing-factors-2011-2020>. (accessed December 2022).
15. Spear, B. B.; Heath-Chiozzi, M.; Huff, J., Clinical application of pharmacogenetics. *Trends in Molecular Medicine* **2001**, 7 (5), 201 - 204.
16. Wilkinson, G. R., Drug Metabolism and Variability among Patients in Drug Response. *The New England Journal of Medicine* **2005**, 352 (21), 2211-21.
17. Phapale, P., Pharmaco-metabolomics opportunities in drug development and clinical research. *Analytical Science Advances* **2021**, 2 (11 - 12), 611 - 616.
18. Calcoen, D.; Elias, L.; Yu, X., What does it take to produce a breakthrough drug? **2015**, 14, 161–162.
19. Suna, D.; Gaoa, W.; Hua, H.; Zhou, S., Why 90% of clinical drug development fails and how to improve it? **2022**, 12 (7), 3049 - 3062.
20. Hingorani, A. D.; Kuan, V.; Finan, C.; Kruger, F. A.; Gaulton, A.; Chopade, S.; Sofat, R.; MacAllister, R. J.; Overington, J. P.; Hemingway, H.; Denaxas, S.; Prieto, D.; Casas, J. P., Improving the odds of drug development success through human genomics: modelling study. *Scientific Reports* **2019**, 9.
21. Letertre, M. P. M.; Giraudeau, P.; de Tullio, P., Nuclear Magnetic Resonance Spectroscopy in Clinical Metabolomics and Personalized Medicine: Current Challenges and Perspectives. *Frontiers in Molecular Biosciences* **2021**, 8.
22. Nicholson, J. K.; Lindon, J. C., Systems biology - Metabonomics. *Nature* **2008**, 455 (7216), 1054-1056.
23. Long, N. P.; Nghi, T. D.; Kang, Y. P.; Anh, N. H.; Kim, H. M.; Park, S. K.; Kwon, S. W., Toward a Standardized Strategy of Clinical Metabolomics for the Advancement of Precision Medicine. *Metabolites* **2020**, 10 (2).
24. *Metabolomics Perspectives: From Theory to Practical Application. Chapter 18 - Metabolomics in public health*. Elsevier Inc: 2022.
25. Laboratories, K. KEGG Metabolic pathways. <https://www.genome.jp/pathway/map01100> (accessed December, 2022).

26. da Silva, R. R.; Dorrestein, P. C.; Quinn, R. A., Illuminating the dark matter in metabolomics. *Proceedings of the National Academy of Sciences of the United States of America* **2015**, *112* (41), 12549-12550.
27. Martinez-Reyes, I.; Chandel, N. S., Mitochondrial TCA cycle metabolites control physiology and disease. *Nature Communications* **2020**, *11* (1).
28. Owen, O. E.; Kalhan, S. C.; Hanson, R. W., The key role of anaplerosis and cataplerosis for citric acid cycle function. *Journal of Biological Chemistry* **2002**, *277* (34), 30409-30412.
29. Konn, M.; Asai, A.; Kawamoto, K.; Nishida, N.; Satoh, T.; Doki, Y.; Mori, M.; Ishii, H., The one-carbon metabolism pathway highlights therapeutic targets for gastrointestinal cancer (Review). *International Journal of Oncology* **2017**, *50* (4), 1057-1063.
30. Inigo, M.; Deja, S.; Burgess, S. C., Ins and Outs of the TCA Cycle: The Central Role of Anaplerosis. *Annual Review of Nutrition, Vol 41, 2021* **2021**, *41*, 19-47.
31. Wang, B.; Tontonoz, P., Phospholipid Remodeling in Physiology and Disease. *Annual Review of Physiology, Vol 81* **2019**, *81*, 165-188.
32. Tavasoli, M.; Lahire, S.; Reid, T.; Brodovsky, M.; McMaster, C. R., Genetic diseases of the Kennedy pathways for membrane synthesis. *Journal of Biological Chemistry* **2020**, *295* (51), 17877-17886.
33. Chen, C. J.; Lee, D. Y.; Yu, J. X.; Lin, Y. N.; Lin, T. M., Recent advances in LC-MS-based metabolomics for clinical biomarker discovery. *Mass Spectrometry Reviews*.
34. Crook, A. A.; Powers, R., Quantitative NMR-Based Biomedical Metabolomics: Current Status and Applications. *Molecules* **2020**, *25* (21).
35. Bloch, F., Nuclear Induction. *Physical Review* **1946**, *70*, 460 - 474.
36. Kemp, W., *Nuclear Magnetic Resonance in Chemistry*. Red Globe Press London: Palgrave, London, 1986; p XIII, 240.
37. Moser, E.; Laistler, E.; Schmitt, F.; Kontaxis, G., Ultra-High Field NMR and MRI - The Role of Magnet Technology to Increase Sensitivity and Specificity. *Frontiers in Physics* **2017**, *5*.
38. NMR Spectroscopy in Pharmaceutical Analysis. *Nmr Spectroscopy in Pharmaceutical Analysis* **2008**, 1-501.
39. Bracewell, R. N., *The Fourier Transform and Its Applications*. Second edition ed.; McGraw-Hill Book Company: 1978; p 444.

40. Lains, I.; Duarte, D.; Barros, A. S.; Martins, A. S.; Carneiro, T. J.; Gil, J. Q.; Miller, J. B.; Marques, M.; Mesquita, T. S.; Barreto, P.; Kim, I. K.; Cachulo, M. D.; Vavvas, D. G.; Carreira, I. M.; Murta, J. N.; Silva, R.; Miller, J. W.; Husain, D.; Gil, A. M., Urine Nuclear Magnetic Resonance (NMR) Metabolomics in Age-Related Macular Degeneration. *Journal of Proteome Research* **2019**, *18* (3), 1278-1288.
41. Tynkkynen, T.; Wang, Q.; Ekholm, J.; Anufrieva, O.; Ohukainen, P.; Vepsalainen, J.; Mannikko, M.; Keinanen-Kiukaanniemi, S.; Holmes, M. V.; Goodwin, M.; Ring, S.; Chambers, J. C.; Kooner, J.; Jarvelin, M. R.; Kettunen, J.; Hill, M.; Davey Smith, G.; Ala-Korpela, M., Proof of concept for quantitative urine NMR metabolomics pipeline for large-scale epidemiology and genetics. *International Journal of Epidemiology* **2019**, *48* (3), 978-993.
42. Lutz, N. W.; Beraud, E.; Cozzzone, P. J., Metabolomic analysis of rat brain by high resolution nuclear magnetic resonance spectroscopy of tissue extracts. *Journal of visualized experiments : JoVE* **2014**, (91), 51829-51829.
43. Lutz, N. W.; Cozzzone, P. J., Principles of multiparametric optimization for phospholipidomics by ³¹P NMR spectroscopy. *Biophysical reviews* **2013**, *5* (4), 295-304.
44. Wenger, K. J.; Hattingen, E.; Franz, K.; Steinbach, J.; Baehr, O.; Pilatus, U., In vivo Metabolic Profiles as Determined by P-31 and short TE H-1 MR-Spectroscopy: No Difference Between Patients with IDH Wildtype and IDH Mutant Gliomas. *Clinical Neuroradiology* **2019**, *29* (1), 27-36.
45. Esmaeili, M.; Hamans, B. C.; Navis, A. C.; van Horssen, R.; Bathen, T. F.; Gribbestad, I. S.; Leenders, W. P.; Heerschap, A., IDH1 R132H Mutation Generates a Distinct Phospholipid Metabolite Profile in Glioma. *Cancer Research* **2014**, *74* (17), 4898-4907.
46. Masuda, R.; Lodge, S.; Whiley, L.; Gray, N.; Lawler, N.; Nitschke, P.; Bong, S. H.; Kimhofer, T.; Loo, R. L.; Boughton, B.; Zeng, A. X.; Hall, D.; Schaefer, H.; Spraul, M.; Dwivedi, G.; Yeap, B. B.; Diercks, T.; Bernardo-Seisdedos, G.; Mato, J. M.; Lindon, J. C.; Holmes, E.; Millet, O.; Wist, J.; Nicholson, J. K., Exploration of Human Serum Lipoprotein Supramolecular Phospholipids Using Statistical Heterospectroscopy in n-Dimensions (SHY-n): Identification of Potential Cardiovascular Risk Biomarkers Related to SARS-CoV-2 Infection. *Analytical Chemistry* **2022**, *94* (10), 4426-4436.

47. Otte, D. A. L.; Borchmann, D. E.; Lin, C.; Weck, M.; Woerpel, K. A., C-13 NMR Spectroscopy for the Quantitative Determination of Compound Ratios and Polymer End Groups. *Organic Letters* **2014**, *16* (6), 1566-1569.
48. Nicholson, J. K.; Foxall, P. J. D.; Spraul, M.; Farrant, R. D.; Lindon, J. C., 750-MHZ H-1 AND H-1-C-13 NMR-SPECTROSCOPY OF HUMAN BLOOD-PLASMA. *Analytical Chemistry* **1995**, *67* (5), 793-811.
49. Gheysen, K.; Mihai, C.; Conrath, K.; Martins, J. C., Rapid Identification of Common Hexapyranose Monosaccharide Units by a Simple TOCSY Matching Approach. *Chemistry-a European Journal* **2008**, *14* (29), 8869-8878.
50. Ludwig, C.; Viant, M. R., Two-dimensional J-resolved NMR Spectroscopy: Review of a Key Methodology in the Metabolomics Toolbox. *Phytochemical Analysis* **2010**, *21* (1), 22-32.
51. Singh, Y.; Trautwein, C.; Dhariwal, A.; Salker, M. S.; Alauddin, M.; Zizmare, L.; Pelzl, L.; Feger, M.; Admard, J.; Casadei, N.; Foeller, M.; Pachauri, V.; Park, D. S.; Mak, T. W.; Frick, J.-S.; Wallwiener, D.; Brucker, S. Y.; Lang, F.; Riess, O., DJ-1 (Park7) affects the gut microbiome, metabolites and the development of innate lymphoid cells (ILCs). *Scientific Reports* **2020**, *10* (1).
52. Bus, C.; Zizmare, L.; Feldkaemper, M.; Geisler, S.; Zarani, M.; Schaedler, A.; Klose, F.; Admard, J.; Mageean, C. J.; Arena, G.; Fallier-Becker, P.; Ugun-Klusek, A.; Maruszczak, K. K.; Kapolou, K.; Schmid, B.; Rapaport, D.; Ueffing, M.; Casadei, N.; Kruger, R.; Gasser, T.; Weisenhorn, D. M. V.; Kahle, P. J.; Trautwein, C.; Gloeckner, C. J.; Fitzgerald, J. C., Human Dopaminergic Neurons Lacking PINK1 Exhibit Disrupted Dopamine Metabolism Related to Vitamin B6 Co-Factors. *Iscience* **2020**, *23* (12).
53. Urzi, C.; Hertig, D.; Meyer, C.; Maddah, S.; Nuoffer, J. M.; Vermathen, P., Determination of Intra- and Extracellular Metabolic Adaptations of 3D Cell Cultures upon Challenges in Real-Time by NMR. *International Journal of Molecular Sciences* **2022**, *23* (12).
54. Nematodzi, L. E.; Vervoort, J.; Prinsloo, G., NMR-Based Metabolomic Analysis and Microbial Composition of Soil Supporting *Burkea africana* Growth. *Metabolites* **2020**, *10* (10).
55. Amargianitaki, M.; Spyros, A., NMR-based metabolomics in wine quality control and authentication. *Chemical and Biological Technologies in Agriculture* **2017**, *4*.

56. Boffo, E. F.; Tavares, L. A.; Tobias, A. C. T.; Ferreira, M. M. C.; Ferreira, A. G., Identification of components of Brazilian honey by H-1 NMR and classification of its botanical origin by chemometric methods. *Lwt-Food Science and Technology* **2012**, *49* (1), 55-63.
57. Ingallina, C.; Cerreto, A.; Mannina, L.; Circi, S.; Vista, S.; Capitani, D.; Spano, M.; Sobolev, A. P.; Marini, F., Extra-Virgin Olive Oils from Nine Italian Regions: An H-1 NMR-Chemometric Characterization. *Metabolites* **2019**, *9* (4).
58. Tang, R. G.; Ding, C. F.; Ma, Y. B.; Wang, J. S.; Zhang, T. L.; Wang, X. X., Time-dependent responses of earthworms to soil contaminated with low levels of lead as detected using H-1 NMR metabolomics. *Rsc Advances* **2017**, *7* (54), 34170-34181.
59. Benaki, D.; Mikros, E., NMR-Based Metabolic Profiling Procedures for Biofluids and Cell and Tissue Extracts. *Metabolic Profiling: Methods and Protocols* **2018**, *1738*, 117-131.
60. Stec, D. E.; Gordon, D. M.; Hipp, J. A.; Hong, S.; Mitchell, Z. L.; Franco, N. R.; Robison, J. W.; Anderson, C. D.; Stec, D. F.; Hinds, T. D., Loss of hepatic PPAR alpha promotes inflammation and serum hyperlipidemia in diet-induced obesity. *American Journal of Physiology-Regulatory Integrative and Comparative Physiology* **2019**, *317* (5), R733-R745.
61. Braud, L.; Pini, M.; Stec, D. F.; Manin, S.; Derumeaux, G.; Stec, D. E.; Foresti, R.; Motterlini, R., Increased Sirt1 secreted from visceral white adipose tissue is associated with improved glucose tolerance in obese Nrf2-deficient mice. *Redox Biology* **2021**, *38*.
62. Laugwitz, L.; Zizmare, L.; Santhanakumaran, V.; Cannet, C.; Böhringer, J.; Okun, J. G.; Spraul, M.; Krägeloh-Mann, I.; Groeschel, S.; Trautwein, C., Identification of neurodegeneration indicators and disease progression in metachromatic leukodystrophy using quantitative NMR-based urinary metabolomics. *JIMD Reports* **2022**, *63*, 168–180.
63. Nitschke, P.; Lodge, S.; Hall, D.; Schaefer, H.; Spraul, M.; Embade, N.; Millet, O.; Holmes, E.; Wist, J.; Nicholson, J. K., Direct low field J-edited diffusional proton NMR spectroscopic measurement of COVID-19 inflammatory biomarkers in human serum. *Analyst* **2022**, *147* (19), 4213-4221.
64. Masuda, R.; Lodge, S.; Nitschke, P.; Spraul, M.; Schaefer, H.; Bong, S. H.; Kimhofer, T.; Hall, D.; Loo, R. L.; Bizkarguenaga, M.; Bruzzone, C.; Gil-Redondo, R.; Embade, N.; Mato, J. M.; Holmes, E.; Wist, J.; Millet, O.; Nicholson, J. K., Integrative

Modeling of Plasma Metabolic and Lipoprotein Biomarkers of SARS-CoV-2 Infection in Spanish and Australian COVID-19 Patient Cohorts. *Journal of Proteome Research* **2021**, *20* (8), 4139-4152.

65. Giskeodegard, G. F.; Madssen, T. S.; Euceda, L. R.; Tessem, M. B.; Moestue, S. A.; Bathen, T. F., NMR-based metabolomics of biofluids in cancer. *Nmr in Biomedicine* **2019**, *32* (10).

66. Debik, J.; Euceda, L. R.; Lundgren, S.; Gythfeldt, H. V.; Garred, O.; Borgen, E.; Engebraaten, O.; Bathen, T. F.; Giskeodegard, G. F., Assessing Treatment Response and Prognosis by Serum and Tissue Metabolomics in Breast Cancer Patients. *Journal of Proteome Research* **2019**, *18* (10), 3649-3660.

67. Berezhnoy, G.; Laske, C.; Trautwein, C., Quantitative NMR-Based Lipoprotein Analysis Identifies Elevated HDL-4 and Triglycerides in the Serum of Alzheimer's Disease Patients. *International Journal of Molecular Sciences* **2022**, *23* (20).

68. Mujagic, Z.; Kasapi, M.; Jonkers, D.; Garcia-Perez, I.; Vork, L.; Weerts, Z.; Serrano-Contreras, J. I.; Zhernakova, A.; Kurilshikov, A.; Scotcher, J.; Holmes, E.; Wijmenga, C.; Keszthelyi, D.; Nicholson, J. K.; Posma, J. M.; Masclee, A. A. M., Integrated fecal microbiome-metabolome signatures reflect stress and serotonin metabolism in irritable bowel syndrome. *Gut Microbes* **2022**, *14* (1).

69. Trautwein, C.; Zizmare, L.; Maurer, I.; Bender, B.; Bayer, B.; Ernemann, U.; Tatagiba, M.; Grau, S. J.; Pichler, B. J.; Skardelly, M.; Tabatabai, G., Tissue metabolites in diffuse glioma and their modulations by IDH1 mutation, histology, and treatment. *JCI Insight* **2022**, *7* (3).

70. Zhang, F. R.; Wang, Y. C.; Chen, G.; Li, Z. L.; Xing, X. H.; Putz-Bankuti, C.; Stauber, R. E.; Liu, X. L.; Madl, T., Growing Human Hepatocellular Tumors Undergo a Global Metabolic Reprogramming. *Cancers* **2021**, *13* (8).

71. Dudzik, D.; Barbas-Bernardos, C.; Garcia, A.; Barbas, C., Quality assurance procedures for mass spectrometry untargeted metabolomics. a review. *Journal of Pharmaceutical and Biomedical Analysis* **2018**, *147*, 149-173.

72. Kirwan, J. A.; Brennan, L.; Broadhurst, D.; Fiehn, O.; Cascante, M.; Dunn, W. B.; Schmidt, M. A.; Velagapudi, V., Preanalytical Processing and Biobanking Procedures of Biological Samples for Metabolomics Research: A White Paper, Community Perspective (for "Precision Medicine and Pharmacometabolomics Task Group"-The Metabolomics Society Initiative). *Clinical Chemistry* **2018**, *64* (8), 1158-1182.

73. Wu, Y. M.; Li, L., Sample normalization methods in quantitative metabolomics. *Journal of Chromatography A* **2016**, *1430*, 80-95.
74. Wehrens, R.; Salek, R., *Metabolomics Practical Guide to Design and Analysis*. Chapman & Hall: 2019.
75. Cloarec, O.; Dumas, M. E.; Craig, A.; Barton, R. H.; Trygg, J.; Hudson, J.; Blancher, C.; Gauguier, D.; Lindon, J. C.; Holmes, E.; Nicholson, J., Statistical total correlation spectroscopy: An exploratory approach for latent biomarker identification from metabolic H-1 NMR data sets. *Analytical Chemistry* **2005**, *77* (5), 1282-1289.
76. Emwas, A. H.; Saccenti, E.; Gao, X.; McKay, R. T.; dos Santos, V.; Roy, R.; Wishart, D. S., Recommended strategies for spectral processing and post-processing of 1D H-1-NMR data of biofluids with a particular focus on urine. *Metabolomics* **2018**, *14* (3).
77. Liu, Y. M.; Chen, T. L.; Qiu, Y. P.; Cheng, Y.; Cao, Y.; Zhao, A. H.; Jia, W., An ultrasonication-assisted extraction and derivatization protocol for GC/TOFMS-based metabolite profiling. *Analytical and Bioanalytical Chemistry* **2011**, *400* (5), 1405-1417.
78. Zelentsova, E. A.; Yanshole, V. V.; Tsentalovich, Y. P., A novel method of sample homogenization with the use of a microtome-cryostat apparatus. *Rsc Advances* **2019**, *9* (65), 37809-37817.
79. Keller, C.; Wei, P. L.; Wancewicz, B.; Cross, T. W. L.; Rey, F. E.; Li, L. J., Extraction optimization for combined metabolomics, peptidomics, and proteomics analysis of gut microbiota samples. *Journal of Mass Spectrometry* **2021**, *56* (4).
80. McHugh, C. E.; Flott, T. L.; Schooff, C. R.; Smiley, Z.; Puskarich, M. A.; Myers, D. D.; Younger, J. G.; Jones, A. E.; Stringer, K. A., Rapid, Reproducible, Quantifiable NMR Metabolomics: Methanol and Methanol: Chloroform Precipitation for Removal of Macromolecules in Serum and Whole Blood. *Metabolites* **2018**, *8* (4).
81. Matyash, V.; Liebisch, G.; Kurzchalia, T. V.; Shevchenko, A.; Schwudke, D., Lipid extraction by methyl-tert-butyl ether for high-throughput lipidomics. *Journal of Lipid Research* **2008**, *49* (5), 1137-1146.
82. Kelly, A. E.; Ou, H. D.; Withers, R.; Dotsch, V., Low-conductivity buffers for high-sensitivity NMR measurements. *Journal of the American Chemical Society* **2002**, *124* (40), 12013-12019.
83. Gardner, A.; Parkes, H. G.; Carpenter, G. H.; So, P. W., Developing and Standardizing a Protocol for Quantitative Proton Nuclear Magnetic Resonance (H-1

NMR) Spectroscopy of Saliva. *Journal of Proteome Research* **2018**, *17* (4), 1521-1531.

84. Tsutsumi, H.; Ohata, T.; Nakashima, R.; Ikeda, H., The cucurbit 7 uril effect on reference substances for NMR in deuterium oxide solution. *New Journal of Chemistry* **2022**, *46* (42), 20217-20224.

85. Gowda, G. A. N.; Hong, N. N.; Raftery, D., Evaluation of Fumaric Acid and Maleic Acid as Internal Standards for NMR Analysis of Protein Precipitated Plasma, Serum, and Whole Blood. *Analytical Chemistry* **2021**, *93* (6), 3233-3240.

86. Dona, A. C., Standardized NMR Protocols for Metabonomics. *Encyclopedia of Spectroscopy and Spectrometry, 3rd Edition, Vol 4: S-Z* **2017**, 218-223.

87. Wishart, D. S.; Guo, A. C.; Oler, E.; Wang, F.; Anjum, A.; Peters, H.; Dizon, R.; Sayeeda, Z.; Tian, S. Y.; Lee, B. L.; Berjanskii, M.; Mah, R.; Yamamoto, M.; Jovel, J.; Torres-Calzada, C.; Hiebert-Giesbrecht, M.; Lui, V. W.; Varshavi, D.; Allen, D.; Arndt, D.; Khetarpal, N.; Sivakumaran, A.; Harford, K.; Sanford, S.; Yee, K.; Cao, X.; Budinski, Z.; Liigand, J.; Zhang, L.; Zheng, J. M.; Mandal, R.; Karu, N.; Dambrova, M.; Schioth, H. B.; Greiner, R.; Gautam, V., HMDB 5.0: the Human Metabolome Database for 2022. *Nucleic Acids Research* **2022**, *50* (D1), D622-D631.

88. Solinas, A.; Chessa, M.; Culeddu, N.; Porcu, M. C.; Virgilio, G.; Arcadu, F.; Deplano, A.; Cossu, S.; Scanu, D.; Migaletto, V., High resolution-magic angle spinning (HR-MAS) NMR-based metabolomic fingerprinting of early and recurrent hepatocellular carcinoma. *Metabolomics* **2014**, *10* (4), 616-626.

89. Bruker NMR Clinical Research Solutions BBIREFCODE. <https://www.bruker.com/en/products-and-solutions/mr/nmr-clinical-research-solutions/bbiorefcode.html> (accessed April 19, 2023).

90. Eghbalnia, H. R.; Romero, P. R.; Westler, W. M.; Baskaran, K.; Ulrich, E. L.; Markley, J. L., Increasing rigor in NMR-based metabolomics through validated and open source tools. *Current Opinion in Biotechnology* **2017**, *43*, 56-61.

91. Chong, J.; Soufan, O.; Li, C.; Caraus, I.; Li, S.; Bourque, G.; Wishart, D. S.; Xia, J., MetaboAnalyst 4.0: towards more transparent and integrative metabolomics analysis. *Nucleic Acids Research* **2018**, *46* (W1), W486-W494.

92. Mahla, R. S.; Kumar, A.; Tutill, H. J.; Krishnaji, S. T.; Sathyamoorthy, B.; Noursadeghi, M.; Breuer, J.; Pandey, A. K.; Kumar, H., NIX-mediated mitophagy regulate metabolic reprogramming in phagocytic cells during mycobacterial infection. *Tuberculosis* **2021**, 126.

93. Fuchs, A. L.; Schiller, S. M.; Keegan, W. J.; Ammons, M. C. B.; Eilers, B.; Tripet, B.; Copie, V., Quantitative H-1 NMR Metabolomics Reveal Distinct Metabolic Adaptations in Human Macrophages Following Differential Activation. *Metabolites* **2019**, *9* (11).
94. Dorocho, E.; Kohm, M.; Hahnefeld, L.; Gurke, R., Metabolic Profiling in Rheumatoid Arthritis, Psoriatic Arthritis, and Psoriasis: Elucidating Pathogenesis, Improving Diagnosis, and Monitoring Disease Activity. *Journal of Personalized Medicine* **2022**, *12* (6).
95. Tarentini, E.; Odorici, G.; Righi, V.; Paganelli, A.; Giacomelli, L.; Mirisola, V.; Mucci, A.; Benassi, L.; D'Aversa, E.; Lasagni, C.; Kaleci, S.; Reali, E.; Magnoni, C., Integrated metabolomic analysis and cytokine profiling define clusters of immuno-metabolic correlation in new-onset psoriasis. *Scientific Reports* **2021**, *11* (1).
96. Ahmed, S.; Dubey, D.; Chowdhury, A.; Chaurasia, S.; Guleria, A.; Kumar, S.; Singh, R.; Kumar, D.; Misra, R., Nuclear magnetic resonance-based metabolomics reveals similar metabolomics profiles in undifferentiated peripheral spondyloarthritis and reactive arthritis. *International Journal of Rheumatic Diseases* **2019**, *22* (4), 725-733.
97. Chen, M. X.; Wang, S. Y.; Kuo, C. H.; Tsai, I. L., Metabolome analysis for investigating host-gut microbiota interactions. *Journal of the Formosan Medical Association* **2019**, *118*, S10-S22.
98. Mirzaei, R.; Bouzari, B.; Hosseini-Fard, S. R.; Mazaheri, M.; Ahmadyousefi, Y.; Abdi, M.; Jalalifar, S.; Karimitabar, Z.; Teimoori, A.; Keyvani, H.; Zamani, F.; Yousefimashouf, R.; Karampoor, S., Role of microbiota-derived short-chain fatty acids in nervous system disorders. *Biomedicine & Pharmacotherapy* **2021**, *139*.
99. Gupta, H.; Min, B. H.; Ganesan, R.; Gebru, Y. A.; Sharma, S. P.; Park, E.; Won, S. M.; Jeong, J. J.; Lee, S. B.; Cha, M. G.; Kwon, G. H.; Jeong, M. K.; Hyun, J. Y.; Eom, J. A.; Park, H. J.; Yoon, S. J.; Choi, M. R.; Kim, D. J.; Suk, K. T., Gut Microbiome in Non-Alcoholic Fatty Liver Disease: From Mechanisms to Therapeutic Role. *Biomedicines* **2022**, *10* (3).
100. Fechine, C.; Monteiro, M.; Tavares, J. F.; Souto, A. L.; Luna, R. C. P.; da Silva, C. S. O.; da Silva, J. A.; dos Santos, S. G.; Costa, M. J. D.; Persuhn, D. C., Choline Metabolites, Hydroxybutyrate and HDL after Dietary Fiber Supplementation in Overweight/Obese Hypertensive Women: A Metabolomic Study. *Nutrients* **2021**, *13* (5).

101. Craciun, C. I.; Neag, M. A.; Catinean, A.; Mitre, A. O.; Rusu, A.; Bala, C.; Roman, G.; Buzoianu, A. D.; Muntean, D. M.; Craciun, A. E., The Relationships between Gut Microbiota and Diabetes Mellitus, and Treatments for Diabetes Mellitus. *Biomedicines* **2022**, *10* (2).
102. Cunningham, A. L.; Stephens, J. W.; Harris, D. A., Gut microbiota influence in type 2 diabetes mellitus (T2DM). *Gut Pathogens* **2021**, *13* (1).
103. Hrnčir, T.; Hrnčířová, L.; Kverka, M.; Hromádka, R.; Machová, V.; Trčková, E.; Kostovčiková, K.; Kralicková, P.; Krejsek, J.; Tlaskalová-Hogenová, H., Gut Microbiota and NAFLD: Pathogenetic Mechanisms, Microbiota Signatures, and Therapeutic Interventions. *Microorganisms* **2021**, *9* (5).
104. Kolodziejczyk, A. A.; Zheng, D. P.; Shibolet, O.; Elinav, E., The role of the microbiome in NAFLD and NASH. *Embo Molecular Medicine* **2019**, *11* (2).
105. Jiang, X. F.; Zheng, J.; Zhang, S. X.; Wang, B. Z.; Wu, C. D.; Guo, X., Advances in the Involvement of Gut Microbiota in Pathophysiology of NAFLD. *Frontiers in Medicine* **2020**, *7*.
106. Leung, H.; Long, X. X.; Ni, Y. Q.; Qian, L. L.; Nychas, E.; Siliceo, S. L.; Pohl, D.; Hanhineva, K.; Liu, Y.; Xu, A. M.; Nielsen, H. B.; Belda, E.; Clement, K.; Loomba, R.; Li, H. T.; Jia, W. P.; Panagiotou, G., Risk assessment with gut microbiome and metabolite markers in NAFLD development. *Science Translational Medicine* **2022**, *14* (648).
107. Zhang, Y. C.; Si, X. M.; Yang, L.; Wang, H.; Sun, Y.; Liu, N., Association between intestinal microbiota and inflammatory bowel disease. *Animal Models and Experimental Medicine* **2022**, *5* (4), 311-322.
108. Ghaffari, P.; Shoaie, S.; Nielsen, L. K., Irritable bowel syndrome and microbiome; Switching from conventional diagnosis and therapies to personalized interventions. *Journal of Translational Medicine* **2022**, *20* (1).
109. Vignoli, A.; Risi, E.; McCartney, A.; Migliaccio, I.; Moretti, E.; Malorni, L.; Luchinat, C.; Biganzoli, L.; Tenori, L., Precision Oncology via NMR-Based Metabolomics: A Review on Breast Cancer. *International Journal of Molecular Sciences* **2021**, *22* (9).
110. Sampsell, K.; Hao, D.; Reimer, R. A., The Gut Microbiota: A Potential Gateway to Improved Health Outcomes in Breast Cancer Treatment and Survivorship. *International Journal of Molecular Sciences* **2020**, *21* (23).

111. Giallourou, N.; Urbaniak, C.; Puebla-Barragan, S.; Vorkas, P. A.; Swann, J. R.; Reid, G., Characterizing the breast cancer lipidome and its interaction with the tissue microbiota. *Communications Biology* **2021**, *4* (1).
112. Fernandez, M. F.; Reina-Perez, I.; Astorga, J. M.; Rodriguez-Carrillo, A.; Plaza-Diaz, J.; Fontana, L., Breast Cancer and Its Relationship with the Microbiota. *International Journal of Environmental Research and Public Health* **2018**, *15* (8).
113. Rebersek, M., Gut microbiome and its role in colorectal cancer. *Bmc Cancer* **2021**, *21* (1).
114. Kim, S. H.; Lim, Y. J., The role of microbiome in colorectal carcinogenesis and its clinical potential as a target for cancer treatment. *Intestinal Research* **2022**, *20* (1), 31-42.
115. Genua, F.; Raghunathan, V.; Jenab, M.; Gallagher, W. M.; Hughes, D. J., The Role of Gut Barrier Dysfunction and Microbiome Dysbiosis in Colorectal Cancer Development. *Frontiers in Oncology* **2021**, *11*.
116. Francavilla, R.; Calasso, M.; Calace, L.; Siragusa, S.; Ndagijimana, M.; Vernocchi, P.; Brunetti, L.; Mancino, G.; Tedeschi, G.; Guerzoni, E.; Indrio, F.; Laghi, L.; Miniello, V. L.; Gobbetti, M.; De Angelis, M., Effect of lactose on gut microbiota and metabolome of infants with cow's milk allergy. *Pediatric Allergy and Immunology* **2012**, *23* (5), 420-427.
117. Vernocchi, P.; Del Chierico, F.; Putignani, L., Gut Microbiota Profiling: Metabolomics Based Approach to Unravel Compounds Affecting Human Health. *Frontiers in Microbiology* **2016**, *7*.
118. Hertel, J.; Fassler, D.; Heinken, A.; Weiss, F. U.; Ruhlemann, M.; Bang, C.; Franke, A.; Budde, K.; Henning, A. K.; Petersmann, A.; Volker, U.; Volzke, H.; Thiele, I.; Grabe, H. J.; Lerch, M. M.; Nauck, M.; Friedrich, N.; Frost, F., NMR Metabolomics Reveal Urine Markers of Microbiome Diversity and Identify Benzoate Metabolism as a Mediator between High Microbial Alpha Diversity and Metabolic Health. *Metabolites* **2022**, *12* (4).
119. Bervoets, L.; Ippel, J. H.; Smolinska, A.; van Best, N.; Savelkoul, P. H. M.; Mommers, M. A. H.; Penders, J., Practical and Robust NMR-Based Metabolic Phenotyping of Gut Health in Early Life. *Journal of Proteome Research* **2021**, *20* (11), 5079-5087.
120. Arnorriaga-Rodriguez, M.; Mayneris-Perxachs, J.; Burokas, A.; Contreras-Rodriguez, O.; Blasco, G.; Coll, C.; Biarnes, C.; Miranda-Olivos, R.; Latorre, J.;

Moreno-Navarrete, J. M.; Castells-Nobau, A.; Sabater, M.; Palomo-Buitrago, M. E.; Puig, J.; Pedraza, S.; Gich, J.; Perez-Brocal, V.; Ricart, W.; Moya, A.; Fernandez-Real, X.; Ramio-Torrenta, L.; Pamplona, R.; Sol, J.; Jove, M.; Portero-Otin, M.; Maldonado, R.; Fernandez-Real, J. M., Obesity Impairs Short-Term and Working Memory through Gut Microbial Metabolism of Aromatic Amino Acids. *Cell Metabolism* **2020**, *32* (4), 548-+.

121. Tian, Y.; Gui, W.; Koo, I.; Smith, P. B.; Allman, E. L.; Nichols, R. G.; Rimal, B.; Cai, J. W.; Liu, Q.; Patterson, A. D., The microbiome modulating activity of bile acids. *Gut Microbes* **2020**, *11* (4).

122. Silva, Y. P.; Bernardi, A.; Frozza, R. L., The Role of Short-Chain Fatty Acids From Gut Microbiota in Gut-Brain Communication. *Frontiers in Endocrinology* **2020**, *11*.

123. Lee, J.; Venna, V. R.; Durgan, D. J.; Shi, H. N.; Hudobenko, J.; Putluri, N.; Petrosino, J.; McCullough, L. D.; Bryan, R. M., Young versus aged microbiota transplants to germ-free mice: increased short-chain fatty acids and improved cognitive performance. *Gut Microbes* **2020**, *12* (1).

124. Venegas, D. P.; De la Fuente, M. K.; Landskron, G.; Gonzalez, M. J.; Quera, R.; Dijkstra, G.; Harmsen, H. J. M.; Faber, K. N.; Hermoso, M. A., Short Chain Fatty Acids (SCFAs)-Mediated Gut Epithelial and Immune Regulation and Its Relevance for Inflammatory Bowel Diseases. *Frontiers in Immunology* **2019**, *10*.

125. Treangen, T. J.; Wagner, J.; Burns, M. P.; Villapol, S., Traumatic Brain Injury in Mice Induces Acute Bacterial Dysbiosis Within the Fecal Microbiome. *Frontiers in Immunology* **2018**, *9*.

126. Opeyemi, O. M.; Rogers, M. B.; Firek, B. A.; Janesko-Feldman, K.; Vagni, V.; Mullett, S. J.; Wendell, S. G.; Nelson, B. P.; New, L. A.; Mario, E.; Kochanek, P. M.; Bayir, H.; Clark, R. S. B.; Morowitz, M. J.; Simon, D. W., Sustained Dysbiosis and Decreased Fecal Short-Chain Fatty Acids after Traumatic Brain Injury and Impact on Neurologic Outcome. *Journal of Neurotrauma* **2021**, *38* (18), 2610-2621.

127. Sze, M. A.; Topçuoğlu, B. D.; Lesniak, N. A.; Ruffin, M. T.; Schloss, P. D., Fecal Short-Chain Fatty Acids Are Not Predictive of Colonic Tumor Status and Cannot Be Predicted Based on Bacterial Community Structure. *American Society for Microbiology* **2019**, *10* (4), e01454-19.

128. Nogal, A.; Louca, P.; Zhang, X. Y.; Wells, P. M.; Steves, C. J.; Spector, T. D.; Falchi, M.; Valdes, A. M.; Menni, C., Circulating Levels of the Short-Chain Fatty Acid

Acetate Mediate the Effect of the Gut Microbiome on Visceral Fat. *Frontiers in Microbiology* **2021**, *12*.

129. Nogal, A.; Valdes, A. M.; Menni, C., The role of short-chain fatty acids in the interplay between gut microbiota and diet in cardio-metabolic health. *Gut Microbes* **2021**, *13* (1).

130. Zheng, H.; Xu, P. T.; Jiang, Q. Y.; Xu, Q. Q.; Zheng, Y. F.; Yan, J. J.; Ji, H.; Ning, J.; Zhang, X.; Li, C.; Zhang, L. M.; Li, Y. P.; Li, X. K.; Song, W. H.; Gao, H. C., Depletion of acetate-producing bacteria from the gut microbiota facilitates cognitive impairment through the gut-brain neural mechanism in diabetic mice. *Microbiome* **2021**, *9* (1).

131. Ranjbar, R.; Vahdati, S. N.; Tavakoli, S.; Khodaie, R.; Behboudi, H., Immunomodulatory roles of microbiota-derived short-chain fatty acids in bacterial infections. *Biomedicine & Pharmacotherapy* **2021**, *141*.

132. Lobel, L.; Garrett, W. S., Butyrate Makes Macrophages "Go Nuclear" against Bacterial Pathogens. *Immunity* **2019**, *50* (2), 275-278.

133. Schulthess, J.; Pandey, S.; Capitani, M.; Rue-Albrecht, K. C.; Arnold, I.; Franchini, F.; Chomka, A.; Ilott, N. E.; Johnston, D. G. W.; Pires, E.; McCullagh, J.; Sansom, S. N.; Arancibia-Carcamo, C. V.; Uhlig, H. H.; Powrie, F., The Short Chain Fatty Acid Butyrate Imprints an Antimicrobial Program in Macrophages. *Immunity* **2019**, *50* (2), 432-+.

134. Brial, F.; Le Lay, A.; Dumas, M. E.; Gauguier, D., Implication of gut microbiota metabolites in cardiovascular and metabolic diseases. *Cell. Mol. Life Sci.* **2018**, *75* (21), 3977-3990.

135. Gold, A.; Zhu, J., Not just a gut feeling: a deep exploration of functional bacterial metabolites that can modulate host health. *Gut Microbes* **2022**, *14* (1), e2125734.

136. Li, D. T.; Feng, Y.; Tian, M. L.; Ji, J. F.; Hu, X. S.; Chen, F., Gut microbiota-derived inosine from dietary barley leaf supplementation attenuates colitis through PPAR gamma signaling activation. *Microbiome* **2021**, *9* (1).

137. Mager, L. F.; Burkhard, R.; Pett, N.; Cooke, N. C. A.; Brown, K.; Ramay, H.; Paik, S.; Stagg, J.; Groves, R. A.; Gallo, M.; Lewis, I. A.; Geuking, M. B.; McCoy, K. D., Microbiome-derived inosine modulates response to checkpoint inhibitor immunotherapy. *Science* **2020**, *369* (6510), 1481-+.

138. Wang, H.; Rong, X. Y.; Zhao, G.; Zhou, Y. F.; Xiao, Y.; Ma, D.; Jin, X.; Wu, Y. L.; Yan, Y. C.; Yang, H.; Zhou, Y.; Qian, M. N.; Niu, C.; Hu, X.; Li, D. Q.; Liu, Q. Y.;

Wen, Y. M.; Jiang, Y. Z.; Zhao, C.; Shao, Z. M., The microbial metabolite trimethylamine N-oxide promotes antitumor immunity in triple-negative breast cancer. *Cell Metabolism* **2022**, *34* (4), 581-+.

139. Bergsbaken, T.; Fink, S. L.; Cookson, B. T., Pyroptosis: host cell death and inflammation. *Nature Reviews Microbiology* **2009**, *7* (2), 99-109.

140. Gao, Y. J.; Chen, H. M.; Li, J. L.; Ren, S. J.; Yang, Z. L.; Zhou, Y. P.; Xuan, R. R., Alterations of gut microbiota-derived metabolites in gestational diabetes mellitus and clinical significance. *Journal of Clinical Laboratory Analysis* **2022**, *36* (4).

141. Taormina, V. M.; Unger, A. L.; Schiksnis, M. R.; Torres-Gonzalez, M.; Kraft, J., Branched-Chain Fatty Acids-An Underexplored Class of Dairy-Derived Fatty Acids. *Nutrients* **2020**, *12* (9).

142. Heimann, E.; Nyman, M.; Palbrink, A. K.; Lindkvist-Petersson, K.; Degerman, E., Branched short-chain fatty acids modulate glucose and lipid metabolism in primary adipocytes. *Adipocyte* **2016**, *5* (4), 359-368.

143. Szczesniak, O.; Hestad, K. A.; Hanssen, J. F.; Rudi, K., Isovaleric acid in stool correlates with human depression. *Nutritional Neuroscience* **2016**, *19* (7), 279-283.

144. Gojda, J.; Cahova, M., Gut Microbiota as the Link between Elevated BCAA Serum Levels and Insulin Resistance. *Biomolecules* **2021**, *11* (10).

145. Manoli, I.; Venditti, C. P., Disorders of Branched Chain Amino Acid Metabolism. *Metabolic Diseases: Foundations of Clinical Management, Genetics, and Pathology, 2nd Edition* **2017**, 117-135.

146. Lips, M. A.; Van Klinken, J. B.; van Harmelen, V.; Dharuri, H. K.; t Hoen, P. A. C.; Laros, J. F. J.; van Ommen, G. J.; Janssen, I. M.; Van Ramshorst, B.; Van Wagenveld, B. A.; Swank, D. J.; Van Dielen, F.; Dane, A.; Harms, A.; Vreeken, R.; Hankemeier, T.; Smit, J. W. A.; Pijl, H.; van Dijk, K. W., Roux-en-Y Gastric Bypass Surgery, but Not Calorie Restriction, Reduces Plasma Branched-Chain Amino Acids in Obese Women Independent of Weight Loss or the Presence of Type 2 Diabetes. *Diabetes Care* **2014**, *37* (12), 3150-3156.

147. Ali, M. R.; Fuller, W. D.; Rasmussen, J., Detailed description of early response of metabolic syndrome after laparoscopic Roux-en-Y gastric bypass. *Surgery for Obesity and Related Diseases* **2009**, *5* (3), 346-351.

148. Chang, S. H.; Stoll, C. R. T.; Song, J.; Varela, J. E.; Eagon, C. J.; Colditz, G. A., The Effectiveness and Risks of Bariatric Surgery An Updated Systematic Review and Meta-analysis, 2003-2012. *Jama Surgery* **2014**, *149* (3), 275-287.

149. Atarashi, K.; Suda, W.; Luo, C. W.; Kawaguchi, T.; Motoo, I.; Narushima, S.; Kiguchi, Y.; Yasuma, K.; Watanabe, E.; Tanoue, T.; Thaiss, C. A.; Sato, M.; Toyooka, K.; Said, H. S.; Yamagami, H.; Rice, S. A.; Gevers, D.; Johnson, R. C.; Segre, J. A.; Chen, K.; Kolls, J. K.; Elinav, E.; Morita, H.; Xavier, R. J.; Hattori, M.; Honda, K., Ectopic colonization of oral bacteria in the intestine drives T(H)1 cell induction and inflammation. *Science* **2017**, *358* (6361), 359-+.
150. Pichler, B. J.; Kneilling, M.; Haubner, R.; Braumuller, H.; Schwaiger, M.; Rocken, M.; Weber, W. A., Imaging of delayed-type hypersensitivity reaction by PET and F-18-Galacto-RGD. *Journal of Nuclear Medicine* **2005**, *46* (1), 184-189.
151. Schwenck, J.; Maurer, A.; Fehrenbacher, B.; Mehling, R.; Knopf, P.; Mucha, N.; Haupt, D.; Fuchs, K.; Griessinger, C. M.; Bukala, D.; Holstein, J.; Schaller, M.; Menendez, I. G.; Ghoreschi, K.; Quintanilla-Martinez, L.; Guetschow, M.; Laufer, S.; Reinheckel, T.; Roecken, M.; Kalbacher, H.; Pichler, B. J.; Kneilling, M., Cysteine-type cathepsins promote the effector phase of acute cutaneous delayed-type hypersensitivity reactions. *Theranostics* **2019**, *9* (13), 3903-3917.
152. Mehling, R.; Schwenck, J.; Lemberg, C.; Trautwein, C.; Zizmare, L.; Kramer, D.; Mueller, A.; Fehrenbacher, B.; Gonzalez-Menendez, I.; Quintanilla-Martinez, L.; Schroeder, K.; Brandes, R. P.; Schaller, M.; Ruf, W.; Eichner, M.; Ghoreschi, K.; Roecken, M.; Pichler, B. J.; Kneilling, M., Immunomodulatory role of reactive oxygen species and nitrogen species during T cell-driven neutrophil-enriched acute and chronic cutaneous delayed-type hypersensitivity reactions. *Theranostics* **2021**, *11* (2), 470-490.
153. Ritze, Y.; Bárdos, G.; D'Haese, J.; G; Ernst, B.; Thurnheer, M.; Schultes, B.; Bischof; Stephan; C., Effect of High Sugar Intake on Glucose Transporter and Weight Regulating Hormones in Mice and Humans. *PLOS One* **2014**, *9* (7), e101702.
154. Zizmare, L.; Mehling, R.; Gonzalez-Menendez, I.; Lonati, C.; Quintanilla-Martinez, L.; Pichler, B. J.; Kneilling, M.; Trautwein, C., Acute and chronic inflammation alter immunometabolism in a cutaneous delayed-type hypersensitivity reaction (DTHR) mouse model. *Communications Biology* **2022**, *5*, 1250.
155. Zizmare, L.; Boyle, C. N.; Buss, S.; Louis, S.; Kuebler, L.; Mulay, K.; Krueger, R.; Steinhauer, L.; Mack, I.; Gomez, M. R.; Herfert, K.; Ritze, Y.; Trautwein, C., Roux-En-Y Gastric Bypass (RYGB) Surgery during High Liquid Sucrose Diet Leads to Gut Microbiota-Related Systematic Alterations. *International Journal of Molecular Sciences* **2022**, *23* (3).

156. Padayatty, S. J.; Levine, M., Vitamin C: the known and the unknown and Goldilocks. *Oral Diseases* **2016**, *22* (6), 463-493.
157. Aumailley, L.; Bourassa, S.; Gotti, C.; Droit, A.; Lebel, M., Vitamin C modulates the levels of several proteins of the mitochondrial complex III and its activity in the mouse liver. *Redox Biology* **2022**, *57*.
158. Rai, S. R.; Bhattacharyya, C.; Sarkar, A.; Chakraborty, S.; Sircar, E.; Dutta, S.; Sengupta, R., Glutathione: Role in Oxidative/Nitrosative Stress, Antioxidant Defense, and Treatments. *Chemistryselect* **2021**, *6* (18), 4566-4590.
159. Kuo, C. L.; Babuharisankar, A. P.; Lin, Y. C.; Lien, H. W.; Lo, Y. K.; Chou, H. Y.; Tangeda, V.; Cheng, L. C.; Cheng, A. N.; Lee, A. Y. L., Mitochondrial oxidative stress in the tumor microenvironment and cancer immunoescape: foe or friend? *Journal of Biomedical Science* **2022**, *29* (1).
160. Palmieri, E. M.; McGinity, C.; Wink, D. A.; McVicar, D. W., Nitric Oxide in Macrophage Immunometabolism: Hiding in Plain Sight. *Metabolites* **2020**, *10* (11).
161. Schwenck, J.; Mehling, R.; Thaiss, W. M.; Kramer, D.; Menendez, I. G.; Oez, H. H.; Hartl, D.; Schulze-Osthoff, K.; Hailfinger, S.; Ghoreschi, K.; Quintanilla-Martinez, L.; Carlsen, H.; Roecken, M.; Pichler, B. J.; Kneilling, M., Temporal Dynamics of Reactive Oxygen and Nitrogen Species and NF-kappa B Activation During Acute and Chronic T Cell-Driven Inflammation. *Molecular Imaging and Biology* **2020**, *22* (3), 504-514.
162. Moffett, J. R.; Ross, B.; Arun, P.; Madhavarao, C. N.; Namboodiri, A. M. A., N-acetylaspartate in the CNS: From neurodiagnostics to neurobiology. *Progress in Neurobiology* **2007**, *81* (2), 89-131.
163. Venkataramani, V.; Tanev, D. I.; Strahle, C.; Studier-Fischer, A.; Fankhauser, L.; Kessler, T.; Korber, C.; Kardorff, M.; Ratliff, M.; Xie, R. F.; Horstmann, H.; Messer, M.; Paik, S. P.; Knabbe, J.; Sahm, F.; Kurz, F. T.; Acikgoz, A. A.; Herrmannsdorfer, F.; Agarwal, A.; Bergles, D. E.; Chalmers, A.; Miletic, H.; Turcan, S.; Mawrin, C.; Hanggi, D.; Liu, H. K.; Wick, W.; Winkler, F.; Kuner, T., Glutamatergic synaptic input to glioma cells drives brain tumour progression. *Nature* **2019**, *573* (7775), 532-+.
164. Lonati, C.; Dondossola, D.; Zizmare, L.; Battistin, M.; Wüst, L.; Vivona, L.; Carbonaro, M.; Zanella, A.; Gatti, S.; Schlegel, A.; Trautwein, C., Quantitative metabolomics of tissue, perfusate, and bile from rat livers subjected to normothermic machine perfusion. *Biomedicines* **2022**, *10*, 538.

165. Feldmann, J.; Martin, P.; Bender, B.; Laugwitz, L.; Zizmare, L.; Trautwein, C.; Krägeloh-Mann, I.; Klose, U.; Groeschel, S., MR-spectroscopy in metachromatic leukodystrophy: A model free approach and clinical correlation. *NeuroImage: Clinical* **2023**, *37*.
166. Bogner-Strauss, J. G., N-Acetylaspartate Metabolism Outside the Brain: Lipogenesis, Histone Acetylation, and Cancer. *Frontiers in Endocrinology* **2017**, *8*.
167. Seyfried, F.; Phetcharaburanin, J.; Glymenaki, M.; Nordbeck, A.; Hankir, M.; Nicholson, J. K.; Holmes, E.; Marchesi, J. R.; Li, J. V., Roux-en-Y gastric bypass surgery in Zucker rats induces bacterial and systemic metabolic changes independent of caloric restriction-induced weight loss. *Gut microbes* **2021**, *13* (1), 1-20.
168. Fitzpatrick, M. A.; Young, S. P., Metabolomics - a novel window into inflammatory disease. *Swiss Medical Weekly* **2013**, *143*.
169. Whipp, A. M.; Vuoksima, E.; Korhonen, T.; Pool, R.; But, A.; Ligthart, L.; Hagenbeek, F. A.; Bartels, M.; Bogl, L. H.; Pulkkinen, L.; Rose, R. J.; Boomsma, D. I.; Kaprio, J., Ketone body 3-hydroxybutyrate as a biomarker of aggression. *Scientific Reports* **2021**, *11* (1).
170. Halinski, L. P.; Pakiet, A.; Jablonska, P.; Kaska, L.; Proczko-Stepaniak, M.; Slominska, E.; Sledzinski, T.; Mika, A., One Anastomosis Gastric Bypass Reconstitutes the Appropriate Profile of Serum Amino Acids in Patients with Morbid Obesity. *Journal of Clinical Medicine* **2020**, *9* (1).
171. Moller, N., Ketone Body, 3-Hydroxybutyrate: Minor Metabolite Major Medical Manifestations. *Journal of Clinical Endocrinology & Metabolism* **2020**, *105* (9), 2884-2892.
172. Ducker, G. S.; Rabinowitz, J. D., One-Carbon Metabolism in Health and Disease. *Cell Metabolism* **2017**, *25* (1), 27-42.
173. White, P. J.; Lapworth, A. L.; An, J.; Wang, L.; McGarrah, R. W.; Stevens, R. D.; Ilkayeva, O.; George, T.; Muehlbauer, M. J.; Bain, J. R.; Trimmer, J. K.; Brosnan, M. J.; Rolph, T. P.; Newgard, C. B., Branched-chain amino acid restriction in Zucker-fatty rats improves muscle insulin sensitivity by enhancing efficiency of fatty acid oxidation and acyl-glycine export. *Molecular Metabolism* **2016**, *5* (7), 538-551.
174. Rosenzweig, A.; Blenis, J.; Gomes, A. P., Beyond the Warburg Effect: How Do Cancer Cells Regulate One-Carbon Metabolism? *Frontiers in Cell and Developmental Biology* **2018**, *6*.

175. Li, J. V.; Ashrafiyan, H.; Sarafian, M.; Homola, D.; Rushton, L.; Barker, G.; Cabrera, P. M.; Lewis, M. R.; Darzi, A.; Lin, E.; Gletsu-Miller, N. A.; Atkin, S. L.; Sathyapalan, T.; Gooderham, N. J.; Nicholson, J. K.; Marchesi, J. R.; Athanasiou, T.; Holmes, E., Roux-en-Y gastric bypass-induced bacterial perturbation contributes to altered host-bacterial co-metabolic phenotype. *Microbiome* **2021**, *9* (1).
176. White, J. P., Amino Acid Trafficking and Skeletal Muscle Protein Synthesis: A Case of Supply and Demand. *Frontiers in Cell and Developmental Biology* **2021**, *9*.
177. Lynch, C. J.; Adams, S. H., Branched-chain amino acids in metabolic signalling and insulin resistance. *Nature Reviews Endocrinology* **2014**, *10* (12), 723-736.
178. Li, C. X.; Cui, L.; Yang, Y. M.; Miao, J.; Zhao, X. Z.; Zhang, J. D.; Cui, G. H.; Zhang, Y., Gut Microbiota Differs Between Parkinson's Disease Patients and Healthy Controls in Northeast China. *Frontiers in Molecular Neuroscience* **2019**, *12*.
179. Hopfner, F.; Kunstner, A.; Muller, S. H.; Kunzel, S.; Zeuner, K. E.; Margraf, N. G.; Deuschl, G.; Baines, J. F.; Kuhlenbaumer, G., Gut microbiota in Parkinson disease in a northern German cohort. *Brain Research* **2017**, *1667*, 41-45.
180. Wang, Y.; Dykes, G. A., Direct Modulation of the Gut Microbiota as a Therapeutic Approach for Alzheimer's Disease. *Cns & Neurological Disorders-Drug Targets* **2022**, *21* (1), 14-25.
181. Szablewski, L., Human Gut Microbiota in Health and Alzheimer's Disease. *Journal of Alzheimers Disease* **2018**, *62* (2), 549-559.
182. Wang, W.; Jiang, S. J.; Xu, C. C.; Tang, L. L.; Liang, Y.; Zhao, Y.; Zhu, G. X., Interactions between gut microbiota and Parkinson's disease: The role of microbiota-derived amino acid metabolism. *Frontiers in Aging Neuroscience* **2022**, *14*.
183. Zhang, Y.; He, X. Q.; Qian, Y. W.; Xu, S. Q.; Mo, C. J.; Yan, Z.; Yang, X. D.; Xiao, Q., Plasma branched-chain and aromatic amino acids correlate with the gut microbiota and severity of Parkinson's disease. *Npj Parkinsons Disease* **2022**, *8* (1).
184. Feng, J.; Ge, C. C.; Li, W. X.; Li, R. S., 3-(3-Hydroxyphenyl)propionic acid, a microbial metabolite of quercetin, inhibits monocyte binding to endothelial cells via modulating E-selectin expression. *Fitoterapia* **2022**, *156*.
185. Auteri, M.; Zizzo, M. G.; Serio, R., The GABAergic System and the Gastrointestinal Physiopathology. *Current Pharmaceutical Design* **2015**, *21* (34), 4996-5016.
186. Krantis, A., GABA in the mammalian enteric nervous system. *News in Physiological Sciences* **2000**, *15*, 284-290.

187. Yang, S.; Li, X.; Yang, F.; Zhao, R.; Pan, X.; Liang, J.; Tian, L.; Li, X.; Liu, L.; Xing, Y.; Wu, M., Gut Microbiota-Dependent Marker TMAO in Promoting Cardiovascular Disease: Inflammation Mechanism, Clinical Prognostic, and Potential as a Therapeutic Target. *Frontiers in Pharmacology* **2019**, *10*.
188. Trautwein, C.; Zizmare, L.; Maurer, I.; Bender, B.; Bayer, B.; Ernemann, U.; Tatagiba, M.; Grau, S. J.; Pichler, B. J.; Skardelly, M.; Tabatabai, G., Tissue metabolites in diffuse glioma and their modulations by IDH1 mutation, histology and treatment. *JCI Insight* **2022**.

6. Acknowledgements

I would like to thank Werner Siemens Foundation, Werner Siemens Imaging Center (WSIC), and Prof. Dr. Bernd J. Pichler for the access to tools, equipment and funds to carry out this doctoral research. I would like to acknowledge the training opportunities and collaboration with Bruker BioSpin GmbH that greatly helped the advancement of my research.

Moreover, I would like to thank Dr. Christoph Trautwein for supervision, opportunities and guidance during these years, and the whole metabolomics and systems medicine research group, especially Georgy Berezhnoy, Aditi Kulkarni, and Miriam Owczorz, whose support I could always rely on.

This work would not have been possible without excellent collaborations. I would like to acknowledge the support, help and collaboration in immunology field with PD Dr. Manfred Kneilling, Dr. Roman Mehling, Dr. Irene Gonzalez-Menendez and Prof. Dr. Leticia Quintanilla-Martinez. I was also greatly supported by the neurology group, especially Prof. Dr. Kristina Herfert, Sabrina (Buss) Haas, Dr. Tudor Ionescu, Laura Kuebler, Dr. Yvonne Ritze, as well as Dr. Sandrine Louis, Dr. Ralf Krüger, Dr. Manuel Rodriguez Gomez from Max Rubner-Institut in Karlsruhe. Moreover, I it has been great working together with Dr. Yogesh Singh, Dr. Lucia Laugwitz and Dr. Julia Fitzgerald from the University of Tübingen. From the oncology, I would like to acknowledge Prof. Dr. Ghazaleh Tabatabai, as well as Dr. Caterina Lonati and Dr. Daniele Dondossola from the center for preclinical research, Fondazione IRCCS Ca' Granda Ospedale Maggiore Policlinico, Italy. I am humbled by the valuable learning experiences, ability to grow my network and am motivated to continue performing excellent research in my future career journey.

Visbeidzot ir laiks pateikties maniem vecākiem un krustvecākiem, kas kaut gan tā arī nesaprot, ko tad īsti es tur tajā laboratorijā daru, vienalga vienmēr sūta atbalsta pilnus un motivējošus vārdus, atļaujot man piepildīt savu izvēlēto mērķi tur tālumā.

I have been lucky to find the best support system here in Tübingen, and I am grateful for all the adventures with Andrés, Marta, Stefania, Remy, Danalyn, and Anaïs. I thank the WSIC people – office mates, fellow PhD students, the office team, and colleagues – for many valuable learning moments during my time here.

7. Appendix

Supplementary Table 1: Common metabolites and pathways in different metabolomics studies. (a) RYGB surgery feces (F) and plasma (P) metabolomics (blue) and (b) acute and chronic DTHR ear tissue (T) metabolomics (purple) studies, classified in super-pathways and sub-pathways. Only metabolites that had significant concentration changes are shown. Metabolites that are important for the main two studies are illustrated in bold. Metabolites that are part of more than one metabolic pathway in this table have a grey cell background. Metabolites that overlap in both studies are colored green. Further collaborative studies that showed some of the metabolite changes are illustrated in the following columns: (c) human glioma tissue (T) biopsy study ¹⁸⁸, (d) preclinical liver tissue (T) and perfusion (PF) viability study ¹⁶⁴, (e) metachromatic leukodystrophy (MLD) patient urine (U) metabolomics ⁶², (f) DJ-1 gene KO mouse serum (S) and feces (F) ⁵¹, and (g) PINK1 gene knockout (KO) cell culture (C) study ⁵².

Super-pathway	Sub-pathway	Metabolites quantified by NMR (p<0.05)	Roux-en-Y gastric bypass (a)	Acute and chronic DTHR (b)	Glioma (c)	Liver perfu-sate (d)	MLD (e)	DJ-1 KO (f)	PINK1 KO (g)	
Amino acid	taurine & hypotaurine	taurine		T	T					
		hypotaurine			T					
	alanine, aspartate and glutamate	alanine				T			F/S	
		aspartate								C
		glutamine								C
		GABA	F							
		glutamate			T	T				
	glycine, serine, threonine	NAA			T			U		
		betaine	P	T						
		serine	P	T	T					
		glycine	P	T						C
		threonine								
		creatine	P			T	T			
	lysine	lysine	F	T						
		phenyl-alanine				T			F/S	C
	phenyl-alanine & tyrosine	tyrosine	P	T					F/S	C
		3-HPPA	F						F	
	tryptophan	tryptophan							S	
	urea cycle, arginine, proline	proline			T					
		arginine			T					
		creatine	P	T	T	T				
		sarcosine				T	PF			
	valine, leucine, isoleucine (BCAA)	isoleucine	P			T			F/S	C
		leucine	P			T			F/S	
		valine	P	T	T				F/S	
	β-alanine	β-alanine		T						
	glutathione	glutathione			T	T				
		GSSG			T	T				C
		5-oxoproline			T					

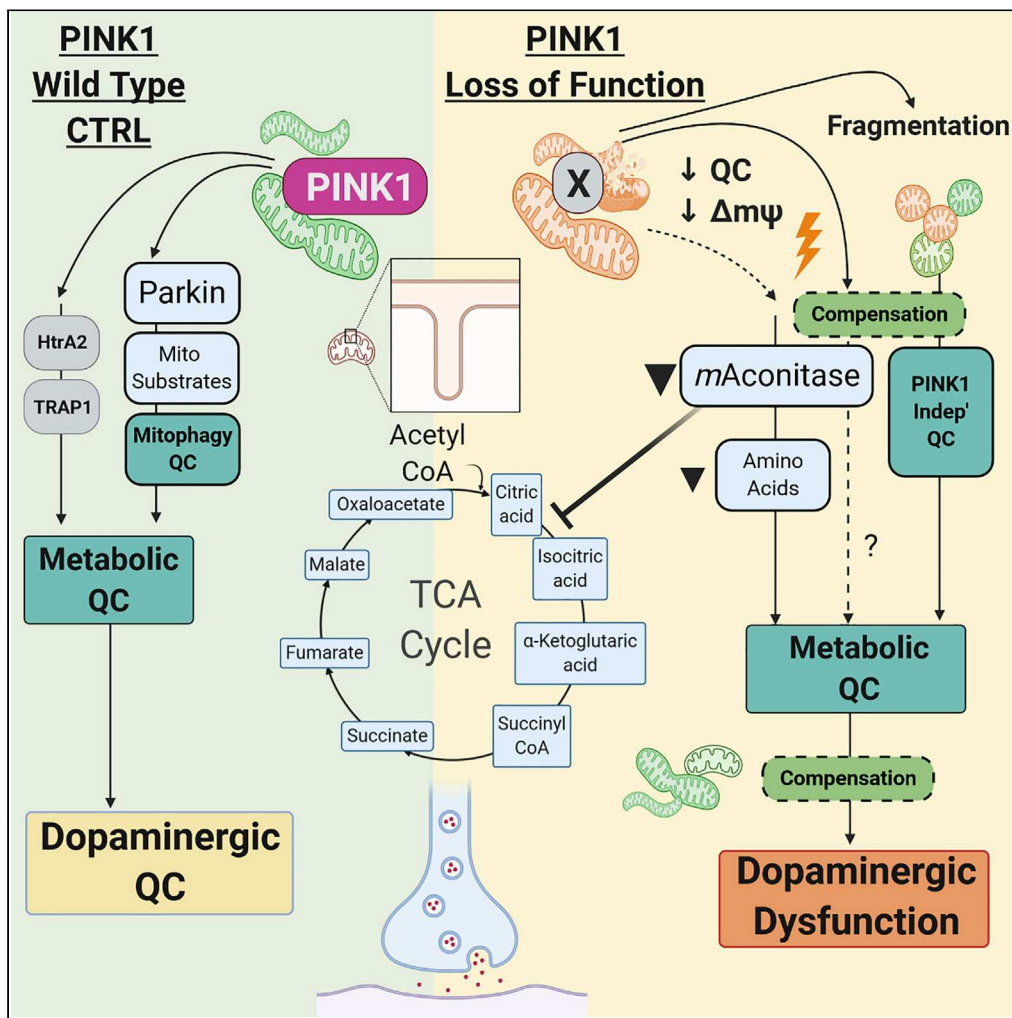
Nucleotide	pyrimidine	uridine				T			
		malonate	F						F/S
Carbohydrate	glycolysis, gluconeogenesis	glucose		T	T				
		acetate		T	T	T	T		
		pyruvate		T					
		lactate		T		T	T		
		formate				T			
Lipid	glycerolipid	glycerol							
		GPC	F	T	T				
	Glycerol-phospholipid	O-phosphocholine					T		
		choline							C
		O-phosphoethanolamine		T	T				
	inositol	myo-inositol		T	T				
	ketone bodies	3-hydroxybutyrate	P	T		T	U		
acetone						U			
Energy	TCA cycle	citrate		T	T		U		C
		succinate		T	T	T			C
		fumarate		T					
	OXPHOS	NAD⁺		T					C
		ATP				T	T		
Co-factors and vitamins	ascorbate and aldarate	ascorbate		T					
	nicotinate and nicotinamide	propionate	F						
		valerate	F						
		nicotinamide riotide					T		
	NAD⁺		T					C	
Methanogenesis	methane	TMAO	F						
		TMA	F				U	S	
One-carbon	folate cycle	neopterin					U		
	methionine cycle	methionine							
		choline							C
		betaine	P	T					
	Trans-sulfuration pathway	serine	P		T				
glutathione			T	T					

7.1. Curriculum Vitae

7.2. Co-authored Publications

Article

Human Dopaminergic Neurons Lacking PINK1 Exhibit Disrupted Dopamine Metabolism Related to Vitamin B6 Co-Factors



Christine Bus,
Laimdota Zizmare,
Marita
Feldkaemper, ...,
Christoph
Trautwein,
Christian J.
Gloeckner, Julia C.
Fitzgerald

julia.fitzgerald@
uni-tuebingen.de

HIGHLIGHTS

PINK1 KO hDANs do not undergo ionophore-induced mitophagy yet CI remains active

PINK1 KO impacts the TCA cycle via mAconitase leading to depletion of key amino acids

PINK1 KO silences PNPO, which provides essential biological co-factors

Dopamine pools and neurotransmitter uptake are reduced by PINK1 loss of function

Bus et al., iScience 23, 101797
December 18, 2020 © 2020
The Authors.
<https://doi.org/10.1016/j.isci.2020.101797>



Tissue metabolites in diffuse glioma and their modulations by *IDH1* mutation, histology, and treatment

Christoph Trautwein,¹ Laimdota Zizmare,¹ Irina Mäurer,^{2,3} Benjamin Bender,^{3,4} Björn Bayer,² Ulrike Ernemann,^{3,4} Marcos Tatagiba,^{3,5} Stefan J. Grau,⁶ Bernd J. Pichler,^{1,7,8} Marco Skardelly,^{2,3,5} and Ghazaleh Tabatabai^{2,3,7,8}

¹Department of Preclinical Imaging and Radiopharmacy, Werner Siemens Imaging Center, ²Department of Neurology & Interdisciplinary Neuro-Oncology, ³Center for Neuro-Oncology, Comprehensive Cancer Center Tübingen, ⁴Department of Neuroradiology, and ⁵Department of Neurosurgery, University Hospital Tübingen, Eberhard Karls University Tübingen, Tübingen, Germany. ⁶Center for Neurosurgery, Department of Neurosurgery, University Hospital Cologne, Cologne, Germany. ⁷Cluster of Excellence, EXC 2180, Image Guided and Functionally Instructed Tumor Therapies, University Hospital Tübingen, Eberhard Karls University of Tübingen, Tübingen, Germany. ⁸German Cancer Consortium (DKTK), Deutsches Krebs Forschungszentrum partner site Tübingen, Tübingen, Germany.

The discovery of the oncometabolite 2-hydroxyglutarate in isocitrate dehydrogenase 1-mutated (*IDH1*-mutated) tumor entities affirmed the role of metabolism in cancer. However, large databases with tissue metabolites that are modulated by *IDH1* mutation remain an area of development. Here, we present an unprecedented and valuable resource for tissue metabolites in diffuse glioma and their modulations by *IDH1* mutation, histology, and tumor treatments in 101 tissue samples from 73 diffuse glioma patients (24 astrocytoma, 17 oligodendroglioma, 32 glioblastoma), investigated by NMR-based metabolomics and supported by RNA-Seq. We discovered comparison-specific metabolites and pathways modulated by *IDH1* (*IDH1* mutation status cohort) and tumor entity. The Longitudinal investigation cohort provides metabolic profiles of untreated and corresponding treated glioma samples at first progression. Most interestingly, univariate and multivariate cox regressions and Kaplan-Meier analyses revealed that tissue metabolites correlate with progression-free and overall survival. Thus, this study introduces potentially novel candidate prognostic and surrogate metabolite biomarkers for future prospective clinical studies, aiming at further refining patient stratification in diffuse glioma. Furthermore, our data will facilitate the generation of so-far-unanticipated hypotheses for experimental studies to advance our molecular understanding of glioma biology.

Conflict of interest: B Bender is cofounder and shareholder of AIRAmed GmbH. IM reports speaker and travel fees from Novocure, a grant from Medac. GT reports Advisory boards of AbbVie, Bayer, and BMS; speaker fees from Medac and Novocure; travel grants from Novocure, Medac, and BMS; and research grants from Roche Diagnostics and Medac. CT and BJP report research grants from Bruker BioSpin GmbH.

Copyright: © 2022, Trautwein et al. This is an open access article published under the terms of the Creative Commons Attribution 4.0 International License.

Reference information: *JCI Insight*. 2022;7(3):e153526. <https://doi.org/10.1172/jci.insight.153526>.

Introduction

Mutations in isocitrate dehydrogenase 1 (*IDH1*) or *IDH2* are frequent in several cancer entities, including diffuse glioma (1–3). They lead to mutated enzymes with neomorphic activity, producing the oncometabolite 2-hydroxyglutarate (2-HG), which modulates cellular epigenetic programs, differentiation patterns, and metabolic profiles (4–6). Recent clinical trials in diffuse glioma have used the *IDH1* mutation (*IDH1*-mut) as a therapeutic target (7, 8). However, the therapeutic efficacy of these therapeutic approaches might critically depend on understanding metabolic alterations that occur in the context of *IDH1* mutations. For example, 2-HG shapes the tumor immune microenvironment by suppressing T cell activity in glioma (9). Furthermore, the nucleotide synthesis utilization and DNA repair capacity is different in *IDH1*-mut and *IDH1*-WT glioma (10). These observations indicate that *IDH1*-mut glioma exhibit distinct therapeutic challenges and mechanisms for resistance to therapy.

Altered metabolism is a major hallmark of cancer, with the potential to promote tumor growth and acquired resistance to therapy (11). Glioma cells display abnormal energy metabolism, including alterations of glucose, amino acid, and fatty acid metabolism (12). Altered metabolic pathways including choline, taurine, hypotaurine, or glutamate/glutamine correlate with different WHO grades in diffuse glioma (13). Noninvasive detection of glutamate by magnetic resonance spectroscopy can serve as a metabolic imaging biomarker of response to temozolomide treatment in *IDH1*-mut glioma (14).



OPEN

DJ-1 (Park7) affects the gut microbiome, metabolites and the development of innate lymphoid cells (ILCs)

Yogesh Singh^{1,4,✉}, Christoph Trautwein², Achal Dhariwal³, Madhuri S. Salker^{1,4}, Md Alauddin⁴, Laimdota Zizmare^{1,2}, Lisann Pelzl^{5,6}, Martina Feger⁷, Jakob Admard¹, Nicolas Casadei¹, Michael Föller⁷, Vivek Pachauri⁸, David S. Park⁹, Tak W. Mak¹⁰, Julia-Stefanie Frick¹¹, Diethelm Wallwiener⁴, Sara Y. Brucker⁴, Florian Lang^{5,12} & Olaf Riess^{1,12}









The proper communication between gut and brain is pivotal for the maintenance of health and, dysregulation of the gut-brain axis can lead to several clinical disorders. In Parkinson's disease (PD) 85% of all patients experienced constipation many years before showing any signs of motor phenotypes. For differential diagnosis and preventive treatment, there is an urgent need for the identification of biomarkers indicating early disease stages long before the disease phenotype manifests. DJ-1 is a chaperone protein involved in the protection against PD and genetic mutations in this protein have been shown to cause familial PD. However, how the deficiency of DJ-1 influences the risk of PD remains incompletely understood. In the present study, we provide evidence that DJ-1 is implicated in shaping the gut microbiome including; their metabolite production, inflammation and innate immune cells (ILCs) development. We revealed that deficiency of DJ-1 leads to a significant increase in two specific genera/species, namely *Alistipes* and *Rikenella*. In DJ-1 knock-out (DJ-1^{-/-}) mice the production of fecal calprotectin and MCP-1 inflammatory proteins were elevated. Fecal and serum metabolic profile showed that malonate which influences the immune system was significantly more abundant in DJ-1^{-/-} mice. DJ-1 appeared also to be involved in ILCs development. Further, inflammatory genes related to PD were augmented in the midbrain of DJ-1^{-/-} mice. Our data suggest that metabolites and inflammation produced in the gut could be used as biomarkers for PD detection. Perhaps, these metabolites and inflammatory mediators could be involved in triggering inflammation resulting in PD pathology.

Parkinson's disease (PD) is the most common movement disorder and the second most prevalent neurodegenerative disease in humans¹. Clinically, PD patients suffer from resting tremor, rigidity, bradykinesia and altered gait¹. PD is an incurable neurodegenerative disease distinguished by the loss of neurons predominantly

¹Institute of Medical Genetics and Applied Genomics, Tübingen University, Calwerstraße 7, 72076 Tübingen, Germany. ²Department of Preclinical Imaging and Radiopharmacy, Werner Siemens Imaging Center (WSIC), Tübingen University, Röntgenweg 13, 72076 Tübingen, Germany. ³Department of Oral Biology, University of Oslo, Oslo, Norway. ⁴Research Institute of Women's Health, Tübingen University, Calwerstraße 7/6, 72076 Tübingen, Germany. ⁵Department of Vegetative Physiology, Tübingen University, Wilhelmstraße 56, 72076 Tübingen, Germany. ⁶Clinical Transfusion Medicine Centre, Tübingen University, Otfried-Müller-Straße 4/1, 72076 Tübingen, Germany. ⁷Department of Physiology, University of Hohenheim, Garbenstraße 30, 70599 Stuttgart, Germany. ⁸Institute of Materials in Electrical Engineering 1, RWTH Aachen University, Aachen, Germany. ⁹Health Research Innovation Centre, Hotchkiss Brain Institute, 3330 Hospital Drive NW, Calgary, Alberta T2N 4N1, Canada. ¹⁰Campbell Family Institute for Breast Cancer Research, Ontario Cancer Institute, UHN, 620 University Ave, Toronto M5G 2C1, Canada. ¹¹Institute for Medical Microbiology and Hygiene, Tübingen University, Elfriede-Aulhorn-Straße 6, 72076 Tübingen, Germany. ¹²These authors jointly supervised this work: Florian Lang and Olaf Riess. ✉email: ysinghbt@gmail.com; yogesh.singh@med.uni-tuebingen.de

Article

Quantitative Metabolomics of Tissue, Perfusate, and Bile from Rat Livers Subjected to Normothermic Machine Perfusion

Caterina Lonati ¹, Daniele Dondossola ^{2,3}, Laimdota Zizmare ⁴, Michele Battistin ¹, Leonie Wüst ⁴, Luigi Vivona ^{3,5}, Margherita Carbonaro ², Alberto Zanella ^{3,5}, Stefano Gatti ¹, Andrea Schlegel ⁶ and Christoph Trautwein ^{4,*}

- ¹ Center for Preclinical Research, Fondazione IRCCS Ca' Granda Ospedale Maggiore Policlinico, Via Pace 9, 20100 Milan, Italy; caterina.lonati@gmail.com (C.L.); michele.battistin@policlinico.mi.it (M.B.); stefano.gatti@policlinico.mi.it (S.G.)
 - ² General and Liver Transplant Surgery Unit, Fondazione IRCCS Ca' Granda Ospedale Maggiore Policlinico, Via Francesco Sforza 35, 20100 Milan, Italy; dondossola.daniele@gmail.com (D.D.); margherita.carbonaro@unimi.it (M.C.)
 - ³ Department of Pathophysiology and Transplantation, University of Milan, Via Francesco Sforza 35, 20100 Milan, Italy; luigi.vivona@unimi.it (L.V.); alberto.zanella1@unimi.it (A.Z.)
 - ⁴ Werner Siemens Imaging Center, Department of Preclinical Imaging and Radiopharmacy, University Hospital Tübingen, Eberhard Karls University of Tübingen, Röntgenweg 13, 72076 Tübingen, Germany; laimdota.zizmare@med.uni-tuebingen.de (L.Z.); leo-h-wuest@t-online.de (L.W.)
 - ⁵ Department of Anesthesia and Critical Care, Fondazione IRCCS Ca' Granda Ospedale Maggiore Policlinico, Via Francesco Sforza 35, 20100 Milan, Italy
 - ⁶ Department of Surgery and Transplantation, Swiss HPB Centre, University Hospital Zurich, 8091 Zürich, Switzerland; schlegel.andrea@outlook.de
- * Correspondence: christoph.trautwein@med.uni-tuebingen.de; Tel.: +49-7071-2983426



Citation: Lonati, C.; Dondossola, D.; Zizmare, L.; Battistin, M.; Wüst, L.; Vivona, L.; Carbonaro, M.; Zanella, A.; Gatti, S.; Schlegel, A.; et al. Quantitative Metabolomics of Tissue, Perfusate, and Bile from Rat Livers Subjected to Normothermic Machine Perfusion. *Biomedicines* **2022**, *10*, 538. <https://doi.org/10.3390/biomedicines10030538>

Academic Editor: Paul Rösch

Received: 30 January 2022

Accepted: 21 February 2022

Published: 24 February 2022

Publisher's Note: MDPI stays neutral with regard to jurisdictional claims in published maps and institutional affiliations.



Copyright: © 2022 by the authors. Licensee MDPI, Basel, Switzerland. This article is an open access article distributed under the terms and conditions of the Creative Commons Attribution (CC BY) license (<https://creativecommons.org/licenses/by/4.0/>).

Abstract: Machine perfusion (MP) allows the maintenance of liver cells in a metabolically active state *ex vivo* and can potentially revert metabolic perturbations caused by donor warm ischemia, procurement, and static cold storage (SCS). The present preclinical research investigated the metabolic outcome of the MP procedure by analyzing rat liver tissue, bile, and perfusate samples by means of high-field (600 MHz) nuclear magnetic resonance (NMR) spectroscopy. An established rat model of normothermic MP (NMP) was used. Experiments were carried out with the addition of an oxygen carrier (Ox) to the perfusion fluid (Ox-NMP, $n = 5$) or without (h-NMP, $n = 5$). Bile and perfusate samples were collected throughout the procedure, while biopsies were only taken at the end of NMP. Two additional groups were: (1) Native, in which tissue or bile specimens were collected from rats in resting conditions; and (2) SCS, in which biopsies were taken from cold-stored livers. Generally, NMP groups showed a distinctive metabolomic signature in all the analyzed biological matrices. In particular, many of the differentially expressed metabolites were involved in mitochondrial biochemical pathways. Succinate, acetate, 3-hydroxybutyrate, creatine, and O-phosphocholine were deeply modulated in *ex vivo* perfused livers compared to both the Native and SCS groups. These novel results demonstrate a broad modulation of mitochondrial metabolism during NMP that exceeds energy production and redox balance maintenance.

Keywords: nuclear magnetic resonance (NMR) spectroscopy; liver machine perfusion (MP); ischemia/reperfusion (IR); mitochondrial metabolism; tricarboxylic acid (TCA) cycle; preclinical research; ketogenesis; succinate; 3-hydroxybutyrate; O-phosphocholine

1. Introduction



The introduction of machine perfusion (MP) significantly changed the clinical scenario of liver transplantation by enabling prolonged *ex situ* preservation, evaluation, and reconditioning of grafts previously deemed unsuitable [1,2]. In fact, relative to static cold storage (SCS), *ex vivo* perfusion allows a paradigm shift from functional suppression to

RESEARCH

Open Access



Acidic ascites inhibits ovarian cancer cell proliferation and correlates with the metabolomic, lipidomic and inflammatory phenotype of human patients

Qianlu Yang¹, Gyuntae Bae², Giorgi Nadiradze^{1,3}, Arianna Castagna^{1,3}, Georgy Berezhnoy², Laimdota Zizmare² , Aditi Kulkarni², Yogesh Singh^{4,5}, Frank J. Weinreich¹, Stefan Kommos⁵, Marc A. Reymond^{1,3} and Christoph Trautwein^{2*} 

Abstract

Background: The poor prognosis of ovarian cancer patients is strongly related to peritoneal metastasis with the production of malignant ascites. However, it remains largely unclear how ascites in the peritoneal cavity influences tumor metabolism and recurrence. This study is an explorative approach aimed at for a deeper molecular and physical–chemical characterization of malignant ascites and to investigate their effect on in vitro ovarian cancer cell proliferation.

Methods: This study included 10 malignant ascites specimens from patients undergoing ovarian cancer resection. Ascites samples were deeply phenotyped by ¹H-NMR based metabolomics, blood-gas analyzer based gas flow analysis and flow cytometry based a 13-plex cytokine panel. Characteristics of tumor cells were investigated in a 3D spheroid model by SEM and metabolic activity, adhesion, anti-apoptosis, migratory ability evaluated by MTT assay, adhesion assay, flowcytometry and scratch assay. The effect of different pH values was assessed by adding 10% malignant ascites to the test samples.

Results: The overall extracellular (peritoneal) environment was alkaline, with pH of ascites at stage II-III = 7.51 ± 0.16, and stage IV = 7.78 ± 0.16. Ovarian cancer spheroids grew rapidly in a slightly alkaline environment. Decreasing pH of the cell culture medium suppressed tumor features, metabolic activity, adhesion, anti-apoptosis, and migratory ability. However, 10% ascites could prevent tumor cells from being affected by acidic pH. Metabolomics analysis identified stage IV patients had significantly higher concentrations of alanine, isoleucine, phenylalanine, and glutamine than stage II-III patients, while stage II-III patients had significantly higher concentrations of 3-hydroxybutyrate. pH was positively correlated with acetate, and acetate positively correlated with lipid compounds. IL-8 was positively

*Correspondence: christoph.trautwein@med.uni-tuebingen.de

² Present Address: Department of Preclinical Imaging and Radiopharmacy, Werner Siemens Imaging Center, University Hospital Tübingen, Tübingen, Germany

Full list of author information is available at the end of the article



© The Author(s) 2022. **Open Access** This article is licensed under a Creative Commons Attribution 4.0 International License, which permits use, sharing, adaptation, distribution and reproduction in any medium or format, as long as you give appropriate credit to the original author(s) and the source, provide a link to the Creative Commons licence, and indicate if changes were made. The images or other third party material in this article are included in the article's Creative Commons licence, unless indicated otherwise in a credit line to the material. If material is not included in the article's Creative Commons licence and your intended use is not permitted by statutory regulation or exceeds the permitted use, you will need to obtain permission directly from the copyright holder. To view a copy of this licence, visit <http://creativecommons.org/licenses/by/4.0/>. The Creative Commons Public Domain Dedication waiver (<http://creativecommons.org/publicdomain/zero/1.0/>) applies to the data made available in this article, unless otherwise stated in a credit line to the data.

RESEARCH REPORT



WILEY

Identification of neurodegeneration indicators and disease progression in metachromatic leukodystrophy using quantitative NMR-based urinary metabolomics

Lucia Laugwitz¹ | Laimdota Zizmare⁴ | Vidiyaah Santhanakumaran¹ |
 Claire Cannet² | Judith Böhringer¹ | Jürgen G. Okun³ | Manfred Spraul¹ |
 Ingeborg Krägeloh-Mann¹ | Samuel Groeschel¹ | Christoph Trautwein⁴

¹Department of Neuropediatrics, Developmental Neurology and Social Pediatrics, University of Tuebingen, Tuebingen, Germany

²Bruker BioSpin GmbH, Ettlingen, Germany

³Dietmar-Hopp Metabolic Center, Children's Hospital Heidelberg, Heidelberg, Germany

⁴Werner Siemens Imaging Center, University of Tuebingen, Tuebingen, Germany

Correspondence

Samuel Gröschel, Department of Neuropediatrics, Developmental Neurology and Social Pediatrics, University of Tuebingen, 72076 Tuebingen, Germany.
 Email: samuel.groeschel@med.uni-tuebingen.de

Funding information

This work was supported by Deutsche Forschungsgemeinschaft grant GR 4688/2-1.

Communicating Editor: Maurizio Scarpa

Abstract

Metachromatic leukodystrophy (MLD) is a lysosomal storage disease caused by a deficiency of the arylsulfatase A (ARSA). ARSA deficiency leads to an accumulation of sulfatides primarily in the nervous system ultimately causing demyelination. With evolving therapeutic options, there is an increasing need for indicators to evaluate disease progression. Here, we report targeted metabolic urine profiling of 56 MLD patients including longitudinal sampling, using ¹H (proton) nuclear magnetic resonance (NMR) spectroscopy. ¹H-NMR urine spectra of 119 MLD samples and 323 healthy controls were analyzed by an in vitro diagnostics research (IVDr) tool, covering up to 50 endogenous and 100 disease-related metabolites on a 600-MHz IVDr NMR spectrometer. Quantitative data reports were analyzed regarding age of onset, clinical course, and therapeutic intervention. The NMR data reveal metabolome changes consistent with a multiorgan affection in MLD patients in comparison to controls. In the MLD cohort, N-acetylaspartate (NAA) excretion in urine is elevated. Early onset MLD forms show a different metabolic profile suggesting a metabolic shift toward ketogenesis in comparison to late onset MLD and controls. In samples of juvenile MLD patients who stabilize clinically after hematopoietic stem cell transplantation (HSCT), the macrophage activation marker neopterin is elevated. We were able to identify different metabolic patterns reflecting variable organ disturbances in MLD, including brain and energy metabolism and inflammatory processes. We suggest NAA in urine as a quantitative biomarker for neurodegeneration. Intriguingly, elevated neopterin after HSCT supports the hypothesis that competent donor macrophages are crucial for favorable outcome.

This is an open access article under the terms of the Creative Commons Attribution License, which permits use, distribution and reproduction in any medium, provided the original work is properly cited.

© 2022 The Authors. *JIMD Reports* published by John Wiley & Sons Ltd on behalf of SSIEM.



MR-spectroscopy in metachromatic leukodystrophy: A model free approach and clinical correlation

Joana Feldmann^{a,1}, Pascal Martin^{b,*,1}, Benjamin Bender^c, Lucia Laugwitz^a, Laimdota Zizmare^d, Christoph Trautwein^d, Ingeborg Krägeloh-Mann^a, Uwe Klose^c, Samuel Groeschel^a

^a Department of Neuropediatrics, Developmental Neurology and Social Pediatrics, University of Tübingen, 72076 Tübingen, Germany

^b Department of Neurology and Epileptology, Hertie Institute for Clinical Brain Research, University of Tübingen, 72076 Tübingen, Germany

^c Department of Diagnostic and Interventional Neuroradiology, University Hospital Tübingen, 72076 Tübingen, Germany

^d Werner Siemens Imaging Center, University of Tübingen, 72076 Tübingen, Germany

ARTICLE INFO

Keywords:

Metachromatic leukodystrophy
MR spectroscopy
NAA
N-acetylaspartate
Urine NMR spectroscopy

ABSTRACT

Background and purpose: Metachromatic leukodystrophy (MLD) is a lysosomal enzyme deficiency disorder leading to demyelination and subsequently to a progressive decline in cognitive and motor function. It affects mainly white matter where changes during the course of the disease can be visualized on T2-weighted MRI as hyperintense areas. Associated changes in brain metabolism can be quantified by MR spectroscopy (MRS) and may give complementary information as biomarkers for disease characterisation and progression. Our study aimed to further investigate the correlation of MRS with clinical parameters for motor and cognitive function by using a model free MRS analysis approach that would be precise and straightforward to implement.

Materials and methods: 53 MRS datasets derived from 29 patients (10 late-infantile, 19 juvenile) and 12 controls were acquired using a semi-LASER CSI sequence covering a slice through the centrum semiovale above the corpus callosum. We defined four regions of interest in the white matter (frontal white matter [FWM] and the cortico-spinal tract [CST] area, each left and right) and one in cortical grey matter. Spectra were analysed using a model and fitting free approach by calculating the definite integral of 10 intervals which were distributed along the whole spectrum. These 10 intervals were orientated towards the main peaks of the metabolites N-acetylaspartate (NAA), creatine, myo-inositol, choline, glutamine/glutamate and aspartate to approximately attribute changes in the intervals to corresponding metabolites. Their ratios to the main creatine peak integral were correlated with clinical parameters assessing motor and cognitive abilities. Furthermore, in a post-hoc analysis, NAA levels of a subset of 21 MR datasets were correlated to NAA levels in urine measured by ¹H (proton) nuclear magnetic resonance (NMR) spectroscopy.

The applied interval integration method was validated in the control cohort against the standard approach, using spectral profile templates of known metabolites (LCModel). Both methods showed good agreement, with coefficients of variance being slightly lower for our approach compared to the related LCModel results. Moreover, the new approach was able to extract information out of the frequency range around the main peaks of aspartate and glutamine where LCModel showed only few usable values for the respective metabolites.

Results: MLD spectra clearly differed from controls. The most pronounced differences were found in white matter (much less in grey matter), with larger values corresponding to main peaks of myo-inositol, choline and aspartate, and smaller values associated with NAA and glutamine. Late-infantile patients had more severe

Abbreviations: ARSA, Arylsulfatase A; Asp, Aspartate; AUC, Area under the curve; Cho, Choline; Cr, Creatine; CSI, Chemical shift imaging; CST, Corticospinal tract; FWM, Frontal white matter; Gln, Glutamine; Glx, Glutamate/Glutamine; GM, Grey matter; GMFC-MLD, Gross motor function score in metachromatic leukodystrophy; IOI, Interval of interest; IQ, Intelligence quotient; MLD, Metachromatic Leukodystrophy; MRI, Magnetic resonance imaging; MRS, Magnetic resonance spectroscopy; Myo, Myo-inositol; NAA, N-acetylaspartate; NMR, Nuclear magnetic resonance; ROI, Region of interest.

* Corresponding author at: Department of Neurology and Epileptology, Hertie Institute for Clinical Brain Research, University of Tübingen, Hoppe-Seyler-Str. 3, 72076 Tübingen, Germany.

E-mail address: pascal.martin@med.uni-tuebingen.de (P. Martin).

¹ Contributed equally.

<https://doi.org/10.1016/j.nicl.2022.103296>

Received 18 July 2022; Received in revised form 23 November 2022; Accepted 14 December 2022

Available online 20 December 2022

2213-1582/© 2022 The Author(s). Published by Elsevier Inc. This is an open access article under the CC BY license (<http://creativecommons.org/licenses/by/4.0/>).



Article

TGF-Beta Modulates the Integrity of the Blood Brain Barrier In Vitro, and Is Associated with Metabolic Alterations in Pericytes

Leonie Schumacher ¹, Rédouane Slimani ^{2,3}, Laimdota Zizmare ⁴ , Jakob Ehlers ¹, Felix Kleine Borgmann ^{2,3} , Julia C. Fitzgerald ⁵ , Petra Fallier-Becker ⁶, Anja Beckmann ⁷, Alexander Grißmer ⁷ , Carola Meier ⁷, Ali El-Ayoubi ¹, Kavi Devraj ^{8,9}, Michel Mittelbronn ^{2,3,10,11,12,13}, Christoph Trautwein ^{4,*} and Ulrike Naumann ^{1,*}

- ¹ Molecular Neurooncology, Department of Vascular Neurology, Hertie Institute for Clinical Brain Research and Center of Neurology, University of Tübingen, 72076 Tübingen, Germany
- ² Department of Cancer Research (DOCR), Luxembourg Institute of Health (LIH), 1445 Strassen, Luxembourg
- ³ Luxembourg Centre of Neuropathology (LCNP), 3555 Dudelange, Luxembourg
- ⁴ Werner Siemens Imaging Center, Department of Preclinical Imaging and Radiopharmacy, University of Tübingen, 72076 Tübingen, Germany
- ⁵ Mitochondrial Biology of Parkinson’s Disease, Department of Neurodegenerative Diseases, Hertie Institute for Clinical Brain Research and Center of Neurology, University of Tübingen, 72076 Tübingen, Germany
- ⁶ Institute for Pathology and Neuropathology, University of Tübingen, 72076 Tübingen, Germany
- ⁷ Department of Anatomy and Cell Biology, Saarland University, 66421 Homburg, Germany
- ⁸ German Cancer Consortium (DKTK), 69120 Heidelberg, Germany
- ⁹ Edinger Institute (Neurological Institute), Goethe University Hospital, 60528 Frankfurt am Main, Germany
- ¹⁰ Luxembourg Centre for Systems Biomedicine (LCSB), University of Luxembourg, 4365 Esch-sur-Alzette, Luxembourg
- ¹¹ Department of Life Sciences and Medicine (DLSM), University of Luxembourg, 4365 Esch-sur-Alzette, Luxembourg
- ¹² Faculty of Science, Technology and Medicine (FSTM), University of Luxembourg, 4365 Esch-sur-Alzette, Luxembourg
- ¹³ National Center of Pathology (NCP), Laboratoire Nationale de Santé (LNS), 3555 Dudelange, Luxembourg
- * Correspondence: christoph.trautwein@med.uni-tuebingen.de (C.T.); ulrike.naumann@uni-tuebingen.de (U.N.)



Citation: Schumacher, L.; Slimani, R.; Zizmare, L.; Ehlers, J.; Kleine Borgmann, F.; Fitzgerald, J.C.; Fallier-Becker, P.; Beckmann, A.; Grißmer, A.; Meier, C.; et al. TGF-Beta Modulates the Integrity of the Blood Brain Barrier In Vitro, and Is Associated with Metabolic Alterations in Pericytes. *Biomedicines* **2023**, *11*, 214. <https://doi.org/10.3390/biomedicines11010214>

Academic Editor: Elmina Mammadova-Bach

Received: 16 December 2022
Accepted: 11 January 2023
Published: 14 January 2023



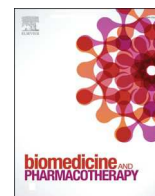
Copyright: © 2023 by the authors. Licensee MDPI, Basel, Switzerland. This article is an open access article distributed under the terms and conditions of the Creative Commons Attribution (CC BY) license (<https://creativecommons.org/licenses/by/4.0/>).

Abstract: The blood–brain barrier (BBB) is a selectively permeable boundary that separates the circulating blood from the extracellular fluid of the brain and is an essential component for brain homeostasis. In glioblastoma (GBM), the BBB of peritumoral vessels is often disrupted. Pericytes, being important to maintaining BBB integrity, can be functionally modified by GBM cells which induce proliferation and cell motility via the TGF- β -mediated induction of central epithelial to mesenchymal transition (EMT) factors. We demonstrate that pericytes strengthen the integrity of the BBB in primary endothelial cell/pericyte co-cultures as an in vitro BBB model, using TEER measurement of the barrier integrity. In contrast, this effect was abrogated by TGF- β or conditioned medium from TGF- β secreting GBM cells, leading to the disruption of a so far intact and tight BBB. TGF- β notably changed the metabolic behavior of pericytes, by shutting down the TCA cycle, driving energy generation from oxidative phosphorylation towards glycolysis, and by modulating pathways that are necessary for the biosynthesis of molecules used for proliferation and cell division. Combined metabolomic and transcriptomic analyses further underscored that the observed functional and metabolic changes of TGF- β -treated pericytes are closely connected with their role as important supporting cells during angiogenic processes.

Keywords: glioblastoma; blood–brain barrier; transforming growth factor beta; metabolomics

1. Introduction

The blood–brain barrier (BBB) is a highly selective barrier that prevents the non-selective transport of molecules from the blood into fluids of the central nervous system



Pyruvate-conjugation of PEGylated liposomes for targeted drug delivery to retinal photoreceptors

Gustav Christensen^a, Yiyi Chen^a, Dileep Urimi^b, Laimdota Zizmare^c, Christoph Trautwein^c, Nicolaas Schipper^b, François Paquet-Durand^{a,*}

^a Institute for Ophthalmic Research, University of Tübingen, Elfriede-Aulhorn Straße 5-7, Tübingen 72076, Germany

^b Division Bioeconomy and Health, Chemical Process and Pharmaceutical Development, RISE Research Institutes of Sweden, Forskargatan 18, Södertälje 15136, Sweden

^c Werner Siemens Imaging Center, Department of Preclinical Imaging and Radiopharmacy, University Hospital Tübingen, Röntgenweg 13, Tübingen 72076, Germany

ARTICLE INFO

Keywords:

Ocular drug delivery
Liposomes
Neurodegenerative therapy
Retinal degeneration
Monocarboxylate transporter
Retinal explant culture

ABSTRACT

Despite several promising candidates, there is a paucity of drug treatments available for patients suffering from retinal diseases. An important reason for this is the lack of suitable delivery systems that can achieve sufficiently high drug uptake in the retina and its photoreceptors. A promising and versatile method for drug delivery to specific cell types involves transporter-targeted liposomes, i.e., liposomes surface-coated with substrates for transporter proteins highly expressed on the target cell. We identified strong lactate transporter (monocarboxylate transporter, MCT) expression on photoreceptors as a potential target for drug delivery vehicles. To evaluate MCT suitability for drug targeting, we used PEG-coated liposomes and conjugated these with different monocarboxylates, including lactate, pyruvate, and cysteine. Monocarboxylate-conjugated and dye-loaded liposomes were tested on both human-derived cell-lines and murine retinal explant cultures. We found that liposomes conjugated with pyruvate consistently displayed higher cell uptake than unconjugated liposomes or liposomes conjugated with lactate or cysteine. Pharmacological inhibition of MCT1 and MCT2 reduced internalization, suggesting an MCT-dependent uptake mechanism. Notably, pyruvate-conjugated liposomes loaded with the drug candidate CN04 reduced photoreceptor cell death in the murine *rd1* retinal degeneration model while free drug solutions could not achieve the same therapeutic effect. Our study thus highlights pyruvate-conjugated liposomes as a promising system for drug delivery to retinal photoreceptors, as well as other neuronal cell types displaying high expression of MCT-type proteins.

1. Introduction

Inherited retinal degeneration (IRD) relates to a group of diseases, including retinitis pigmentosa and Leber's congenital amaurosis, characterized by the progressive loss of photoreceptors, which ultimately leads to blindness [1–3]. Typically, IRD-type diseases display a primary loss of rod photoreceptors, which are responsible for vision under dim light conditions. Accordingly, initial disease symptoms include night-blindness. Once rods are lost, the cone photoreceptors, which mediate color and high acuity vision under daylight conditions, are also degenerating, ultimately leading to complete blindness. To date, IRD-type diseases remain essentially untreatable, creating a high need for new therapeutic developments.

In many types of IRD, high levels of cyclic guanosine monophosphate (cGMP) in rod photoreceptors, caused for instance by the impairment of

phosphodiesterase 6 (PDE6), are found [3]. Pathological concentrations of cGMP cause over-activation of important cGMP-dependent proteins, which eventually leads to cell death [4]. The drug candidate CN04 is an inhibitory analogue to cGMP (Fig. 1) and has been shown to promote survival of rod photoreceptors in mouse models of IRD, including the *rd1* mouse model [5]. The rescue of rod photoreceptors typically provides functional protection of cone photoreceptors [6].

To ensure a successful translation for clinical use, CN04 will need to be delivered to photoreceptors in high enough concentrations to provide a protective effect. For this, a suitable drug delivery system is necessary. Previously, glutathione-conjugated liposomes were shown to enhance the therapeutic effect of cGMP analogues in IRD mouse models after systemic administration [5]. These liposomes were designed for drug permeation across the blood-retinal barrier [7,8]. However, as a local administration, intravitreal (IVT) injections are superior in delivering

* Corresponding author.

E-mail address: francois.paquet-durand@uni-tuebingen.de (F. Paquet-Durand).

<https://doi.org/10.1016/j.bioph.2023.114717>

Received 16 March 2023; Received in revised form 13 April 2023; Accepted 14 April 2023

Available online 21 April 2023

0753-3322/© 2023 The Authors. Published by Elsevier Masson SAS. This is an open access article under the CC BY license (<http://creativecommons.org/licenses/by/4.0/>).

7.3. Poster Presentations

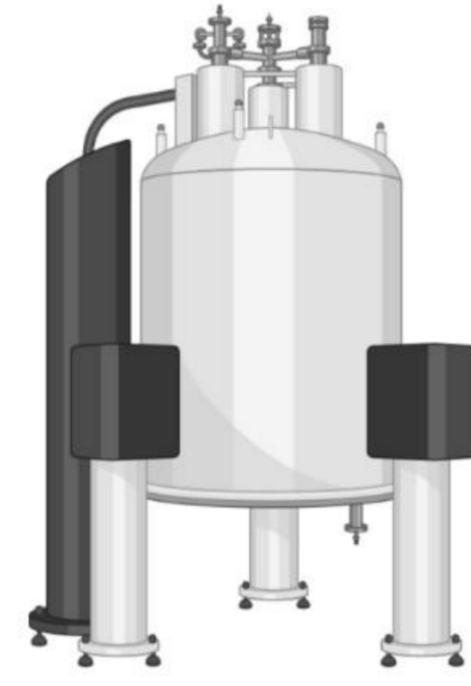


NMR spectroscopy-based metabolomics assessment of immunometabolism and oxidative stress-related metabolism in murine and human samples

Laimdota Zizmare¹, Roman Mehling¹, Irina Mäurer^{2,3}, Christina N. Boyle⁴, Sabrina Buss¹, Sandrine Louis⁵, Ralf Krüger⁵, Manuel Rodriguez Gomez⁵, Irene Gonzalez-Menendez^{6,7}, Caterina Lonati⁸, Leticia Quintanilla-Martinez^{6,7}, Marco Skardelly^{2,3,9}, Ghazaleh Tabatabai^{2,3,7,10}, Bernd J. Pichler^{1,7,10}, Yvonne Ritze¹¹, Kristina Herfert¹, Manfred Kneilling^{1,7,12}, Christoph Trautwein¹

INTRODUCTION

- Immunometabolism and oxidative stress-related metabolism play a crucial role in health maintenance and disease progression.
- Our aim:** to identify metabolic processes and bio-molecular events under oxidative stress in two preclinical and one clinical research project. The obtained knowledge should stratify **novel targets** for **future diagnostics** and **therapeutic interventions**.
- We employed 14.1 T (600 MHz for proton) nuclear magnetic resonance ¹H-NMR spectroscopy tissue, plasma and fecal metabolomics with a ultra-sensitive 1.7 mm triple resonance (TXI) room temperature microprobe. This allowed performing experiments with very low sampling material, ideal for precious samples from preclinical and clinical biopsy tissues.



SUMMARY

- Our findings underpin several biomolecular events taking place during **inflammation progression, gut-brain axis** and **tumor stratification** providing crucial knowledge for early therapeutic intervention:
- Project #1:** Acute inflammation results in increased GSH and GSSG concentrations suggesting a **systemic immune response** and ongoing reactive oxygen and nitrogen species (RONS) activity while ascorbate and taurine increase was characteristic to chronic DTHR in a mouse model;
- Project #2:** Immune and hormonal parameter, such as C-reactive protein and lipopolysaccharide-binding protein, correlations with metabolomics revealed **de novo lipogenesis** pathway upregulation as one of many factors leading to RYGB surgery success in rats;
- Project #3:** Human brain **tumor origin and mutations** have a direct effect of metabolomic readout, progression speed and also susceptibility to therapy.

RESULTS

Project #1: Acute and chronic inflammation alter immunometabolism in a cutaneous delayed-type hypersensitivity reaction (DTHR) mouse model

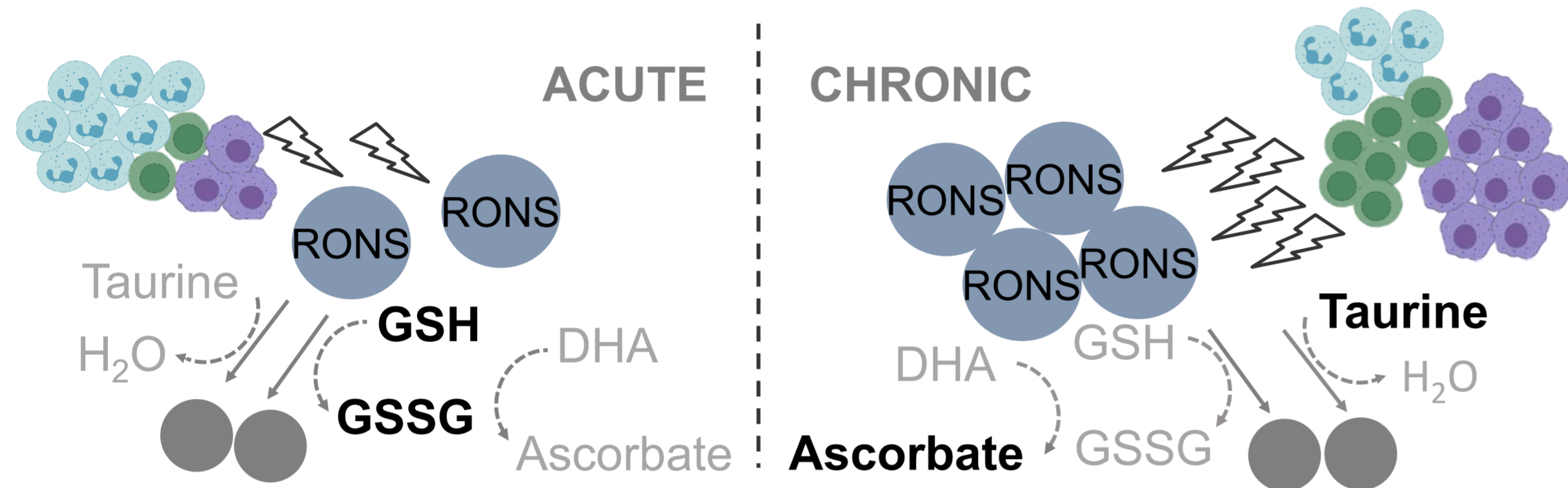


Fig. 1: Different reactive oxygen and nitrogen species scavengers dominate in acute and chronic inflammation phase, related to resident and infiltrated immune cell presence, inflammation persistence and substrate availability.

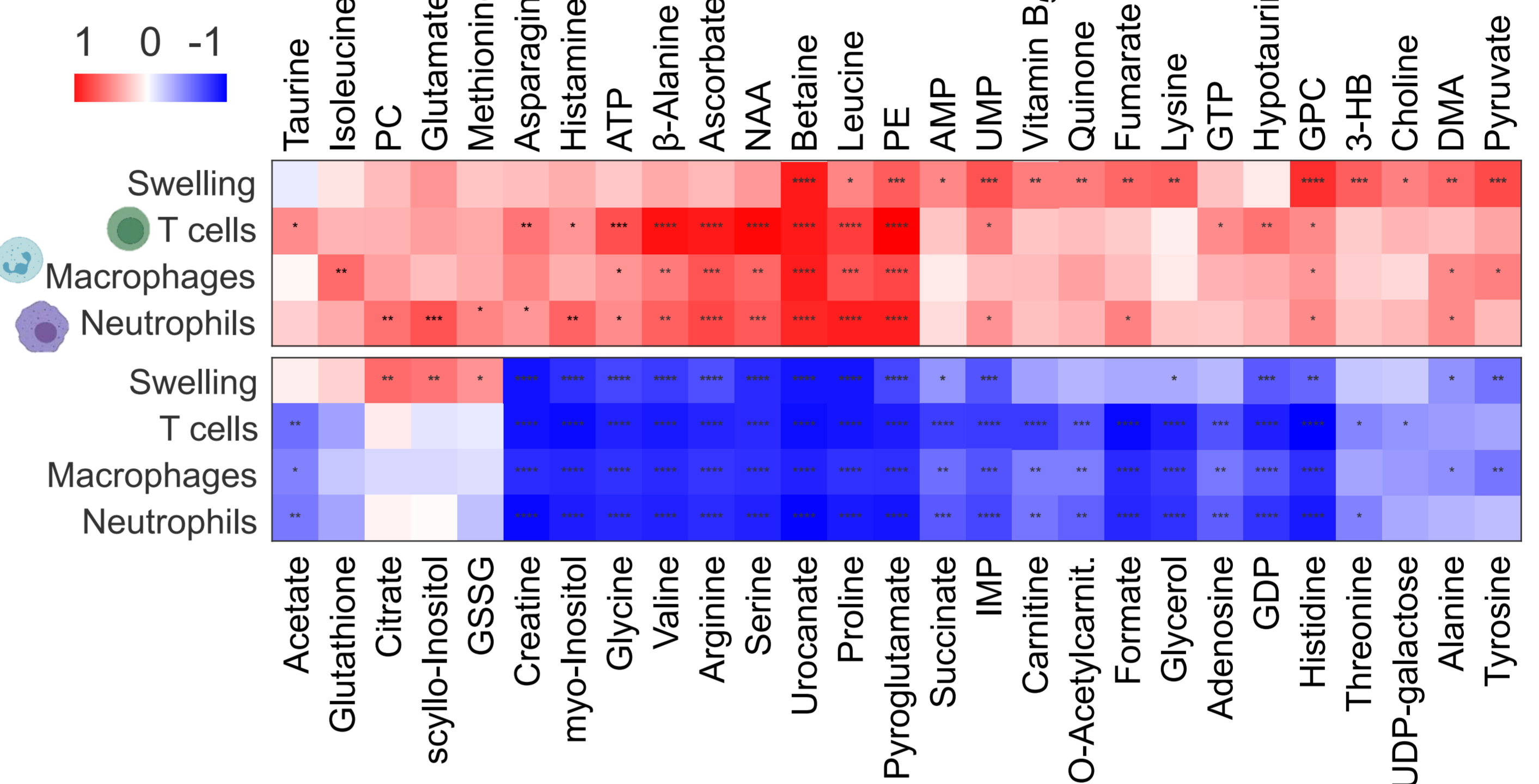


Fig. 2: Ear swelling thickness, T cell, macrophage and neutrophil epidermal inflammation scores were correlated to metabolite concentration changes over, positive correlation (red) and negative correlation (blue) with correlation coefficient statistical significance p values: **** < 0.0001, *** < 0.001, ** < 0.01, * < 0.05.

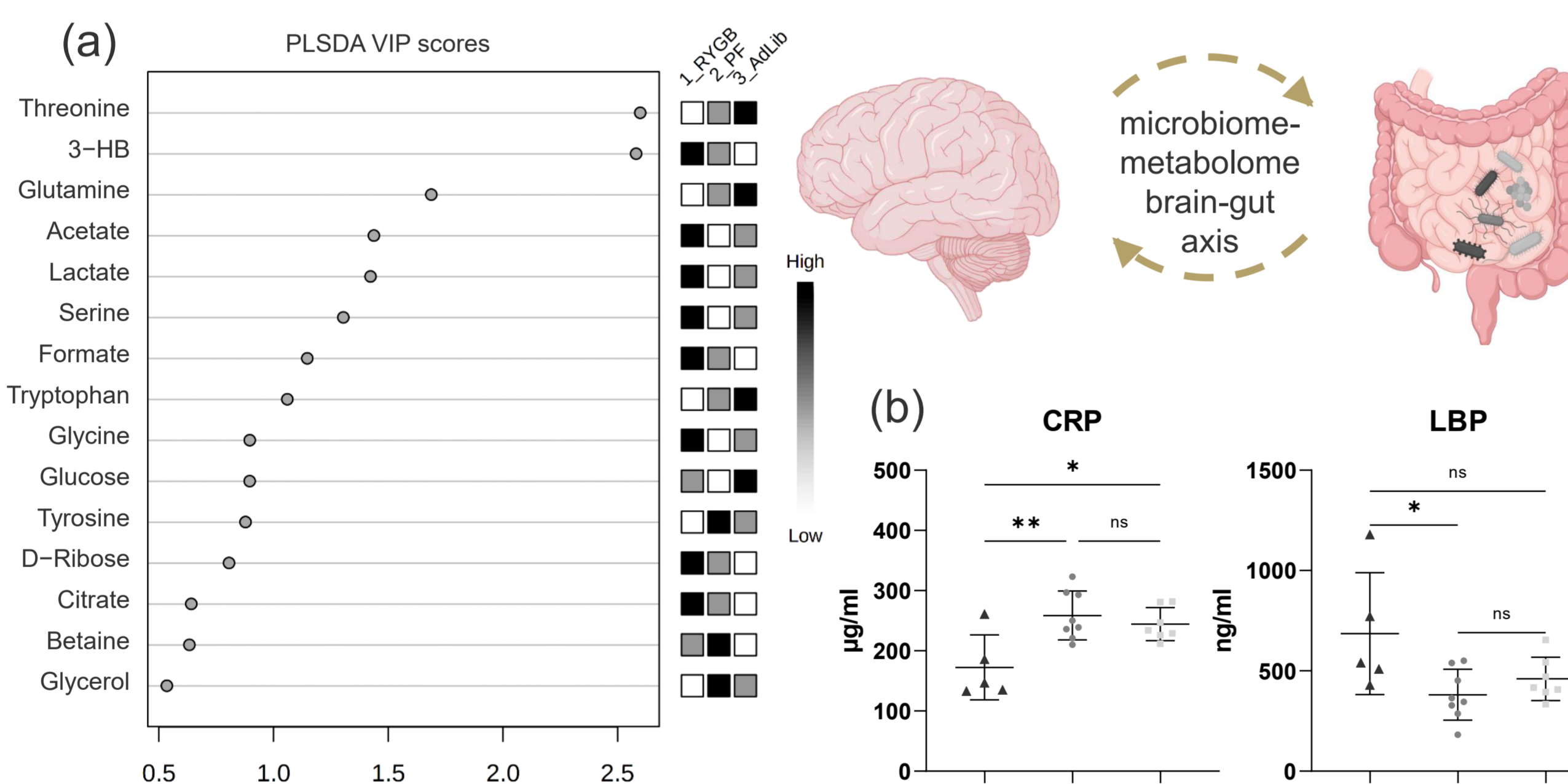
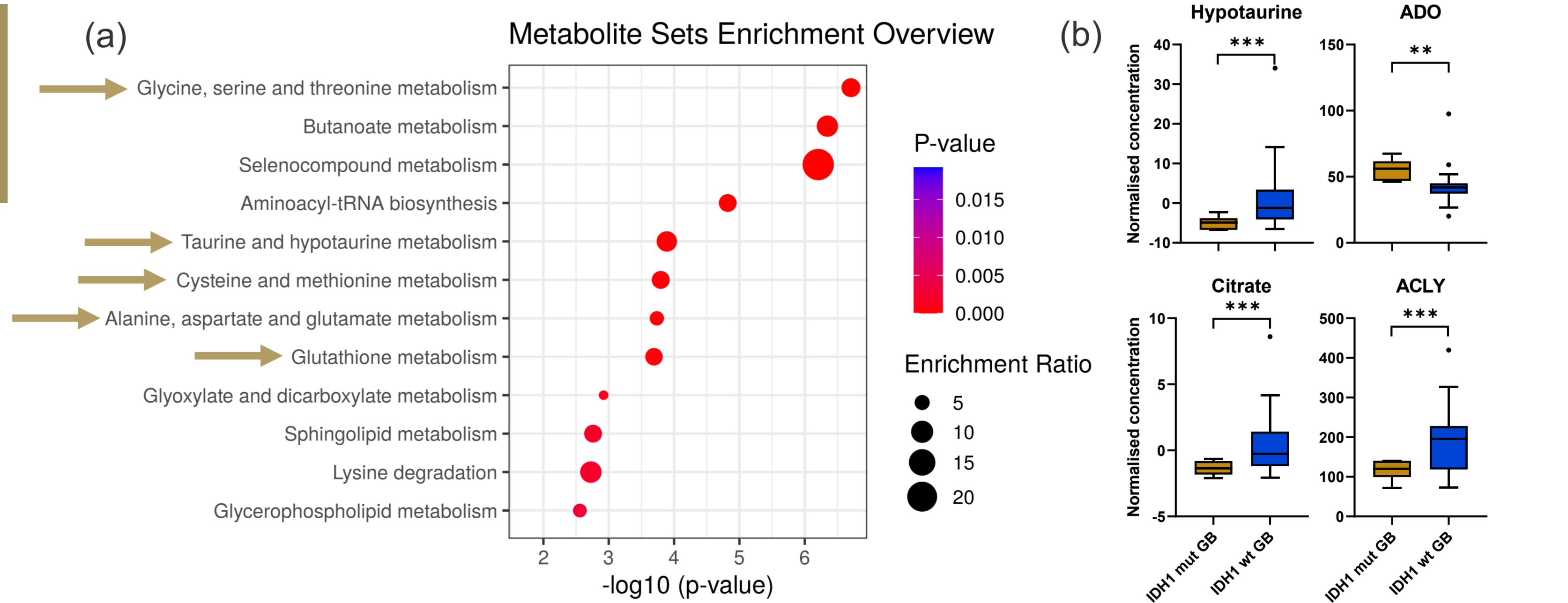


Fig. 3: Rat plasma metabolites (a) together with blood parameters (b) and fecal metabolites (c) indicate systemic alterations in RYGB animals compared to paired (PF) and ad libitum-fed (AdLib) towards upregulated de novo lipogenesis, together with lowered appetite and weight gain.

Project #3: Tissue metabolites in diffuse glioma and their modulations by IDH1 mutation, histology, and treatment



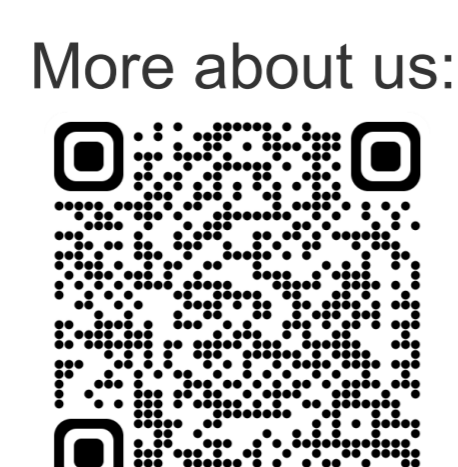
Fig. 4: (a) Amino acid metabolism and redox-related metabolic pathways were mostly altered when comparing 62 IDH1 mutated and 39 IDH1 wildtype (wt) glioma patients by ¹H-NMR tissue biopsy metabolomics. (b) Mutated and wt glioblastoma (GB) subtype metabolomics revealed correlating trends in gene expression for hypotaurine and 2-aminoethanethiol dioxigenase (ADO), and citrate with ATP citrate synthase (ACLY) confirming oxidative-stress related observed metabolic alterations on the transcriptome level.



ACKNOWLEDGEMENTS

We acknowledge the support from Werner Siemens Foundation and technical support by Funda Cay, Maren Harant, Natalie Hermann, Miriam Owczorz, Georgy Berezhnoy and Aditi Kulkarni. Further details, people involved, detailed methods, literature references and funding are disclosed in corresponding publication links.

¹Werner Siemens Imaging Center, Department of Preclinical Imaging and Radiopharmacy, Eberhard Karls University of Tübingen; ²Department of Neurology & Interdisciplinary Neuro-Oncology, ³Center for Neuro-Oncology, Comprehensive Cancer Center Tübingen; ⁴Institute of Veterinary Physiology, University of Zurich, Switzerland; ⁵Department of Physiology and Biochemistry of Nutrition, Max Rubner-Institut, Karlsruhe; ⁶Institute of Pathology and Neuropathology, Comprehensive Cancer Center; ⁷Cluster of Excellence iFIT (EXC 2180) "Image-Guided and Functionally Instructed Tumor Therapies", Eberhard Karls University of Tübingen; ⁸Center for Preclinical Research, Fondazione IRCCS Ca' Granda Ospedale Maggiore Policlinico, Via Pace 9, 20100 Milan, Italy; ⁹Department of Neurosurgery, University Hospital Tübingen, Eberhard Karls University Tübingen; ¹⁰German Cancer Consortium (DKTK), Deutsches Krebs Forschungszentrum partner site Tübingen, ¹¹Department of Medical Psychology, Eberhard Karls University of Tübingen; ¹²Department of Dermatology, Eberhard Karls University of Tübingen.



Acute and chronic inflammation exhibit oxidative stress-responsive dynamic immunometabolism phenotype in a cutaneous delayed-type hypersensitivity reaction (DTHR) mouse model

Laimdota Zizmare¹, Roman Mehling¹, Irene Gonzalez-Menendez^{2,3}, Caterina Lonati⁴, Leticia Quintanilla-Martinez^{2,3}, Bernd J. Pichler^{1,2}, Manfred Kneilling^{1,2,5}, Christoph Trautwein¹

¹Werner Siemens Imaging Center, Department of Preclinical Imaging and Radiopharmacy, Eberhard Karls University of Tübingen; ²Cluster of Excellence iFIT (EXC 2180) "Image-Guided and Functionally Instructed Tumor Therapies", Eberhard Karls University of Tübingen; ³Institute of Pathology and Neuropathology, Comprehensive Cancer Center, Eberhard Karls University, Tübingen; ⁴Center for Preclinical Research, Fondazione IRCCS Ca' Granda Ospedale Maggiore Policlinico, Via Pace 9, 20100 Milan, Italy; ⁵Department of Dermatology, Eberhard Karls University of Tübingen, Germany

INTRODUCTION

- T-cell-driven acute and chronic **inflammatory immune responses** characterise inflammatory disorders, such as psoriasis, rheumatoid arthritis and ulcerative colitis.
- Our aim:** to identify the longitudinal metabolic processes and biomolecular events, responsible for the switch from **acute** to **chronic inflammation**.
- Such metabolic markers can further serve as diagnostic and therapeutic targets providing valuable knowledge towards the development of **personalised anti-inflammatory theranostics**.

METHODS

- Cutaneous DTHR was induced by repeated trinitrochlorobenzene (TNCB) sensitisation of the mouse abdomen and ear [1,2].
- Acute and chronic DTHR selected points in time [2] were characterised by:
 - ¹H-NMR spectroscopy-based metabolomics;
 - histopathology (H&E) and immunohistochemistry.

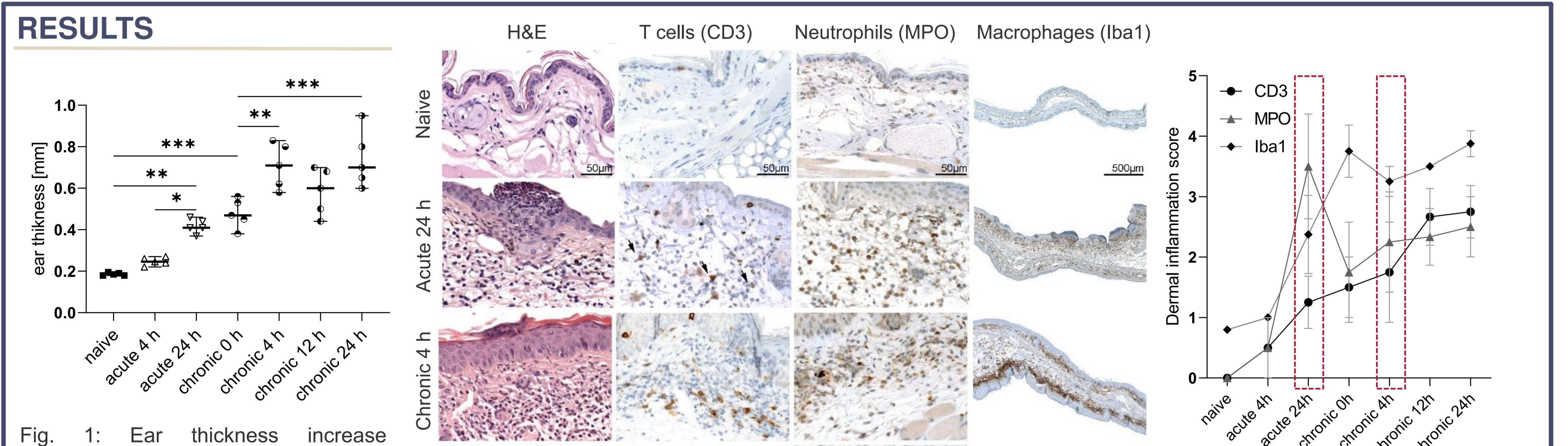


Fig. 1: Ear thickness increase alongside the progression of inflammation.

Fig. 2: Histopathology and immunohistochemistry reveal immune cell infiltration upon acute DTHR 24 h post 1st TNCB challenge, and chronic DTHR 4 h after 5th cutaneous TNCB ear tissue challenge.

Fig. 3: Dermal inflammation score illustrated for CD3, MPO and Iba1 with highlighted inflammation peaks.

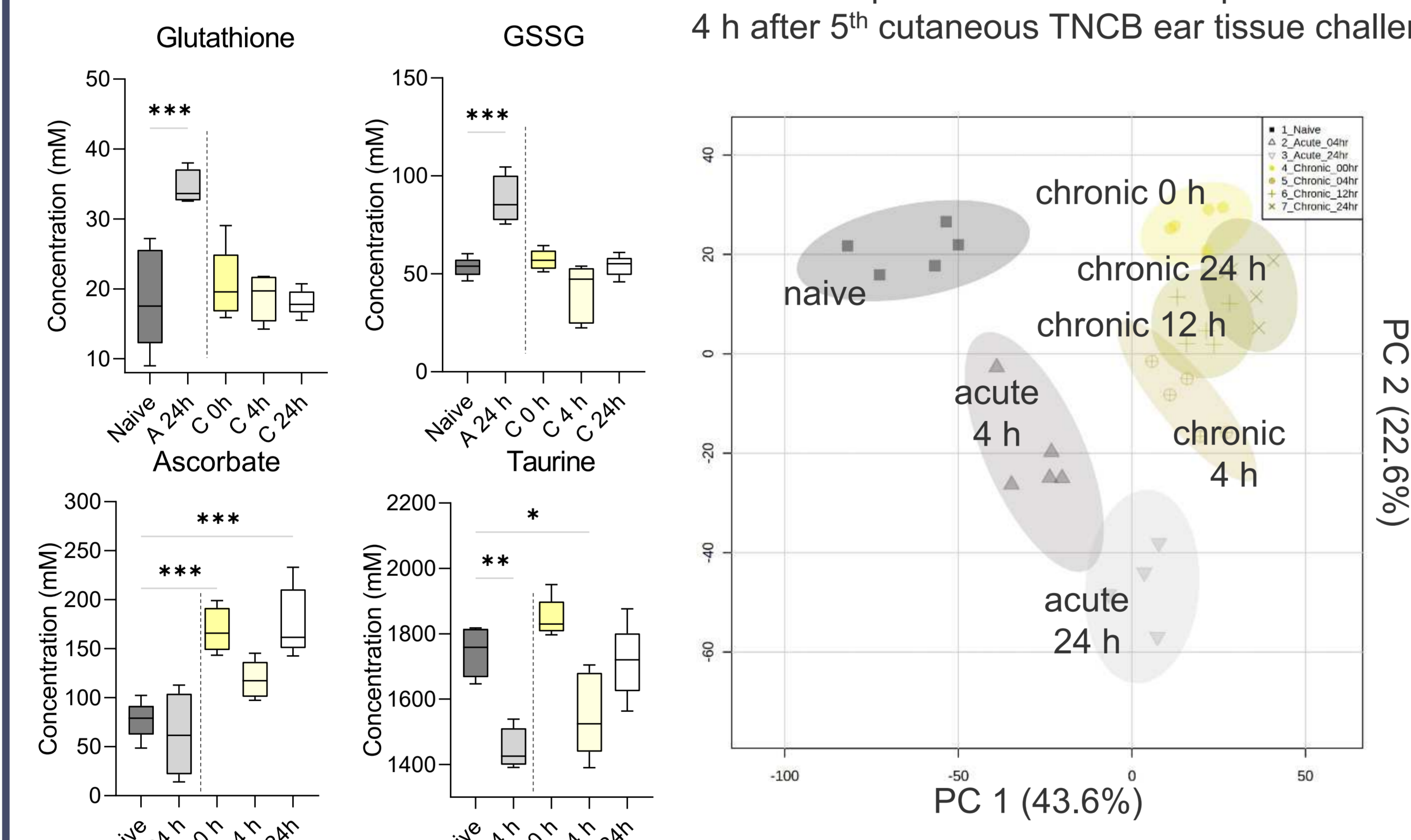


Fig. 4: Redox metabolism-related metabolites changed upon acute and chronic DTHR.

Fig. 5: Principal component analysis (PCA) illustrates a distinctive metabolite profiles at each point in time of the investigation.

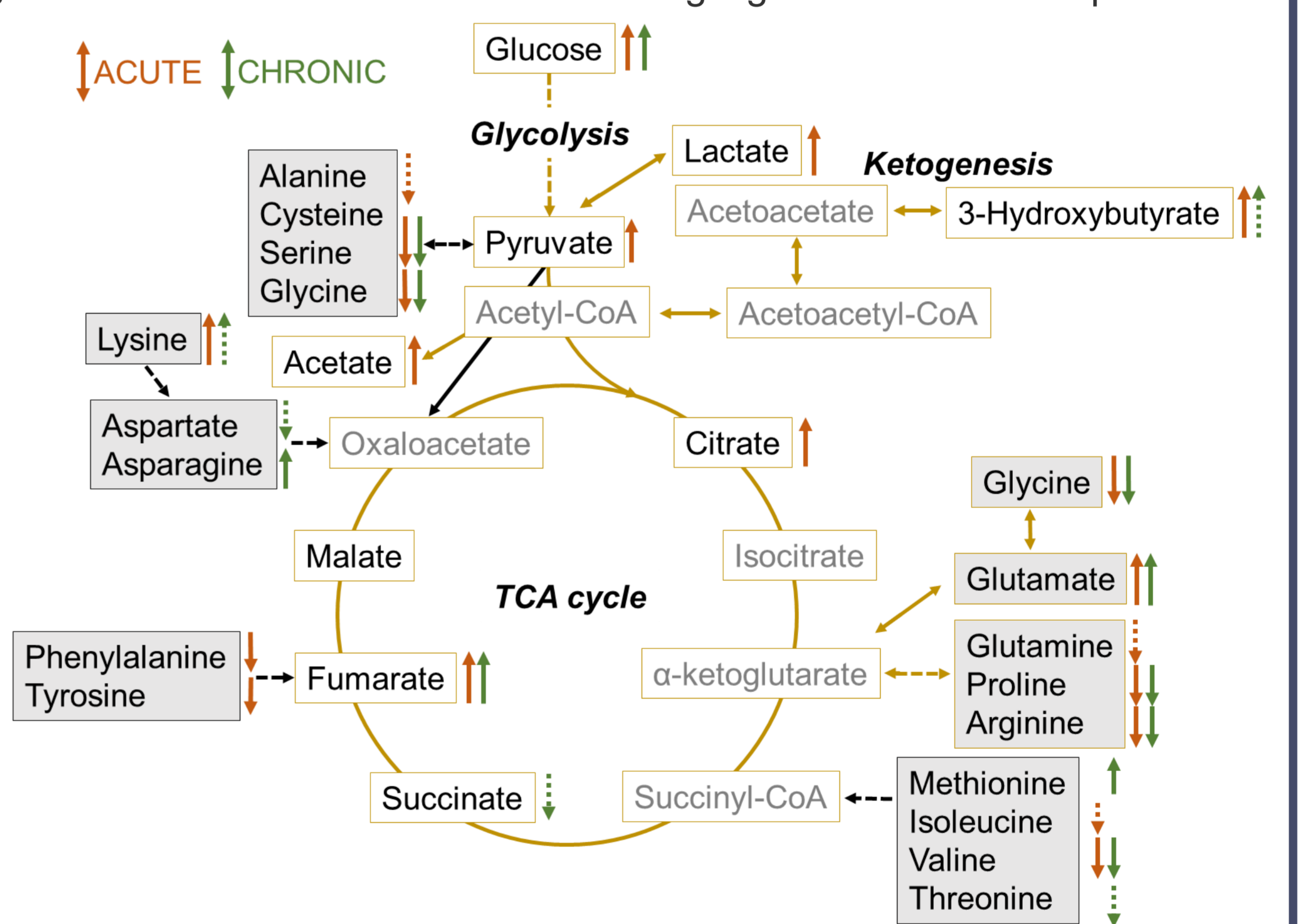


Fig. 6: Pathway connection illustration of glycolysis, ketogenesis and TCA cycle with related metabolite concentration changes compared to naive control.

CONCLUSIONS

ACUTE

CHRONIC

- Our findings underpin several biomolecular events taking place during **inflammation progression** providing crucial knowledge for early therapeutic intervention;
- Acute inflammation is driven by resident cells and infiltrating neutrophils, while the chronic phase has an increased accumulation of T cells and macrophages;
- Acute DTHR resulted in increased GSH and GSSG concentrations suggesting **systemic immune response** and ongoing reactive oxygen and nitrogen species (RONS) activity; ascorbate and taurine increase was characteristic of chronic DTHR;
- TCA cycle** activity was **disrupted** both by acute and chronic DTHR, indicated by downregulated amino acids, accumulated glycolysis metabolites and ketone bodies.

REFERENCES

[1] Mehling, R. et al. Immunomodulatory role of reactive oxygen species and nitrogen species during T cell-driven neutrophil-enriched acute and chronic cutaneous delayed-type hypersensitivity reactions. *Theranostics* 11, 470-490 (2021). <https://doi.org/10.7155/thno.51462>.
 [2] Schwenc, J. et al. Temporal Dynamics of Reactive Oxygen and Nitrogen Species and NF-kappa B Activation During Acute and Chronic T Cell-Driven Inflammation. *Molecular Imaging and Biology* 22, 504-514 (2020). <https://doi.org/10.1007/s11307-019-01412-8>.
 [3] Images and figures have been created with www.MetaboAnalyst.ca 4.0 (PCA), GraphPad Prism (box plots) and www.biorender.com (2022).

ACKNOWLEDGEMENTS This work was supported by Werner Siemens Foundation and German Research Foundation (SFB TRR156, TP C03 to M.K.). The authors thank Funda Cay, Maren Harant, Natalie Hermann, Miriam Owczorz, Georgy Berezhnoy and Aditi Kulkarni for technical support. This work has been submitted for publication.

Investigation of Roux-en-Y gastric bypass (RYGB) and high-sucrose diet influence on the rat brain-gut axis communication

Laimdota Zizmare¹, Sabrina Buss¹, Laura Kuebler¹, Christina Neuner Boyle², Ketki Mulay³, Lara Steinhauer⁴, Manuel Rodriguez Gomez⁴, Kristina Herfert¹, Sandrine Louis⁴, Yvonne Ritze³, Christoph Trautwein¹

¹Werner Siemens Imaging Center, Department of Preclinical Imaging and Radiopharmacy, Eberhard Karls University of Tübingen, Germany

³Department of Medical Psychology, Eberhard Karls University of Tübingen, Germany

⁴Department of Physiology and Biochemistry of Nutrition, Max Rubner-Institut, Karlsruhe, Germany

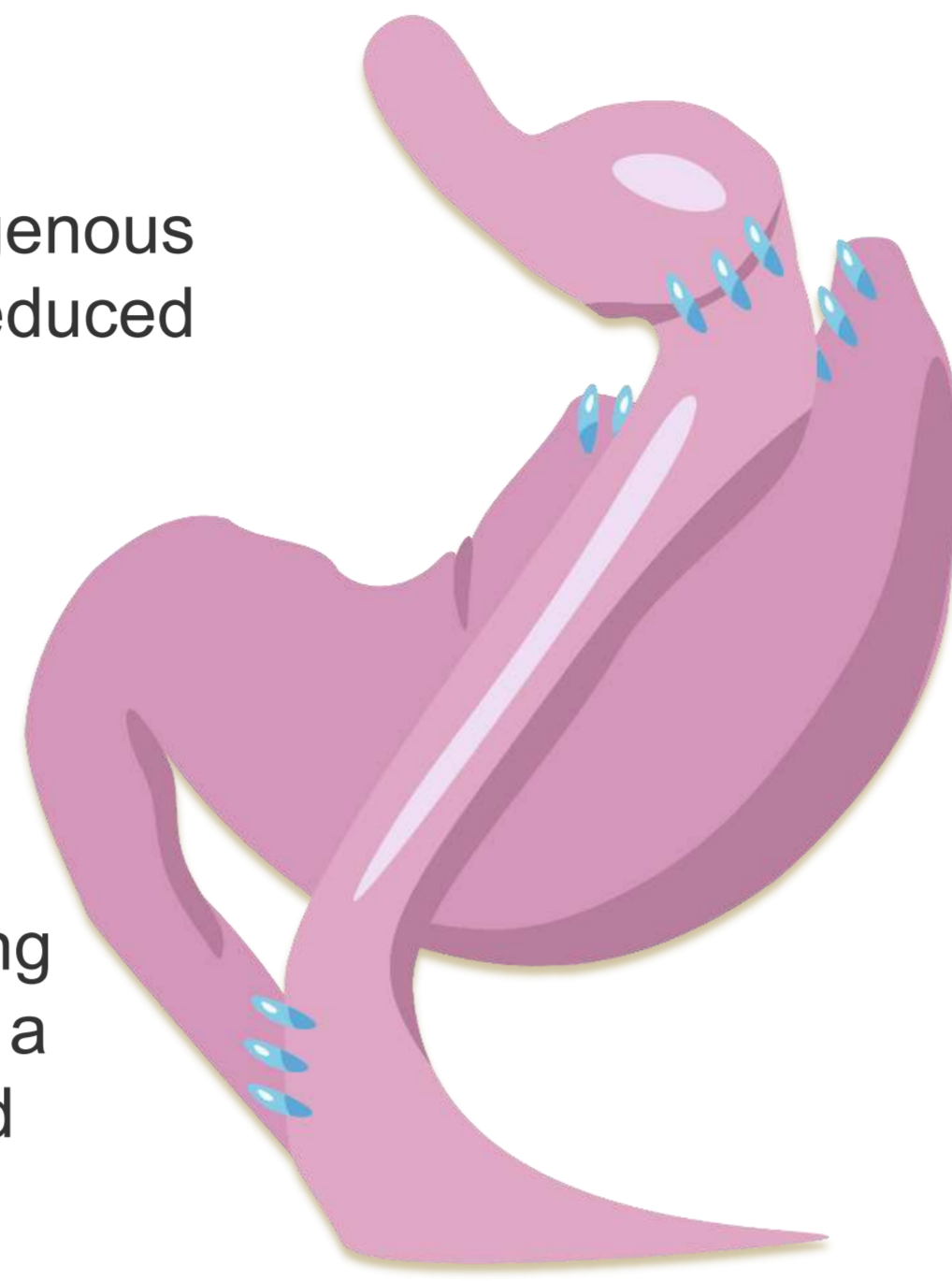
²Institute of Veterinary Physiology, University of Zurich, Switzerland

INTRODUCTION

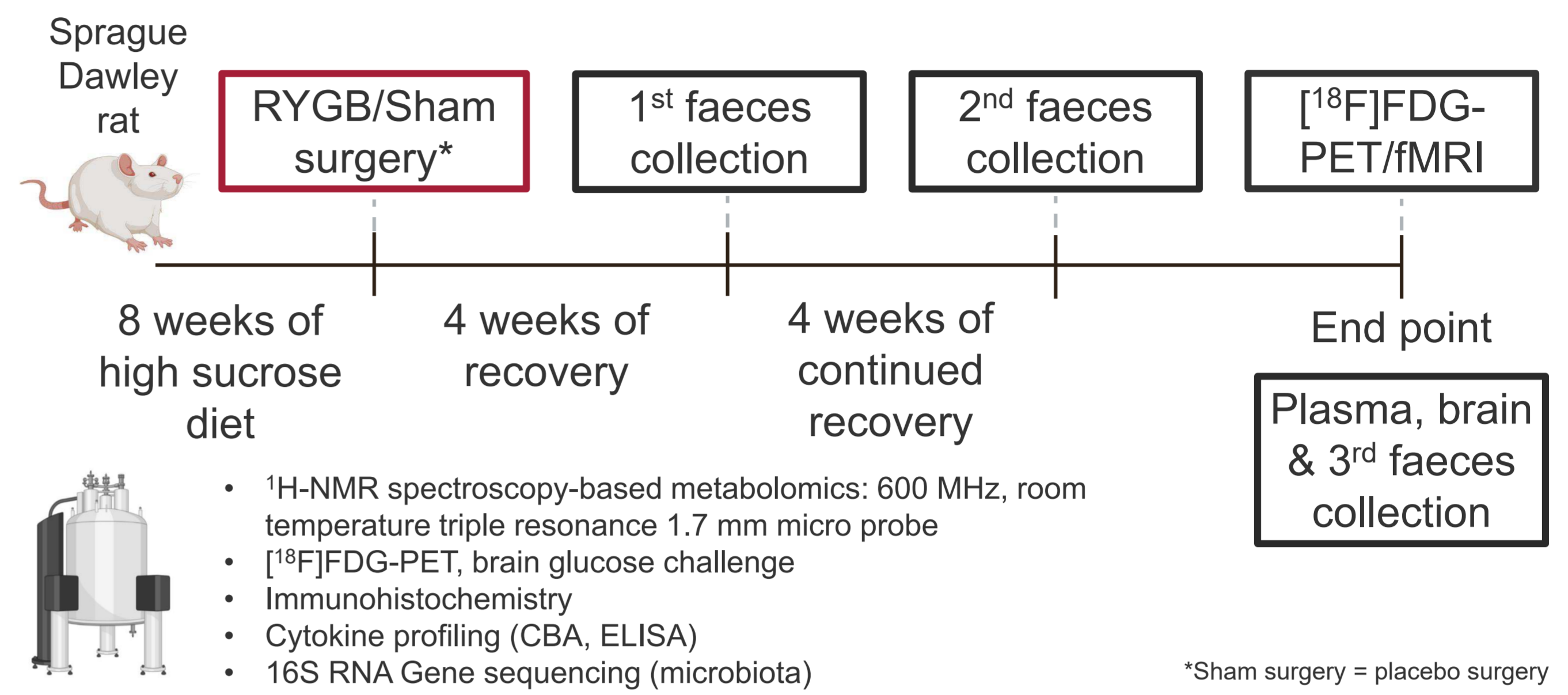
RYGB surgery has been linked to an endogenous neurological brain response resulting in reduced obesity^(1,2).

Hypothesis: weight loss could be achieved by pharmaceutical agent, triggering a similar brain response without the invasive RYGB surgery.

Our aim: to characterise the effects on brain activity and metabolome by surgically modifying the brain-gut axis (RYGB) and comparing it to a Sham surgery with high sucrose liquid diet (Ad Libitum) or similar caloric intake (Pair Fed).



METHODS



RESULTS

Body weight, sucrose water and food intake

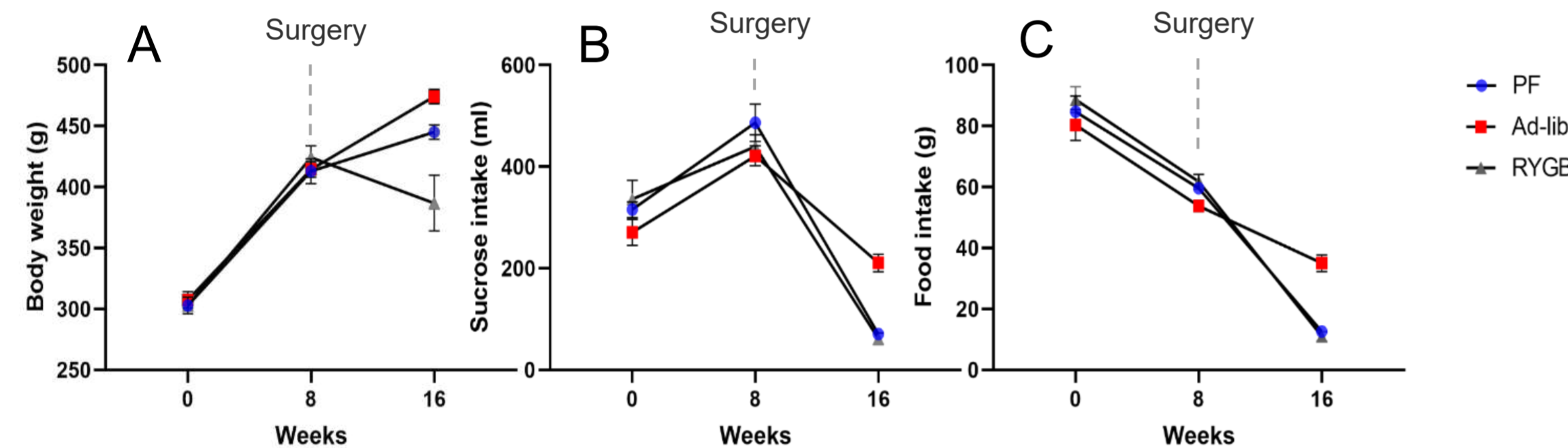


Figure 1: Average body weight (A), sucrose water intake (B) and food intake (C) before and after the RYGB/Sham surgery. Ad Libitum weight increase correlated to their food intake. Pair Fed (PF) animal weight continued increasing despite the limited food and sucrose intake compared to RYGB group.

Faeces metabolomics

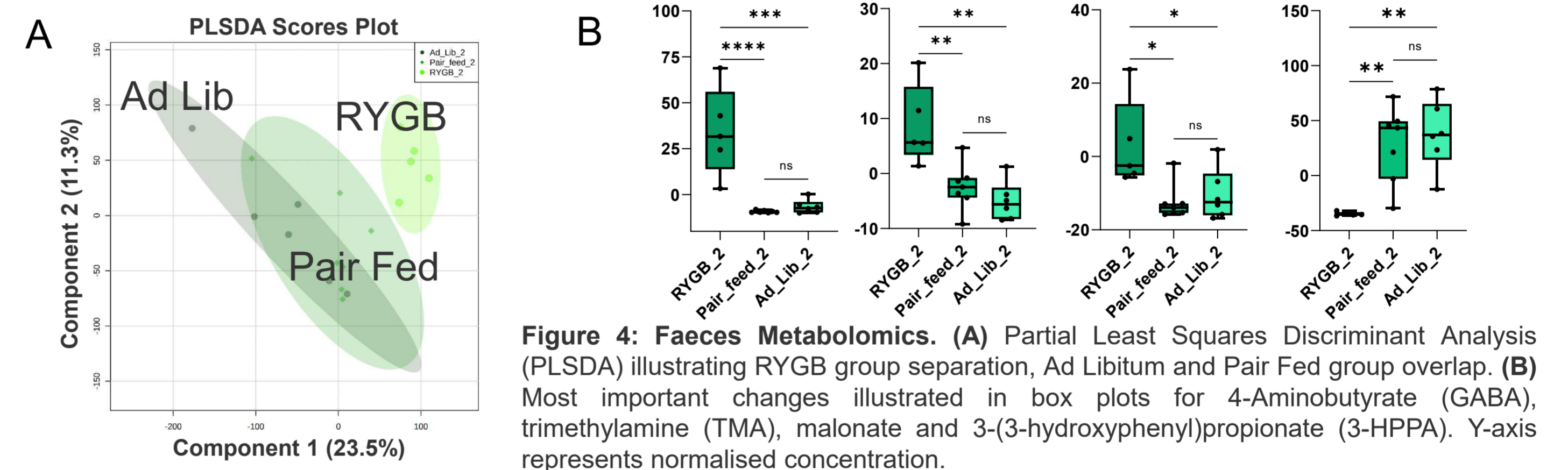


Figure 4: Faeces Metabolomics. (A) Partial Least Squares Discriminant Analysis (PLS-DA) illustrating RYGB group separation, Ad Libitum and Pair Fed group overlap. (B) Most important changes illustrated in box plots for 4-Aminobutyrate (GABA), trimethylamine (TMA), malonate and 3-(3-hydroxyphenyl)propionate (3-HPPA). Y-axis represents normalised concentration.

Immunofluorescent staining of c-Fos

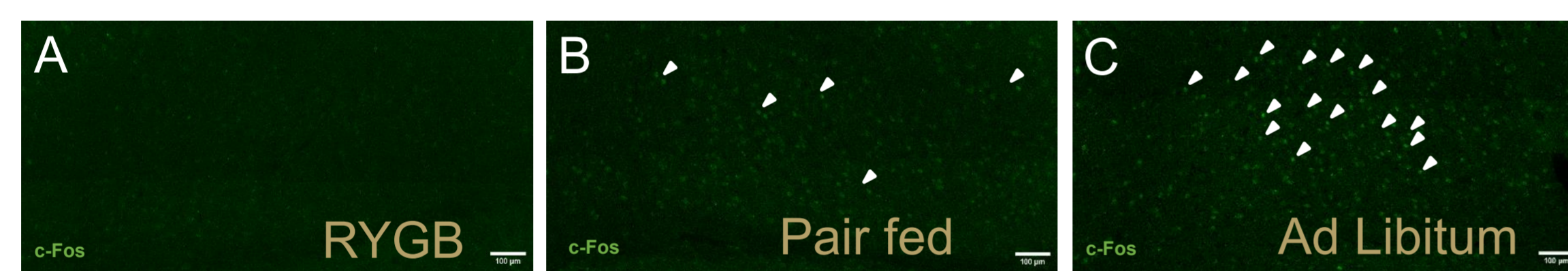


Figure 2: c-Fos staining in dorsal endopiriform nucleus (Den). Decreased c-Fos (marker for neuronal activation) cell count (green) in RYGB (A) and pair feed (B) rat groups compared to Ad Libitum (C).

Cytokines

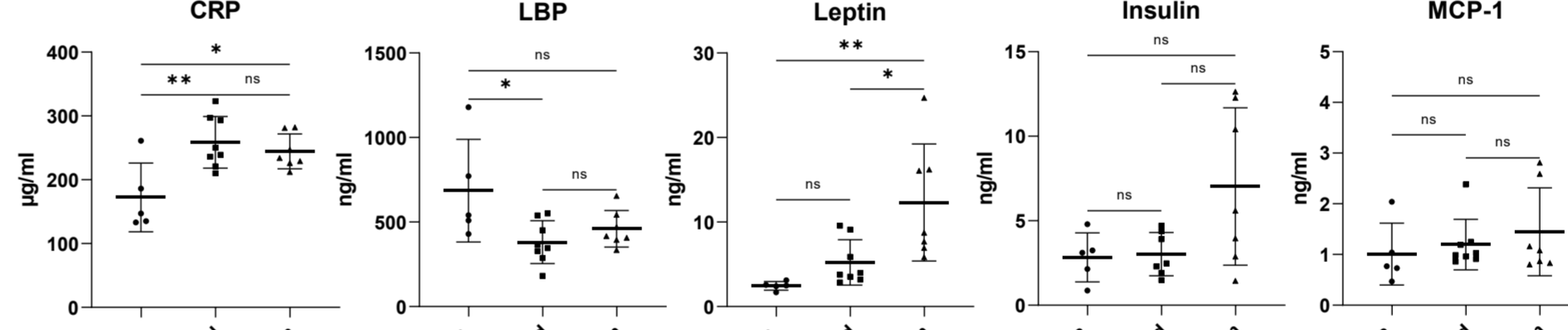


Figure 5: Cytokine profiling. Box plots visualising the downregulated C-reactive protein (CRP) and upregulated lipopolysaccharide-binding protein (LBP) in RYGB compared to Pair Fed animals. Leptin was downregulated both in RYGB and Pair fed animals compared to Ad Libitum. We did not quantify significant differences in insulin and monocyte chemoattractant protein 1 (MCP-1) concentrations.

Plasma metabolomics

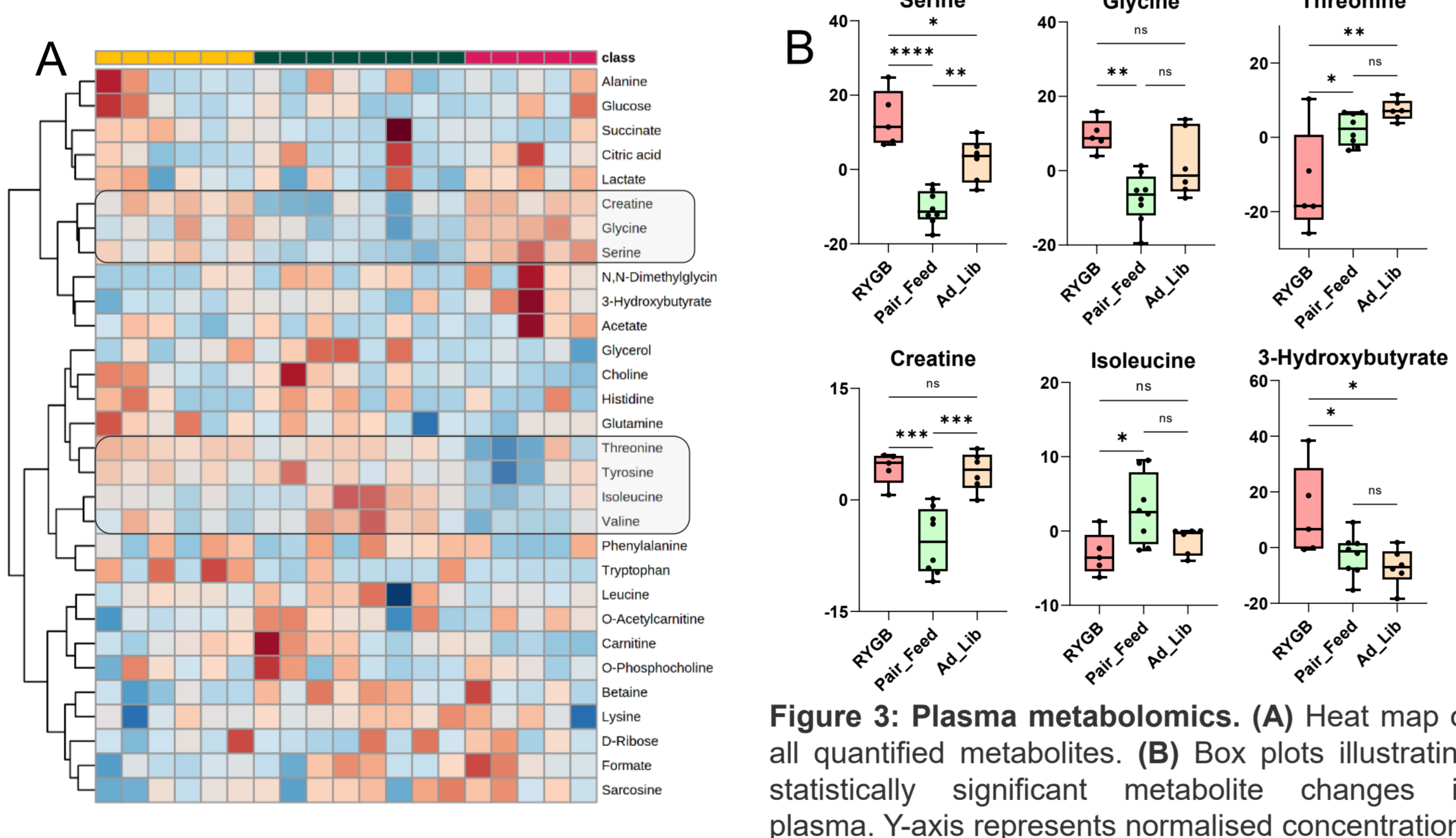


Figure 3: Plasma metabolomics. (A) Heat map of all quantified metabolites. (B) Box plots illustrating statistically significant metabolite changes in plasma. Y-axis represents normalised concentration.

[18F]FDG-PET imaging

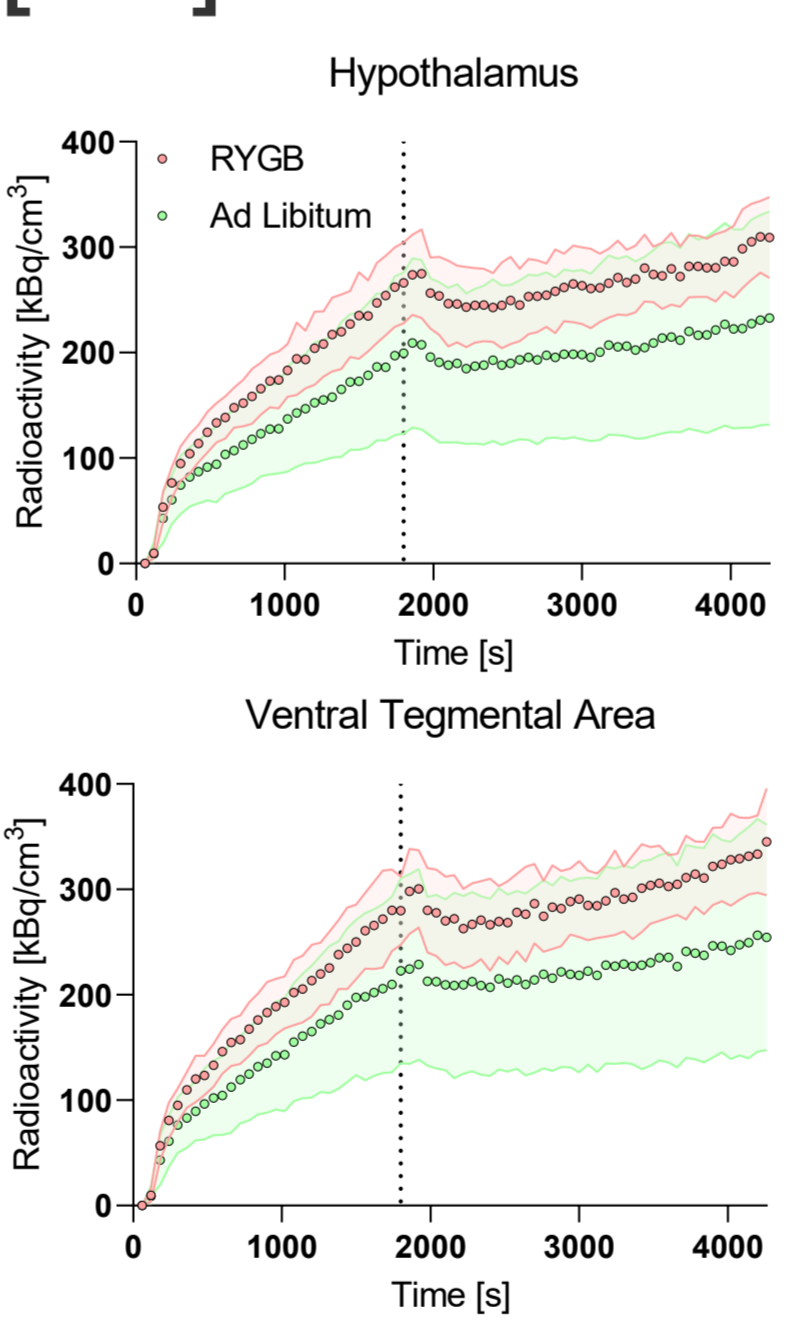


Figure 6: Time activity curves of continuous [18F]FDG infusion with glucose challenge. Fluorodeoxyglucose (¹⁸F) ([18F]FDG) – a radiolabeled glucose analogue – mean time activity curves showing an increased uptake in hypothalamus (responsible for body homeostasis, including appetite and weight control) and ventral tegmental area (responsible for reward cognition) in RYGB animals compared to Ad Libitum group. Glucose challenge was applied at 1800 s (dotted line) and resulted in reduced tracer uptake.

Microbiome

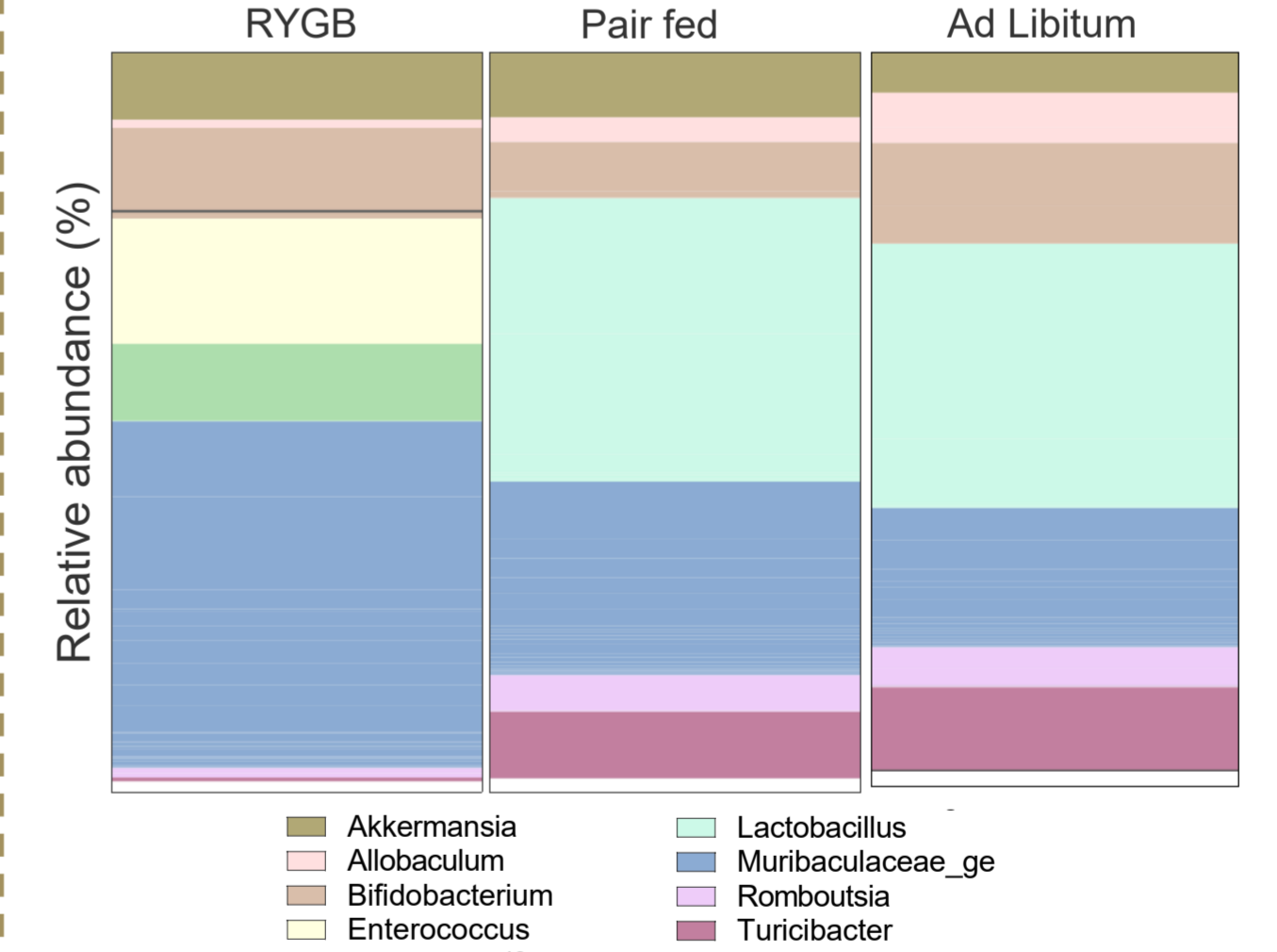
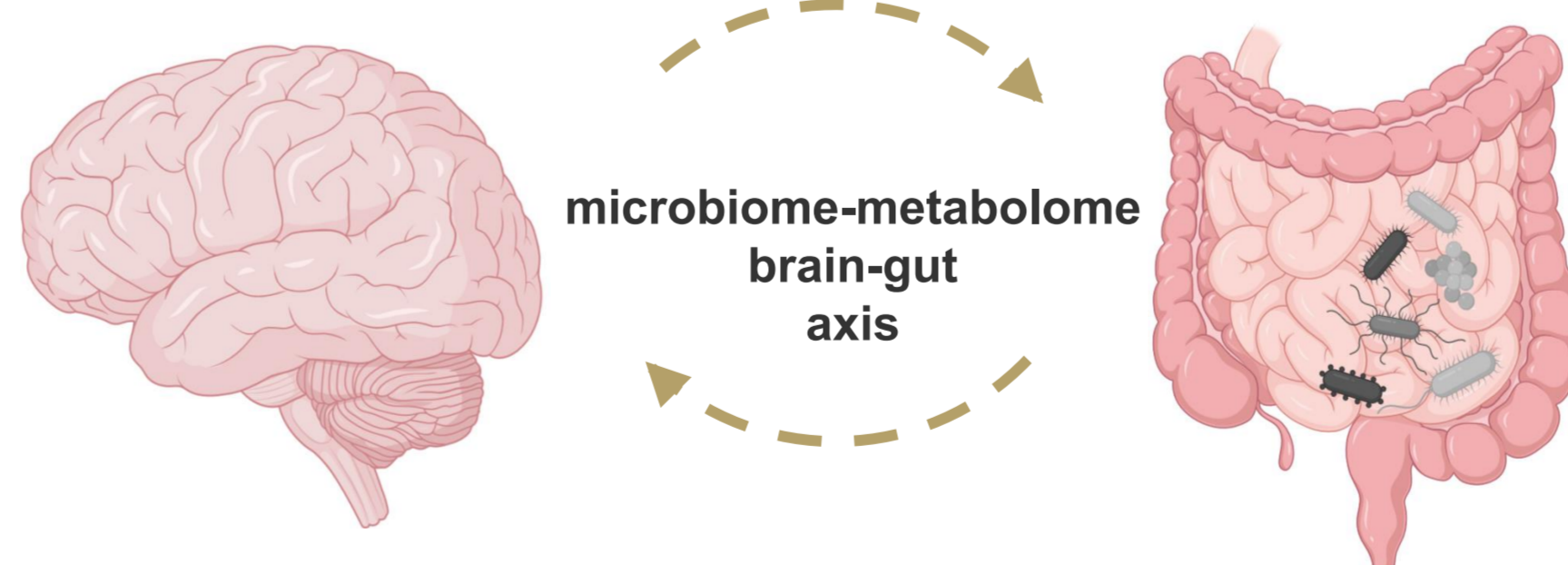


Figure 7: 16S rRNA_{seq} panel. RYGB is characterised by higher Muribaculaceae, Enterococcus and Escherichia/Shigella, and a lower abundance of Lactobacillus, Turicibacter and Romboutsia in their microbiota at 8 weeks post-surgery.

CONCLUSIONS

- Mean FDG tracer uptake was higher in RYGB animal group suggesting sucrose diet effect on glucose consumption in the brain
- dorsal endopiriform nucleus (Den) brain region had reduced c-Fos (neuronal activity marker) cell count indicating RYGB surgery effect



- RYGB leads to higher ketone body 3-hydroxybutyrate plasma concentrations which typically increases under fasting conditions ("ketogenic") diet, pointing towards "fastening-alike" metabolic state
- Significant changes in microbiota composition lead to affected metabolism by lowered short chain fatty acids, branch chain amino acids, GABA build-up which agrees to similar studies in literature⁽⁴⁾
- Lowered C-reactive protein has been associated with health benefits and decreased risk for heart disease⁽⁵⁾

REFERENCES

- Hankir, M. K.; Patt, M.; Patt, J. T. W.; Becker, G. A.; Rullmann, M.; Kranz, M.; Deuther-Conrad, W.; Schischke, K.; Seyfried, F.; Brust, P.; Hesse, S.; Sabri, O.; Krugel, U.; Fenske, W. K., Suppressed Fat Appetite after Roux-en-Y Gastric Bypass Surgery Associates with Reduced Brain mu-opioid Receptor Availability in Diet-Induced Obese Male Rats. *Frontiers in Neuroscience* 2017, 10, (2) Hankir, M. K.; Seyfried, F.; Miras, A. D.; Cowley, M. A., Brain Feeding Circuits after Roux-en-Y Gastric Bypass. *Trends in Endocrinology and Metabolism* 2018, 29 (4), 218-237.
- Gastric bypass depiction. https://en.wikipedia.org/wiki/Gastric_bypass_surgery#/media/File:Gastric_bypass_icon.svg (4) Seyfried, F.; Phetcharaburanin, J.; Glymenaki, M.; Nordbeck, A.; Hankir, M.; Nicholson, J. K.; Holmes, E.; Marchesi, J. R.; Li, J. V., Roux-en-Y gastric bypass surgery in Zucker rats induces bacterial and systemic metabolic changes independent of caloric restriction-induced weight loss. *Gut microbes* 2021, 13 (1), 1-20. (5) Holdstock, C.; Lind, L.; Engstrom, B. E.; Ohrvall, M.; Sundbom, M.; Larsson, A.; Karlsson, F. A., CRP reduction following gastric bypass surgery is most pronounced in insulin-sensitive subjects. *International Journal of Obesity* 2005, 29 (10), 1275-1280.

ACKNOWLEDGEMENT

LZ, SB, LK, KH and CT thank the Werner Siemens Imaging Center, Prof. Dr. Bernd J. Pichler and the Werner Siemens Foundation. We thank Metabolomics 2021 online organisers and you for your attention!





Investigation of crosslinks between DJ-1 (Park7) mutation and murine faeces and serum metabolomics studied by 1.7 mm ¹H-NMR spectroscopy

Laimdota Zizmare¹, Yogesh Singh^{2,3}, Bernd J. Pichler¹, Christoph Trautwein¹

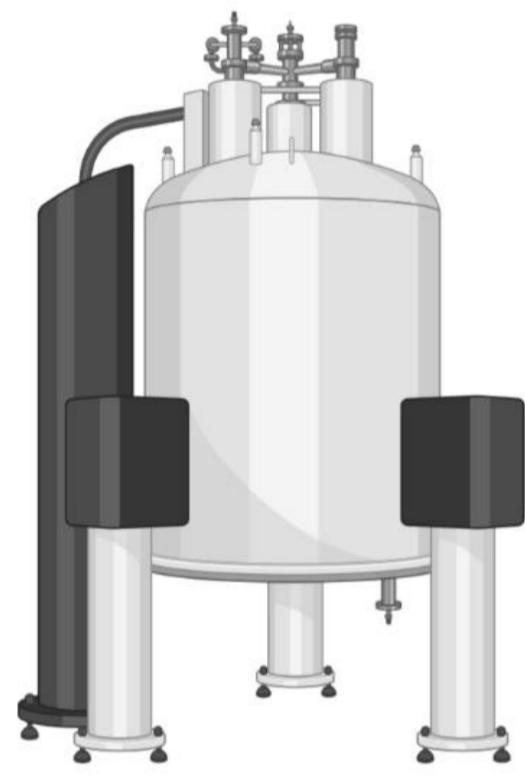
¹Werner Siemens Imaging Center (WSIC), Department of Preclinical Imaging and Radiopharmacy, Röntgenweg 13, 72076, Eberhard Karls University of Tübingen, Germany. ²Institute of Medical Genetics and Applied Genomics, Calwerstraße 7, 72076, Eberhard Karls University of Tübingen, Germany. ³Department of Women Health, Calwerstraße 7, 72076, Eberhard Karls University of Tübingen, Germany.

INTRODUCTION

❖ DJ-1 (Park7) gene mutations are associated with **Parkinson's disease (PD)**.



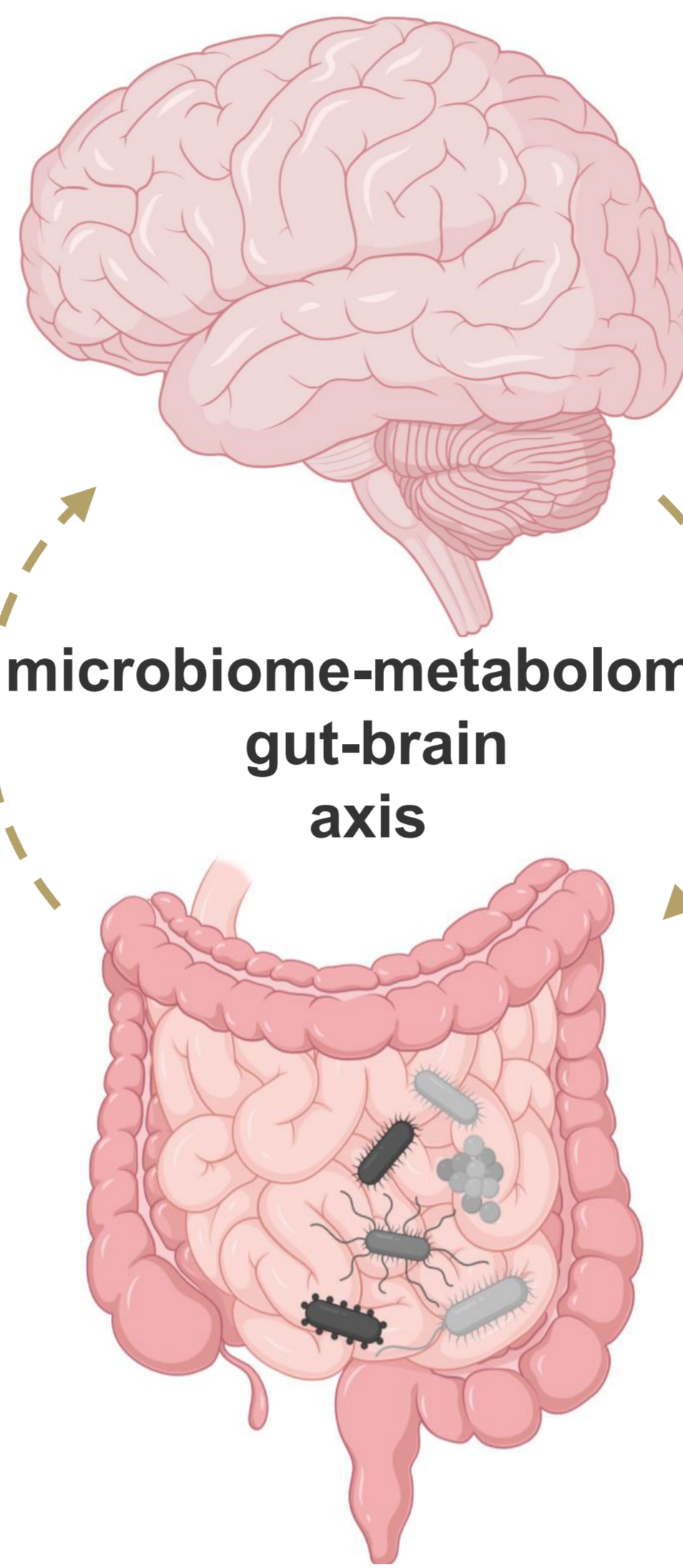
❖ Our aim: to identify metabolic changes that could relate DJ-1 triggered PD with **gut bacterial activity**⁽¹⁾.



❖ Hypothesis: DJ-1 has a regulatory role in the inflammatory and immune processes affecting gut microbiome.

❖ We analysed **serum** and **faeces** samples from DJ-1^{-/-} (KO) and DJ-1^{+/+} (WT) mice by ¹H NMR metabolomics.

microbiome-metabolome gut-brain axis



METHODS

Sample preparation

1. Ultrasonic 2-phase metabolite extraction⁽²⁾
2. Centrifugation and phase separation
3. Solvent evaporation to dryness
4. Metabolite pellet re-suspension and 1.7 mm tube filling

Spectra acquisition

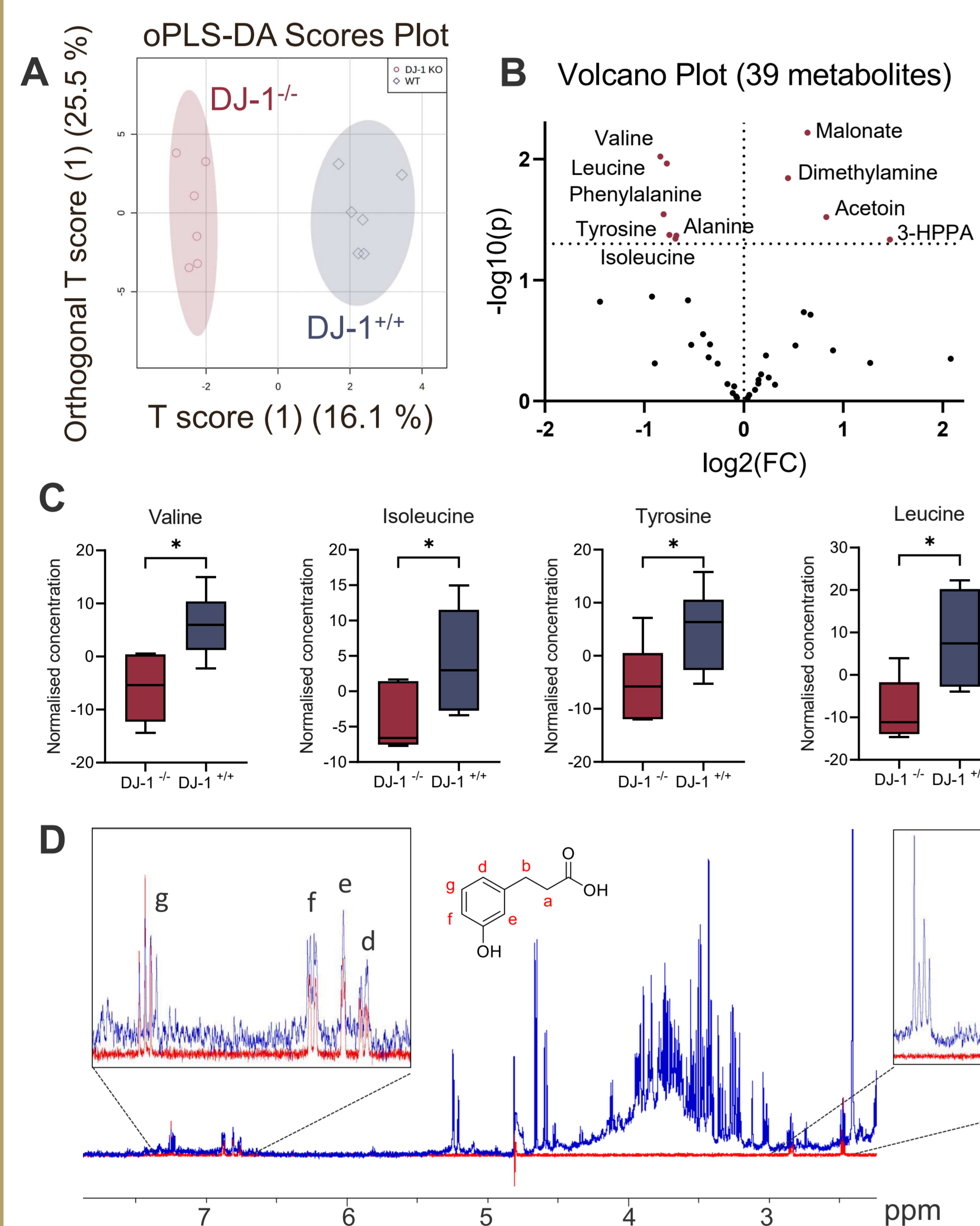
5. 600 MHz NMR spectrometer with 1.7 mm triple resonance room temperature probe
6. Short ZG and 1h CPMG (Carr-Purcell-Meiboom-Gill)

Data analysis

7. Spectra processing with TopSpin 3.6.1
8. Metabolite quantification with ChenomX 8.5
9. Metabolite statistical analysis with MetaboAnalyst 3.0

RESULTS

Faeces metabolites



Serum metabolites

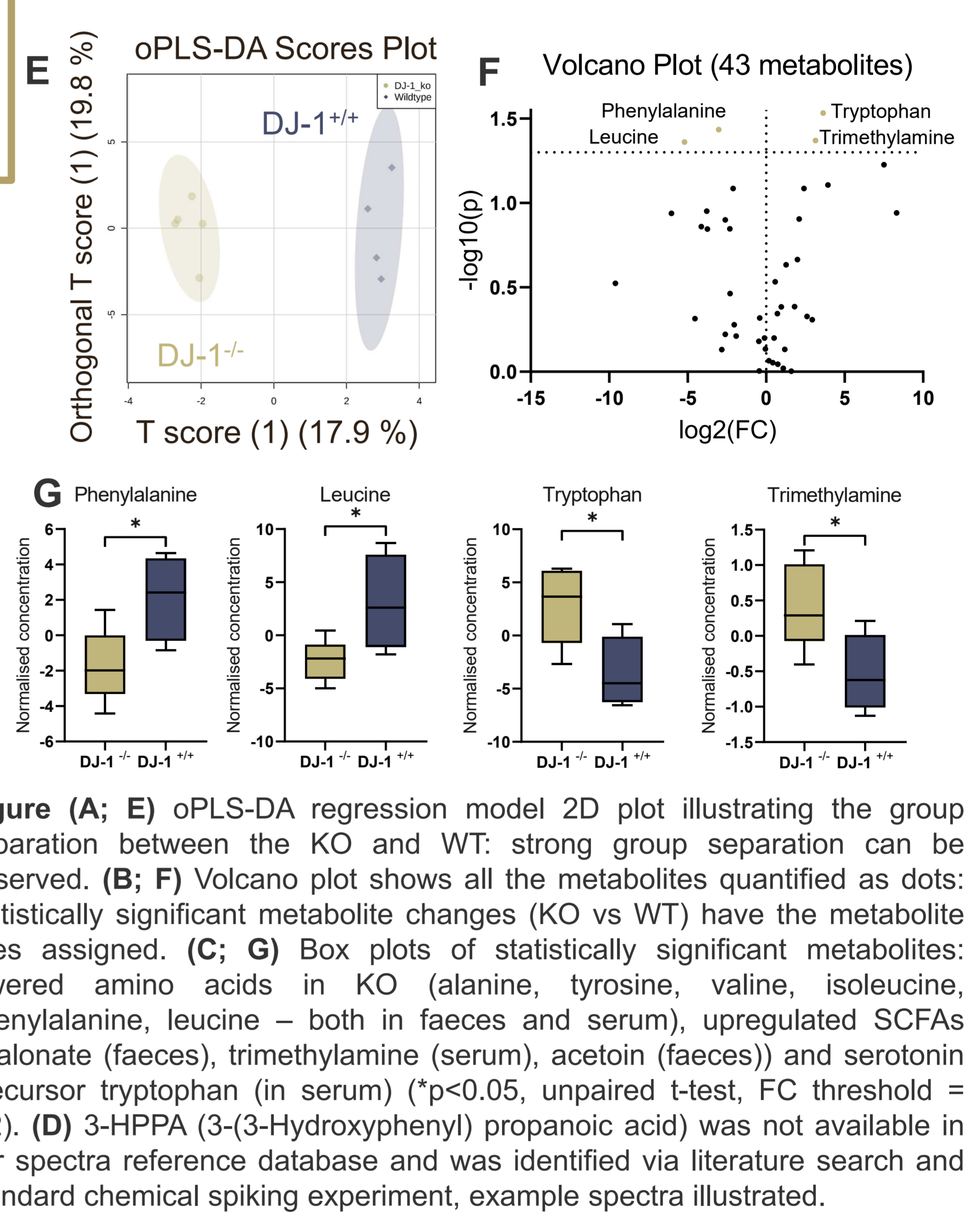
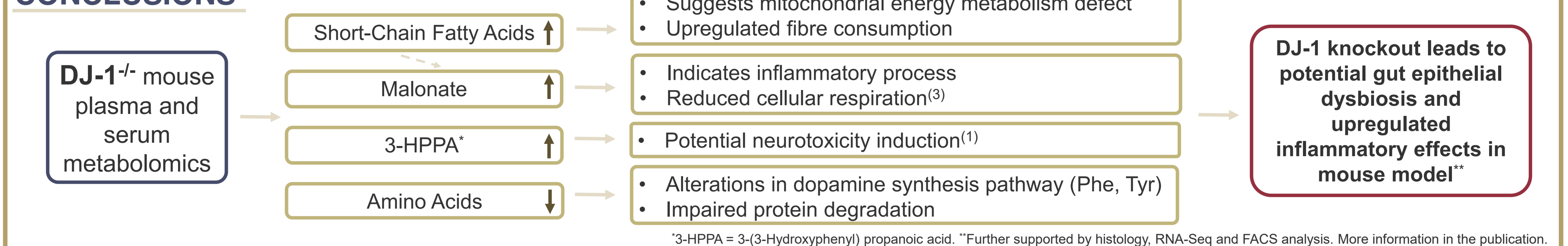


Figure (A; E) oPLS-DA regression model 2D plot illustrating the group separation between the KO and WT: strong group separation can be observed. **(B; F)** Volcano plot shows all the metabolites quantified as dots: statistically significant metabolite changes (KO vs WT) have the metabolite titles assigned. **(C; G)** Box plots of statistically significant metabolites: lowered amino acids in KO (alanine, tyrosine, valine, isoleucine, phenylalanine, leucine – both in faeces and serum), upregulated SCFAs (malonate (faeces), trimethylamine (serum), acetoin (faeces)) and serotonin precursor tryptophan (in serum) (*p<0.05, unpaired t-test, FC threshold = 1.2). **(D)** 3-HPPA (3-(3-Hydroxyphenyl) propanoic acid) was not available in our spectra reference database and was identified via literature search and standard chemical spiking experiment, example spectra illustrated.

CONCLUSIONS



REFERENCES

1. Pasinetti, G. M.; Singh, R.; Westfall, S.; Herman, F.; Faith, J.; Ho, L., The Role of the Gut Microbiota in the Metabolism of Polyphenols as Characterized by Gnotobiotic Mice. *Journal of Alzheimers Disease* 2018, 63 (2), 409-421.
2. Matyash, V.; Liebisch, G.; Kurzchalia, T. V.; Shevchenko, A.; Schwudke, D., Lipid extraction by methyl-tert-butyl ether for high-throughput lipidomics. *Journal of Lipid Research* 2008, 49 (5), 1137-1146.
3. Sancho, D., Enamorado, M. & Garaude, J. Innate immune function of mitochondrial metabolism. *Front. Immunol.* 2017, 8, 527.
4. The images and figures have been created with MetaboAnalyst (oPLS-DA), GraphPad Prism (Volcano, box plots) and www.biorender.com (2020).

ACKNOWLEDGEMENT

This work has been recently published as part of the research paper: Singh, Y., Trautwein, C., Dhariwal, A. et al. *DJ-1 (Park7) affects the gut microbiome, metabolites and the development of innate lymphoid cells (ILCs)*. *Sci Rep* 10, 16131 (2020). <https://doi.org/10.1038/s41598-020-72903-w>



EX VIVO ANALYSIS OF HUMAN GLIOMA TISSUE EXTRACTS BY ³¹P-NMR SPECTROSCOPY AS POTENTIAL DIAGNOSTIC MEASURE FOR GLIOMA SUBTYPE AND IDH MUTATION STATUS DISCRIMINATION BY IN VIVO MR SPECTROSCOPY

LAIMDOTA ZIZMARE¹, CHRISTOPH TRAUTWEIN¹, BJÖRN BAYER², IRINA GEPFNER-TUMA², GHAZALEH TABATABAI^{2,3}, BERND J. PICHLER^{1,3}

¹ Werner Siemens Imaging Center, Department of Preclinical Imaging and Radiopharmacy, University Hospital Tübingen, Eberhard Karls University Tübingen;

² Interdisciplinary Division of Neuro-Oncology, Departments of Neurology & Neurosurgery, University Hospital Tübingen, Hertie Institute for Clinical Brain Research, Eberhard Karls University Tübingen; ³ German Cancer Consortium (DKTK), DKFZ partner site Tübingen, University Hospital Tübingen, Eberhard Karls University Tübingen

INTRODUCTION

70% of gliomas (heterogeneous central nervous system primary tumors) carry an isocitrate dehydrogenase (IDH) mutation that results in changed intracellular signalling and epigenetics by increased levels of the oncometabolite 2-hydroxyglutarate (2-HG) (1,2) (Figure 1).

Previous *ex vivo* phospholipid ³¹P-NMR spectroscopy shows a clinically relevant ratio of PtdCho to the rest of phospholipid peaks that could serve as a diagnostic measure for *in vivo* MRS (3).

When employing ¹H-NMR spectroscopy for polar tissue extracts of glioma (unpublished) we found that the ratio of the phosphometabolites phosphocholine/glycerophosphocholine (PC/GPC) is much higher in wildtype than in IDH-mutated tumors. This can be seen as growth marker while both PC and GPC are precursors to PtdCho (Figure 1C).

We aimed to 1) optimize the metabolite extraction protocol for ³¹P-NMR and 2) assess if different phospholipid species and ratios from ³¹P-NMR spectra can be correlated with tumor entity, WHO grade and IDH mutation status and could have a potential to serve for *in vivo* MRS.

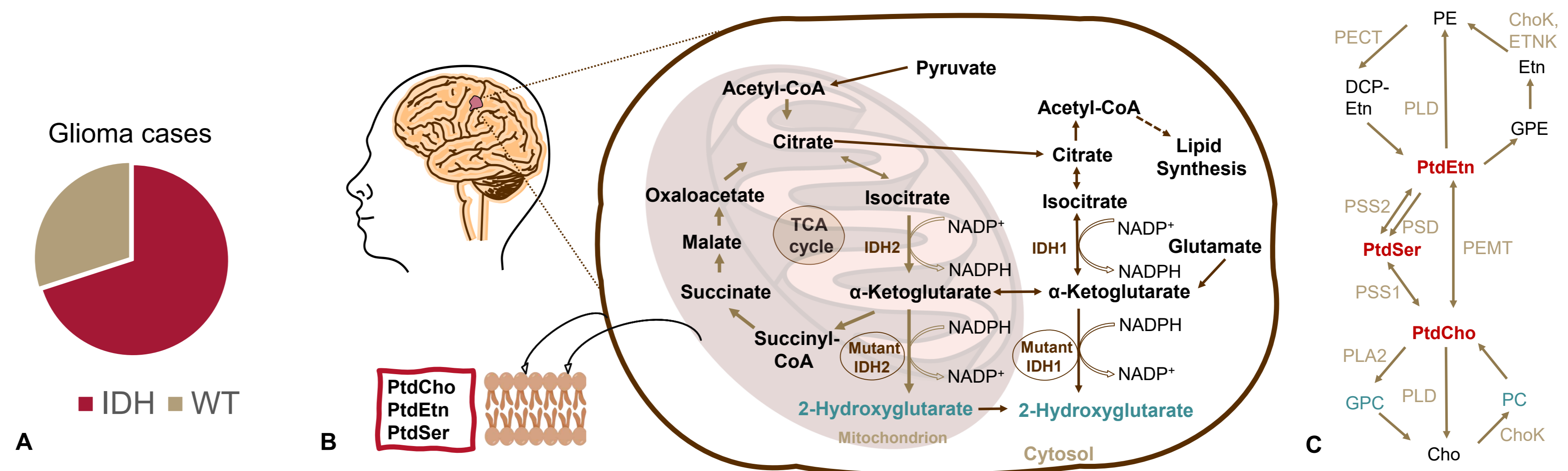


Figure 1: The majority (70%) of glioma cases have an IDH mutation (A). IDH 1/2 catalyzes the oxidative decarboxylation of isocitrate and further oncometabolite synthesis due to gene mutations. Mutant IDH alters the TCA cycle and citrate generation which is involved in lipid synthesis. While axon membranes of neurons consist mainly of glycolipids (28%) and cholesterol (22%) with low PtdCho (10%), PtdEtn (15%), PtdSer (9%) and SM (8%), mitochondrial membranes consist of mainly PtdCho (44%) + PtdEtn (28%) and lack SM (4). Most phospholipids can be detected by ³¹P-NMR (B); Schematic representation of choline and ethanolamine phospholipid metabolism (C). B&C adapted from Esmaili et al., 2014 (5).

Abbreviations: Etn, ethanolamine; CDP-Etn, cytidinediphosphate ethanolamine; PtdSer, phosphatidylserine; PtdCho, phosphatidylcholine; PtdEtn, phosphatidylethanolamine; PC, phosphocholine; Cho, choline; GPC, glycerophosphocholine; PE, phosphoethanolamine; GPE, glycerophosphoethanolamine; ChoK, choline kinase; ETNK, ethanolamine kinase; cPLA2, cytosolic phospholipase A2; PLC, phospholipase C; PSD, phosphatidylserine decarboxylase; PSS1, phosphatidylserine synthase I; PSS2, phosphatidylserine synthase II; PEMT, phosphatidylethanolamine N-methyltransferase.

METHODS

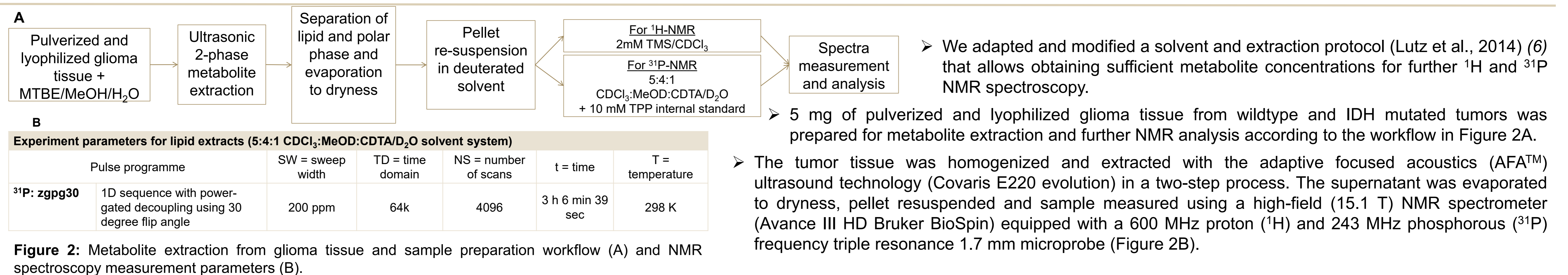


Figure 2: Metabolite extraction from glioma tissue and sample preparation workflow (A) and NMR spectroscopy measurement parameters (B).

RESULTS

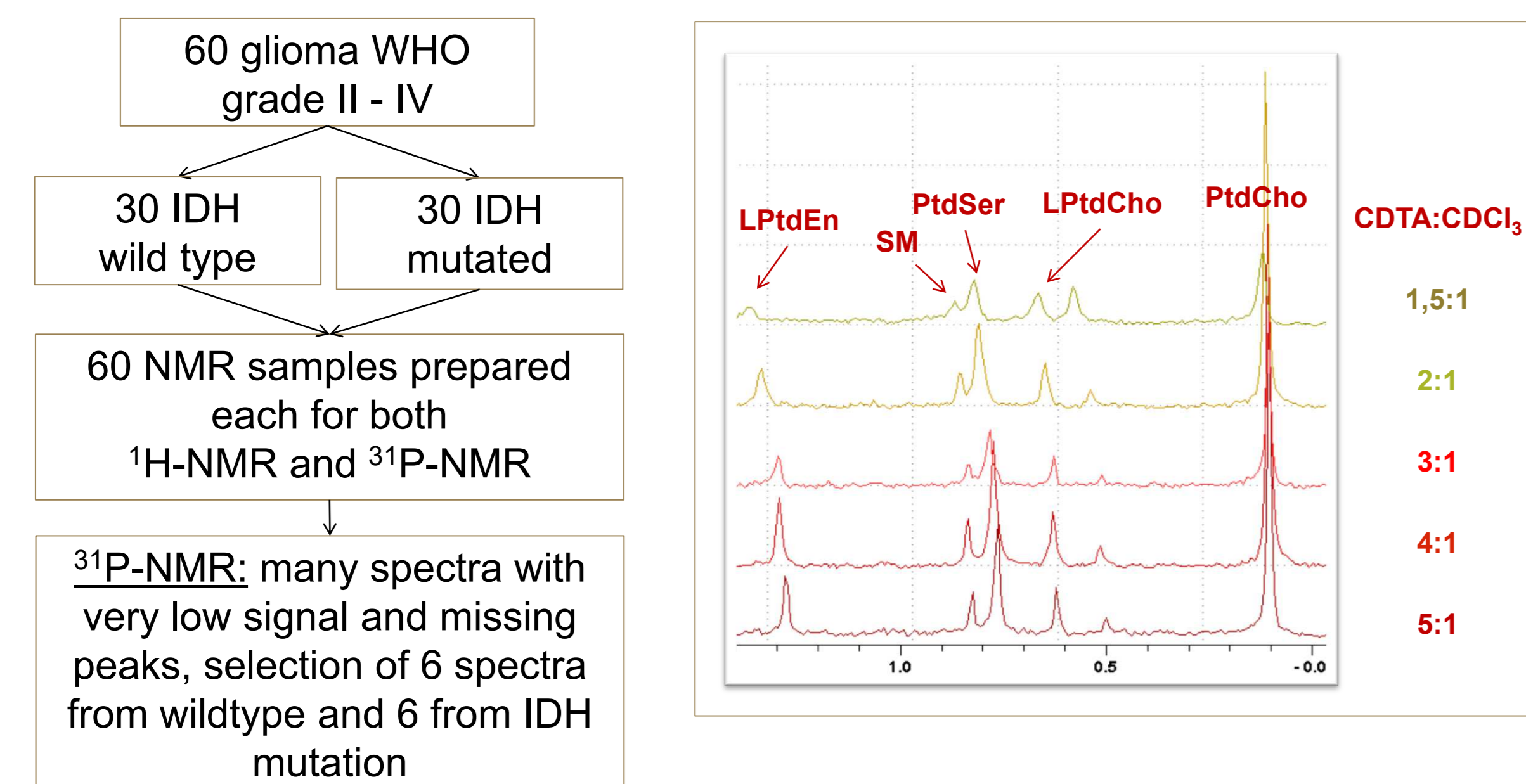


Figure 3: Overview of the sample cohort and the outcome after ³¹P-NMR spectroscopy. Due to a very complex heterogeneous sample group the spectral peaks were not always well separated or some signals were missing, overlapping, therefore only small subset was obtained that would qualify for necessary analysis.

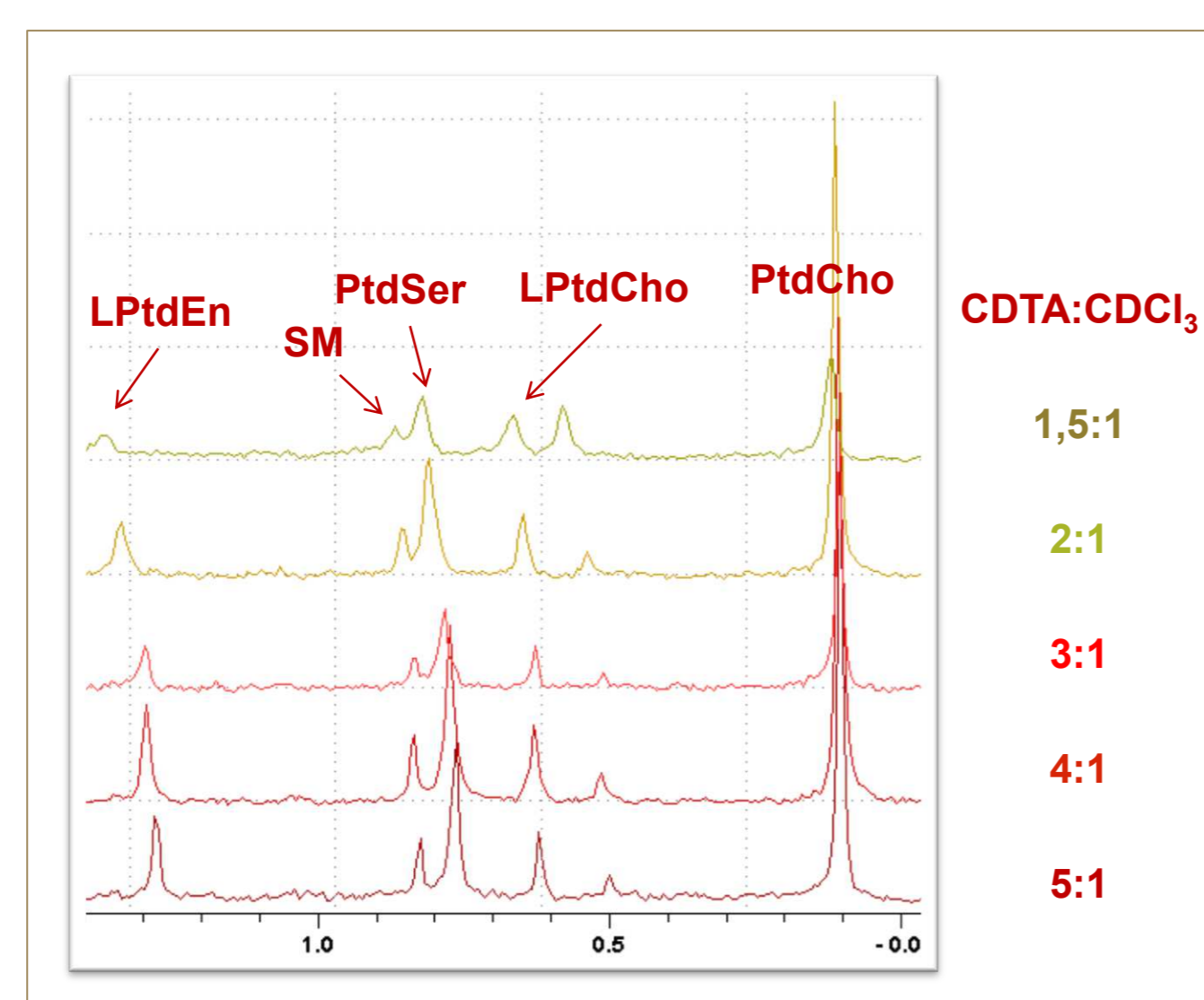


Figure 4: Characteristic ³¹P-NMR spectra (scale: ppm) of a standard solution, illustrating the solvent composition impact on the peak position. ³¹P spectra are very sensitive to slight changes in the CDTA:CDCl₃ mixture which leads to the peak shifts with minor solvent ratio changes (CDTA = 5:4:1 solution).

Abbreviations for peak annotation:

1) PtdCho, Phosphatidylcholine; 2) PS, Phosphatidylserine; 3) LPtdCho, Lysophosphatidylcholine; 4) SM, Sphingomyelin; 5) PtdEtn, Phosphoethanolamine; 6) PtdEtn_(plasm), Ethanolamine plasmalogen, 1-alkenyl-2-acyl-sn-glycero-3-phosphoethanolamine; 7) LPtdEn, Lysophosphatidylethanolamine.

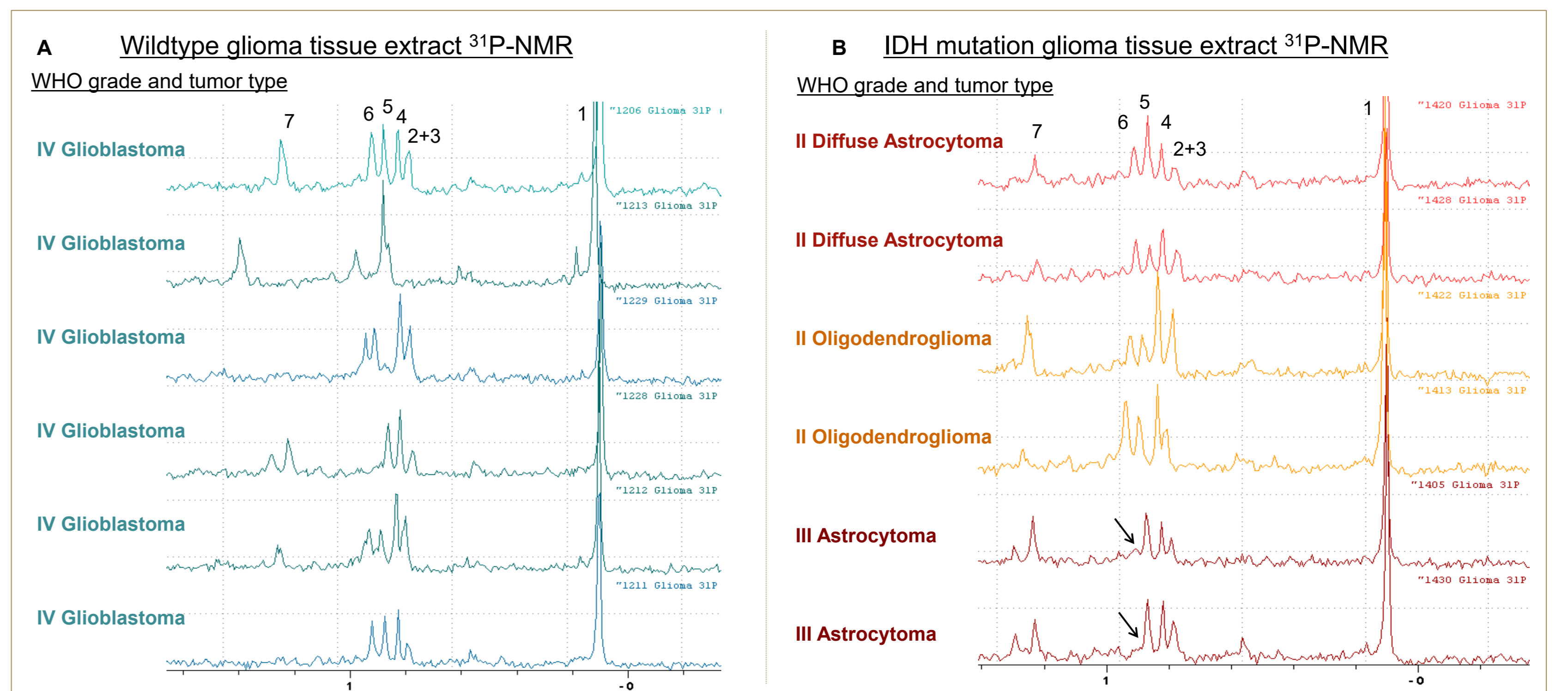


Figure 5: ³¹P-NMR spectra of glioma tissue lipid extracts from wildtype (A) and IDH-mutated tumor biopsies (B). All wildtype tumors are WHO grade IV Glioblastoma. The IDH mutated tumors vary from grade and tumor type as well as their spectra have significant peak differences between the types and within the groups. Annotation based on spiking experiments (compounds 1 – 4 & 7) and previous literature (5 & 6) by Lutz et al., 2014 (6).

CONCLUSION

Metabolite extraction protocol optimization for ³¹P-NMR

- Our adopted and modified metabolite extraction protocol allows obtaining well-resolved ¹H (data not shown here) and ³¹P-NMR spectra of the phospholipid metabolites from the same pellet of the extract under a passable acquisition time.
- Metabolites, such as PtdCho, LPtdCho, PtdEtn, LPtdEn, PtdEtn_(plasm), as well as PtdSer, Ptdl, PG, SM can be identified by ³¹P-NMR and their concentrations or ratios can be obtained and further calculated.
- Current study limitations potentially derive from the heterogeneity of tumor samples (WHO grade, IDH status, drug treatment, vascularisation), buffer contaminations or storage and transportation non-optimized conditions.

Glioma and ³¹P-NMR: correlations between IDH mutation, tumor entity and classification

- Our findings suggest that there are phosphometabolite concentration differences between Astrocytoma (grade III) and other IDH in the ethanolamine PtdEtn_(plasm) region (arrows Figure 5B).
- We also observed a potential PtdEtn_(plasm) peak intensity decrease when LPtdEn peak increases suggesting that these two metabolites are balancing each other.
- This preliminary study of 60 glioma samples (30 IDH-mutated and 30 wildtype) provided only 6 well-resolved ³¹P-NMR spectra in wildtype and 10 in IDH mutated glioma tissue samples with all the expected peaks. Thus, larger sample cohort with strict SOP is necessary to be able to draw strong conclusions.
- Due to current limitations, we cannot provide a strict epigenetic distinction between IDH-mutated and wildtype glioma cases yet. Future studies should therefore include epigenetic and transcriptomic analysis from the same tissue extract for a better understanding of the tumor biology.

REFERENCES

- (1) LOUIS, D. N., PERRY, A., REIFENBERGER, G., VON DEIMLING, A., FIGARELLA-BRANGER, D., CAVENEE, W. K., OHGAKI, H., WIESTLER, O. D., KLEIHUES, P. & ELLISON, D. W. 2016. The 2016 World Health Organization Classification of Tumors of the Central Nervous System: a summary. *Acta Neuropathologica*, 131, 803-820. (2) KAMINSKA, B., CZAPSKI, B., GUZIK, R., KRÓL, S. K. & GIELNIEWSKI, B. 2019. Consequences of IDH1/2 Mutations in Gliomas and an Assessment of Inhibitors Targeting Mutated IDH Proteins. *Molecules*, 24. (3) SRIVASTAVA, N. K., PRADHAN, S., GOWDA, G. A. N. & KUMAR, R. 2010. *In vitro*, high-resolution H-1 and P-31 NMR based analysis of the lipid components in the tissue, serum, and CSF of the patients with primary brain tumors: one possible diagnostic view. *NMR in Biomedicine*, 23, 113-122. (4) LAMOND, A. I. 2002. Molecular biology of the cell, 4th edition. Nature, 417, 383-383. (5) ESMAELI, M., HAMANS, B. C., NAVIS, A. C., VAN HORSSEN, R., BATHEN, T. F., GRIBBESTAD, I. S., LEENDERS, W. P. & HEERSCHAP, A. 2014. IDH1 R132H Mutation Generates a Distinct Phospholipid Metabolite Profile in Glioma. *Cancer Research*, 74, 4898-4907. (6) LUTZ, N. W., BERAUD, E. & COZZONE, P. J. 2014. Metabolomic analysis of rat brain by high resolution nuclear magnetic resonance spectroscopy of tissue extracts. *Journal of visualized experiments : JoVE*, 51829-51829.